



SAPIENZA
UNIVERSITÀ DI ROMA

DEPARTMENT OF BASIC AND APPLIED SCIENCES FOR ENGINEERING

**PhD Thesis in Mathematical Models for Engineering,
Electromagnetism and Nanosciences**

**Second order traffic flow models on road networks
and real data applications**

Supervisor
Dr. Maya Briani

Candidate
Caterina Balzotti

Cycle XXXIII

Roads? Where we're going
We don't need roads!
Doc Brown

Abstract

This thesis concerns macroscopic traffic models and data-driven models. In the first part we deal with the extension of Generic Second Order Models (GSOM) for traffic flow to road networks. We define a Riemann Solver at the junction based on a priority rule, providing an iterative algorithm able to build the solution to junctions with n incoming and m outgoing roads. The logic underlying our solver is the following: the flow is maximised respecting the priority rule, but the latter can be modified if the outgoing road supply exceeds the demand of the road with higher priority. We provide bounds on the total variation of waves interacting with the junction, giving explicit computations for intersections with two incoming and two outgoing roads. These estimates are fundamental to prove the existence of weak solutions to Cauchy problems on networks via Wave-Front-Tracking.

GSOM are used to analyse traffic dynamics and their effects on the production of pollutant emissions. First we apply the proposed Riemann Solver to simulate traffic dynamics on diverge and merge junctions and on roundabouts obtained by combining these two types of intersection. Then, we propose a methodology to estimate the pollutant emissions deriving from traffic dynamics. The emission model is calibrated and validated using the NGSIM dataset of real trajectory data. Furthermore, we set up a minimisation problem aimed at finding the optimal priority rule for our Riemann Solver that reduces the emission rates due to the traffic dynamic. Finally, we analyse some chemical reactions which lead to the production of ozone, focusing on the effects on pollution of the presence of traffic lights on the road.

Next, we introduce a macroscopic two-dimensional multi-class traffic model on a single road, aimed at including lane-changes and different types of vehicles. The multi-class model consists of a coupled system of conservation laws in two space dimensions. Besides the study of the Riemann problems, we present a Lax-Friedrichs type discretisation scheme and we recover the theoretical results by means of numerical tests. We then calibrate and validate the multi-class model with real trajectory data and we test its ability of simulating vehicles overtaking.

Finally, we present a new methodology to recover mass movements from snapshots of its distribution. To this end we put in place an algorithm based on the combination of two methods: first, we use the dynamic mode decomposition to create a system of equations describing the mass transfer; second, we use the Wasserstein distance to reconstruct the underlying velocity field that is responsible for the displacement. We conclude this part with a real-life application: the algorithm is employed to study the travel flows of people in large populated areas using, as input, presence data of people in given region domains derived from the mobile phone network, at different time instants.

Acknowledgments

I would like to express all my gratitude to my supervisor Maya Briani, for the continued support she has given me over the last few years. She taught me a lot, with great patience, and contributed to my growth both from a scientific and a personal point of view.

A special thanks goes to Simone Göttlich and all the SCICOM team for welcoming me during my research stay at Mannheim. I really appreciated the two months spent there and our collaboration. I am much obliged to Benedetto Piccoli for all the fruitful discussions we have had during these three years, and to Emiliano Cristiani for introducing me to the world of traffic models that brought me here. I would also like to thank my collaborators Alessandro Alla, Barbara De Filippo, Mirko D'Ovidio and Paola Loreti for allowing me to enlarge my research interests.

I am very grateful to Michael Herty and Paola Goatin for accepting to be the reviewers of my thesis and for their careful comments that helped me to improve it.

This experience would not have been the same without the special colleagues I found at the SBAI Department. I wish to express my appreciation to Elisa, Nicole, Laura, Lorenzo, Michela, Gabriele, Davide, Simone, Salvo, Alessandro and Raul. I would also like to thank Davide, Mara and Claudia for making lighter even the most stressful days at IAC.

I wouldn't be here without the encouragement of my family and friends. I am blessed to have by my side my old friends Katia, Sara, Giulia and Francesco who still support me, as they always do. I am infinitely grateful to Mom and Dad for giving me the opportunity to study and for being such lovely parents, and to my wonderful brothers, Lorenzo and Francesco, who always know how to make me laugh.

Last but not least, my deepest gratitude goes to Antonio. His love helped me to overcome any difficulties and brought out the best in me. I would do it all over again just to meet you.

Contents

Introduction	1
1 Preliminaries	7
1.1 Riemann problem for systems of conservation laws	7
1.2 Macroscopic traffic models	11
1.3 Macroscopic traffic models on road networks	13
1.4 Data-fitting: reconstruction of macroscopic quantities from microscopic data	14
2 Generic Second Order Models for traffic on road networks	17
2.1 Introduction to GSOM	17
2.1.1 The CGARZ model	19
2.2 The Riemann problem for GSOM on a single road	21
2.3 The Riemann problem for GSOM at junctions	23
2.3.1 Basic definitions	23
2.3.2 The case of one incoming road and one outgoing road at junctions	30
2.3.3 The case of diverge junction	31
2.3.4 The case of merge junction	32
2.4 The APRSOM algorithm for n incoming and m outgoing roads at junctions	36
3 Bounds on the total variation at the junction	41
3.1 Preliminaries for the estimates	41
3.2 Estimates for the case of two incoming and two outgoing roads at junctions	43
3.2.1 Case A	47
3.2.2 Case B	53
3.2.3 Case C	59
4 Application of GSOM to traffic dynamics on road networks	65
4.1 Numerical method for GSOM	65
4.1.1 Comparing CGARZ with LWR	67
4.2 The CGARZ model on road networks with APRSOM	68
4.2.1 The case of $1 \rightarrow 2$ junction	69
4.2.2 The case of $2 \rightarrow 1$ junction	71
4.2.3 The case of a roundabout	71
5 Application of traffic dynamics to pollution	77
5.1 Approximation of traffic quantities	77
5.1.1 An alternative discrete formula for vehicles acceleration	78
5.2 Estimating emissions from traffic quantities	78

Contents

5.2.1	Validation of the emission model	79
5.3	Optimising the priority rule to minimise emission rates	83
5.3.1	Estimate of NO_x emission rates on a network	86
5.4	Chemical reactions	87
5.4.1	Numerical discretisation of the complete procedure	90
5.4.2	Estimate of NO_x emission rates and ozone production on a single road	91
6	A two-dimensional multi-class traffic model	97
6.1	A LWR-type two-dimensional multi-class model	97
6.1.1	The Riemann problem associated to the model	98
6.2	Numerical discretisation	101
6.2.1	Validation	102
6.3	Data-driven multi-class model in 2D	103
6.3.1	Fundamental diagrams	104
6.3.2	Reconstruction of density from data	106
6.3.3	Numerical test	107
6.4	Further data analyses	109
6.4.1	Test with real data	109
6.4.2	Vehicles overtaking	110
7	Understanding mass transfer directions via data-driven models	113
7.1	Mathematical background	114
7.1.1	DMD method	114
7.1.2	Wasserstein distance and optimal mass transfer problem	115
7.1.3	Numerical approximation of the Wasserstein distance	116
7.2	Coupling DMD and optimal mass transfer problem	117
7.2.1	Main idea	117
7.2.2	A toy example for the complete algorithm: the advection equation	118
7.3	Application to real mobile phone data	121
7.3.1	Dataset	122
7.3.2	DMD approach on TIM data	123
7.3.3	Understanding human mobility flows	123
7.3.4	Numerical results	125
	Conclusions	129
	Bibliography	131

Notation

We collect here a list of notation commonly used in this thesis.

Spaces

\mathbb{R}	The set of real numbers.
C^1	The set of continuous functions with continuous derivatives.
L^1_{loc}	The set of locally integrable functions.

Riemann Solver notation

ρ_i^-, w_i^-, q_i^-	Density, w and flux on incoming road i at junctions.
$\hat{\rho}_i, \hat{w}_i, \hat{q}_i$	Density, w and flux on incoming road i , solution of the Riemann Solver at junctions.
ρ_j^+, w_j^+, q_j^+	Density, w and flux on outgoing road j at junctions.
$\hat{\rho}_j, \hat{w}_j, \hat{q}_j$	Density, w and flux on outgoing road j , solution of the Riemann Solver at junctions.

Units of measurement

m	Metre.
cm	Centimetre.
km	Kilometre.
s	Second.
min	Minute.
h	Hour.
m/s	Metres per second.
km/h	Kilometres per hour.
veh/km	Number of vehicles per kilometre.
g	Gram.
molec.	Number of molecules.

Introduction

Mathematical models for vehicular traffic are a topic of growing interest for the scientific community, due to their connections with problems of everyday life, such as pollution and congestions in large cities. The development of mathematical models is useful to improve traffic management, providing solutions to optimise transport for economic and environmental benefits, including the reduction of vehicle queues and pollution. In recent years, the ever-increasing amount of real data, due to new technologies, has widely influenced the research on mathematical models. The presence of such a huge amount of data allows not only the calibration of new models but also their validation by comparison between simulations and real data. This thesis is mainly devoted to traffic flow models, ranging from theoretical and modelling aspects to real life applications and data-driven modelling. The contribution on traffic modelling concerns second order models on networks and a two-dimensional multi-class model. The applications involve the analysis of traffic dynamics and their environmental impact in terms of pollutant emissions. Finally, real data is used to calibrate and validate traffic models as well as to define a methodology aimed at reconstructing people movements from the mobile phone network data.

Traffic flow models have now a long history and are divided into three main categories, depending on the scale of observation: microscopic, macroscopic and kinetic models. *Microscopic* models [5, 34, 39, 67] follow the trajectory of every single vehicle on the road, whose dynamic is described by systems of ordinary differential equations (ODEs). The dynamic of vehicles is usually assumed to be influenced by the first vehicle on the road, thus they are called *follow-the-leader* models. *Macroscopic* models are described by aggregated quantities, such as the density, the velocity and the flux of vehicles. These models are based on fluid dynamic equations, with the basic evolution equation defined by the conservation of vehicles, and are described by systems of partial differential equations (PDEs). The first macroscopic model for traffic flow was proposed in the 1950s by Lighthill, Whitham and Richards [63, 79] and numerous other models have followed since then, see e.g. [6, 59, 72, 92, 94]. *Kinetic* models [48, 66, 75, 76] are between the previous two classes since they can be derived by microscopic models as well as macroscopic models can be derived by kinetic descriptions. Kinetic models track the position and the velocity of each vehicle as microscopic models, but the dynamic of the system relies on a probability distribution over the microscopic state. For a more complete review on traffic models we refer to [13, 74] and references therein.

This thesis is mainly focused on macroscopic second order traffic models on road networks, based on a system of PDEs which usually couples an equation for the conservation of vehicles with an equation for the evolution of the flux. We deal with Generic Second Order Models (GSOM) [59] which are a family of traffic models described by a first order scalar conservation law for the density of vehicles ρ combined with an advection equation of a certain property of drivers w

$$\begin{cases} \partial_t \rho + \partial_x(\rho v) = 0 \\ \partial_t w + v \partial_x w = 0 \end{cases}$$

with $v = V(\rho, w)$, for a proper velocity function V . Through the variable w it is possible to take

into account various driving behaviours, in fact it parametrises the family of fundamental diagrams $Q(\rho, w) = \rho V(\rho, w)$, whose curves correspond to different driving aptitudes.

One of the main results of this thesis is the extension of GSOM to road networks. Traffic models on networks have been widely studied in recent years and authors have considered many different traffic scenarios proposing a rich amount of alternative models at junctions. For instance, the first order Lighthill-Whitham-Richards (LWR) model [63, 79] has been extended to road networks in several papers, see [26, 32, 33, 46], as well as the second order Aw-Rascle-Zhang (ARZ) model [6, 94], see [31, 36, 42, 44].

The solution of traffic models on networks is generally based on the concept of the Riemann problem at a junction [32], which is a Cauchy problem with constant initial data on each road connected at the intersection. The treatment of traffic models on networks requires coupling conditions to define a unique solution, and the choice of such conditions distinguishes the models from each other. There are two assumptions shared by the great part of existing models: the flux is conserved through the junction and the waves generated at junctions have non-positive speed on incoming roads and non-negative speed on outgoing roads. Other common assumptions are: (A) The maximisation of the flux through the junction. (B) The distribution of vehicles on outgoing roads according to a proper distribution matrix.

Before describing our methodology, we recall the main approaches proposed for the treatment of the second order ARZ model at junctions. In [31], the authors add to assumptions (A) and (B) the maximisation of speed or density or alternatively the minimisation of the total variation of density. This approach does not conserve the generalised momentum ρw and thus the solutions of the Riemann problem at junctions are not weak solutions to the ARZ model. In [42], in addition to (B) the authors assume the conservation of the pseudo momentum $\rho v w$ and introduce a mixture rule governing how vehicles of the incoming road mix into the outgoing ones. In [55], in addition to (B) the authors assume that each incoming flux is maximised and that vehicles follow a priority rule for incoming roads. Finally, it is worth mentioning the paper [26], which deals with the first order LWR and where the authors define the solution assuming again (A) and (B) and a priority rule on incoming roads. Our treatment of junctions can be seen as an extension to second order models of this approach.

We now focus on our method, which is designed for the GSOM family, including the ARZ model. We define a Riemann Solver at junctions. The idea is to solve a left-half Riemann problem (waves have non-positive speed) for incoming roads and a right-half Riemann problem (waves have non-negative speed) for outgoing roads, defining the region of admissible states such that waves do not enter the junction. We assume the maximisation of the flux, i.e. assumption (A), and the conservation of ρ and $y = \rho w$ through the junction. The identification of a unique solution is attained introducing a priority rule on the incoming roads, as in [26, 55]. Let us consider a generic junction with n incoming and m outgoing roads. The priority rule is defined by a vector (p_1, \dots, p_n) such that $\sum_{i=1}^n p_i = 1$, and vehicles are distributed on the outgoing roads according to a proper matrix $A = \{\alpha_{ji}\}_{j=n+1, \dots, n+m}^{i=1, \dots, n}$ such that $\sum_{j=n+1}^{n+m} \alpha_{ji} = 1$, $i = 1, \dots, n$, i.e. we assume (B). We propose a new logic to obtain a unique solution as follows: the flow is maximised respecting the priority rule, but the latter can be modified if the outgoing road supply exceeds the demand of the road with higher priority. In Chapter 2 we define the Adapting Priority Riemann Solver for Second Order Models (APRSOM) that is an iterative algorithm able to construct the solution to generic junctions with n incoming and m outgoing roads, computing the incoming fluxes at the junction step by step.

The n in m case is obtained generalising the simpler cases of diverge (one incoming and two outgoing roads) and merge (two incoming and one outgoing roads) junctions. For the diverge junction the unique solution is attained by fixing a distribution parameter of the flux of vehicles among the two outgoing roads, i.e. the matrix A is reduced to a vector $(\alpha, 1 - \alpha)$. The treatment we propose in this case is similar to the one proposed in [44, 55] for the ARZ model. For the merge junction the priority rule is given by a

Introduction

vector (p_1, p_2) such that $p_1 + p_2 = 1$ and leads to the following relation between the two incoming fluxes at the junction (\hat{q}_1 and \hat{q}_2)

$$p_1 \hat{q}_2 = p_2 \hat{q}_1.$$

For example, let us assume that road 1 has the highest priority. The conservation of ρ and y at junctions implies that

$$\begin{aligned} \hat{q}_1 + \hat{q}_2 &= \hat{q}_3 \\ \hat{q}_1 w_1^- + \hat{q}_2 w_2^- &= \hat{q}_3 \hat{w}_3 \end{aligned}$$

where w_1^- and w_2^- (i.e. the properties of road 1 and 2) are given. The goal of the Riemann Solver is to compute the unknown variables \hat{q}_1 , \hat{q}_2 , \hat{q}_3 and \hat{w}_3 (i.e. the fluxes from 1 and 2, the flux to road 3 and the property of road 3, respectively). The demand of incoming roads represents the maximum flux that can be sent and defines the set Ω of possible solutions, while the supply of the outgoing road represents the maximum flux that can be received. When the priority rule identifies a couple (\hat{q}_1, \hat{q}_2) which is outside Ω , the algorithm looks for a new priority closest to the given one which maximises the flux through the junction. Hence, in our example, the algorithm sets \hat{q}_1 equal to its demand and modifies \hat{w}_3 and the couple (p_1, p_2) until it finds the solution which allows the highest flow of vehicles and respects the conservation of ρ and y .

The Riemann Solver at junctions allows the study of the following Cauchy problem on networks associated to GSOM in conservative form

$$\begin{cases} \partial_t \rho_r + \partial_x (\rho_r v_r) = 0 \\ \partial_t y_r + \partial_x (y_r v_r) = 0 \\ (\rho_r(x, 0), y_r(x, 0)) = (\rho_{r,0}(x), y_{r,0}(x)) \end{cases} \quad \text{for } r = 1, \dots, n + m$$

for the initial data $(\rho_{r,0}(x), y_{r,0}(x))$ with bounded variation, where n is the number of incoming roads and m of outgoing roads. To prove the existence of weak solutions to the Cauchy problem, a typical approach relies on the Wave-Front-Tracking (WFT) method. The latter requires the study of Riemann problems along the roads and at junctions. Following the strategy originally proposed in [33] and extended in [26], we introduce four properties that a Riemann Solver must satisfy in order to guarantee bounds on the total variation of the flux Q and of the variable w for waves that interact with the junction. More precisely, these properties allow to estimate the increase in the total variation of Q and w . In Chapter 3 we prove that our algorithm APRSOM satisfies these properties for junctions with two incoming and two outgoing roads. The proof is obtained by perturbing an equilibrium state of the network by sending waves in ρ and w along each road and estimating the resulting increase in the total variation of Q and w . The proof is divided into three cases, according to the initial condition of the equilibrium of the network. The technical details to prove the convergence of approximate solutions via WFT to the weak solution to the Cauchy problem deserve further investigations and will be contained in a forthcoming work.

Another important issue in traffic modelling is the inclusion of lane changes and the treatment of different types of vehicles. Indeed, most of traffic data collected in dataset such as [50, 88] contain information on multi-lane highways with different classes of vehicles. In order to take into account these two aspects on a single road, we propose a two-dimensional model which incorporates two types of vehicles interacting through the flux functions. The most common approaches which include lane-changing are the two-dimensional models and the multi-lane models. The former is an emerging topic, and we refer to [19, 40, 43] for some examples. The latter has been used for instance in [53, 54], where the authors propose a microscopic, a kinetic and a fluid dynamic model with lane changing. Here we propose an extension of the single-class traffic model in two space dimensions described in [40] to a multi-class model. Such model

is obtained by coupling two LWR-type models for two classes of vehicles in two space dimensions. Vehicles interact between the two classes through the flux functions which depend on the sum of vehicle densities as in [41]. With suitable assumptions on the flux functions, we study the two-dimensional Riemann problem and validate the model by comparing the theoretical results with the solutions given by a numerical approximation of Lax-Friedrichs type [57]. We then provide two applications of the model. First, we calibrate the flux functions with the German dataset [50], and we validate the model by comparing the numerical approximation of solutions with real trajectories data. Finally, we test the ability of the model of simulating vehicles overtaking.

One of the topics treated in this thesis is the environmental impact of vehicular traffic. The effects of vehicular traffic on society are huge and multifaceted, including economic, social, health and environmental aspects. The problem is complex and hard to model since it requires to consider traffic patterns, air pollutant emissions, chemical reactions as well as diffusion of pollutants in the low atmosphere. In this thesis we analyse how vehicles affect the environment by providing a tool based on three consecutive steps, each powered by the previous one. The steps are the following: 1) Estimate of traffic quantities, i.e. density, speed and acceleration of vehicles; 2) Estimate of the emission rates of specific pollutants exploiting the traffic variables; 3) Study of the chemical reactions associated to the pollutant under analysis. Such a tool can be used to support practical choices in traffic management aimed at reducing pollution due to vehicular traffic. As a first application we investigate how to reduce the pollutants emission rates through actions on the priority rule of APRSOM. Indeed, we define a minimisation problem which finds the optimal priority in terms of emissions produced. The mere request to minimise emissions can lead to unrealistic priority rules, such as a fixed red traffic light on one of the two incoming roads of a merge junction. To fix this, we set up a minimisation problem which finds the priority that minimises the emission rates and the travel time. We propose two different approaches of APRSOM: one which strictly respects the priority and one which adapts it looking for the maximisation of the flux. It is interesting to note that the travel time is automatically optimised by APRSOM when it adapts the priority rule, but this leads to an increase in emissions compared to those produced following the given priority. The compromise of minimising both the emissions and the travel time allows to find realistic and efficient solutions for the management of vehicles flows and the reduction of pollution.

The emission model is calibrated and validated through the NGSIM dataset [88], which contains real vehicles trajectory data, by processing microscopic information in macroscopic quantities. The analysis of the environmental impact of traffic is then focused on nitrogen oxides (NO_x) emissions and on the chemical reactions which lead to ozone (O_3) production, due to its negative effects on health. The chemical reactions are modelled through a system of ODEs, where the traffic model is responsible for the source term of the system, representing the NO_x emissions produced by vehicles. We perform several numerical tests, aimed at comparing the NO_x emissions and O_3 production derived from different traffic dynamics, focusing on the impact of traffic lights. The results show that the NO_x emission rates increase with the growth of vehicles restarts, suggesting to prefer long rather than short traffic light cycles.

The final chapter of the thesis is placed in the framework of data-fitted modelling and describes the results of a research project born with the aim of using data from the mobile phone network. The data consists of density profiles, i.e. the spatial distribution, of people in a given area at various instants of time. Mobile devices are not singularly tracked, but their logs are aggregated in order to obtain the total number of users in a given area. Such a data are provided by the Italian telecommunication company TIM and contain six months of presence records in the area of the Province of Milan.

The goal of the research is to “assign a direction” to the presence data. In fact, the mere representation of time-varying density of people clearly differentiate attractive from repulsive or neutral areas but does not give any information about the directions of flows of people. In other words, we are interested in a

“where-from-where-to” type of information, which reveals travel flows and patterns of people. The goal is pursued by computing a suitable approximation of the Wasserstein distance between two consecutive density profiles. The computation of the Wasserstein distance gives, as a by-product, the optimal flow which, in our case, coarsely corresponds to the main directions followed by people.

Despite the good preliminary results obtained by the above described Wasserstein-based approach [7, 96], the algorithm is found to be excessively expensive both in terms of CPU time and memory requirements. The main problem of this approach is the time interval of the analysed data, which is 15 minutes long. Such a time frame does not allow to limit the set of possible movements that can be done by the mass, which is the key point to simplify the computation of the Wasserstein distance. To fix the problem we propose a new methodology [1] obtained by coupling the Wasserstein distance with the Dynamic Mode Decomposition (DMD) [87]. DMD is a data-driven technique that takes in input the snapshots of the mass distribution and returns an analytical approximation of the dynamics underlying the mass transfer, providing a system of ODEs which describes the evolution of the mass in any point of the domain. Solving the ODEs, we are able to recover the mass distribution at any time, thus decreasing at will the time frame between them. Therefore, the coupled methodology can be applied to solve inverse problems which have as input some snapshots of a mass distribution and gives as output the reconstruction of its movements. Finally, the real life application to people movements from TIM data is investigated with the coupled procedure, obtaining more accurate dynamics and showing the gains obtained in terms of CPU cost.

The contents of this thesis contribute to articles [1, 7, 9, 11] and preprints [8, 10]. In Chapter 1 we introduce the mathematical background. Chapter 2 concerns GSOM and their extension to road networks. In Chapter 3 we provide estimates on the total variation of the flux and of w for waves interacting with the junctions. Chapter 4 deals with some numerical tests simulating GSOM on road networks. In Chapter 5 we analyse the environmental impact of vehicular traffic. Chapter 6 is devoted to a two-dimensional multi-class traffic model on a single road. Finally, Chapter 7 deals with the reconstruction of mass movements from snapshots of real data.

Chapter 1

Preliminaries

In this chapter we introduce the main mathematical notions and tools which will be used throughout the thesis. First of all, we recall the main definitions related to the theory of conservation laws. In particular, we focus on the treatment of the Riemann problem for systems, which will be used to describe traffic dynamics on a single road as well as on road networks, see Chapter 2. We then introduce the macroscopic traffic models, fixing the notations and giving a brief history of existing models. Furthermore, we recall the main approaches for the treatment of traffic models on networks. Finally, we describe a technique to reconstruct macroscopic quantities from microscopic data, which will be used in the applications proposed in Chapters 5 and 6.

1.1 Riemann problem for systems of conservation laws

From a modelling point of view, conservation laws naturally appear in the study of traffic flow since, as a basic assumption, we require the conservation of the total number of vehicles, so that no vehicle is created or destroyed. The theory on systems of conservation laws is now standard and we refer to the books by Bressan, Dafermos and Smoller [16, 23, 85] for an accurate and complete review. In this section we report only the definitions necessary for the introduction of the Riemann problem for systems.

Let us first introduce a scalar conservation law, i.e. a first order hyperbolic partial differential equation

$$u_t(x, t) + f(u(x, t))_x = 0, \quad (1.1)$$

where $u : \mathbb{R} \times [0, +\infty) \rightarrow \mathbb{R}$ is the *conserved quantity* and $f : \mathbb{R} \rightarrow \mathbb{R}$ is the *flux*. We say that u is conserved since, if we integrate (1.1) on a space interval $[a, b] \subset \mathbb{R}$, we have

$$\frac{d}{dt} \int_a^b u(x, t) dx = - \int_a^b f(u(x, t))_x dx = \underbrace{f(u(a, t))}_{\text{Incoming flux at } a} - \underbrace{f(u(b, t))}_{\text{Outgoing flux at } b},$$

therefore, the variation of the amount of u only depends on the flow through the interval $[a, b]$. A $N \times N$ system of conservation laws is defined as

$$\begin{cases} (u_1)_t + f_1(u_1, \dots, u_N)_x = 0 \\ \dots \\ (u_N)_t + f_N(u_1, \dots, u_N)_x = 0. \end{cases} \quad (1.2)$$

For simplicity of notation we introduce the vectors $U = (u_1, \dots, u_N)$ and $F = (f_1, \dots, f_N)$ in order to rewrite (1.2) as

$$U_t + F(U)_x = 0. \quad (1.3)$$

Assuming enough regularity of F and U , system (1.3) can be rewritten in quasilinear form as

$$U_t + A(U)U_x = 0, \quad (1.4)$$

where $A(U) = DF(U)$ is the Jacobian of F .

Definition 1.1.1. *System (1.4) is hyperbolic if the $N \times N$ matrix $A(U)$ has N real eigenvalues $\lambda_1(U) \leq \dots \leq \lambda_N(U)$. It is strictly hyperbolic if the eigenvalues are also distinct $\lambda_1(U) < \dots < \lambda_N(U)$.*

Let us consider the Cauchy problem

$$\begin{cases} U_t(x, t) + F(U(x, t))_x = 0 & x \in \mathbb{R}, t > 0 \\ U(x, 0) = U_0(x) & x \in \mathbb{R}. \end{cases} \quad (1.5)$$

The first problem which arises from the theory of conservation laws is the regularity of solutions. Indeed, the smoothness of initial data U_0 is not sufficient to ensure regularity of solutions to (1.5), which may give rise to discontinuities. For this reason we introduce the definition of *weak solutions*. In the following, $L^1_{\text{loc}}(\mathbb{R}; \mathbb{R}^N)$ denotes the set of locally integrable functions on \mathbb{R} with values in \mathbb{R}^N , and C^1 the set of continuous functions with continuous derivatives.

Definition 1.1.2. *A function $U : [0, T] \times \mathbb{R} \rightarrow \mathbb{R}^N$ is a weak solution to (1.5) if U is continuous as a function from $[0, T]$ into $L^1_{\text{loc}}(\mathbb{R}; \mathbb{R}^N)$ and for every test function $\varphi \in C^1(\mathbb{R} \times (-\infty, T))$ with compact support it holds*

$$\int_0^T \int_{\mathbb{R}} (U \varphi_t + F(U) \varphi_x) dx dt + \int_{\mathbb{R}} U_0(x) \varphi(x, 0) dx = 0.$$

Although we are working with solutions with low regularity, weak solutions to (1.5) have to respect specific jump conditions on the discontinuities. Let us consider a piecewise constant function

$$U(x, t) = \begin{cases} U^- & \text{if } x < st \\ U^+ & \text{if } x > st, \end{cases}$$

with $U^-, U^+ \in \mathbb{R}^N$ and $s \in \mathbb{R}$.

Definition 1.1.3. *The Rankine-Hugoniot condition for piecewise constant functions with left state $U^- \in \mathbb{R}^N$ and right state $U^+ \in \mathbb{R}^N$ is*

$$s(U^+ - U^-) = F(U^+) - F(U^-). \quad (1.6)$$

Weak solutions to (1.3) have to satisfy (1.6), but this condition does not guarantee the uniqueness of solution. Among the set of weak solutions, we look for the one which is physically relevant, thus we add conditions to our problem in order to identify it.

Definition 1.1.4. *A C^1 function $\eta : \mathbb{R}^N \rightarrow \mathbb{R}$ is an entropy associated to (1.3) if it is convex and there exists a C^1 function $\Phi : \mathbb{R}^N \rightarrow \mathbb{R}$, called entropy flux, such that*

$$D\eta(U)DF(U) = D\Phi(U)$$

for every $U \in \mathbb{R}^N$. The couple (η, Φ) is called entropy-entropy flux pair.

1.1. Riemann problem for systems of conservation laws

Definition 1.1.5. A weak solution $U = U(x, t)$ to (1.5) is called entropy admissible if, for every C^1 test function $\varphi \geq 0$ with compact support in $\mathbb{R} \times [0, T)$ and for every entropy-entropy flux pair (η, Φ) , it holds

$$\int_0^T \int_{\mathbb{R}} (\eta(U)\varphi_t + \Phi(U)\varphi_x) dx dt \geq 0.$$

Definition 1.1.6. A weak solution U to (1.3) satisfies the Lax admissibility condition if the speed of the jump s between two left and right states U^- and U^+ is such that

$$\lambda_i(U^-) \geq s \geq \lambda_i(U^+), \quad (1.7)$$

with λ_i eigenvalues of the Jacobian $DF(U)$.

We are now ready to introduce the Riemann problem for system of conservation laws. The Riemann problem is a Cauchy problem with piecewise constant initial data

$$\begin{cases} U_t + F(U)_x = 0 \\ U_0(x) = \begin{cases} U^- & \text{if } x \leq 0 \\ U^+ & \text{if } x > 0, \end{cases} \end{cases} \quad (1.8)$$

with U^- and U^+ in \mathbb{R}^N , $N \geq 1$.

Let us consider a strictly hyperbolic system (1.3). The treatment of the Riemann problem for system of conservation laws makes use of the eigenvalues and eigenvectors of the Jacobian of F , denoted by A as in (1.4). We denote by λ_i the eigenvalues, l_i the left eigenvectors ($l_i A = \lambda_i l_i$) and with r_i the right eigenvectors ($A r_i = \lambda_i r_i$).

It is well known that the *characteristics* are curves along which the solution is constant. The eigenvalues λ_i represent the speed of the characteristic and define a characteristic field, which will be called i -th field. In what follows we denote by ∇ the gradient with respect to U , ∇_U , and by \cdot the inner product.

Definition 1.1.7. Let (1.4) be a strictly hyperbolic system. For each $i = 1, \dots, N$ we say that the i -th field is

- genuinely nonlinear if $\nabla \lambda_i(U) \cdot r_i(U) \neq 0$ for all U ,
- linearly degenerate if $\nabla \lambda_i(U) \cdot r_i(U) = 0$ for all U .

Definition 1.1.8. A i -Riemann invariant is a smooth function z_i such that

$$r_i(U) \cdot \nabla z_i(U) = 0.$$

Such functions are constant through the i -th curve.

The solution to Riemann problems combines elementary waves, which can be shocks or rarefaction waves, associated to the genuinely nonlinear fields, or contact discontinuities, associated to the linearly degenerate fields. Following [86] we recall the main properties of elementary waves which will be used through the thesis, and we refer to [16, 85] for a more detailed discussion.

Shock waves. A left and right state U^- and U^+ are connected by a i -shock wave if the i -th field is genuinely nonlinear and if the Rankine-Hugoniot (1.6) and Lax entropy (1.7) conditions hold. The corresponding Riemann invariant z_i is constant through the wave, i.e.

$$s(U^+ - U^-) = F(U^+) - F(U^-)$$

$$\begin{aligned}\lambda_i(U^-) &> s > \lambda_i(U^+) \\ z_i(U^-) &= z_i(U^+),\end{aligned}$$

and the shock curve is written as

$$U(x, t) = \begin{cases} U^- & \text{if } x < st \\ U^+ & \text{if } x > st. \end{cases} \quad (1.9)$$

Rarefaction waves. A left and right state U^- and U^+ are connected by a i -rarefaction wave if the i -th field is genuinely nonlinear and the curve is such that

$$\lambda_i(U^-) < \lambda_i(U^+).$$

The corresponding Riemann invariant z_i is constant through the wave, i.e.

$$z_i(U^-) = z_i(U^+).$$

We look for self-similar solutions $\mathcal{U}(x/t) = U(x, t)$, thus we introduce the variable $\xi = x/t$. System (1.3) becomes

$$(\xi I - DF)\mathcal{U}'(\xi) = 0,$$

therefore ξ is an eigenvalue of DF and $\mathcal{U}'(\xi)$ is the corresponding eigenvector. We then define the rarefaction wave as

$$U(x, t) = \begin{cases} U^- & \text{if } x \leq \lambda_i(U^-)t \\ \mathcal{U}(x/t) & \text{if } \lambda_i(U^-)t < x < \lambda_i(U^+)t \\ U^+ & \text{if } x \geq \lambda_i(U^+)t \end{cases} \quad (1.10)$$

where \mathcal{U} is such that $\mathcal{U}'(\xi) = r_i(\mathcal{U}(\xi))$ with $\xi = \lambda_i(\mathcal{U}(\xi))$, $\mathcal{U}(\lambda_i(U^-)) = U^-$ and $\mathcal{U}(\lambda_i(U^+)) = U^+$.

Contact discontinuities. A left and right state U^- and U^+ are connected by a i -contact discontinuity if the i -th field is linearly degenerate, the Rankine-Hugoniot (1.6) condition holds, the characteristics are parallel and the corresponding Riemann invariant z_i is constant through the wave, i.e.

$$\begin{aligned}s(U^+ - U^-) &= F(U^+) - F(U^-) \\ \lambda_i(U^-) &= \lambda_i(U^+) = s \\ z_i(U^-) &= z_i(U^+).\end{aligned}$$

The contact discontinuity is written as

$$U(x, t) = \begin{cases} U^- & \text{if } x < \lambda_i(U^-)t \\ U^+ & \text{if } x > \lambda_i(U^-)t. \end{cases} \quad (1.11)$$

In Figure 1.1 we show the graphical representation of a shock, rarefaction waves and a contact discontinuity.

The study of Riemann problems is fundamental to build solution to Cauchy problems (1.5) by means of the Wave Front Tracking (WFT) method [47]. Such a methodology can be resumed in the following steps:

1. Approximate the initial data U_0 of (1.5) with a piecewise constant function.
2. Solve the Riemann problem associated to each discontinuity.

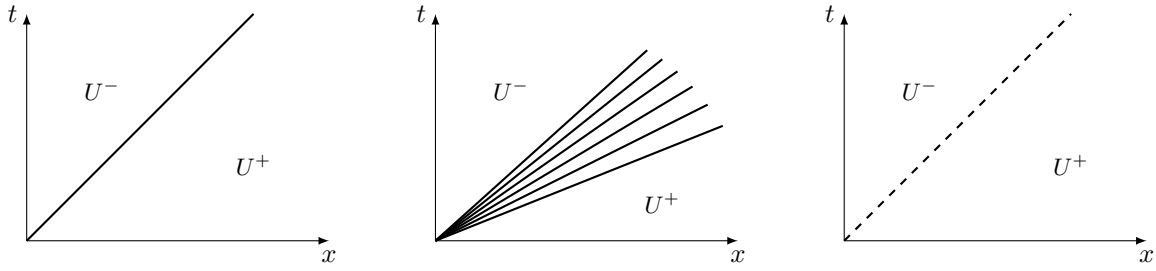


Figure 1.1. Example of shock (left), rarefaction wave (centre) and contact discontinuity (right).

3. Define the solution to (1.5) by combining the solutions to Riemann problems.
4. Repeat the procedure of the first three steps every time two waves interact together.
5. Study the limit of the constructed solution, proving that it is an entropy admissible solution.

1.2 Macroscopic traffic models

In this section we present the basic notion on macroscopic models for vehicular traffic, which are the main topic of the thesis. As the name suggests, macroscopic traffic models describe the dynamic of traffic by means of macroscopic variables, such as the density, speed and flux of vehicles. To fix the ideas, let us consider a unidirectional road (a, b) . The evolution of traffic depends on the following variables:

- The density $\rho = \rho(x, t)$, i.e. the number of vehicles per unit of length.
- The flux $f = f(\rho)$, i.e. the number of vehicles per unit of time.
- The velocity $v = v(x, t)$, that is assumed to depend only on density.

These three quantities are linked by the relation

$$f(\rho) = \rho v(\rho). \quad (1.12)$$

The first macroscopic traffic model was introduced in 1955 by Lighthill and Whitham [63] and independently in 1956 by Richards [79]. The Lighthill-Whitham-Richards (LWR) model is a first order scalar conservation law

$$\rho_t + f(\rho)_x = 0, \quad (1.13)$$

which represents the conservation of the number of vehicles. The flux function f is assumed to be C^2 , concave and such that $f(0) = f(\rho^{\max}) = 0$, where ρ^{\max} is the maximum density. The last hypothesis implies that the flux is null both when the road is empty and completely congested. As a consequence of (1.12) and the concavity of the flux function, the velocity v is non-increasing with respect to ρ . We denote by V^{\max} the maximum velocity.

One of the most important aspects of macroscopic traffic models is the fundamental diagram, i.e. the relation between the flux and the density. The two most famous fundamental diagrams are the Greenshields (or quadratic) type [37]

$$f(\rho) = \frac{V^{\max}}{\rho^{\max}} \rho (\rho^{\max} - \rho), \quad (1.14)$$

and the Newell-Daganzo (or triangular) type [68, 24]

$$f(\rho) = \begin{cases} \frac{f^{\max}}{\sigma} \rho & \text{if } \rho \leq \sigma \\ \frac{f^{\max}(\rho^{\max} - \rho)}{\rho^{\max} - \sigma} & \text{if } \rho > \sigma \end{cases} \quad (1.15)$$

where σ is the critical density, i.e. the density value at which the flux function attains its maximum f^{\max} . In Figure 1.2 we show the plot of (1.14) and of (1.15). Note that for the Greenshields type flux function the critical density σ corresponds to $\rho^{\max}/2$.

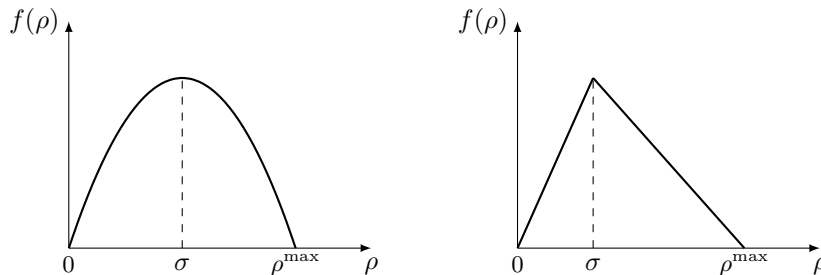


Figure 1.2. Greenshields fundamental diagram in (1.14) (left) and Newell-Daganzo type in (1.15) (right).

Although the LWR model is able to describe simple traffic dynamics, it has some well-known drawbacks, such as the formation of infeasible solutions with unbounded acceleration [58] or the impossibility of capturing phantom traffic jams, since perturbations never grow. To overcome the deficiencies of the LWR model, Payne [72] and independently Whitham [92] introduced in 1971 and 1974, respectively, a second order model, i.e. a model with two equations. Specifically the Payne-Whitham (PW) model is defined as

$$\begin{cases} \rho_t + (\rho v)_x = 0 \\ v_t + v v_x = \frac{p(\rho)_x}{\rho} + \frac{1}{\tau}(v^{eq}(\rho) - v), \end{cases}$$

where $p(\rho)$ a pressure term, τ is a relaxation time and v^{eq} is the equilibrium (or desired) velocity.

In 1995 Daganzo [25] proved that the PW model can produce negative speeds, a not negligible drawback that led Daganzo to a “death sentence” for the second order models. However, Aw and Rascle [6] in 2000 and independently Zhang [94] in 2002 proposed a new approach which “resurrected” the second order models, giving rise to the Aw-Rascle-Zhang (ARZ) model. The ARZ model is defined by

$$\begin{cases} \rho_t + (\rho v)_x = 0 \\ (v + p(\rho))_t + v(v + p(\rho))_x = 0, \end{cases} \quad (1.16)$$

where p is a pressure term, defined by a smooth increasing function. The prototype of p is $p(\rho) = \rho^\gamma$, $\gamma > 0$.

The ARZ has been widely studied and extended in the last years, see for instance [28, 30, 59]. We refer in particular to the Generic Second Order Models (GSOM), defined by a couple of conservation laws

$$\begin{cases} \rho_t + (\rho v)_x = 0 \\ y_t + (y v)_x = 0, \end{cases} \quad (1.17)$$

with $v = V(\rho, w)$ for a proper velocity function V . GSOM possess a family of fundamental diagrams $Q(\rho, w) = \rho V(\rho, w)$ parametrised by w . The advantage of using the family $Q(\rho, w)$ rather than a unique

flux curve is clear from the experimental observations, see e.g. [51, 52]. Indeed, the observations of traffic flow highlighted its multi-phase nature, consisting of the *free* and the *congested* phase. The former corresponds to low density of cars, the latter to traffic states with a high number of vehicles congesting the flow. In particular, real data observations show that a single flux function well fits with the free-flow phase, but is inadequate to describe the congested one.

Finally, we mention the phase-transition models [15, 20, 21], which are based on the multi-phase nature of traffic flow. The original idea of Colombo [20] was to describe the two phases of traffic flow through distinct evolutionary laws. More precisely, Colombo coupled a scalar conservation law for the free-flow phase with a 2×2 system of conservation laws for the congested one. Indeed, as observations suggest, the LWR model is appropriate for the free-flow phase, but is inadequate for the congested one, where it is replaced by a second order model.

1.3 Macroscopic traffic models on road networks

The aim of this section is to give a brief overview of traffic models on road network. We define a network as a couple $(\mathcal{I}, \mathcal{J})$ where \mathcal{I} is a finite collection of N_r roads $I_r = (a_r, b_r) \subset \mathbb{R}$, $r = 1, \dots, N_r$, possibly with $a_r = -\infty$ and $b_r = +\infty$, and \mathcal{J} is a finite collection of junctions J . Traffic models on networks have been widely studied in recent years and authors have considered many different traffic scenarios proposing a rich amount of alternative models at junctions. We refer to [26, 32, 33, 46] for some examples of extension of the LWR model to road networks.

The solution of traffic models on networks is generally based on the concept of the Riemann problem at a junction [32], which is a Cauchy problem with constant initial data on each road connected at the intersection. The treatment of traffic models on networks requires coupling conditions to define a unique solution. The choice of these conditions differentiates the existing models and the most common assumptions are:

- (A1) The flux is conserved through the junction.
- (A2) Waves generated at junctions have non-positive speed on incoming roads and non-negative speed on outgoing roads.
- (A3) The flux at the junction is maximised.
- (A4) Vehicles from incoming roads are distributed on outgoing roads according to a proper matrix of distribution.

Since the thesis is focused on second order models, here we recall the main approaches [31, 36, 42, 44, 55] proposed for the treatment of the ARZ model at junctions

$$\begin{cases} \partial_t \rho_r + \partial_x(\rho_r v_r) = 0 \\ \partial_t(\rho_r w_r) + \partial_x(\rho_r w_r v_r) = 0 \\ w_r = v_r + p_r(\rho_r) \end{cases} \quad (1.18)$$

where $p_r(\rho)$ is the known pressure function and $r = 1, \dots, n + m$ (with n number of incoming roads and m of outgoing roads at the junction). In [31], the authors add to (A1) – (A4) the following assumption.

- ◊ Either density or speed is maximised or the total variation of density is minimised.

It is worth noting that the proposed approach implies the conservation of the density ρ but not of the generalised momentum ρw and thus the solutions of the Riemann problem at junctions are not weak solutions to (1.18). In [38], in addition to (A1) – (A3) the authors assume the following conditions.

- ◊ Vehicles try to keep their behaviour w through the junction and the resulting w on outgoing roads is an average value of the different incoming behaviours.
- ◊ The speed of outgoing roads is maximised when the previous conditions are not sufficient to define a unique solution.

Note that in this case both the density ρ and the generalised momentum ρw are conserved. In [44], the authors add to (A1), (A2) and (A4) the following assumptions.

- ◊ The pseudo momentum $\rho v w$ is conserved.
- ◊ The w value of outgoing roads is defined by a mixture rule of the w of incoming roads.

The flux is not necessary maximised, as it is in [42], where the results in [44] are extended. Note that the condition on w corresponds to the homogenisation of the pressure at the junction and leads to changes in the definition of the pressure function p . This approach has been extended in the recent paper [36], where the authors propose an approximation of the homogenised pressure, which allows to perform numerical tests. In [55], in addition to (A1), (A2) and (A4) the authors assume the following conditions.

- ◊ Each incoming flux is maximised.
- ◊ Vehicles follow a priority rule on incoming roads.

The proposed approach is defined by an iterative algorithm based on the Pareto front, i.e. the set of incoming fluxes which cannot be improved without decreasing at least one other flux. The solution lies on the Pareto front, therefore, if the solution which respects the priority rule is not Pareto optimal, then it is defined by the closest point to the priority rule on the Pareto front.

Finally, we mention [26, 60], which refer to the LWR model and to GSOM, respectively. In [26] the authors assume (A1) – (A4) and add a priority rule for the construction of a unique solution. In [60] the authors treat the junction through a buffer mixing the incoming fluxes.

1.4 Data-fitting: reconstruction of macroscopic quantities from microscopic data

A recurrent topic of this thesis is the validation of traffic models exploiting real data. In this section we describe how to treat the microscopic data to recover the macroscopic density ρ and velocity v of vehicles. Indeed, several public datasets, such as [50, 88], contain vehicles trajectory data, i.e. their position at different time frames. The aim of this section is to introduce a methodology to recover ρ and v from point-wise data. We use a kernel density estimation, the Parzan-Rosenblatt window method [71, 80]. The idea of this method is to consider the data points as a density distribution and then recover the global density by summing these distributions.

Let $C(t)$ be the number of vehicles at time t , $x_i(t)$ their positions and $v_i(t)$ their velocity. We define

$$\tilde{\rho}(x) = \sum_{i=1}^{C(t)} \delta(x - x_i(t)),$$

where δ is the Dirac delta function. Note that, since $\int_{\mathbb{R}} \delta(x) dx = 1$, we have

$$\int_{\mathbb{R}} \tilde{\rho}(x) dx = \sum_{i=1}^{C(t)} \int_{\mathbb{R}} \delta(x - x_i(t)) dx = C(t).$$

1.4. Data-fitting: reconstruction of macroscopic quantities from microscopic data

In order to recover the smooth functions ρ and v , we introduce the Gaussian kernel $K(x)$

$$K(x) = \frac{1}{2\pi h_x} \exp\left(-\frac{x^2}{2h^2}\right),$$

and we define

$$\rho(x, t) = \int_{\mathbb{R}} K(x - \xi) \tilde{\rho}(\xi) d\xi = \sum_{i=1}^{C(t)} K(x - x_i(t)) \quad (1.19)$$

$$v(x, t) = \frac{\sum_{i=1}^n v_i(t) K(x - x_i(t))}{\sum_{i=1}^n K(x - x_i(t))}. \quad (1.20)$$

The parameter h is a bandwidth chosen in order to obtain an almost constant density profile for equidistant vehicles [29], and it depends on the dimensions of the road. In Chapter 5 we will see an application of this methodology, and in Chapter 6 we will extend it to traffic models in two-dimensions.

Chapter 2

Generic Second Order Models for traffic on road networks

This chapter is devoted to Generic Second Order Models (GSOM) [59], a family of macroscopic second order traffic models, described by a first order scalar conservation law for the density of vehicles ρ combined with an advection equation of a certain property of drivers w

$$\begin{cases} \partial_t \rho + \partial_x(\rho v) = 0 \\ \partial_t w + v \partial_x w = 0 \end{cases}$$

with $v = V(\rho, w)$ and V is the velocity function.

The main goal of this chapter is to extend GSOM to road networks. To this end, we assume the maximisation of the flux, the conservation of ρ and $y = \rho w$ through the junction and we introduce a matrix A which distributes the flux on outgoing roads. The identification of a unique solution is attained introducing a priority rule on the incoming roads, as in [26, 55]. We define the Adapting Priority Riemann Solver for Second Order Models (APRSOM) providing an iterative algorithm able to construct the solution to generic junctions with n incoming and m outgoing roads. The logic underlying our algorithm is the following: the flow is maximised respecting the priority rule, but the latter can be adapted if the outgoing road supply exceeds the demand of the road with higher priority.

The chapter is organised as follows. In Section 2.1 we introduce the GSOM and their properties, focusing on the Collapsed Generalized Aw-Rascle-Zhang (CGARZ) model, which belongs to GSOM. In Section 2.2 we describe the Riemann problem for GSOM on a single road, and we extend it to networks in Section 2.3, analysing the diverge and merge junctions. Finally, in Section 2.4 we provide the APRSOM algorithm for the construction of the solution for the n in m junctions.

2.1 Introduction to GSOM

GSOM were introduced in [59] as a generalisation of the ARZ model (1.16). They represent a family of macroscopic traffic models which are described by a first order LWR model with variable fundamental diagrams. Such models are defined by

$$\begin{cases} \partial_t \rho + \partial_x(\rho v) = 0 \\ \partial_t w + v \partial_x w = 0 \end{cases} \quad (2.1)$$

with $v = V(\rho, w)$,

where $\rho(x, t)$, $v(x, t)$ and $w(x, t)$ represent the density, the speed and a property of vehicles advected by the flow, respectively, and V is a specific velocity function. The first equation of (2.1) is the conservation of vehicles, the second one is the advection of the attribute of drivers, which defines their driving aptitude by means of different fundamental diagrams. Indeed, the variable w identifies the flux curve $Q(\rho, w)$ and thus the speed of vehicles $V(\rho, w) = Q(\rho, w)/\rho$ which characterises the behaviour of drivers. System (2.1) is written in conservative form as

$$\begin{cases} \partial_t \rho + \partial_x(\rho v) = 0 \\ \partial_t y + \partial_x(yv) = 0 \end{cases} \quad (2.2)$$

with $v = V\left(\rho, \frac{y}{\rho}\right)$,

where $y = \rho w$ denotes the total property of vehicles.

Remark 2.1.1. *Note that when all drivers share the same property, i.e. w is equal to a certain constant \bar{w} , then (2.2) is reduced to the LWR model.*

The flux function $Q(\rho, w)$ and the velocity function $V(\rho, w) = Q(\rho, w)/\rho$ are assumed to satisfy the following properties.

(H1) $Q(0, w) = 0$ and $Q(\rho^{\max}(w), w) = 0$ for each $w \in [w_L, w_R]$, where $\rho^{\max}(w)$ is the maximum density of vehicles for $Q(\cdot, w)$ and $w \in [w_L, w_R]$, for suitable w_L and w_R .

(H2) $Q(\rho, w)$ is strictly concave with respect to ρ , i.e. $\frac{\partial^2 Q}{\partial \rho^2} < 0$.

(H3) $Q(\rho, w)$ is non-decreasing with respect to w , i.e. $Q_w(\rho, w) \geq 0$.

(H4) $V(\rho, w) \geq 0$ for each ρ and w .

(H5) $V(\rho, w)$ is strictly decreasing with respect to ρ , i.e. $V_\rho(\rho, w) < 0$ for each w .

(H6) $V(\rho, w)$ is non-decreasing with respect to w , i.e. $V_w(\rho, w) \geq 0$.

Note that properties (H5) is a consequence of (H2). Indeed, for $\rho \neq 0$

$$V_\rho(\rho, w) = \frac{\rho Q_\rho(\rho, w) - Q(\rho, w)}{\rho^2} = \frac{h(\rho)}{\rho^2} < 0 \quad \text{for each } w$$

since $h(0) = 0$ and $h'(\rho) = -\frac{\partial^2 Q}{\partial \rho^2} > 0$ by (H2). Property (H6) follows by (H3) trivially. Properties (H1) and (H2) imply that the flux curve $Q(\cdot, w)$ has a unique point of maximum for any w . We denote by $\sigma(w)$ the critical density, i.e. the density value where the flux attains its maximum $Q^{\max}(w)$. Moreover, for any ρ there exists a unique $\tilde{\rho}(w)$ such that $Q(\rho, w) = Q(\tilde{\rho}(w), w)$.

The use of a family of fundamental diagrams is suggested by real data. Figure 2.1 shows an example of density-flow and speed-flow diagrams obtained from the Next Generation SIMulation (NGSIM) dataset [88]. From this figure it is clear that multiple flow values correspond to a fixed density, due to the different attitudes of drivers. Therefore, multivalued density flow relationships better fit real traffic data.

In order to study the properties of the traffic model (2.2), for notational convenience we introduce the variable

$$u = u(\rho, y) = V\left(\rho, \frac{y}{\rho}\right),$$

and we rewrite the system as

$$\begin{cases} \partial_t \rho + \partial_x(\rho u) = 0 \\ \partial_t y + \partial_x(yu) = 0, \end{cases}$$

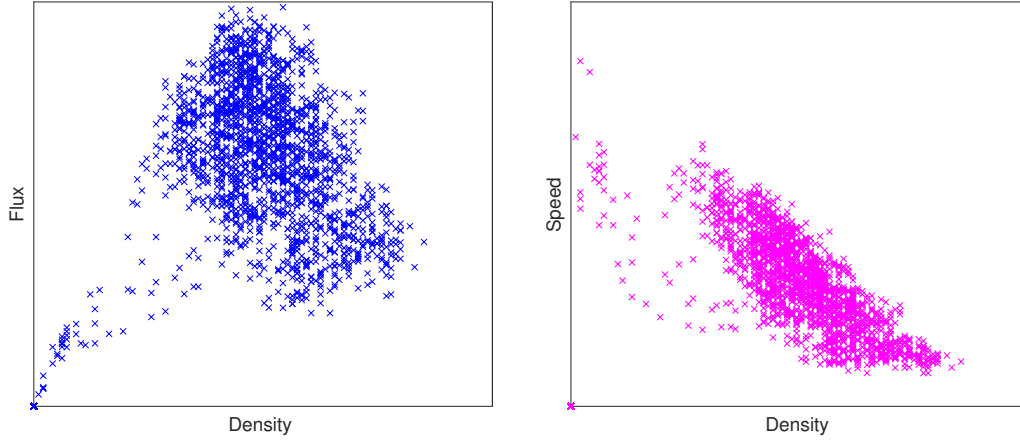


Figure 2.1. Example of density-flow (left) and density-speed (right) relations computed from real data.

whose Jacobian is

$$DF(\rho, y) = \begin{pmatrix} u + \rho u_\rho & \rho u_y \\ y u_\rho & u + y u_y \end{pmatrix}. \quad (2.3)$$

Since it is easier to work with the couple (ρ, w) , hereafter we will use these variables. The eigenvalues of (2.3), as a function of (ρ, w) , are

$$\lambda_1(\rho, w) = V(\rho, w) + \rho V_\rho(\rho, w) \quad (2.4)$$

$$\lambda_2(\rho, w) = V(\rho, w). \quad (2.5)$$

By property (H5) follows $\lambda_1 \leq \lambda_2$ and $\lambda_1 = \lambda_2$ if and only if $\rho = 0$, thus the system is strictly hyperbolic except for $\rho = 0$.

The right eigenvectors associated to the eigenvalues are

$$\begin{aligned} \gamma_1(\rho, w) &= (\rho, \rho w) \\ \gamma_2(\rho, w) &= \left(-\frac{1}{\rho} V_w(\rho, w), V_\rho(\rho, w) - \frac{1}{\rho^2} V_w(\rho, w) \right). \end{aligned}$$

The first eigenvalue is genuinely nonlinear, i.e. $\nabla \lambda_1 \cdot \gamma_1 \neq 0$ (see Definition 1.1.7), while the second one is linearly degenerate, i.e. $\nabla \lambda_2 \cdot \gamma_2 = 0$. Hence, the curves of the first family are 1-shocks or 1-rarefaction waves, while the curves of the second family are 2-contact discontinuities.

Finally, the Riemann invariants are

$$\begin{aligned} z_1(\rho, w) &= w \\ z_2(\rho, w) &= V(\rho, w). \end{aligned}$$

The 1-shock and 1-rarefaction waves are defined by the first Riemann invariant z_1 and the 2-contact discontinuities by the second Riemann invariant z_2 .

2.1.1 The CGARZ model

Among the models in the GSOM family, we focus our attention on the Collapsed Generalized Aw-Rascle-Zhang (CGARZ) model [27, 30]. Such model is described by system (2.1), with a particular choice of the flux function $Q(\rho, w) = \rho V(\rho, w)$. The idea of the CGARZ model is to differentiate the flux function for the two traffic phases, i.e. the free-flow (low density) and the congested phase (high density). As

observed in Section 1.2, at low density regimes the flux is well described by a single curve, but the latter is not appropriate for congestion. In light of this, the CGARZ model possesses a single-valued fundamental diagram in free-flow, and a multi-valued function in congestion. The flux function has then the following form

$$Q(\rho, w) = \begin{cases} Q_f(\rho) & \text{if } 0 \leq \rho \leq \rho_f \\ Q_c(\rho, w) & \text{if } \rho_f \leq \rho \leq \rho^{\max}, \end{cases} \quad (2.6)$$

where ρ_f is the *free-flow threshold density* independent on w , and ρ^{\max} is the maximum density. Following [30], the flux function (2.6) must be continuously differentiable in ρ and satisfy properties (H2) and (H3), while (H1) becomes

(Q1) The flux curves have a common ρ^{\max} independent of w , i.e. $Q(\rho^{\max}, w) = 0$ for all $w \in [w_L, w_R]$.

The velocity function $V(\rho, w)$ is in C^1 for each w and satisfies:

(V1) ρ^{\max} is the only density such that $V(\rho^{\max}, w) = 0$.

(V2) In the free-flow regime, the traffic velocity is independent of w , i.e. $V_w(\rho, w) = 0$ if $0 \leq \rho \leq \rho_f$.

(V3) In the congestion regime, the traffic velocity is increasing with respect to w , i.e. $V_w(\rho, w) > 0$ if $\rho_f \leq \rho \leq \rho^{\max}$.

Choosing the flux and velocity functions

Here we make a choice for the flux function of the CGARZ family, thus determining a unique model to be used. Differently from [30], we choose the flux function to be an interpolation between a Newell-Daganzo fundamental diagram (1.15) and a Greenshields fundamental diagram (1.14). The reason for this choice is that those two diagrams are the most known and used in traffic modelling and they present two somehow opposite behaviour, with the triangular one presenting a unique characteristic speed in congested regime, thus allowing contact discontinuities, while the Greenshields one being genuinely nonlinear in congested regime thus exhibiting rarefaction waves.

The model parameters to be calibrated from data are the maximum speed V^{\max} , the threshold density ρ_f from the free-flow to the congested phase, the density ρ_c in which the flux function reaches its maximum value, and a lower and upper bound for w , denoted by w_L and w_R respectively. Moreover, we set the maximal density ρ^{\max} as a property of the road.

As in [30], we assume the Greenshields model in the free-flow regime, i.e.

$$Q_f(\rho) = \frac{V^{\max}}{\rho^{\max}} \rho(\rho^{\max} - \rho),$$

and as a novelty we define the flux function $Q_c(\rho, w)$ in the congested phase, as a convex combination of a lower-bound function $f(\rho)$ and an upper-bound function $g(\rho)$. In particular, we set

$$f(\rho) = \frac{V^{\max}}{\rho^{\max}} \rho_f(\rho^{\max} - \rho) \quad (2.7)$$

as the straight-line which connects $(\rho_f, Q_f(\rho_f))$ with $(\rho^{\max}, 0)$, and

$$g(\rho) = \frac{V^{\max}}{\rho^{\max}} \rho(\rho^{\max} - \rho) \quad (2.8)$$

which corresponds to the free-flow phase flux function. Defining

$$\theta(w) = \frac{w - w_L}{w_R - w_L}, \quad (2.9)$$

then our flux function $Q_c(\rho, w)$ is

$$Q_c(\rho, w) = (1 - \theta(w))f(\rho) + \lambda(w)g(\rho),$$

with f and g given in (2.7) and (2.8) respectively. The resulting flux function is

$$Q(\rho, w) = \begin{cases} \frac{V^{\max}}{\rho^{\max}}\rho(\rho^{\max} - \rho) & \text{if } 0 \leq \rho \leq \rho_f \\ (1 - \theta(w))f(\rho) + \theta(w)g(\rho) & \text{if } \rho_f \leq \rho \leq \rho^{\max}, \end{cases} \quad (2.10)$$

while the velocity function is obtained as

$$V(\rho, w) = \frac{Q(\rho, w)}{\rho} = \begin{cases} \frac{V^{\max}}{\rho^{\max}}(\rho^{\max} - \rho) & \text{if } 0 \leq \rho \leq \rho_f \\ (1 - \theta(w))\frac{f(\rho)}{\rho} + \theta(w)\frac{g(\rho)}{\rho} & \text{if } \rho_f \leq \rho \leq \rho^{\max}. \end{cases}$$

Proposition 2.1.2. *The flux function (2.10) is C^1 in $[0, \rho^{\max}] \setminus \{\rho_f\}$ and verifies the properties (Q1), (H2) and (H3).*

Proof. The function Q is C^1 in $[0, \rho^{\max}] \setminus \{\rho_f\}$ by construction: the free-flow part Q_f is C^1 for all ρ , and the congested one is a convex combination of C^1 functions. Condition (Q1) follows directly from the definition of f and g which satisfy $f(\rho^{\max}) = g(\rho^{\max}) = 0$. Condition (H2) is easily verified by the strictly negativity of the second derivative of function in (2.10). Finally, condition (H3) follows from the relation

$$\frac{\partial Q(\rho, w)}{\partial w} = \theta'(w)(g(\rho) - f(\rho))$$

which is strictly positive since $g(\rho) \geq f(\rho)$ by construction. \square

Remark 2.1.3. *To define a flux function continuously differentiable for all $\rho \in [0, \rho^{\max}]$, it is sufficient to choose a different function f that joins with regularity to free-flow regime.*

2.2 The Riemann problem for GSOM on a single road

Before introducing the Riemann problem on road networks, we describe the case of a single road for GSOM. As explained in Section 1.1, the solution to Riemann problems for systems of conservation laws is given by a combination of elementary waves, i.e. shocks, rarefaction waves and contact discontinuities. The analysis on GSOM described in Section 2.1 shows that the waves associated to the first eigenvalue λ_1 of (2.3) are shock or rarefaction waves, while those associated to λ_2 are contact discontinuities. We recall that the Riemann invariants are $z_1(\rho, w) = w$ and $z_2(\rho, w) = V(\rho, w)$.

Given two generic left and right states U^- and U^+ , the solution to Riemann problems (1.8) is defined by an intermediate state $U^* = (\rho^*, w^*)$ such that

1. We first connect the left state U^- to U^* by a 1-shock or a 1-rarefaction wave. As already observed in Section 1.1, shock and rarefaction waves are such that the first Riemann invariant is conserved, i.e. $z_1(U^-) = z_1(U^*)$. Moreover, shock waves satisfy $\lambda_1(U^-) > \lambda_1(U^*)$ while rarefaction waves satisfy $\lambda_1(U^-) < \lambda_1(U^*)$. Since $\lambda_1(\rho, w)$ in (2.4) coincides with $Q_\rho(\rho, w)$, property (H2) of the flux function implies that Q_ρ is decreasing with respect to ρ . Therefore, shock waves are described by

$$w^- = w^* \quad \text{and} \quad \rho^- < \rho^*,$$

while rarefaction waves by

$$w^- = w^* \quad \text{and} \quad \rho^- > \rho^*.$$

2.2. The Riemann problem for GSOM on a single road

2. We then connect U^* to the right state U^+ by a 2-contact discontinuity, which is such that

$$v^* = v^+,$$

with $v^* = V(\rho^*, w^*)$ and $v^+ = V(\rho^+, w^+)$.

Let us denote by $V^{\max}(w)$ the maximum velocity value reachable along the velocity curve $V(\cdot, w)$. The identification of the intermediate state U^* is divided in two cases:

- If $v^+ \leq V^{\max}(w^-)$ then U^* is defined as

$$w^* = w^- \quad \text{and} \quad V(\rho^*, w^*) = v^+.$$

The density ρ^* is obtained by means of a proper function $G(v, w) = V^{-1}(v, w)$ which defines the density $\rho^* = G(v^+, w^*)$ such that $V(\rho^*, w^*) = v^+$.

- If $v^+ > V^{\max}(w^-)$ then we look for two intermediate vacuum states \widehat{U} and U^* . Indeed, the hypothesis implies that we cannot directly find any density value ρ^* such that $V(\rho^*, w^-) = v^+$. We proceed as follows: we first connect U^- to a vacuum state \widehat{U} by a 1-shock or 1-rarefaction wave, we then move from \widehat{U} to U^* by a vacuum wave with “fake” velocity and finally we move to U^+ . The intermediate states \widehat{U} and U^* are defined by

$$\begin{aligned} \widehat{\rho} &= 0, & \widehat{w} &= w^-, & \widehat{v} &= v^- \\ \rho^* &= 0, & w^* &= w^-, & v^* &= v^+. \end{aligned}$$

Therefore, the vacuum wave represents a wave that does not physically exist and is such that the density is zero and the “fake” velocity jumps from v^- to v^+ , keeping w fixed.

Remark 2.2.1. *The advantage of the CGARZ model is that the case of $v^+ > V^{\max}(w^-)$ never holds, since all the velocity curves have a common V^{\max} .*

We now show two examples of Riemann problems on a single road using the CGARZ model. Let us consider U^- and U^+ with $\rho^- < \rho^+$ and $v^- < v^+$, see Figure 2.2(a). The intermediate state is identified by the intersection between the level curves $\{z_1 = w^-\}$ and $\{z_2 = v^+\}$. In this case we connect the left state U^- to the intermediate state U^* by a 1-shock, since the resulting $\rho^* = G(v^+, w^-)$ is such that $\rho^* > \rho^-$. We then move from U^* along the level curve $\{z_2 = v^+\}$ towards the right state U^+ . Recalling the Rankine-Hugoniot condition (1.6), the shock speed is given by

$$\begin{aligned} s_1 &= \frac{Q(\rho^*, w^-) - Q(\rho^-, w^-)}{\rho^* - \rho^-} \\ s_2 &= \frac{w^* Q(\rho^*, w^-) - w^- Q(\rho^-, w^-)}{w^* \rho^* - w^- \rho^-}. \end{aligned}$$

Since $w^* = w^-$ we obtain the speed $s = s_1 = s_2$. Combining (1.9) and (1.11), the solution is then defined as

$$U(x, t) = \begin{cases} U^- & \text{if } x < st \\ U^* & \text{if } st < x < v^+t \\ U^+ & \text{if } x > v^+t \end{cases}$$

where we exploit $\lambda_2(U^*) = v^+$.

In Figure 2.2(b) we show the case of $\rho^- > \rho^+$ and $v^- > v^+$. Hence, since $\rho^* < \rho^-$ we connect U^- to U^* by a 1-rarefaction wave, and then we connect U^* to U^+ by a 2-contact discontinuity. Combining

(1.10) and (1.11), the solution is given by

$$U(x, t) = \begin{cases} U^- & \text{if } x < \lambda_1(U^-)t \\ \mathcal{U}(x/t) & \text{if } \lambda_1(U^-)t < x < \lambda_1(U^*)t \\ U^* & \text{if } \lambda_1(U^*)t < x < v^+t \\ U^+ & \text{if } x > v^+t \end{cases}$$

where

$$\mathcal{U}\left(\frac{x}{t}\right) = \left(\frac{\rho^* - \rho^-}{\lambda_1(U^*) - \lambda_1(U^-)} \frac{x}{t} + \rho^- - \frac{\lambda_1(U^-)(\rho^* - \rho^-)}{\lambda_1(U^*) - \lambda_1(U^-)}, w^- \right).$$

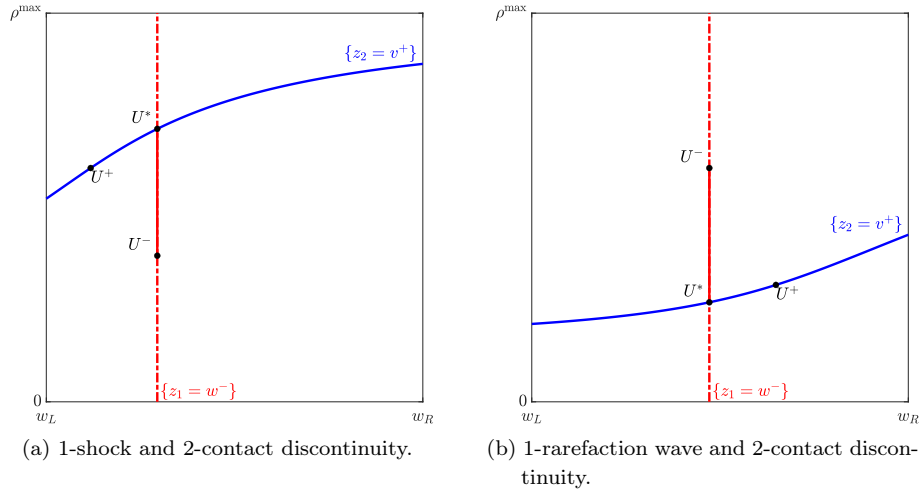


Figure 2.2. Two examples of solution to Riemann problems for the CGARZ model.

2.3 The Riemann problem for GSOM at junctions

In this section we collect the main definitions of traffic models on networks which will be used for the treatment of the Riemann problem at the junction. We then define the solution to the simplest case of two roads connected by a junction and to the diverge and merge junctions, laying the foundations for the definition of the general algorithm.

2.3.1 Basic definitions

First of all, we recall the main definitions concerning traffic models on road networks and we refer to [26, 32, 33, 46] for further details. Let us consider a junction J with n incoming and m outgoing roads $I_r = (a_r, b_r) \subset \mathbb{R}$, $r = 1, \dots, n + m$, possibly with $a_r = -\infty$ and $b_r = +\infty$. We define a network as a couple $(\mathcal{I}, \mathcal{J})$ where \mathcal{I} is a finite collection of roads I_r , and \mathcal{J} is a finite collection of junctions J .

On each road I_r , $r = 1, \dots, n + m$, the traffic dynamic is described by system (2.2) with $x \in I_r$. Our aim is to develop a Riemann Solver for GSOM, which is a map that provides a solution to Riemann problems at junctions, i.e., Cauchy problems with constant initial data on each road. We look for weak solutions at the junction, defined as follows.

Definition 2.3.1. *A collection of functions $(\rho_r, y_r) \in C([0, +\infty); L^1_{loc}(I_r)^2)$, $r = 1, \dots, n + m$, is a weak solution at J if*

2.3. The Riemann problem for GSOM at junctions

- For every $r \in \{1, \dots, n+m\}$ the couple (ρ_r, y_r) is an entropy admissible solution to (2.2) in the road I_r in the sense of Definition 1.1.5.
- For every $r \in \{1, \dots, n+m\}$ and for a.e. $t > 0$ the function $x \mapsto (\rho_r(x, t), y_r(x, t))$ has a version with bounded total variation.
- For a.e. $t > 0$, it holds

$$\sum_{i=1}^n Q(\rho_i(b_i-, t), w_i(b_i-, t)) = \sum_{j=n+1}^{n+m} Q(\rho_j(a_j+, t), w_j(a_j+, t))$$

where $w_r = y_r/\rho_r$ and (ρ_r, y_r) is the version with bounded total variation of the previous point.

We now focus on the Riemann problems at the junction: on each road I_r , $r = 1, \dots, n+m$, we solve

$$\begin{cases} \partial_t \rho_r + \partial_x(\rho_r v_r) = 0 \\ \partial_t y_r + \partial_x(y_r v_r) = 0 \\ (\rho_r(x, 0), y_r(x, 0)) = \begin{cases} (\rho^-, y^-) & \text{for } x < x_0 \\ (\rho^+, y^+) & \text{for } x > x_0, \end{cases} \end{cases} \quad (2.11)$$

with $v_r = V(\rho_r, y_r/\rho_r)$ and where only one between the left and right state is known. Depending on the road if it is incoming or outgoing, we have the following possibilities:

- If I_i is an incoming road at the junction then $x_0 = b_i$ and only the left state (ρ^-, y^-) is known. In this case we look for weak solutions of (2.11) such that the waves have non-positive speed.
- If I_j is an outgoing road at the junction then $x_0 = a_j$ and only the right state (ρ^+, y^+) is known. In this case we look for weak solutions of (2.11) such that the waves have non-negative speed.

Definition 2.3.2. A Riemann solver \mathcal{RS} is a function

$$\begin{aligned} \mathcal{RS} : ([0, \rho^{\max}] \times [w_L, w_R])^{n+m} &\longrightarrow ([0, \rho^{\max}] \times [w_L, w_R])^{n+m} \\ (U_1^-, \dots, U_n^-, U_{n+1}^+, \dots, U_{n+m}^+) &\longmapsto (\hat{U}_1, \dots, \hat{U}_n, \hat{U}_{n+1}, \dots, \hat{U}_{n+m}) \end{aligned}$$

such that

1. $\sum_{i=1}^n \hat{q}_i = \sum_{j=n+1}^{n+m} \hat{q}_j$, with $\hat{q}_i = Q(\hat{\rho}_i, \hat{w}_i)$ and $\hat{q}_j = Q(\hat{\rho}_j, \hat{w}_j)$.

2. For every $i = 1, \dots, n$ the Riemann problem (2.11) has initial datum

$$(\rho_i(x, 0), y_i(x, 0)) = \begin{cases} (\rho_i^-, \rho_i^- w_i^-) & \text{for } x < b_i \\ (\hat{\rho}_i, \hat{\rho}_i \hat{w}_i) & \text{for } x > b_i, \end{cases}$$

and is solved with waves with non-positive speed.

3. For every $j = n+1, \dots, n+m$ the Riemann problem (2.11) has initial datum

$$(\rho_j(x, 0), y_j(x, 0)) = \begin{cases} (\hat{\rho}_j, \hat{\rho}_j \hat{w}_j) & \text{for } x < a_j \\ (\rho_j^+, \rho_j^+ w_j^+) & \text{for } x > a_j, \end{cases}$$

and is solved with waves with non-negative speed.

4. It satisfies the consistency condition

$$\mathcal{RS}(\mathcal{RS}(U_1^-, \dots, U_n^-, U_{n+1}^+, \dots, U_{n+m}^+)) = \mathcal{RS}(U_1^-, \dots, U_n^-, U_{n+1}^+, \dots, U_{n+m}^+)$$

for every $(U_1^-, \dots, U_n^-, U_{n+1}^+, \dots, U_{n+m}^+) \in ([0, \rho^{\max}] \times [w_L, w_R])^{n+m}$.

Roughly speaking, for every incoming (outgoing) road the Riemann Solver computes the right (left) state to be given to the Riemann problem (2.11) in order to solve it with waves with non-negative (non-positive) speed preserving the flux of vehicles crossing the junction. The construction of Riemann Solvers requires additional assumptions, which will be stated in the next sections. In particular, we will assume that it maximises the flux of vehicles at the junction.

It is now clear that we are interested in constructing waves with non-negative or non-positive speed at junctions, thus we study the sign of the eigenvalues defined in (2.4) and (2.5). The first eigenvalue $\lambda_1(\rho, w) = \rho + \rho V_\rho(\rho, w) = Q_\rho(\rho, w)$ is such that $\lambda_1 \geq 0$ for $\rho \leq \sigma(w)$ and $\lambda_1 < 0$ for $\rho > \sigma(w)$, by properties (H1) and (H2) of the flux function. Hence, for each $w \in [w_L, w_R]$ the 1-shocks and 1-rarefaction waves have non-negative speed for $\rho \leq \sigma(w)$ and negative speed for $\rho > \sigma(w)$. In Figure 2.3 we show an example of the positive and negative regions of λ_1 obtained with the CGARZ model where the flux and velocity functions are defined in Section 2.1.1. The second eigenvalue $\lambda_2(\rho, w) = V(\rho, w) \geq 0$ by definition of V , thus the speed of the 2-contact discontinuities is always non-negative.

Remark 2.3.3. All the figures and the examples shown hereafter refer to the CGARZ model introduced in Section 2.1.1.

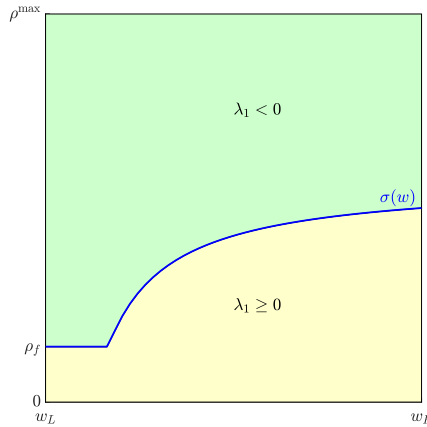


Figure 2.3. Example of positive (yellow-down) and negative (green-up) regions for λ_1 depending on w .

In order to maximise the flux in the following sections we will make use of the supply and demand functions. For each $w \in [w_L, w_R]$, the supply function $s(\rho, w)$ is defined as

$$s(\rho, w) = \begin{cases} Q^{\max}(w) & \text{if } \rho \leq \sigma(w) \\ Q(\rho, w) & \text{if } \rho > \sigma(w). \end{cases} \quad (2.12)$$

Analogously, we define the demand function $d(\rho, w)$ as

$$d(\rho, w) = \begin{cases} Q(\rho, w) & \text{if } \rho \leq \sigma(w) \\ Q^{\max}(w) & \text{if } \rho > \sigma(w). \end{cases} \quad (2.13)$$

In Figure 2.4 we show an example of the supply function on the left and of the demand function on the right.

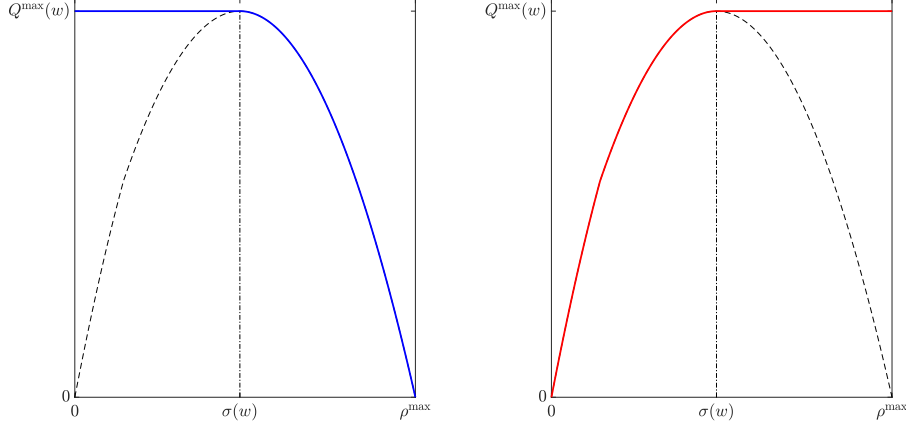


Figure 2.4. Supply function (left) and demand function (right).

Incoming road at the junction

Let us consider an incoming road at the junction. We are then interested only in the waves with non-positive speed. Since $\lambda_2 \geq 0$, we can just have 1-shock or 1-rarefaction waves. Let us fix a left state $U^- = (\rho^-, w^-)$, our aim is to define the set of all possible right states $\hat{U} = (\hat{\rho}, \hat{w})$ that can be connected to U^- with a wave with non-positive speed. We denote by $\mathcal{N}(U^-)$ the set of admissible densities.

Proposition 2.3.4. *Let $U^- = (\rho^-, w^-)$ be a left state on an incoming road with $\rho^- \neq 0$. The set of possible right states $\hat{U} = (\hat{\rho}, \hat{w})$ that can be connected to the left state lies on the level curve $\{z_1 = w^-\}$, i.e. $\hat{w} = w^-$, and is such that:*

1. *If $\rho^- \leq \sigma(w^-)$, then $\hat{\rho}$ must be in $\mathcal{N}(U^-) = [\tilde{\rho}^-(w^-), \rho^{\max}(w^-)]$, where $\tilde{\rho}^-(w^-)$ is the density such that $Q(\tilde{\rho}^-(w^-), w^-) = Q(\rho^-, w^-)$.*
2. *If $\rho^- > \sigma(w^-)$, then $\hat{\rho}$ must be in $\mathcal{N}(U^-) = [\sigma(w^-), \rho^{\max}(w^-)]$.*

If $\rho^- = 0$ then the only admissible right state is $\hat{U} = U^-$.

Proof. Let us first consider the case of $U^- = (\rho^-, w^-)$ with $\rho^- \neq 0$. Since $v^- \geq 0$, we cannot have 2-contact discontinuities with negative speed, therefore we focus on waves of the 1-family.

If $\rho^- \leq \sigma(w^-)$, see the left plot of Figure 2.5, then we have two possibilities: not moving at all, obtaining $\hat{U} = U^-$, or moving to the density value $\tilde{\rho}^-(w^-) > \sigma(w^-)$ by a jump with zero speed. Indeed, since $Q(\tilde{\rho}^-(w^-), w^-) = Q(\rho^-, w^-)$, the Rankine-Hugoniot condition (1.6) implies that $s = 0$. In this case we can move with a 1-shock towards any right state \hat{U} with $\hat{w} = w^-$ and $\tilde{\rho}^-(w^-) \leq \hat{\rho} \leq \rho^{\max}(w^-)$. Note that if $\rho^- = 0$ then $\tilde{\rho}^-(w^-) = \rho^{\max}(w^-)$, therefore the solution is $\hat{U} = U^-$.

If $\rho^- > \sigma(w^-)$ then every state \hat{U} with $\hat{w} = w^-$ and $\hat{\rho} \in (\sigma(w^-), \rho^{\max}(w^-)]$ is connected to U^- with waves with negative speed, see the right plot of Figure 2.5. In particular we move with a 1-rarefaction wave if $\hat{\rho} \leq \rho^-$ and with a 1-shock if $\hat{\rho} > \rho^-$. □

Remark 2.3.5. *We observe that the flux of the right state satisfies*

$$Q(\hat{\rho}, \hat{w}) \leq d(\rho^-, w^-), \quad (2.14)$$

where d is the demand function defined in (2.13). Indeed, if $\rho^- \leq \sigma(w^-)$ then $\hat{\rho}$ must be in $\mathcal{N}(U^-) = [\tilde{\rho}^-(w^-), \rho^{\max}(w^-)]$, where the flux is lower than or equal to $Q(\rho^-, w^-)$; if $\rho^- > \sigma(w^-)$, then $\hat{\rho}$ must

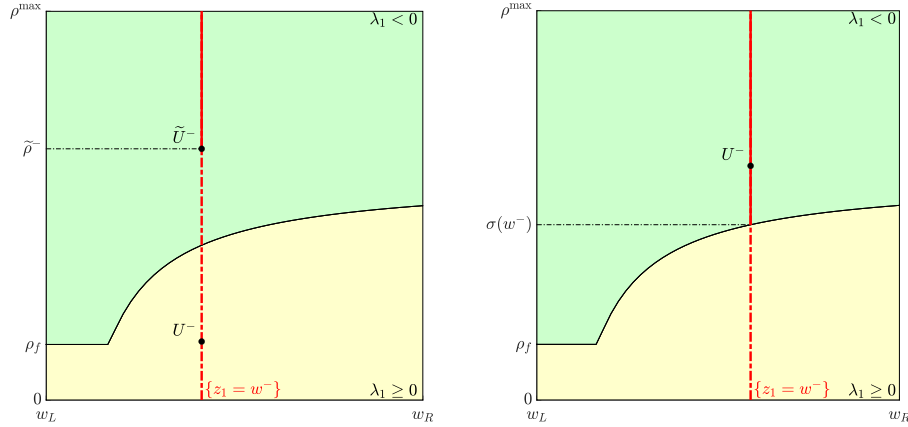


Figure 2.5. Two possible configurations of incoming road states. The red segment identifies the set of possible right states \hat{U} reachable from the left state U^- .

be in $\mathcal{N}(U^-) = [\sigma(w^-), \rho^{\max}(w^-)]$, where the flux is lower than $Q^{\max}(w^-)$. These two possibilities are summarised in (2.14).

Outgoing road at the junction

Let us consider an outgoing road at the junction. We are interested in the waves with non-negative speed, thus we can have a 1-shock or 1-rarefaction wave and a 2-contact discontinuity. Let us fix a right state $U^+ = (\rho^+, w^+)$, our aim is to define the set of all possible left states $\hat{U} = (\hat{\rho}, \hat{w})$ that can be connected to U^+ with waves with non-negative speed. We denote by $\mathcal{P}(U^+)$ the set of admissible densities.

Proposition 2.3.6. *Let $U^+ = (\rho^+, w^+)$ be a right state on an outgoing road and v^+ the associated velocity $V(\rho^+, w^+)$. Let $U^* = (\rho^*, w^*)$ be the intersection point, if it exists, between the level curves $\{z_2 = v^+\}$ and $\{z_1 = c\}$, for a certain $c \in [w_L, w_R]$, with $\rho^* = \rho^*(v^+, c)$ and $w^* = c$. The set of possible left states $\hat{U} = (\hat{\rho}, \hat{w})$ that can be connected to the right state is such that $\hat{w} = c$ and*

1. *If $\rho^* \leq \sigma(w^*)$, then $\hat{\rho}$ must be in $\mathcal{P}(U^+) = [0, \sigma(w^*)]$.*
2. *If $\rho^* > \sigma(w^*)$, then $\hat{\rho}$ must be in $\mathcal{P}(U^+) = [0, \tilde{\rho}^*(w^*)] \cup \{\rho^*\}$, where $\tilde{\rho}^*(w^*)$ is the density such that $Q(\tilde{\rho}^*(w^*), w^*) = Q(\rho^*, w^*)$.*

If it does not exist the intersection between the level curves, then $U^ = (0, w^*)$, with $w^* = \hat{w} = c$, and $\hat{\rho}$ must be in $\mathcal{P}(U^+) = [0, \sigma(w^*)]$.*

Proof. Let $U^+ = (\rho^+, w^+)$ be a right state. For the outgoing roads we look for waves with non-negative speed, thus we can have waves of both the two families. Given v^+ and c , if $v^+ \leq V^{\max}(c)$ then the state $U^* = (\rho^*, w^*)$ is well-defined, since $\{z_2 = v^+\}$ and $\{z_1 = w^*\}$ have a unique intersection point, with $w^* = c$.

If $\rho^* \leq \sigma(w^*)$ then every state \hat{U} with $\hat{w} = c$ and $\hat{\rho} \in [0, \sigma(w^*)]$ is connected to U^* with waves with positive speed, see the left plot of Figure 2.6. In particular we move with a 1-rarefaction wave if $\rho^* \leq \hat{\rho}$ and with a 1-shock if $\rho^* > \hat{\rho}$, and then we connect U^* to U^+ by a 2-contact discontinuity.

If $\rho^* > \sigma(w^*)$, see the right plot of Figure 2.6, then we have two possibilities: not moving at all, obtaining $\hat{U} = U^*$, or moving to the density value $\tilde{\rho}^*(w^*) < \sigma(w^*)$ by a jump with zero speed, similarly to Proposition 2.3.4. In this case we can move with a 1-rarefaction wave towards any right state \hat{U} with $\hat{w} = w^*$ and $0 \leq \hat{\rho} \leq \tilde{\rho}^*(w^*)$, and then move to U^+ by a 2-contact discontinuity.

2.3. The Riemann problem for GSOM at junctions

If $v^+ > V^{\max}(c)$ then, as described in Section 2.2, $U^* = (0, w^*)$ with $w^* = c$, and the left state \hat{U} must be in $[0, \sigma(w^*)]$. \square

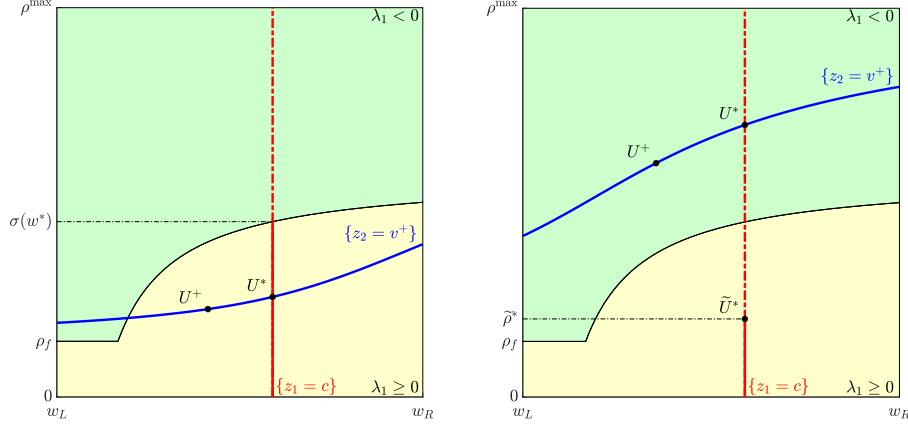


Figure 2.6. Two possible configurations of outgoing road. The red segment identifies the set of possible left states \hat{U} reachable from the right state U^+ .

Remark 2.3.7. We observe that $w^* = \hat{w} = c$ and that the flux of the left state satisfies

$$Q(\hat{\rho}, \hat{w}) \leq s(\rho^*, w^*), \quad (2.15)$$

where s is the supply function defined in (2.12). Indeed, if $\rho^* \leq \sigma(w^+)$ then $\hat{\rho}$ must be in $\mathcal{P}(U^+) = [0, \sigma(w^*)]$, where the flux is lower than or equal to $Q^{\max}(w^*)$; if $\rho^* > \sigma(w^+)$, then $\hat{\rho}$ must be in $\mathcal{P}(U^+) = [0, \tilde{\rho}^*(w^*)] \cup \{\rho^*\}$, where the flux is lower than $Q(\rho^*, w^*)$. These two possibilities are summarised in (2.15).

Definition 2.3.8. Given $v^+ \in [0, V^{\max}(w^+)]$ and $w^- \in [w_L, w_R]$, we define

$$\rho^*(v^+, w^-) = \begin{cases} V^{-1}(v^+, w^-) & \text{if } v^+ \leq V^{\max}(w^-) \\ 0 & \text{if } v^+ > V^{\max}(w^-) \end{cases}$$

where V^{-1} is the inverse of the velocity function such that $V(\rho^*, w^-) = v^+$.

Let us introduce a definition derived by Propositions 2.3.4 and 2.3.6 which will be used in Chapter 3.

Definition 2.3.9. For every incoming road we say that a datum (ρ^-, w^-) is a good datum if $\rho^- \in [\sigma(w^-), \rho^{\max}(w^-)]$ and a bad datum otherwise. For every outgoing road and $c \in [w_L, w_R]$ we say that a datum (ρ^+, w^+) is a good datum if $\rho^* \in [0, \sigma(w^*)]$, with $w^* = c$, and a bad datum otherwise.

Now we focus on the intersection point U^* between the level curves of the two Riemann invariants $\{z_1 = w^-\}$ and $\{z_2 = v^+\}$, for some w^- and v^+ . In the propositions which follow, we refer to Figures 2.7 and 2.8, whose plots are obtained with the CGARZ model and flux functions defined in Section 2.1.1. However, the statements of Propositions 2.3.10 and 2.3.11 hold for any GSOM with flux and velocity functions satisfying properties (H1)-(H6).

Proposition 2.3.10. Let V be a velocity function verifying hypotheses (H5) and (H6), given w^- and v^+ the following statements hold.

1. If $v^+ \leq V^{\max}(w^-)$, the intersection point $U^* = (\rho^*, w^*)$ between $\{z_1 = w^-\}$ and $\{z_2 = v^+\}$ is such that $w^* = w^-$ and $\rho^* = \rho^*(v^+, w^-)$ is the unique density value such that $V(\rho^*, w^-) = v^+$.

2. The function $\rho^*(v^+, w)$ in Definition 2.3.8 is non-decreasing in w .

Proof. We have $w^* = w^-$ by construction, while the uniqueness of ρ^* follows by the property (H5) of the velocity function V . To prove the monotonicity of ρ^* , let us consider the family of speed functions $V(\rho, w)$ (see for example the left plot of Figure 2.7). If we cut the speed-family with a horizontal line $V = v^+$, we obtain the density values whose velocity is equal to v^+ as w changes. By property (H6) follows that ρ is non-decreasing in w , thus the level curve $\{z_2 = v^+\}$ is non-decreasing in the (w, ρ) -plane, see the right plot of Figure 2.7. Since ρ^* lies on these curves the thesis follows.

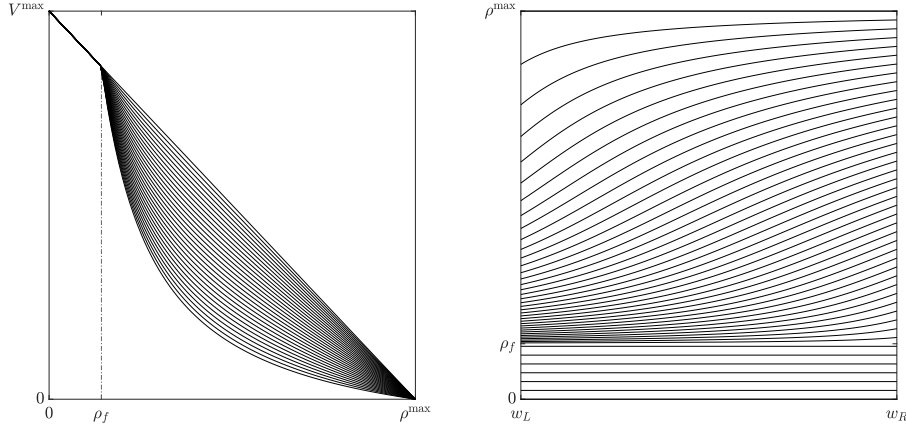


Figure 2.7. Example of family of speed functions (left) and level curves of ρ^* for different values of v^+ (right).

□

Proposition 2.3.11. For any $v^+ \in [0, V^{\max}(w^+)]$ and $w \in [w_L, w_R]$ the function $s(\rho^*, w)$ in (2.12) is non-decreasing in w , where $\rho^* = \rho^*(v^+, w)$ is given in Definition 2.3.8.

Proof. First of all we observe that all the points ρ^* along the level curve $\{z_2 = v^+\}$ are such that $Q(\rho^*, w) = v^+ \rho^*$, for any $w \in [w_L, w_R]$. Since ρ^* is non-decreasing in w by Proposition 2.3.10, also the flux along the curve is non-decreasing in w . We divide the proof in four cases.

1. The level curve $\{z_2 = v^+\}$ is entirely below the curve $\rho = \sigma(w)$, see Figure 2.8(a). In this case we have $s(\rho^*, w) = Q^{\max}(w)$, which is non-decreasing in w by property (H3).
2. The level curve $\{z_2 = v^+\}$ has a unique intersection point with the curve $\rho = \sigma(w)$, see Figure 2.8(b). In this case, denoting by $U^\dagger = (w^\dagger, \rho^\dagger)$ the intersection point, we have

$$s(\rho^*, w) = \begin{cases} v^+ \rho^* & \text{if } w \leq w^\dagger \\ Q^{\max}(w) & \text{if } w > w^\dagger, \end{cases}$$

which is non-decreasing in w by Proposition 2.3.10 and property (H3).

3. The level curve $\{z_2 = v^+\}$ has two intersection points with the curve $\rho = \sigma(w)$, see Figure 2.8(c). We denote by $U^\dagger = (w^\dagger, \rho^\dagger)$ and $\bar{U} = (\bar{w}, \bar{\rho})$ the intersection points. We have

$$s(\rho^*, w) = \begin{cases} v^+ \rho^* & \text{if } w \leq w^\dagger \\ Q^{\max}(w) & \text{if } w^\dagger < w \leq \bar{w} \\ v^+ \rho^* & \text{if } w > \bar{w}. \end{cases}$$

2.3. The Riemann problem for GSOM at junctions

We observe that we recover the previous case for the points $U = (w, \rho)$ such that $w \leq \bar{w}$. Since \bar{U} intersects $\sigma(w)$, we have $Q(\bar{\rho}, \bar{w}) = Q^{\max}(\bar{w}) = v^+ \bar{\rho}$. For any $\delta, \varepsilon > 0$, if $(w + \delta, \bar{\rho} + \varepsilon) \in \{z_2 = v^+\}$ then $Q(\bar{\rho} + \varepsilon, \bar{w} + \delta) = v^+(\bar{\rho} + \varepsilon) > Q(\bar{\rho}, \bar{w})$, thus the supply function is always non-decreasing also for $w > \bar{w}$.

4. The level curve $\{z_2 = v^+\}$ is entirely above the curve $\rho = \sigma(w)$, see Figure 2.8(d). In this case we have $s(\rho^*, w) = v^+ \rho^*$, which is non-decreasing in w by Proposition 2.3.10.

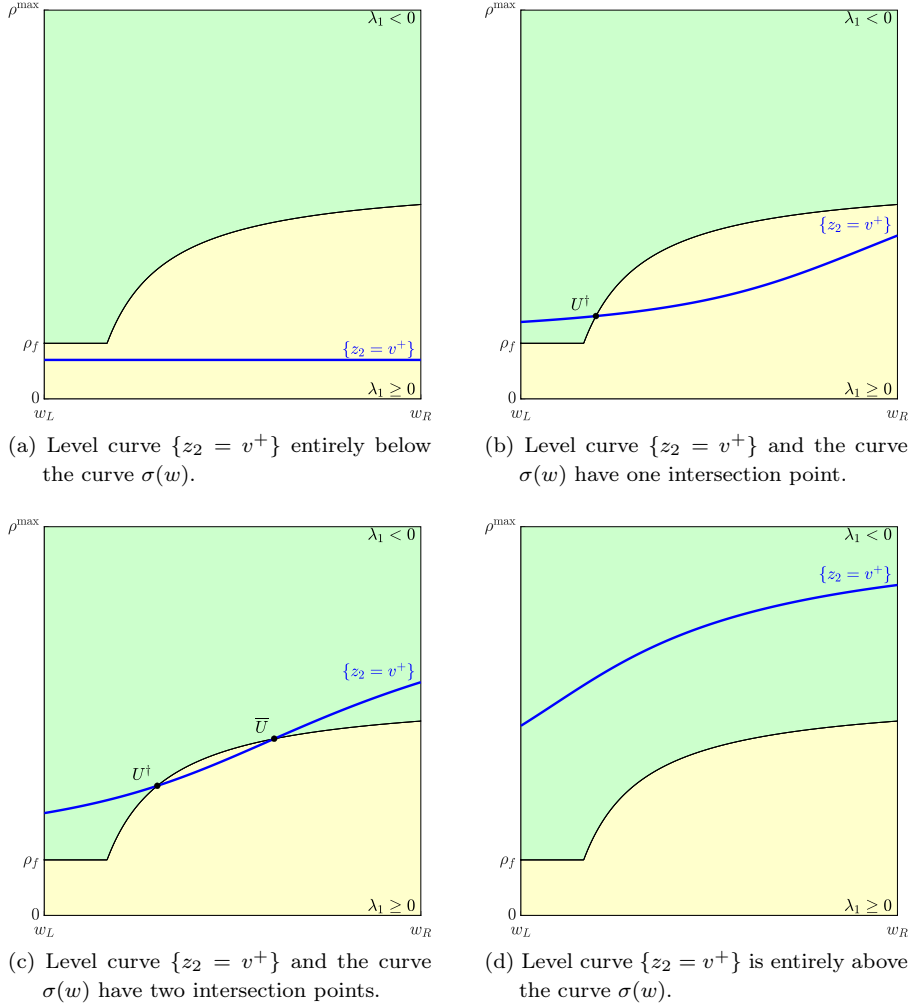


Figure 2.8. Four possible cases of the position of the level curve $\{z_2 = v^+\}$ with respect to the curve $\rho = \sigma(w)$.

□

2.3.2 The case of one incoming road and one outgoing road at junctions

We consider the simplest case of two roads connected by a junction. We have a left state U_1^- for the incoming road and a right state U_2^+ for the outgoing road and we have to solve the Riemann problem at the junction. Thus, our aim is to recover \hat{U}_1 and \hat{U}_2 .

We assume that ρ and y are conserved at the junction, i.e.

$$\hat{\rho}_1 \hat{v}_1 = \hat{\rho}_2 \hat{v}_2 \quad (2.16)$$

$$\hat{\rho}_1 \hat{v}_1 \hat{w}_1 = \hat{\rho}_2 \hat{v}_2 \hat{w}_2. \quad (2.17)$$

Equation (2.16) implies that $\hat{q}_1 = \hat{q}_2$, therefore equation (2.17) implies $\hat{w}_1 = \hat{w}_2$. Since w is the first Riemann invariant, by the preliminary studies on the incoming road we have $w_1^- = \hat{w}_1 = \hat{w}_2$. This means that \hat{U}_1 and \hat{U}_2 must lay along the level curve $\{z_1 = w_1^-\}$. Thus the point $U_2^* = (\rho_2^*, w_2^*)$ of the outgoing road is defined by the intersection between $\{z_1 = w_1^-\}$ and the level curve $\{z_2 = v_2^+\}$ passing through U_2^+ , where $v_2^+ = V(\rho_2^+, w_2^+)$, i.e. $w_2^* = \hat{w}_2 = w_1^-$.

In order to define a unique solution, we look for the one which maximises the flux. By Remarks 2.3.5 and 2.3.7, we know that

$$\begin{aligned} 0 &\leq q \leq d(\rho_1^-, w_1^-) \\ 0 &\leq q \leq s(\rho_2^*, w_1^-), \end{aligned}$$

which implies that we are looking for

$$\bar{q} = \min\{d(\rho_1^-, w_1^-), s(\rho_2^*, w_1^-)\}. \quad (2.18)$$

Thus, $\hat{q}_1 = \hat{q}_2 = \bar{q}$. Once \hat{q}_1 and \hat{q}_2 are known, we define $\hat{\rho}_1 \in \mathcal{N}(U_1^-)$ such that $Q(\hat{\rho}_1, \hat{w}_1) = \hat{q}_1$, and $\hat{\rho}_2 \in \mathcal{P}(U_2^+)$ such that $Q(\hat{\rho}_2, \hat{w}_2) = \hat{q}_2$.

Remark 2.3.12. *The solution to the 1 → 1 junction coincides with the solution to the Riemann problem on a single road. Indeed, the state U_2^* coincides with the intermediate state U^* described in Section 2.2.*

Example 2.3.13. *In Figure 2.9 we show an example of a junction with one incoming and one outgoing road. Following the procedure above described, we have $\hat{w}_1 = \hat{w}_2 = w_2^* = w_1^-$, $\mathcal{N}(U_1^-) = [\tilde{\rho}_1^-(w_1^-), \rho^{\max}]$, $\mathcal{P}(U_2^+) = [0, \tilde{\rho}_2^*(w_2^+)] \cup \{\rho_2^*\}$ and $\bar{q} = Q(\rho_2^*, w_1^-)$. Therefore \hat{U}_1 and \hat{U}_2 coincide and are defined by*

$$\hat{U}_1 = \hat{U}_2 = (\rho_2^*, w_1^-).$$

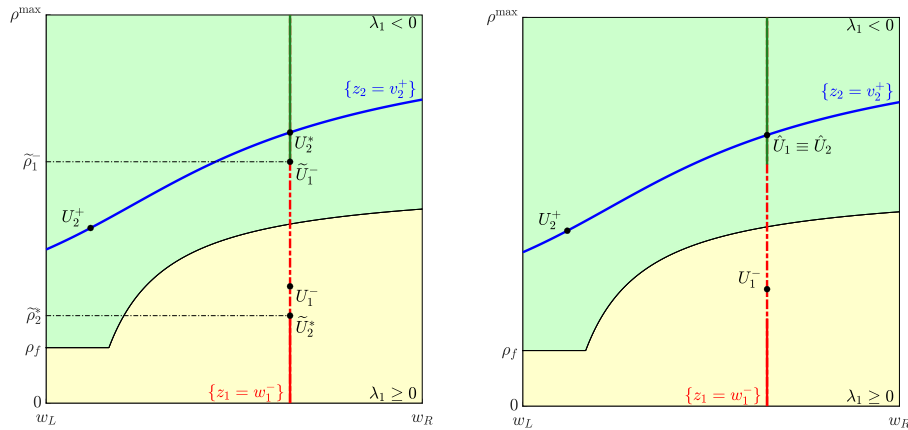


Figure 2.9. Example of 1 → 1 junction: the procedure to follow (left) and the solution (right). The green segment along $\{z_1 = w_1^-\}$ is $\mathcal{N}(U_1^-)$, the red segment is $\mathcal{P}(U_2^+)$.

2.3.3 The case of diverge junction

We consider the case of one incoming road and two outgoing roads at junctions. We have a left state U_1^- for the incoming road and two right states U_2^+ and U_3^+ for the outgoing roads and our aim is to recover

2.3. The Riemann problem for GSOM at junctions

\hat{U}_1 , \hat{U}_2 and \hat{U}_3 . We introduce the parameter $\alpha \in (0, 1)$ which defines how vehicles distribute from the incoming road to the outgoing roads. Indeed, vehicles are distributed in proportion α and $1 - \alpha$ on the roads 2 and 3 respectively. Note that the cases and $\alpha = 0$ or $\alpha = 1$ reduce the problem to a $1 \rightarrow 1$ junction, thus we exclude the extreme values from this analysis.

We assume the conservation of ρ and y , thus we have

$$\alpha \hat{\rho}_1 \hat{v}_1 = \hat{\rho}_2 \hat{v}_2 \quad (2.19) \quad (1 - \alpha) \hat{\rho}_1 \hat{v}_1 = \hat{\rho}_3 \hat{v}_3 \quad (2.21)$$

$$\alpha \hat{\rho}_1 \hat{v}_1 \hat{w}_1 = \hat{\rho}_2 \hat{v}_2 \hat{w}_2 \quad (2.20) \quad (1 - \alpha) \hat{\rho}_1 \hat{v}_1 \hat{w}_1 = \hat{\rho}_3 \hat{v}_3 \hat{w}_3. \quad (2.22)$$

Equation (2.19) in (2.20) implies $\hat{w}_1 = \hat{w}_2$. Analogously, equation (2.21) in (2.22) implies $\hat{w}_1 = \hat{w}_3$. As in Section 2.3.2, we have $w_1^- = \hat{w}_1$ hence $\hat{w}_2 = \hat{w}_3 = w_1^-$. Thus, the two intersection points U_2^* and U_3^* between the two level curves of the second Riemann invariant passing through U_2^+ and U_3^+ are defined by their intersection with the level curve $\{z_1 = w_1^-\}$, i.e. $w_2^* = w_3^* = w_1^-$ while ρ_2^* and ρ_3^* depend on $V(\rho_2^*, w_1^-) = v_2^+$ and $V(\rho_3^*, w_1^-) = v_3^+$, respectively.

In this case, in order to define a unique solution which maximises the flux, we observe that Remarks 2.3.5 and 2.3.7 imply

$$\begin{aligned} 0 &\leq q \leq d(\rho_1^-, w_1^-) \\ 0 &\leq \alpha q \leq s(\rho_2^*, w_1^-) \\ 0 &\leq (1 - \alpha)q \leq s(\rho_3^*, w_1^-), \end{aligned}$$

which leads us to look for $\bar{q} = \min\{d(\rho_1^-, w_1^-), s(\rho_2^*, w_1^-)/\alpha, s(\rho_3^*, w_1^-)/(1 - \alpha)\}$. Once \bar{q} is found we have

$$\begin{aligned} \hat{q}_1 &= \bar{q} \\ \hat{q}_2 &= \alpha \bar{q} \\ \hat{q}_3 &= (1 - \alpha) \bar{q}, \end{aligned}$$

and then we define $\hat{\rho}_1 \in \mathcal{N}(U_1^-)$ such that $Q(\hat{\rho}_1, \hat{w}_1) = \hat{q}_1$, $\hat{\rho}_2 \in \mathcal{P}(U_2^+)$ such that $Q(\hat{\rho}_2, \hat{w}_2) = \hat{q}_2$ and $\hat{\rho}_3 \in \mathcal{P}(U_3^+)$ such that $Q(\hat{\rho}_3, \hat{w}_3) = \hat{q}_3$.

Example 2.3.14. In Figure 2.10 we show an example of a junction with one incoming and two outgoing roads. Following the procedure above described, we have $\hat{w}_1 = \hat{w}_2 = \hat{w}_3 = w_2^* = w_3^* = w_1^-$, $\mathcal{N}(U_1^-) = [\tilde{\rho}_1^-(w_1^-), \rho^{\max}]$, $\mathcal{P}(U_2^+) = [0, \tilde{\rho}_2^*(w_1^-)) \cup \{\rho_2^*\}$, $\mathcal{P}(U_3^+) = [0, \sigma(w_1^-)]$. We fix $\alpha = 0.7$ and then we have $\bar{q} = Q(\rho_1^-, w_1^-)$. Therefore $\hat{\rho}_1 = \tilde{\rho}_1^-(w_1^-)$, while $\hat{\rho}_2$ and $\hat{\rho}_3$ are defined by

$$Q(\hat{\rho}_2, w_1^-) = 0.7\bar{q} \quad \text{and} \quad Q(\hat{\rho}_3, w_1^-) = (1 - 0.7)\bar{q}.$$

2.3.4 The case of merge junction

We consider the case of two incoming roads and one outgoing road at junctions. We have two left states U_1^- and U_2^- for the incoming roads and a right state U_3^+ for the outgoing road and our aim is to recover \hat{U}_1 , \hat{U}_2 and \hat{U}_3 . The approach we propose for the merge junction is based on a priority rule, defined by a vector (p_1, p_2) , with $p_1 + p_2 = 1$. We observe that the special cases of $(p_1, p_2) = (0, 1)$ and $(p_1, p_2) = (1, 0)$ imply that no vehicles can cross the intersection from road 1 and 2, respectively, reducing the junction to the $1 \rightarrow 1$ case. Hence, we assume that both p_1 and p_2 are different from 0.

Let us begin assuming the conservation of ρ and y at junction, i.e.

$$\hat{q}_1 + \hat{q}_2 = \hat{q}_3 \quad (2.23)$$

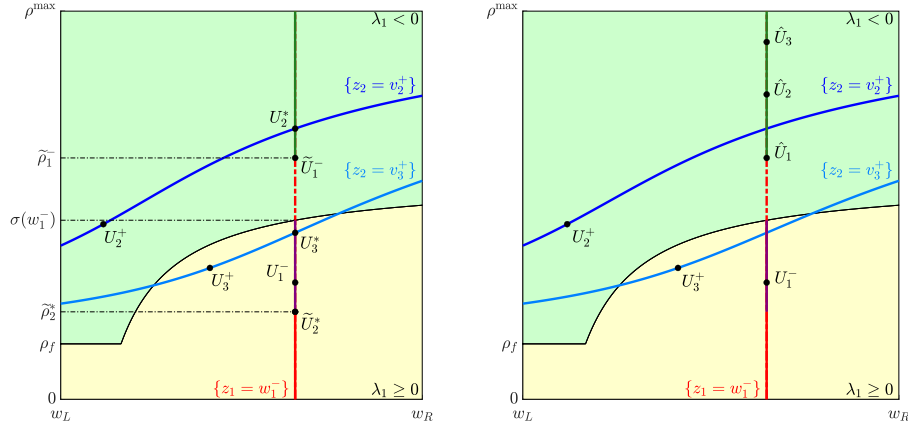


Figure 2.10. Example of $1 \rightarrow 2$ junction: the procedure to follow (left) and the solution (right). The green segment along $\{z_1 = w_1^-\}$ is $\mathcal{N}(U_1^-)$, the red segment is $\mathcal{P}(U_2^+)$ and the red segment combined with the purple one is $\mathcal{P}(U_3^+)$.

$$\hat{q}_1 \hat{w}_1 + \hat{q}_2 \hat{w}_2 = \hat{q}_3 \hat{w}_3. \quad (2.24)$$

Since the first Riemann invariant is w , we have $\hat{w}_1 = w_1^-$ and $\hat{w}_2 = w_2^-$. Equation (2.23) in (2.24) implies

$$\hat{w}_3 = \frac{\hat{q}_1 w_1^- + \hat{q}_2 w_2^-}{\hat{q}_1 + \hat{q}_2}. \quad (2.25)$$

We now move to the (q_1, q_2) -plane and we look for the maximisation of the flow. We introduce $d_1 = d(\rho_1^-, w_1^-)$, $d_2 = d(\rho_2^-, w_2^-)$ and the rectangle of possible solutions $\Omega = [0, d_1] \times [0, d_2]$. We assume that both d_1 and d_2 are greater than 0. Indeed, the trivial case of $d_1 = d_2 = 0$ means that no vehicles cross the intersection while the case of one of d_1 or d_2 equal to 0 reduces the junction to the $1 \rightarrow 1$ case. We define the straight line r of priority rule in parametric form as

$$r : \begin{cases} q_1 = hp_1 \\ q_2 = hp_2, \end{cases}$$

and the parameters

$$h_1 = \max\{h : hp_1 \leq d_1\} = \frac{d_1}{p_1} \quad (2.26)$$

$$h_2 = \max\{h : hp_2 \leq d_2\} = \frac{d_2}{p_2}. \quad (2.27)$$

Note that, $(d_1, h_1 p_2)$ is the intersection point between the straight line r and the vertical line d_1 while $(h_2 p_1, d_2)$ is the intersection point between the straight line r and the horizontal line d_2 . By setting $\hat{q}_1 = hp_1$ and $\hat{q}_2 = hp_2$ in (2.25) we have

$$\hat{w}_3 = p_1 w_1^- + p_2 w_2^- \quad (2.28)$$

$$s_3 = s(\rho^*(v_3^+, \hat{w}_3), \hat{w}_3),$$

where $v_3^+ = V(\rho_3^+, w_3^+)$ and ρ_3^* given in Definition 2.3.8. We then define

$$h_3 = \min\{h : hp_1 + hp_2 = s_3\} = s_3, \quad (2.29)$$

which identifies the intersection point $(h_3 p_1, h_3 p_2)$ between the straight line r and the straight line

$$z : q_1 + q_2 = s_3 \quad (2.30)$$

where the outgoing flux is maximised (see Remark 2.3.7). In order to understand which is the first point we find along the straight line r , we define

$$h_1 = \min\{h_1, h_2, h_3\}. \quad (2.31)$$

Figure 2.11 shows an example of the three points identified by h_1 , h_2 and h_3 , i.e. $P_1 = (d_1, h_1 p_2)$, $P_2 = (h_2 p_1, d_2)$ and $P_3 = (h_3 p_1, h_3 p_2)$, where $h_1 = h_1$.

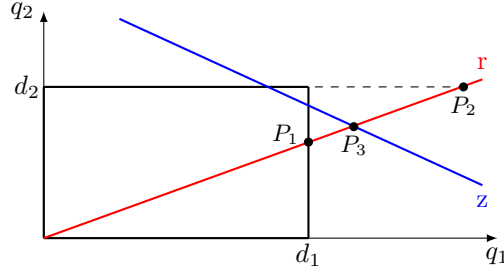


Figure 2.11. Example of the three points $P_1 = (h_1 p_1, h_1 p_2)$, $P_2 = (h_2 p_1, h_2 p_2)$ and $P_3 = (h_3 p_1, h_3 p_2)$.

We now have two possibilities: $h_1 = h_3$ or $h_1 \neq h_3$. In the first case we immediately find a couple of incoming fluxes (\hat{q}_1, \hat{q}_2) which satisfy the priority rule and that maximise the flux. In the second case the priority first intersects the boundary of the set of possible solutions Ω and does not maximise the outgoing flux. The approach we propose is divided in two cases:

- (a) We need to strictly respect the priority rule. This case is necessary to simulate traffic scenarios such as traffic lights, where the priority rule must be satisfied.
- (b) We are free to adapt, i.e. to change, the priority rule. This case is useful to maximise the flux when the intersection between the straight lines r and z is outside the set of possible solutions Ω . The idea is to change the priority r , and consequently the parameter \hat{w}_3 and the maximisation straight line z , looking for the intersection between the modified r and z which maximises the flux at the junction.

Case $h_1 = h_3$. In this case, the priority rule first intersects the straight line z , see Figure 2.12. This means that the intersection point identifies two incoming fluxes satisfying the priority and which maximise the outgoing flux. Therefore, we have \hat{w}_3 in (2.28) and

$$\hat{q}_1 = p_1 h_3, \quad \hat{q}_2 = p_2 h_3, \quad \hat{q}_3 = h_3.$$

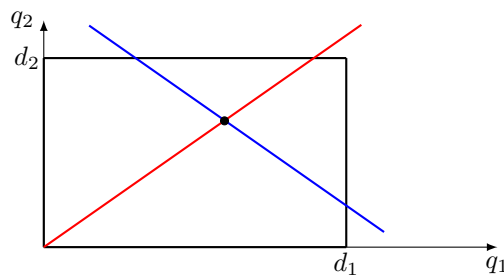


Figure 2.12. Merge junction with $h_1 = h_3$.

Case $h_1 = h_1$. In this case the straight line r first intersects the vertical line $q_1 = d_1$.

- (a) If we need to respect the priority rule, then the solution is given by

$$\hat{q}_1 = p_1 h_1, \quad \hat{q}_2 = p_2 h_1, \quad \hat{q}_3 = h_1,$$

with \hat{w}_3 defined in (2.28). This case is represented in 2.13(a).

- (b) If we can adapt the priority rule, we fix $\hat{q}_1 = h_1 p_1 = d_1$ and we move along the vertical side of Ω , looking for $\hat{q}_2 = h_2 p_2$ for a proper h_2 . The idea of our approach is to modify both r and z in order to find the intersection between the two straight lines along the vertical line $q_1 = d_1$. By equation (2.25) with $\hat{q}_1 = d_1$ and $\hat{q}_2 = h p_2$ we have

$$\hat{w}_3(h) = \frac{d_1 w_1^- + h p_2 w_2^-}{d_1 + h p_2} \quad (2.32)$$

which is such that

$$\lim_{h \rightarrow 0} \hat{w}_3(h) = w_1^-, \quad \lim_{h \rightarrow +\infty} \hat{w}_3(h) = w_2^-.$$

Let $s_3(\hat{w}_3) := s(\rho^*(v_3^+, \hat{w}_3), \hat{w}_3)$, we define h_3 as

$$h_3 = \min\{h \in [h_1, +\infty) : d_1 + h p_2 = s_3(\hat{w}_3(h)), \text{ for } \hat{w}_3(h) \text{ in (2.32)}\}. \quad (2.33)$$

Note that there exists at least a value of h satisfying $d_1 + h p_2 = s_3(\hat{w}_3(h))$. Indeed, $d_1 + h_1 p_2 < s_3(\hat{w}_3(h_1))$ by hypothesis of $h_1 \neq h_3$, and

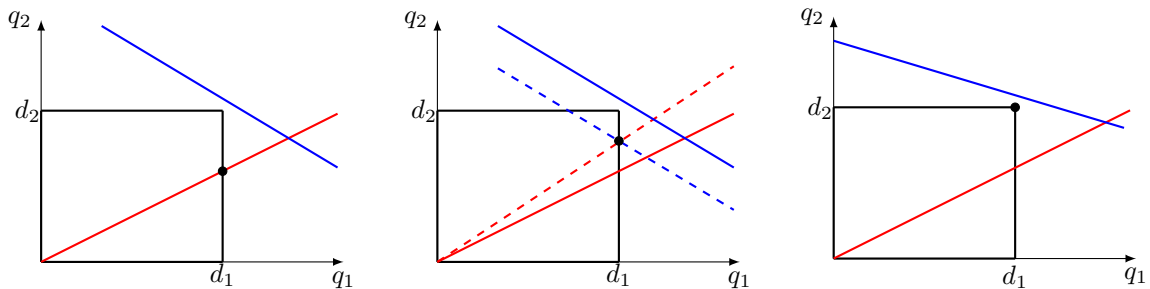
$$\lim_{h \rightarrow +\infty} d_1 + h p_2 = +\infty, \quad \lim_{h \rightarrow +\infty} s_3(\hat{w}_3(h)) = s_3(w_2^-) < +\infty,$$

hence, by continuity, $d_1 + h p_2$ must intersect $s_3(w_3^-(h))$ for some h .

Once computed the new h_3 , we define $h_2 = \min\{h_2, h_3\}$, with h_2 in (2.27), and the fluxes crossing the junction as

$$\hat{q}_1 = d_1, \quad \hat{q}_2 = h_2 p_2, \quad \hat{q}_3 = d_1 + h_2 p_2.$$

In Figures 2.13(b) and 2.13(c) we show the solution with $h_2 = h_3$ and $h_2 = h_2$, respectively. Moreover, the new vector of priority rule is $(\hat{p}_1, \hat{p}_2) = (\hat{q}_1/\hat{q}_3, \hat{q}_2/\hat{q}_3)$.



(a) Solution that respects the priority rule. (b) Solution that adapts the priority rule with $h_2 = h_3$. (c) Solution that adapts the priority rule with $h_2 = h_2$.

Figure 2.13. Merge junction with $h_1 = h_1$.

Case $h_1 = h_2$. This case is completely analogous to the previous one, but the straight line r first intersects the horizontal line $q_2 = d_2$.

(a) If we need to respect the priority rule then the solution is given by

$$\hat{q}_1 = p_1 h_2, \quad \hat{q}_2 = p_2 h_2, \quad \hat{q}_3 = h_2,$$

with \hat{w}_3 in (2.28). This case is shown in Figure 2.14(a).

(b) If we can adapt the priority rule then we define

$$\begin{aligned} \hat{w}_3(h) &= \frac{hp_1 w_1^- + d_2 w_2^-}{hp_1 + d_2} \\ h_3 &= \min\{h \in [h_2, +\infty) : hp_1 + d_2 = s_3(\hat{w}_3(h))\} \\ h_2 &= \min\{h_1, h_3\}, \end{aligned}$$

with h_1 in (2.26), from which we recover

$$\hat{q}_1 = h_2 p_1, \quad \hat{q}_2 = d_2, \quad \hat{q}_3 = h_2 p_1 + d_2.$$

In Figures 2.14(b) and 2.14(c) we show the solution with $h_2 = h_3$ and $h_2 = h_1$, respectively.

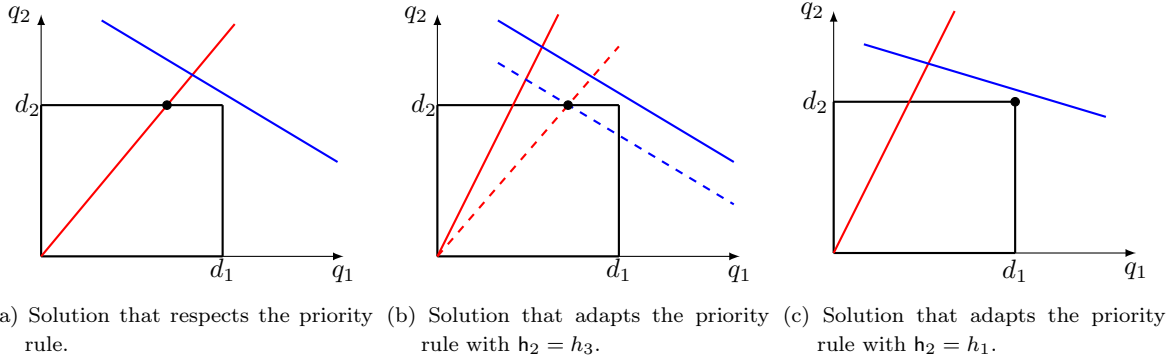


Figure 2.14. Merge junction with $h_1 = h_2$.

Example 2.3.15. In Figure 2.15 we show an example of a junction with two incoming and one outgoing roads. Following the procedure above described, we fix $(p_1, p_2) = (0.4, 0.6)$ and we have $\hat{w}_1 = w_1^-$, $\hat{w}_2 = w_2^-$, $\hat{w}_3 = p_1 w_1^- + p_2 w_2^-$, $\mathcal{N}(U_1^-) = [\sigma(\rho_1^-), \rho^{\max}]$, $\mathcal{N}(U_2^-) = \{\rho_2^*\} \cup (\tilde{\rho}_2^*(w_2^-), \rho^{\max}]$, $\mathcal{P}(U_3^+) = [0, \sigma(\hat{w}_3)]$. The point of intersection between the straight lines r and z is inside the rectangle Ω , thus $h_1 = h_3 = s_3(\hat{w}_3)$ which means that $\hat{q}_1 = p_1 h_3$, $\hat{q}_2 = p_2 h_3$ and $\hat{q}_3 = h_3$. Finally we compute the densities $\hat{\rho}_1$, $\hat{\rho}_2$ and $\hat{\rho}_3$ such that $\hat{q}_1 = Q(\hat{\rho}_1, \hat{w}_1)$, $\hat{q}_2 = Q(\hat{\rho}_2, \hat{w}_2)$ and $\hat{q}_3 = Q(\hat{\rho}_3, \hat{w}_3)$, as shown in the right plot of Figure 2.15.

2.4 The APRSOM algorithm for n incoming and m outgoing roads at junctions

In this section we extend the previous results to the generic case, defining our Riemann Solver for GSOM on network. Let us consider the general case of a junction with n incoming roads and m outgoing roads. We have n left states U_i^- and m right states U_j^+ , and our aim is to find \hat{U}_i and \hat{U}_j for $i = 1, \dots, n$ and $j = n + 1, \dots, n + m$. We introduce a vector of priority (p_1, \dots, p_n) which establishes which incoming road has the priority of sending vehicles with respect to the other ones. The components p_i are such that $\sum_{i=1}^n p_i = 1$. We assume that $p_i \neq 0$ for all $i = 1, \dots, n$. Indeed, if we have $p_{i_1} = \dots = p_{i_\kappa} = 0$ for κ

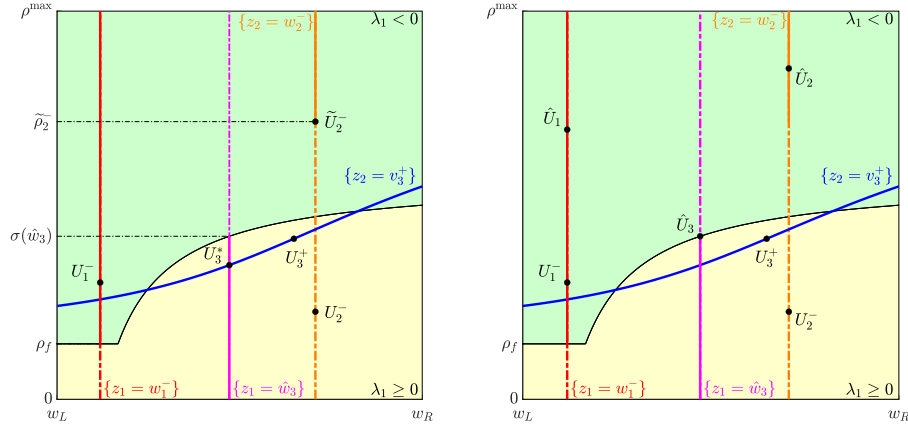


Figure 2.15. Example of 2 → 1 junction: the procedure to follow (left) and the solution (right).

distinct indexes i_1, \dots, i_κ , then no vehicles from these roads cross the junction, and thus we reduce to the $(n - \kappa) \rightarrow m$ case. Then, we define the matrix of distribution

$$A = \begin{pmatrix} \alpha_{n+11} & \dots & \alpha_{n+m1} \\ \vdots & \ddots & \vdots \\ \alpha_{n+1n} & \dots & \alpha_{n+mn} \end{pmatrix} \quad (2.34)$$

whose elements α_{ji} define the percentage of distribution of vehicles from road i to road j and are such that $\sum_{j=n+1}^{n+m} \alpha_{ji} = 1$, $i = 1, \dots, n$. We stress that if we have κ columns of A zero, then no vehicle enters the corresponding outgoing roads, reducing the problem to case $n \rightarrow (m - \kappa)$. Therefore we assume that for each j there exists at least a value $\alpha_{ji} \neq 0$ for $i = 1, \dots, n$.

The approach we propose is similar to the case of merge junction. The idea can be resumed as follows:

- We define the set $\Omega_{\text{inc}} \subset \mathbb{R}^n$ of possible solutions identified by the incoming roads, and m hyperplanes where the outgoing flux is maximised.
- We establish if the straight line of priority rule first intersects a maximising hyperplane or a side of Ω_{inc} . If it first intersects a maximising hyperplane then we have immediately found the solution which maximises the flux and respects the priority. Otherwise, we fix the component \hat{q}_i corresponding the side of Ω_{inc} crossed by the priority rule, and we move iteratively along that side, reducing the dimension of the problem at each step and looking for the maximisation of the flow.

Let us start assuming the conservation of ρ and y , i.e. for each $j = n + 1, \dots, n + m$

$$\sum_{i=1}^n \alpha_{ji} \hat{q}_i = \hat{q}_j \quad (2.35)$$

$$\sum_{i=1}^n \alpha_{ji} \hat{q}_i \hat{w}_i = \hat{q}_j \hat{w}_j. \quad (2.36)$$

By (2.35) in (2.36), for each outgoing road we have

$$\hat{w}_j = \frac{\sum_{i=1}^n \alpha_{ji} \hat{q}_i \hat{w}_i}{\sum_{i=1}^n \alpha_{ji} \hat{q}_i}, \quad (2.37)$$

where $\hat{w}_i = w_i^-$ are known, since w is the first Riemann invariant. We now move to the (q_1, \dots, q_n) -hyperplane and we look for the maximisation of the flow.

2.4. The APRSOM algorithm for n incoming and m outgoing roads at junctions

Step 1. For each incoming road we consider $d_i = d(\rho_i^-, w_i^-)$ in order to define the set

$$\Omega_{\text{inc}} = [0, d_1] \times \cdots \times [0, d_n]. \quad (2.38)$$

We assume that $d_i \neq 0$ for each $i = 1, \dots, n$. Indeed, the trivial case of $d_i = 0$ for all i means that no vehicles cross the intersection, while the case of $d_{i_1} = \cdots = d_{i_\kappa} = 0$ for κ distinct indexes i_1, \dots, i_κ reduces the junction to the $(n - \kappa) \rightarrow m$ case. We then introduce the straight line of priority rule in parametric form

$$r : \begin{cases} q_1 = hp_1 \\ \vdots \\ q_n = hp_n, \end{cases} \quad (2.39)$$

and the parameters

$$h_i = \max\{h : hp_i \leq d_i\} = \frac{d_i}{p_i}. \quad (2.40)$$

Note that $(h_1 p_1, \dots, h_n p_n)$ is the intersection point between the straight line r and the hyperplane d_i . Next, we set $(\hat{q}_1, \dots, \hat{q}_n) = (h_1 p_1, \dots, h_n p_n)$ in (2.37) and we obtain

$$\hat{w}_j = \frac{\sum_{i=1}^n \alpha_{ji} p_i w_i^-}{\sum_{i=1}^n \alpha_{ji} p_i}. \quad (2.41)$$

By (2.41) for $j = n + 1, \dots, n + m$ we define

$$\begin{aligned} s_j(\hat{w}_j) &= s(\rho^*(v_j^+, \hat{w}_j), \hat{w}_j), \\ \Omega_{\text{out}} &= [0, s_{n+1}] \times \cdots \times [0, s_{n+m}]. \end{aligned} \quad (2.42)$$

We recall that $\rho^*(v, w)$ is given in Definition 2.3.8. We then introduce

$$\psi_j(h) = h \sum_{i=1}^n \alpha_{ji} p_i \quad (2.43)$$

and we define

$$h_j = \min\{h > 0 : \psi_j(h) = s_j(\hat{w}_j), \text{ for } \hat{w}_j \text{ in (2.41)}\} = \frac{s_j(\hat{w}_j)}{\sum_{i=1}^n \alpha_{ji} p_i} \quad (2.44)$$

which identifies the intersection points $(h_j p_1, \dots, h_j p_n)$ between r and the hyperplanes

$$z_j : \sum_{i=1}^n \alpha_{ji} q_i = s_j(\hat{w}_j)$$

where the outgoing flux is maximised (see Remark 2.3.7). We define

$$\mathbf{h}_1 = \min_{i,j} \{h_i, h_j\}. \quad (2.45)$$

We have the following possibilities:

- (1) If there exists an index $j \geq n + 1$ such that $\mathbf{h}_1 = h_j$ then the straight line r first intersects a hyperplane z_j which maximises the outgoing flux of road j and satisfies the priority rule, thus we define the fluxes $(\hat{q}_1, \dots, \hat{q}_n) = (\mathbf{h}_1 p_1, \dots, \mathbf{h}_1 p_n)$ and the procedure stops.
- (2) There is no index $j \geq n + 1$ such that $\mathbf{h}_1 = h_j$. In this case we proceed as follows.
 - (a) If we need to respect the priority rule then we define the fluxes $(\hat{q}_1, \dots, \hat{q}_n) = (\mathbf{h}_1 p_1, \dots, \mathbf{h}_1 p_n)$, with $\mathbf{h}_1 = h_i$ for some $i \leq n$, and we stop.
 - (b) If we can adapt the priority rule, let $\ell_1 \leq n$ be the index of the incoming road such that $h_{\ell_1} = \mathbf{h}_1$. We set $\hat{q}_{\ell_1} = d_{\ell_1}$, we introduce $I = \{\ell_1\}$ and we proceed by iteration.

Step $S + 1$. Assume to have already defined S components of the vector $(\hat{q}_1, \dots, \hat{q}_n)$, i.e. for each $\ell_k \in I = \{\ell_1, \dots, \ell_S\}$ we have $\hat{q}_{\ell_k} = d_{\ell_k}$ and we have to determine the remaining $\hat{q}_i = hp_i$ for $i \leq n$ and $i \notin I$. We now introduce the function

$$\varphi_j(h) = h \sum_{i \notin I} \alpha_{ji} p_i w_i^- + \sum_{k \in I} \alpha_{j\ell_k} d_{\ell_k} w_{\ell_k}^-$$

and modify $\psi_j(h)$ in (2.43) as

$$\psi_j(h) = h \sum_{i \notin I} \alpha_{ji} p_i + \sum_{k \in I} \alpha_{j\ell_k} d_{\ell_k}.$$

We rewrite (2.37) as

$$\hat{w}_j(h) = \frac{\varphi_j(h)}{\psi_j(h)}, \quad (2.46)$$

and we exploit it to define $s_j(\hat{w}_j(h)) := s(\rho^*(v_j^+, \hat{w}_j(h)), \hat{w}_j(h))$, $j = n + 1, \dots, n + m$, and

$$h_j = \min\{h \in [h_S, +\infty) : \psi_j(h) = s_j(\hat{w}_j(h)), \text{ with } \hat{w}_j(h) \text{ in (2.46)}\}. \quad (2.47)$$

To conclude the iterative step we define

$$h_{S+1} = \min_{i \notin I, j} \{h_i, h_j\}. \quad (2.48)$$

with h_i in (2.40). Again we have two possibilities:

- (1) If there exists an index $j \geq n + 1$ such that $h_j = h_{S+1}$ then the straight line r first intersects a hyperplane z_j which maximises the outgoing flux of road j and thus we define the remaining fluxes $\hat{q}_i = h_{S+1} p_i$ for $i \notin I$.
- (2) Otherwise $h_{S+1} = h_{\ell_{S+1}}$ for some $\ell_{S+1} \leq n$, $\ell_{S+1} \notin I$. We add the new index in I , i.e. $I = \{\ell_1, \dots, \ell_{S+1}\}$, and we continue iteratively until we have defined all the elements of the vector $(\hat{q}_1, \dots, \hat{q}_n)$.

Remark 2.4.1. We observe that the set $\mathcal{H} = \{h \in [h_S, +\infty) : \psi_j(h) = s_j(\hat{w}_j(h)), \text{ with } \hat{w}_j(h) \text{ in (2.46)}\}$ is not empty for each step S of the algorithm. Indeed, we have

$$\begin{aligned} \lim_{h \rightarrow \infty} \psi_j(h) &= +\infty \\ \lim_{h \rightarrow \infty} s_j(\hat{w}_j(h)) &= s_j(\tilde{w}_j) < +\infty, \end{aligned}$$

where $\tilde{w}_j = \lim_{h \rightarrow \infty} \hat{w}_j(h) < +\infty$, and $\psi_j(h_S) \leq s_j(\hat{w}_j(h_S))$ by construction. Therefore, by continuity, for each j there exists a certain $h > h_S$ such that the equality $\psi_j(h) = s_j(\hat{w}_j(h))$ holds.

We now define our Riemann Solver for GSOM on road networks.

Definition 2.4.2. Let $\mathcal{Q} = (\hat{q}_1, \dots, \hat{q}_n)$ be the vector of incoming fluxes at the junction defined by the previous procedure applied to the initial state $(U_1^-, \dots, U_n^-, U_{n+1}^+, \dots, U_{n+m}^+)$, and $A \cdot \mathcal{Q}^T = (\hat{q}_{n+1}, \dots, \hat{q}_{n+m})$ the vector of outgoing fluxes, where A is the matrix of distribution. For every $i = 1, \dots, n$ set

- $\hat{w}_i = w_i^-$,
- $\hat{\rho}_i \in \mathcal{N}(U_i^-)$ such that $Q(\hat{\rho}_i, \hat{w}_i) = \hat{q}_i$, where $\mathcal{N}(U_i^-)$ is the set of possible right states for incoming roads (see Proposition 2.3.4),

2.4. The APRSOM algorithm for n incoming and m outgoing roads at junctions

and $\hat{U}_i = (\hat{\rho}_i, \hat{w}_i)$. For every $j = n + 1, \dots, n + m$ set

- \hat{w}_j as in (2.37) if $\hat{q}_i \neq 0$ for at least an index i , or equal to w_j^+ otherwise,
- $\hat{\rho}_j \in \mathcal{P}(U_j^+)$ such that $Q(\hat{\rho}_j, \hat{w}_j) = \hat{q}_j$, where $\mathcal{P}(U_j^+)$ is the set of possible left states for outgoing roads (see Proposition 2.3.6),

and $\hat{U}_j = (\hat{\rho}_j, \hat{w}_j)$. The Adapting Priority Riemann Solver for Second Order Models (APRSOM) on network is such that

$$\text{APRSOM}(U_1^-, \dots, U_n^-, U_{n+1}^+, \dots, U_{n+m}^+) = (\hat{U}_1, \dots, \hat{U}_n, \hat{U}_{n+1}, \dots, \hat{U}_{n+m}).$$

Chapter 3

Bounds on the total variation at the junction

This chapter deals with estimates of the total variation. Our aim is to provide bounds on the total variation of the flux Q and of the variable w for waves which interact with the junction. In Section 3.1 we collect the necessary definitions to provide the desired estimates. In Section 3.2 we prove that APRSOM satisfies four properties that guarantee the sought bounds on the total variation for junctions with two incoming and two outgoing roads. Starting from an equilibrium of the network, the proof is obtained by sending a wave, which first involves only ρ and then also w , on each one of the four roads and computing the variation of Q and w . The computations are divided into three cases, which depend on the initial condition of the equilibrium state of the network. These estimates are fundamental to prove the existence of weak solutions to Cauchy problems on networks through the Wave-Front-Tracking technique.

3.1 Preliminaries for the estimates

In this section we gather the necessary definitions to provide bounds on the total variation of the flux function $Q(\rho, w)$ and of the variable w for waves which interact with the junction. Let us consider a network with n incoming and m outgoing roads at junctions whose traffic dynamic is described by (2.2). We recall that $I_r = (a_r, b_r) \subset \mathbb{R}$, $r = 1, \dots, n + m$, are the roads of the network. For a collection of functions $(\rho_r, y_r) \in C([0, +\infty); L^1_{\text{loc}}(I_r)^2)$ such that, for every $r \in \{1, \dots, n + m\}$ and a.e. $t > 0$, the map $x \mapsto \rho_r(x, t)$ has a version with bounded total variation, we define the functionals

$$\begin{aligned}\Gamma(t) &= \sum_{i=1}^n Q(\rho_i(b_i-, t), w_i(b_i-, t)) \\ \text{TV}_Q(t) &= \sum_{r=1}^{n+m} \text{TV}(Q(\rho_r(\cdot, t), w_r(\cdot, t))) \\ \text{TV}_w(t) &= \sum_{r=1}^{n+m} \text{TV}(w_r(\cdot, t))\end{aligned}\tag{3.1}$$

where TV is the total variation and $w_r = y_r/\rho_r$. Note that $\Gamma(t)$ represents the flux crossing the junction at time t and involves only the incoming roads.

Definition 3.1.1. *We say that the state $(U_1^-, \dots, U_n^-, U_{n+1}^+, \dots, U_{n+m}^+)$ is an equilibrium for a Riemann*

Solver \mathcal{RS} if

$$\mathcal{RS}(U_1^-, \dots, U_n^-, U_{n+1}^+, \dots, U_{n+m}^+) = (U_1^-, \dots, U_n^-, U_{n+1}^+, \dots, U_{n+m}^+).$$

We now focus on the algorithm APRSOM introduced in Section 2.4. We recall that A is the matrix of distribution defined in (2.34) and that (p_1, \dots, p_n) is the vector defining the priority rule r . Let $\mathcal{Q} = (\hat{q}_1, \dots, \hat{q}_n)$ be the set of incoming fluxes obtained with APRSOM and $A \cdot \mathcal{Q}^T = (\hat{q}_{n+1}, \dots, \hat{q}_{n+m})$ the resulting set of outgoing fluxes. We introduce

$$\Theta = \{\mathcal{Q} \in \Omega_{\text{inc}} : A \cdot \mathcal{Q}^T \in \Omega_{\text{out}}, \text{ with } \Omega_{\text{inc}} \text{ in (2.38) and } \Omega_{\text{out}} \text{ in (2.42)}\} \quad (3.2)$$

so that we define

$$\bar{h} = \sup\{h \in \mathbb{R} : h(p_1, \dots, p_n) \in \Theta\}. \quad (3.3)$$

This parameter \bar{h} identifies the intersection point $\bar{h}(p_1, \dots, p_n)$ between the straight line r in (2.39) and the set Θ in (3.2).

We now introduce four properties of the Riemann Solver to estimate the total variation of Q and w for waves interacting with the junction. The first one says that equilibria depends only on bad data (see Definition 2.3.9) and can be used to provide bounds on the number of waves as done in [33, Proposition 10].

(P1) We say that a Riemann solver \mathcal{RS} has the property (P1) if, given $(U_1^-, \dots, U_n^-, U_{n+1}^+, \dots, U_{n+m}^+)$ and $(\hat{U}_1^-, \dots, \hat{U}_n^-, \hat{U}_{n+1}^+, \dots, \hat{U}_{n+m}^+)$ such that $w_i^- = \hat{w}_i^-$ for $i = 1, \dots, n$, $w_j^+ = \hat{w}_j^+$ for $j = n+1, \dots, n+m$ and $\rho_i^- = \hat{\rho}_i^-$ ($\rho_j^+ = \hat{\rho}_j^+$) whenever either U_i^- or \hat{U}_i^- (U_j^+ or \hat{U}_j^+) is a bad datum, then

$$\mathcal{RS}(U_1^-, \dots, U_n^-, U_{n+1}^+, \dots, U_{n+m}^+) = \mathcal{RS}(\hat{U}_1^-, \dots, \hat{U}_n^-, \hat{U}_{n+1}^+, \dots, \hat{U}_{n+m}^+).$$

The second property refers to interacting waves which involve only the density ρ . This means that, starting from an equilibrium of \mathcal{RS} , we perturb the density of one of the roads keeping its w value unchanged. The following property tells us that the increase in the variation of the flux and of w at the junction is bounded by the strength of the interacting wave as well as by the sum of the variations in the incoming fluxes and in \bar{h} defined in (3.3). Note that, even when the wave does not directly perturb the property w , the latter varies by interacting with the junction.

(P2) We say that a Riemann solver \mathcal{RS} has the property (P2) if there exists a constant $C \geq 1$ such that for every equilibrium $(U_1^-, \dots, U_n^-, U_{n+1}^+, \dots, U_{n+m}^+)$ of \mathcal{RS} and for every wave $\tilde{\rho}_i$ perturbing ρ_i^- for $i = 1, \dots, n$ ($\tilde{\rho}_j$ perturbing ρ_j^+ for $j = n+1, \dots, n+m$, respectively) interacting with J at time $\bar{t} > 0$ and producing waves in the arcs according to \mathcal{RS} , for $r = i$ ($r = j$) we have

$$\begin{aligned} \text{TV}_Q(\bar{t}+) - \text{TV}_Q(\bar{t}-) &\leq C \min\{|\tilde{q}_r - q_r|, |\Gamma(\bar{t}+) - \Gamma(\bar{t}-)| + |\bar{h}(\bar{t}+) - \bar{h}(\bar{t}-)|\} \\ \bar{h}(\bar{t}+) - \bar{h}(\bar{t}-) &\leq C|\tilde{q}_r - q_r| \\ \text{TV}_w(\bar{t}+) - \text{TV}_w(\bar{t}-) &\leq C \min\{|\tilde{q}_r - q_r|, |\Gamma(\bar{t}+) - \Gamma(\bar{t}-)| + |\bar{h}(\bar{t}+) - \bar{h}(\bar{t}-)|\}, \end{aligned}$$

with $\tilde{q}_r = Q(\tilde{\rho}_i, w_i^-)$ and $q_r = Q(\rho_i^-, w_i^-)$ ($\tilde{q}_r = Q(\tilde{\rho}_j, w_j^+)$ and $q_r = Q(\rho_j^+, w_j^+)$, respectively).

The third property also refers to interacting waves which involve only the density ρ . It tells us that, when the interacting wave with the junction determines a decrease in the flux, then also \bar{h} decreases and the variation of Γ is bounded by the variation of \bar{h} .

(P3) We say that a Riemann solver \mathcal{RS} has the property (P3) if there exists a constant $C \geq 1$ such that for every equilibrium $(U_1^-, \dots, U_n^-, U_{n+1}^+, \dots, U_{n+m}^+)$ of \mathcal{RS} and for every wave $\tilde{\rho}_i$ perturbing

ρ_i^- with $\tilde{q}_i = Q(\tilde{\rho}_i, w_i^-) < q_i^-$ for $i = 1, \dots, n$ ($\tilde{\rho}_j$ perturbing ρ_j^+ with $\tilde{q}_j = Q(\tilde{\rho}_j, w_j^+) < q_j^+$ for $j = n+1, \dots, n+m$, respectively) interacting with J at time $\bar{t} > 0$ and producing waves in the arcs according to \mathcal{RS} , we have

$$\begin{aligned}\Gamma(\bar{t}+) - \Gamma(\bar{t}-) &\leq C|\bar{h}(\bar{t}+) - \bar{h}(\bar{t}-)| \\ \bar{h}(\bar{t}+) &\leq \bar{h}(\bar{t}-).\end{aligned}$$

Finally, we consider an interacting wave with the junction which perturbs both ρ and w on one of the incoming roads. The fourth property says that the increase in the variation of w is bounded by the variation of the interacting wave in w and the strength of the interacting wave as well as by the sum of the variations in the incoming fluxes and in \bar{h} .

(P4) We say that a Riemann solver \mathcal{RS} has the property (P4) if there exist two constants $C_1 \geq 1$ and $C_2 \geq 1$ such that for every equilibrium $(U_1^-, \dots, U_n^-, U_{n+1}^+, \dots, U_{n+m}^+)$ of \mathcal{RS} and for every wave $(\tilde{\rho}_i, \tilde{w}_i)$ perturbing (ρ_i^-, w_i^-) , $i = 1, \dots, n$, interacting with J at time $\bar{t} > 0$ and producing waves in the arcs according to \mathcal{RS} , the estimates on TV_Q , \bar{h} and Γ hold and we have

$$\text{TV}_w(\bar{t}+) - \text{TV}_w(\bar{t}-) \leq C_1|\tilde{w}_i - w_i^-| + C_2 \min\{|\tilde{q}_i - q_i|, |\Gamma(\bar{t}+) - \Gamma(\bar{t}-)| + |\bar{h}(\bar{t}+) - \bar{h}(\bar{t}-)|\},$$

with $\tilde{q}_i = Q(\tilde{\rho}_i, \tilde{w}_i)$ and $q_i = Q(\rho_i^-, w_i^-)$.

Remark 3.1.2. Property (P4) only refers to the incoming roads. Indeed, given a left state $U^- = (\rho^-, w^-)$ and a right state $U^+ = (\rho^+, w^+)$, the solution to Riemann problems for GSOM on a single road is defined by an intermediate state $U^* = (\rho^*, w^*)$ such that $w^* = w^-$, since the 1-Riemann invariant is $z_1(\rho, w) = w$. This implies that for any outgoing road $j > n$, if we perturb the equilibrium (ρ_j^+, w_j^+) with a wave $(\tilde{\rho}_j, \tilde{w}_j)$, the solution which arrives at the junction is such that $w^* = w_j^+$, thus the variation in w does not affect the junction.

The above introduced properties are fundamental to study the following Cauchy problem for GSOM in conservative form on networks

$$\begin{cases} \partial_t \rho_r + \partial_x(\rho_r v_r) = 0 \\ \partial_t y_r + \partial_x(y_r v_r) = 0 \\ (\rho_r(x, 0), y_r(x, 0)) = (\rho_{r,0}(x), y_{r,0}(x)) \end{cases} \quad \text{for } r = 1, \dots, n+m \quad (3.4)$$

with initial data $(\rho_{r,0}(x), y_{r,0}(x))$ of bounded variation. Indeed, properties (P1) – (P4) guarantee bounds on the total variation of Q and w for waves interacting with the junctions. These estimates are necessary to prove that the approximate solutions via Wave-Front-Tracking (see Section 1.1) converge to weak solutions to (3.4) in the sense of Definition 2.3.1. The idea is to estimate the number of waves, the number of waves interactions and the total variation of solutions. The strategy consists in recovering bounds on the total variation of the flux and of w in space from bounds on the variation in time of Γ and \bar{h} . We are working on the estimates on waves returning to the junctions and on the effects along the roads of waves generated at the intersections. The technical details are still under investigation and will be contained in a forthcoming work.

3.2 Estimates for the case of two incoming and two outgoing roads at junctions

In this section we show that our solver APRSOM satisfies properties (P1) – (P4) in the case of two incoming and two outgoing roads at the junction. Let us begin fixing the notation. The priority rule r is

3.2. Estimates for the case of two incoming and two outgoing roads at junctions

defined by the vector (p_1, p_2) with $p_1 + p_2 = 1$, while the matrix of distribution is

$$A = \begin{pmatrix} \alpha_{31} & \alpha_{41} \\ \alpha_{32} & \alpha_{42} \end{pmatrix}$$

with $\alpha_{31} + \alpha_{41} = 1$ and $\alpha_{32} + \alpha_{42} = 1$. The conservation of ρ in (2.35) implies

$$\begin{aligned} \alpha_{31}\hat{q}_1 + \alpha_{32}\hat{q}_2 &= \hat{q}_3 \\ \alpha_{41}\hat{q}_1 + \alpha_{42}\hat{q}_2 &= \hat{q}_4. \end{aligned} \tag{3.5}$$

We denote by $d_1 = d(\rho_1^-, w_1^-)$, $d_2 = d(\rho_2^-, w_2^-)$, $s_3 = s(\rho_3^*(v_3^+, \hat{w}_3), \hat{w}_3)$ and $s_4 = s(\rho_4^*(v_4^+, \hat{w}_4), \hat{w}_4)$, where \hat{w}_3 and \hat{w}_4 are determined by (2.37), and $\rho_j^*(v_j^+, \hat{w}_j)$, $j = 3, 4$, is given in Definition 2.3.8. The quantities d_1, d_2, s_3 and s_4 define the sets Ω_{inc} and Ω_{out} , see (2.38) and (2.42). Finally, we denote by

$$r : \begin{cases} q_1 = hp_1 \\ q_2 = hp_2. \end{cases} \tag{3.6}$$

the priority rule straight line and by

$$\begin{aligned} z_3 : \alpha_{31}q_1 + \alpha_{32}q_2 &= s_3 \\ z_4 : \alpha_{41}q_1 + \alpha_{42}q_2 &= s_4, \end{aligned} \tag{3.7}$$

the straight lines that maximise the outgoing flux.

Proposition 3.2.1. *APRSOM satisfies property (P1).*

Proof. Let us consider two states $(U_1^-, U_2^-, U_3^+, U_4^+)$ and $(\hat{U}_1^-, \hat{U}_2^-, \hat{U}_3^+, \hat{U}_4^+)$ such that $w_i^- = \hat{w}_i^-$ for $i = 1, 2$, $w_j^+ = \hat{w}_j^+$ for $j = 3, 4$ and $\rho_i^- = \hat{\rho}_i^-$ ($\rho_j^+ = \hat{\rho}_j^+$) whenever either U_i^- or \hat{U}_i^- (U_j^+ or \hat{U}_j^+) is a bad datum. This implies that for every bad datum we have

$$\begin{aligned} d_i &= \hat{d}_i = Q(\rho_i^-, w_i^-) \\ s_j &= \hat{s}_j = Q(\rho_j^+, w_j^+). \end{aligned}$$

On the other hand, for any good datum, since $w_i^- = \hat{w}_i^-$ for $i = 1, 2$ and $w_j^+ = \hat{w}_j^+$ for $j = 3, 4$, we have

$$\begin{aligned} d_i &= \hat{d}_i = Q^{\max}(w_i^-) \\ s_j &= \hat{s}_j = Q^{\max}(w_j^+). \end{aligned}$$

Therefore, $\Omega_{\text{inc}} = [0, d_1] \times [0, d_2] = [0, \hat{d}_1] \times [0, \hat{d}_2]$ and $\Omega_{\text{out}} = [0, s_3] \times [0, s_4] = [0, \hat{s}_3] \times [0, \hat{s}_4]$. Since the Riemann Solver APRSOM only depends on the priority rule, the matrix A and the sets Ω_{inc} and Ω_{out} , then it holds

$$\text{APRSOM}(U_1^-, \dots, U_n^-, U_{n+1}^+, \dots, U_{n+m}^+) = \text{APRSOM}(\hat{U}_1^-, \dots, \hat{U}_n^-, \hat{U}_{n+1}^+, \dots, \hat{U}_{n+m}^+).$$

□

We now consider properties (P2), (P3) and (P4). For convenience, we work in the (q_1, q_2) -plane. Starting from an equilibrium for APRSOM, we estimate the variation of the flux and of w sending a wave on each one of the roads. Our aim is to show that we can control the variation of Q and w . Let us begin with (P2) and (P3); starting from a certain equilibrium $(U_1^+, U_2^+, U_3^-, U_4^-)$, we send a wave $\tilde{\rho}_i$ (or $\tilde{\rho}_j$), with corresponding flux \tilde{q}_i (or \tilde{q}_j), and we compute the solution of APRSOM, $(\hat{U}_1, \hat{U}_2, \hat{U}_3, \hat{U}_4)$, with corresponding fluxes $(\hat{q}_1, \hat{q}_2, \hat{q}_3, \hat{q}_4)$. We are interested in computing (see (3.1))

$$\Delta\Gamma(\bar{t}) = (\hat{q}_1 - q_1^-) + (\hat{q}_2 - q_2^-)$$

$$\Delta \text{TV}_w = |\hat{w}_3 - w_3^+| + |\hat{w}_4 - w_4^+|. \quad (3.8)$$

The variation of the flux is

$$\Delta \text{TV}_Q(\bar{t}) = |\hat{q}_i - \tilde{q}_i| + |\hat{q}_\ell - q_\ell^-| + |\hat{q}_3 - q_3^+| + |\hat{q}_4 - q_4^+| - |\tilde{q}_i - q_i^-|$$

if the interacting wave is in the incoming road I_i , with $\ell = 3 - i$, and

$$\Delta \text{TV}_Q(\bar{t}) = |\hat{q}_1 - q_1^-| + |\hat{q}_2 - q_2^-| + |\hat{q}_j - \tilde{q}_j| + |\hat{q}_k - q_k^+| - |\tilde{q}_j - q_j^+|$$

if the interacting wave is in the outgoing road I_j , with $k = 7 - j$. Note that in (3.8) we only have variations of w in the outgoing roads since w is a Riemann invariant and thus $\hat{w}_i = w_i^-$, $i = 1, 2$. For property (P4), in the case of a wave $(\tilde{\rho}_i, \tilde{w}_i)$ along an incoming road I_i , $i \in \{1, 2\}$, the variation in w becomes

$$\Delta \text{TV}_w = |\hat{w}_3 - w_3^+| + |\hat{w}_4 - w_4^+| - |\tilde{w}_i - w_i^-|.$$

The computations related to TV_w showed two possible configurations to obtain the desired estimates. First of all, we observe that by (2.37) we have

$$\begin{aligned} \hat{w}_3 &= w_2^- + \frac{\hat{q}_1}{\hat{q}_3} \alpha_{31} (w_1^- - w_2^-) = w_1^- + \frac{\hat{q}_2}{\hat{q}_3} \alpha_{32} (w_2^- - w_1^-) \\ w_3^+ &= w_2^- + \frac{q_1^-}{q_3^+} \alpha_{31} (w_1^- - w_2^-) = w_1^- + \frac{q_2^-}{q_3^+} \alpha_{31} (w_2^- - w_1^-), \end{aligned}$$

where we choose one of the two formulations for \hat{w}_3 and w_3^+ , depending on which one is the more convenient from data. Analogously for \hat{w}_4 and w_4^+ . More generally we have

$$\begin{aligned} \hat{w}_3 &= w_\ell^- + \frac{\hat{q}_i}{\hat{q}_3} \alpha_{3i} (w_i^- - w_\ell^-), & w_3^+ &= w_\ell^- + \frac{q_i^-}{q_3^+} \alpha_{3i} (w_i^- - w_\ell^-) \\ \hat{w}_4 &= w_\ell^- + \frac{\hat{q}_i}{\hat{q}_4} \alpha_{4i} (w_i^- - w_\ell^-), & w_4^+ &= w_\ell^- + \frac{q_i^-}{q_4^+} \alpha_{4i} (w_i^- - w_\ell^-) \end{aligned} \quad (3.9)$$

with $i \in \{1, 2\}$ and $\ell = 3 - i$. In particular, when we send a wave $(\tilde{\rho}_i, \tilde{w}_i)$ on road i , we have

$$\hat{w}_3 = w_\ell^- + \frac{\hat{q}_i}{\hat{q}_3} \alpha_{3i} (\tilde{w}_i - w_\ell^-), \quad \hat{w}_4 = w_\ell^- + \frac{\hat{q}_i}{\hat{q}_4} \alpha_{4i} (\tilde{w}_i - w_\ell^-). \quad (3.10)$$

Configuration 1. The following configuration is obtained when $\hat{q}_1 = q_1^-$ or $\hat{q}_2 = q_2^-$. Let $\hat{q}_i = q_i^-$, $i = 1, 2$, and set $\ell = 3 - i$, then $|\hat{q}_3 - q_3^+| = \alpha_{3\ell} |\hat{q}_\ell - q_\ell^-|$. Sending a wave $\tilde{\rho}_r$, $r = 1, \dots, 4$, by (3.9) we have

$$|\hat{w}_3 - w_3^+| = \frac{\alpha_{3i} q_i^- |w_1^- - w_2^-| |q_3^+ - \hat{q}_3|}{\hat{q}_3 q_3^+} = \frac{\alpha_{31} \alpha_{32} q_i^- |w_1^- - w_2^-|}{\hat{q}_3 q_3^+} |\hat{q}_\ell - q_\ell^-| \quad (3.11)$$

$$|\hat{w}_4 - w_4^+| = \frac{\alpha_{4\ell} q_i^- |w_1^- - w_2^-| |q_4^+ - \hat{q}_4|}{\hat{q}_4 q_4^+} = \frac{\alpha_{41} \alpha_{42} q_i^- |w_1^- - w_2^-|}{\hat{q}_4 q_4^+} |\hat{q}_\ell - q_\ell^-|. \quad (3.12)$$

Sending a wave $(\tilde{\rho}_i, \tilde{w}_i)$, $i \in \{1, 2\}$ and $\ell = 3 - i$, by (3.9) and (3.10) we have

$$\begin{aligned} |\hat{w}_3 - w_3^+| &= \frac{\alpha_{3i} |\hat{q}_i q_3^+ (\tilde{w}_i - w_\ell^-) - q_i^- \hat{q}_3 (w_i^- - w_\ell^-)|}{\hat{q}_3 q_3^+} \\ &= \frac{\alpha_{3i} |\hat{q}_i q_3^+ (\tilde{w}_i - w_i^- + w_i^- - w_\ell^-) - q_i^- \hat{q}_3 (w_i^- - w_\ell^-)|}{\hat{q}_3 q_3^+} \end{aligned}$$

3.2. Estimates for the case of two incoming and two outgoing roads at junctions

$$\begin{aligned}
&\leq \frac{\alpha_{3i}\hat{q}_i|\tilde{w}_i - w_i^-|}{\hat{q}_3} + \frac{\alpha_{3i}|w_1^- - w_2^-||\hat{q}_i q_3^+ - q_i^- \hat{q}_3|}{\hat{q}_3 q_3^+} \\
&= \frac{\alpha_{3i}\hat{q}_i|\tilde{w}_i - w_i^-|}{\hat{q}_3} + \frac{\alpha_{31}\alpha_{32}q_\ell^-|w_1^- - w_2^-|}{\hat{q}_3 q_3^+} |\hat{q}_i - q_i^-|
\end{aligned} \tag{3.13}$$

$$|\hat{w}_4 - w_4^+| \leq \frac{\alpha_{4i}\hat{q}_i|\tilde{w}_i - w_i^-|}{\hat{q}_4} + \frac{\alpha_{41}\alpha_{42}q_\ell^-|w_1^- - w_2^-|}{\hat{q}_4 q_4^+} |\hat{q}_i - q_i^-|. \tag{3.14}$$

Configuration 2. The following configuration is obtained when $\hat{q}_1 \neq q_1^-$ and $\hat{q}_2 \neq q_2^-$. Sending a wave $\tilde{\rho}_r$, $r = 1, \dots, 4$, by (3.9) we have

$$\begin{aligned}
|\hat{w}_3 - w_3^+| &= \frac{\alpha_{3i}|w_1^- - w_2^-||\hat{q}_i q_3^+ - q_i^- \hat{q}_3|}{\hat{q}_3 q_3^+} \\
&= \frac{\alpha_{3i}|w_1^- - w_2^-||\hat{q}_i(\alpha_{3i}q_i^- + \alpha_{3\ell}q_\ell^-) - q_i^-(\alpha_{3i}\hat{q}_i + \alpha_{3\ell}\hat{q}_\ell)|}{\hat{q}_3 q_3^+} \\
&= \frac{\alpha_{31}\alpha_{32}|w_1^- - w_2^-|}{\hat{q}_3 q_3^+} |\hat{q}_1 q_2^- - q_1^- \hat{q}_2| \\
&= \frac{\alpha_{31}\alpha_{32}|w_1^- - w_2^-|}{\hat{q}_3 q_3^+} |\hat{q}_1 q_2^- - \hat{q}_1 \hat{q}_2 + \hat{q}_1 \hat{q}_2 - q_1^- \hat{q}_2| \\
&= \frac{\alpha_{31}\alpha_{32}|w_1^- - w_2^-|}{\hat{q}_3 q_3^+} |\hat{q}_2(\hat{q}_1 - q_1^-) - \hat{q}_1(\hat{q}_2 - q_2^-)|
\end{aligned} \tag{3.15}$$

$$|\hat{w}_4 - w_4^+| = \frac{\alpha_{41}\alpha_{42}|w_1^- - w_2^-|}{\hat{q}_4 q_4^+} |\hat{q}_2(\hat{q}_1 - q_1^-) - \hat{q}_1(\hat{q}_2 - q_2^-)|. \tag{3.16}$$

Note that, in the case of $\Delta\bar{h}(\bar{t}) \propto (\hat{q}_1 - q_1^-)$, since $\Delta\Gamma(\bar{t}) = (\hat{q}_1 - q_1^-) + (\hat{q}_2 - q_2^-)$, we rewrite (3.15) and (3.16) as

$$\begin{aligned}
|\hat{w}_3 - w_3^+| &= \frac{\alpha_{31}\alpha_{32}|w_1^- - w_2^-|}{\hat{q}_3 q_3^+} |(\hat{q}_1 + \hat{q}_2)(\hat{q}_1 - q_1^-) - \hat{q}_1 \Delta\Gamma(\bar{t})| \\
&\leq \frac{\alpha_{31}\alpha_{32}|w_1^- - w_2^-|}{\hat{q}_3 q_3^+} |\hat{q}_1 + \hat{q}_2| (|\Delta\Gamma| + |\Delta\bar{h}(\bar{t})|)
\end{aligned} \tag{3.17}$$

$$|\hat{w}_4 - w_4^+| \leq \frac{\alpha_{41}\alpha_{42}|w_1^- - w_2^-|}{\hat{q}_4 q_4^+} |\hat{q}_1 + \hat{q}_2| (|\Delta\Gamma| + |\Delta\bar{h}(\bar{t})|). \tag{3.18}$$

In the case of $\Delta\bar{h}(\bar{t}) \propto (\hat{q}_2 - q_2^-)$ we follow similar computations and obtain the same result.

Finally, sending a wave $(\tilde{\rho}_i, \tilde{w}_i)$, $i \in \{1, 2\}$ and $\ell = 3 - i$, we have

$$\begin{aligned}
|\hat{w}_3 - w_3^+| &= \frac{\alpha_{3i}|\hat{q}_i q_3^+(\tilde{w}_i - w_\ell^-) - q_i^- \hat{q}_3(w_i^- - w_\ell^-)|}{\hat{q}_3 q_3^+} \\
&= \frac{\alpha_{3i}|\hat{q}_i q_3^+(\tilde{w}_i - w_i^- + w_i^- - w_\ell^-) - q_i^- \hat{q}_3(w_i^- - w_\ell^-)|}{\hat{q}_3 q_3^+} \\
&\leq \frac{\alpha_{3i}\hat{q}_i|\tilde{w}_i - w_i^-|}{\hat{q}_3} + \frac{\alpha_{3i}|w_1^- - w_2^-||\hat{q}_i q_3^+ - q_i^- \hat{q}_3|}{\hat{q}_3 q_3^+} \\
&= \frac{\alpha_{3i}\hat{q}_i|\tilde{w}_i - w_i^-|}{\hat{q}_3} + \frac{\alpha_{31}\alpha_{32}|w_1^- - w_2^-|}{\hat{q}_3 q_3^+} |\hat{q}_2(\hat{q}_1 - q_1^-) - \hat{q}_1(\hat{q}_2 - q_2^-)|
\end{aligned} \tag{3.19}$$

$$|\hat{w}_4 - w_4^+| \leq \frac{\alpha_{4i}\hat{q}_i|\tilde{w}_i - w_i^-|}{\hat{q}_4} + \frac{\alpha_{41}\alpha_{42}|w_1^- - w_2^-|}{\hat{q}_4 q_4^+} |\hat{q}_2(\hat{q}_1 - q_1^-) - \hat{q}_1(\hat{q}_2 - q_2^-)|. \tag{3.20}$$

Note that, in the case of $\Delta\bar{h}(\bar{t}) \propto (\hat{q}_1 - q_1^-)$ or $\Delta\bar{h}(\bar{t}) \propto (\hat{q}_2 - q_2^-)$ we rewrite (3.19) and (3.20) as

$$|\hat{w}_3 - w_3^+| = \frac{\alpha_{3i}\hat{q}_i|\tilde{w}_i - w_i^-|}{\hat{q}_3} + \frac{\alpha_{31}\alpha_{32}|w_1^- - w_2^-|}{\hat{q}_3 q_3^+} |\hat{q}_1 + \hat{q}_2| (|\Delta\Gamma| + |\Delta\bar{h}(\bar{t})|) \quad (3.21)$$

$$|\hat{w}_4 - w_4^+| \leq \frac{\alpha_{4i}\hat{q}_i|\tilde{w}_i - w_i^-|}{\hat{q}_4} + \frac{\alpha_{41}\alpha_{42}|w_1^- - w_2^-|}{\hat{q}_4 q_4^+} |\hat{q}_1 + \hat{q}_2| (|\Delta\Gamma| + |\Delta\bar{h}(\bar{t})|). \quad (3.22)$$

To show that APRSOM satisfies (P2) – (P4), we divide the proof in three cases, depending on the initial position of the equilibrium. Since we work in the (q_1, q_2) -plane, we identify the equilibrium $(U_1^-, U_2^-, U_3^+, U_4^+)$ with the corresponding fluxes $(q_1^-, q_2^-, q_3^+, q_4^+)$. Therefore, with a slight abuse of notation we will write the equilibrium condition as APRSOM($q_1^-, q_2^-, q_3^+, q_4^+$) = $(q_1^-, q_2^-, q_3^+, q_4^+)$. Note that this implies that q_3^+ and q_4^+ satisfy (3.5).

Case A: We start from the equilibrium $(q_1^-, q_2^-, q_3^+, q_4^+) = (d_1, d_2, \alpha_{31}d_1 + \alpha_{32}d_2, \alpha_{41}d_1 + \alpha_{42}d_2)$.

Case B: We start from the equilibrium along one of the straight lines $q_1 = d_1$ or $q_2 = d_2$.

Case C: We start from the equilibrium defined by the intersection between the priority rule r in (3.6) and one of the straight lines z_3 or z_4 in (3.7).

3.2.1 Case A

This case is verified when the equilibrium is $(q_1^-, q_2^-, q_3^+, q_4^+) = (d_1, d_2, \alpha_{31}d_1 + \alpha_{32}d_2, \alpha_{41}d_1 + \alpha_{42}d_2)$. Without loss of generality, we assume that the priority rule r first intersects the straight line $q_2 = d_2$. We study the effects produced by a single wave sent on each road.

Case A1: Wave on road 1

Let us start with a wave on road 1.

- i) We assume $\tilde{q}_1 > q_1^-$. First of all we analyse the effects of a wave related only to the density ρ , i.e. we send a certain $\tilde{\rho}_1$ on road 1 keeping w_1^- fixed. In Figure 3.1(a) we show a possible solution given by the algorithm. Specifically we have

$$q_1^- \leq \hat{q}_1 \leq \tilde{q}_1, \quad q_2^- = \hat{q}_2, \quad \hat{q}_3 = \alpha_{31}\hat{q}_1 + \alpha_{32}q_2^- \geq q_3^+, \quad \hat{q}_4 = \alpha_{41}\hat{q}_1 + \alpha_{42}q_2^- \geq q_4^+.$$

We refer to the Appendix of [26] for the estimates of $\Delta\Gamma$, $\Delta\bar{h}$ and ΔTV_Q of (P2). By (3.11) and (3.12) we have

$$|\hat{w}_3 - w_3^+| \leq \frac{\alpha_{31}\alpha_{32}q_2^-|w_2^- - w_1^-|}{(q_3^+)^2} |\tilde{q}_1 - q_1^-|, \quad |\hat{w}_4 - w_4^+| \leq \frac{\alpha_{41}\alpha_{42}q_2^-|w_2^- - w_1^-|}{(q_4^+)^2} |\tilde{q}_1 - q_1^-|$$

$$\Rightarrow \Delta\text{TV}_w(\bar{t}) \leq \left(\frac{\alpha_{31}\alpha_{32}}{(q_3^+)^2} + \frac{\alpha_{41}\alpha_{42}}{(q_4^+)^2} \right) q_2^- |w_2^- - w_1^-| |\tilde{q}_1 - q_1^-|.$$

Next, we analyse the effects of a wave in ρ and w , i.e. we send a couple $(\tilde{\rho}_1, \tilde{w}_1)$ on road 1 such that we still have $\tilde{q}_1 > q_1^-$. The estimates on Γ , \bar{h} and TV_Q do not change, while for TV_w by (3.13) and (3.14) we have

$$|\hat{w}_3 - w_3^+| \leq \frac{\alpha_{31}\tilde{q}_1}{q_3^+} |\tilde{w}_1 - w_1^-| + \frac{\alpha_{31}\alpha_{32}q_2^-|w_2^- - w_1^-|}{(q_3^+)^2} |\tilde{q}_1 - q_1^-|$$

$$|\hat{w}_4 - w_4^+| \leq \frac{\alpha_{41}\tilde{q}_1}{q_4^+} |\tilde{w}_1 - w_1^-| + \frac{\alpha_{41}\alpha_{42}q_2^-|w_2^- - w_1^-|}{(q_4^+)^2} |\tilde{q}_1 - q_1^-|$$

$$\begin{aligned}
 \text{TV}_w(\bar{t}+) &\leq \left(\frac{\alpha_{31}}{q_3^+} + \frac{\alpha_{41}}{q_4^+} \right) \tilde{q}_1 |\tilde{w}_1 - w_1^-| + \left(\frac{\alpha_{31}\alpha_{32}}{(q_3^+)^2} + \frac{\alpha_{41}\alpha_{42}}{(q_4^+)^2} \right) q_2^- |w_2^- - w_1^-| |\tilde{q}_1 - q_1^-| \\
 \text{TV}_w(\bar{t}-) &= |\tilde{w}_1 - w_1^-| \\
 \Rightarrow \Delta \text{TV}_w(\bar{t}) &\leq \left[\left(\frac{\alpha_{31}}{q_3^+} + \frac{\alpha_{41}}{q_4^+} \right) \tilde{q}_1 - 1 \right] |\tilde{w}_1 - w_1^-| \\
 &\quad + \left(\frac{\alpha_{31}\alpha_{32}}{(q_3^+)^2} + \frac{\alpha_{41}\alpha_{42}}{(q_4^+)^2} \right) q_2^- |w_2^- - w_1^-| |\tilde{q}_1 - q_1^-|.
 \end{aligned}$$

Therefore (P2) and (P4) hold.

- ii) We assume $\tilde{q}_1 < q_1^-$. First of all we analyse the effects of a wave related only to the density ρ , i.e. we send a certain $\tilde{\rho}_1$ on road 1 keeping w_1^- fixed. In Figure 3.1(b) we show a possible solution given by the algorithm. Specifically we have

$$q_1^- > \hat{q}_1 = \tilde{q}_1, \quad q_2^- = \hat{q}_2, \quad \hat{q}_3 = \alpha_{31}\tilde{q}_1 + \alpha_{32}q_2^- \leq q_3^+, \quad \hat{q}_4 = \alpha_{41}\tilde{q}_1 + \alpha_{42}q_2^- \leq q_4^+.$$

We refer to the Appendix of [26] for the estimates of $\Delta\Gamma$, $\Delta\bar{h}$ and ΔTV_Q of (P2) and (P3). Note that $\hat{q}_3 \geq \alpha_{32}q_2^-$ and $\hat{q}_4 \geq \alpha_{42}q_2^-$. By (3.11) and (3.12) we have

$$\begin{aligned}
 |\hat{w}_3 - w_3^+| &\leq \frac{\alpha_{31}|w_2^- - w_1^-|}{q_3^+} |\tilde{q}_1 - q_1^-|, \quad |\hat{w}_4 - w_4^+| \leq \frac{\alpha_{41}|w_2^- - w_1^-|}{q_4^+} |\tilde{q}_1 - q_1^-| \\
 \Rightarrow \Delta \text{TV}_w(\bar{t}) &\leq \left(\frac{\alpha_{31}}{q_3^+} + \frac{\alpha_{41}}{q_4^+} \right) |w_2^- - w_1^-| |\tilde{q}_1 - q_1^-|.
 \end{aligned}$$

Next, we analyse the effects of a wave in ρ and w , i.e. we send a couple $(\tilde{\rho}_1, \tilde{w}_1)$ on road 1 such that we still have $\tilde{q}_1 < q_1^-$. The estimates on Γ , \bar{h} and TV_Q do not change, while for TV_w by (3.13) and (3.14) we have

$$\begin{aligned}
 |\hat{w}_3 - w_3^+| &\leq \frac{\alpha_{31}\tilde{q}_1}{q_3^+} |\tilde{w}_1 - w_1^-| + \frac{\alpha_{31}|w_2^- - w_1^-|}{q_3^+} |\tilde{q}_1 - q_1^-| \\
 |\hat{w}_4 - w_4^+| &\leq \frac{\alpha_{41}\tilde{q}_1}{q_4^+} |\tilde{w}_1 - w_1^-| + \frac{\alpha_{41}|w_2^- - w_1^-|}{q_4^+} |\tilde{q}_1 - q_1^-| \\
 \text{TV}_w(\bar{t}+) &\leq \left(\frac{\alpha_{31}}{q_3^+} + \frac{\alpha_{41}}{q_4^+} \right) \tilde{q}_1 |\tilde{w}_1 - w_1^-| + \left(\frac{\alpha_{31}}{q_3^+} + \frac{\alpha_{41}}{q_4^+} \right) |w_2^- - w_1^-| |\tilde{q}_1 - q_1^-| \\
 \text{TV}_w(\bar{t}-) &= |\tilde{w}_1 - w_1^-| \\
 \Rightarrow \Delta \text{TV}_w(\bar{t}) &\leq \left[\left(\frac{\alpha_{31}}{\alpha_{32}} + \frac{\alpha_{41}}{\alpha_{42}} \right) \frac{\tilde{q}_1}{q_2^-} - 1 \right] |\tilde{w}_1 - w_1^-| + \left(\frac{\alpha_{31}}{q_3^+} + \frac{\alpha_{41}}{q_4^+} \right) |w_2^- - w_1^-| |\tilde{q}_1 - q_1^-|.
 \end{aligned}$$

Therefore (P2), (P3) and (P4) hold.

Case A2: Wave on road 2

We now consider a wave on road 2.

- i) We assume $\tilde{q}_2 > q_2^-$. First of all we analyse the effects of a wave related only to the density ρ , i.e. we send a certain $\tilde{\rho}_2$ on road 2 keeping w_2^- fixed. We have two possibilities: \tilde{d}_2 is big enough to find an intersection between a straight line which maximises the outgoing flux z_3 or z_4 and the priority rule r (see Figure 3.2(a)), or the solution is along $q_2 = \tilde{d}_2$ (see Figure 3.2(b)).

In the first case we have

$$q_1^- > \hat{q}_1, \quad q_2^- \leq \hat{q}_2 \leq \tilde{q}_2, \quad \hat{q}_3 = \alpha_{31}\hat{q}_1 + \alpha_{32}\hat{q}_2, \quad \hat{q}_4 = \alpha_{41}\hat{q}_1 + \alpha_{42}\hat{q}_2.$$

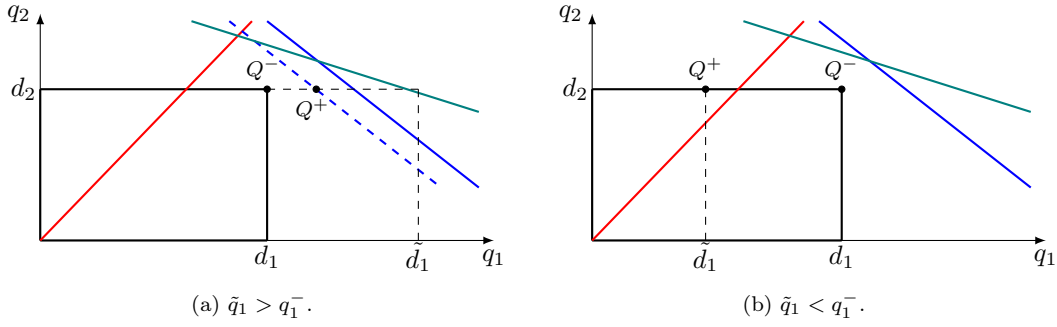


Figure 3.1. Case A1: Wave on road 1.

Note that, since $\hat{q}_1 \geq p_1 q_2^- / p_2$, then $\hat{q}_3 \geq \alpha_{31} p_1 q_2^- / p_2$ and $\hat{q}_4 \geq \alpha_{41} p_1 q_2^- / p_2$. We refer to the Appendix of [26] for the estimates of $\Delta\Gamma$, $\Delta\bar{h}$ and ΔTV_Q of (P2). We only observe that

$$\Delta\bar{h}(\bar{t}) = \frac{\hat{q}_2 - q_2^-}{p_2} \leq \frac{|\tilde{q}_2 - q_2^-|}{p_2}.$$

By (3.17) and (3.18) we have

$$\begin{aligned} |\hat{w}_3 - w_3^+| &\leq \frac{\alpha_{32} p_2 |w_1^- - w_2^-| (\tilde{q}_2 + q_1^-)}{p_1 q_2^- q_3^+} (|\Delta\Gamma(\bar{t})| + |\Delta\bar{h}(\bar{t})|) \\ |\hat{w}_4 - w_4^+| &\leq \frac{\alpha_{42} p_2 |w_1^- - w_2^-| (\tilde{q}_2 + q_1^-)}{p_1 q_2^- q_4^+} (|\Delta\Gamma(\bar{t})| + |\Delta\bar{h}(\bar{t})|) \\ \Rightarrow \Delta\text{TV}_w(\bar{t}) &\leq \left(\frac{\alpha_{32}}{q_3^+} + \frac{\alpha_{42}}{q_4^+} \right) \frac{p_2 |w_1^- - w_2^-| (\tilde{q}_2 + q_1^-)}{p_1 q_2^-} (|\Delta\Gamma(\bar{t})| + |\Delta\bar{h}(\bar{t})|). \end{aligned}$$

Next, we analyse the effects of a wave in ρ and w , i.e. we send a couple $(\tilde{\rho}_2, \tilde{w}_2)$ on road 2 such that we still have $\tilde{q}_2 > q_2^-$. The estimates on Γ , \bar{h} and TV_Q do not change, while for TV_w by (3.21) and (3.22) we have

$$\begin{aligned} |\hat{w}_3 - w_3^+| &\leq \frac{\alpha_{32} p_2 \tilde{q}_2 |\tilde{w}_2 - w_2^-|}{\alpha_{31} p_1 q_1^-} + \frac{\alpha_{32} p_2 |w_1^- - w_2^-| (\tilde{q}_2 + q_1^-)}{p_1 q_2^- q_3^+} (|\Delta\Gamma(\bar{t})| + |\Delta\bar{h}(\bar{t})|) \\ |\hat{w}_4 - w_3^+| &\leq \frac{\alpha_{42} p_2 \tilde{q}_2 |\tilde{w}_2 - w_2^-|}{\alpha_{41} p_1 q_1^-} + \frac{\alpha_{42} p_2 |w_1^- - w_2^-| (\tilde{q}_2 + q_1^-)}{p_1 q_2^- q_4^+} (|\Delta\Gamma(\bar{t})| + |\Delta\bar{h}(\bar{t})|) \\ \Rightarrow \Delta\text{TV}_w(\bar{t}) &\leq \left(\frac{\alpha_{32}}{q_3^+} + \frac{\alpha_{42}}{q_4^+} \right) \frac{p_2 \tilde{q}_2 |\tilde{w}_2 - w_2^-|}{p_1 q_2^-} |\tilde{w}_2 - w_2^-| \\ &\quad + \left(\frac{\alpha_{32}}{q_3^+} + \frac{\alpha_{42}}{q_4^+} \right) \frac{p_2 |w_1^- - w_2^-| (\tilde{q}_2 + q_1^-)}{p_1 q_2^-} (|\Delta\Gamma(\bar{t})| + |\Delta\bar{h}(\bar{t})|). \end{aligned}$$

In the second case we have

$$q_1^- > \hat{q}_1, \quad q_2^- < \tilde{q}_2 = \hat{q}_2, \quad \hat{q}_3 = \alpha_{31} \hat{q}_1 + \alpha_{32} \hat{q}_2, \quad \hat{q}_4 = \alpha_{41} \hat{q}_1 + \alpha_{42} \hat{q}_2.$$

Note that $\hat{q}_3 \geq \alpha_{32} \tilde{q}_2$ and $\hat{q}_4 \geq \alpha_{42} \tilde{q}_2$. We are interested in property (P2) thus we compute

$$\begin{aligned} * \quad \Gamma(\bar{t}+) &= \hat{q}_1 + \hat{q}_2 = \hat{q}_1 + \tilde{q}_2, \quad \Gamma(\bar{t}-) = q_1^- + q_2^- \\ \Rightarrow \Delta\Gamma(\bar{t}) &= (\hat{q}_1 - q_1^-) + (\tilde{q}_2 - q_2^-). \end{aligned}$$

3.2. Estimates for the case of two incoming and two outgoing roads at junctions

$$\begin{aligned}
 * \quad & \bar{h}(\bar{t}+) = \frac{\tilde{q}_2}{p_2}, \quad \bar{h}(\bar{t}-) = \frac{q_2^-}{p_2} \\
 \Rightarrow \Delta \bar{h}(\bar{t}) &= \frac{\tilde{q}_2 - q_2^-}{p_2} \leq \frac{|\tilde{q}_2 - q_2^-|}{p_2}.
 \end{aligned}$$

$$\begin{aligned}
 * \quad & \text{TV}_Q(\bar{t}+) = |\hat{q}_1 - q_1^-| + |\alpha_{31}\hat{q}_1 + \alpha_{32}\tilde{q}_2 - \alpha_{31}q_1^- - \alpha_{32}q_2^-| \\
 & \quad + |\alpha_{41}\hat{q}_1 + \alpha_{42}\tilde{q}_2 - \alpha_{41}q_1^- - \alpha_{42}q_2^-| \leq 2|\hat{q}_1 - q_1^-| + |\tilde{q}_2 - q_2^-| \\
 & \text{TV}_Q(\bar{t}-) = |\tilde{q}_2 - q_2^-| \\
 \Rightarrow \Delta \text{TV}_Q(\bar{t}) &\leq 2|\hat{q}_1 - q_1^-| \leq 2(|\Delta \Gamma(\bar{t})| + |\Delta \bar{h}(\bar{t})|).
 \end{aligned}$$

* By (3.17) and (3.18) we have

$$\begin{aligned}
 |\hat{w}_3 - w_3^+| &\leq \frac{\alpha_{31}|w_1^- - w_2^-|(\tilde{q}_2 + q_1^-)}{\tilde{q}_2 q_3^+} (|\Delta \Gamma(\bar{t})| + |\Delta \bar{h}(\bar{t})|) \\
 |\hat{w}_4 - w_4^+| &\leq \frac{\alpha_{41}|w_1^- - w_2^-|(\tilde{q}_2 + q_1^-)}{\tilde{q}_2 q_4^+} (|\Delta \Gamma(\bar{t})| + |\Delta \bar{h}(\bar{t})|) \\
 \Rightarrow \Delta \text{TV}_w(\bar{t}) &\leq \left(\frac{\alpha_{31}}{q_3^+} + \frac{\alpha_{41}}{q_4^+} \right) \frac{|w_1^- - w_2^-|(\tilde{q}_2 + q_1^-)}{\tilde{q}_2} (|\Delta \Gamma(\bar{t})| + |\Delta \bar{h}(\bar{t})|).
 \end{aligned}$$

Next, we analyse the effects of a wave in ρ and w , i.e. we send a couple $(\tilde{\rho}_2, \tilde{w}_2)$ on road 2 such that we still have $\tilde{q}_2 > q_2^-$. The estimates on Γ , \bar{h} and TV_Q do not change, while for TV_w by (3.21) and (3.22) we have

$$\begin{aligned}
 |\hat{w}_3 - w_3^+| &\leq |\tilde{w}_2 - w_2^-| + \frac{\alpha_{31}|w_1^- - w_2^-|(\tilde{q}_2 + q_1^-)}{\tilde{q}_2 q_3^+} (|\Delta \Gamma(\bar{t})| + |\Delta \bar{h}(\bar{t})|) \\
 |\hat{w}_4 - w_4^+| &\leq |\tilde{w}_2 - w_2^-| + \frac{\alpha_{41}|w_1^- - w_2^-|(\tilde{q}_2 + q_1^-)}{\tilde{q}_2 q_4^+} (|\Delta \Gamma(\bar{t})| + |\Delta \bar{h}(\bar{t})|) \\
 \text{TV}_w(\bar{t}-) &= |\tilde{w}_2 - w_2^-| \\
 \Rightarrow \Delta \text{TV}_w(\bar{t}) &\leq |\tilde{w}_2 - w_2^-| + \left(\frac{\alpha_{31}}{q_3^+} + \frac{\alpha_{41}}{q_4^+} \right) \frac{|w_1^- - w_2^-|(\tilde{q}_2 + q_1^-)}{\tilde{q}_2} (|\Delta \Gamma(\bar{t})| + |\Delta \bar{h}(\bar{t})|).
 \end{aligned}$$

Therefore (P2) and (P4) hold.

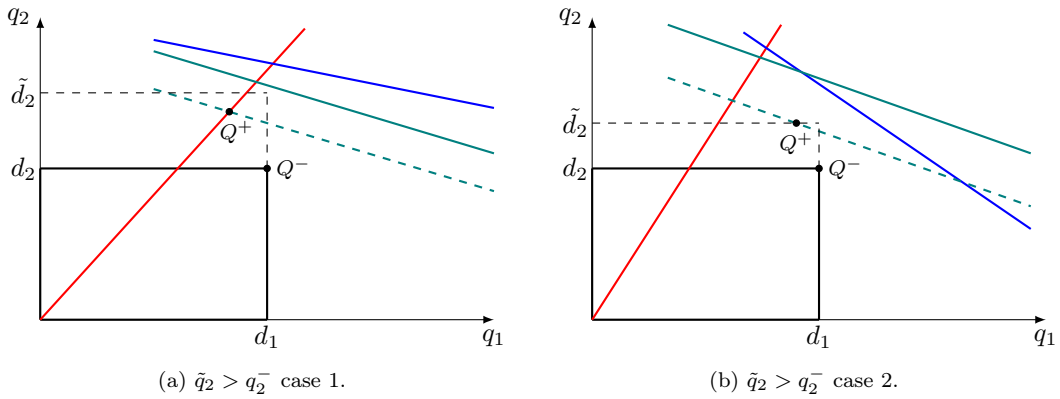


Figure 3.2. Case A2: Wave on road 2 with $\tilde{q}_2 > q_2^-$.

ii) We assume $\tilde{q}_2 < q_2^-$. First of all we analyse the effects of a wave related only to the density ρ , i.e. we send a certain $\tilde{\rho}_2$ on road 2 keeping w_2^- fixed. In Figure 3.3 we show a possible solution given

by the algorithm. Specifically we have

$$q_1^- = \hat{q}_1, \quad q_2^- > \hat{q}_2 = \tilde{q}_2, \quad \hat{q}_3 = \alpha_{31}q_1^- + \alpha_{32}\tilde{q}_2 \leq q_3^+, \quad \hat{q}_4 = \alpha_{41}q_1^- + \alpha_{42}\tilde{q}_2 \leq q_4^+.$$

We refer to the Appendix of [26] for the estimates of $\Delta\Gamma$, $\Delta\bar{h}$ and ΔTV_Q of (P2) and (P3). Note that $\hat{q}_3 \geq \alpha_{31}q_1^-$ and $\hat{q}_4 \geq \alpha_{41}q_1^-$. By (3.11) and (3.12) we have

$$\begin{aligned} |\hat{w}_3 - w_3^+| &\leq \frac{\alpha_{32}|w_1^- - w_2^-|}{q_3^+} |\tilde{q}_2 - q_2^-|, & |\hat{w}_4 - w_4^+| &\leq \frac{\alpha_{42}|w_1^- - w_2^-|}{q_4^+} |\tilde{q}_2 - q_2^-| \\ \Rightarrow \Delta\text{TV}_w(\bar{t}) &= \left(\frac{\alpha_{32}}{q_3^+} + \frac{\alpha_{42}}{q_4^+} \right) |w_1^- - w_2^-| |\tilde{q}_2 - q_2^-|. \end{aligned}$$

Next, we analyse the effects of a wave in ρ and w , i.e. we send a couple $(\tilde{\rho}_2, \tilde{w}_2)$ on road 2 such that we still have $\tilde{q}_2 < q_2^-$. The estimates on Γ , \bar{h} and TV_Q do not change, while for TV_w by (3.13) and (3.14) we have

$$\begin{aligned} |\hat{w}_3 - w_3^+| &\leq \frac{\alpha_{32}\tilde{q}_2}{\alpha_{31}q_1^-} |\tilde{w}_2 - w_2^-| + \frac{\alpha_{32}|w_2^- - w_1^-|}{q_3^+} |\tilde{q}_2 - q_2^-| \\ |\hat{w}_4 - w_4^+| &\leq \frac{\alpha_{42}\tilde{q}_2}{\alpha_{41}q_1^-} |\tilde{w}_2 - w_2^-| + \frac{\alpha_{42}|w_2^- - w_1^-|}{q_4^+} |\tilde{q}_2 - q_2^-| \\ \text{TV}_w(\bar{t}+) &\leq \left(\frac{\alpha_{32}}{\alpha_{31}} + \frac{\alpha_{42}}{\alpha_{41}} \right) \frac{\tilde{q}_2}{q_1^-} |\tilde{w}_2 - w_2^-| + \left(\frac{\alpha_{32}}{q_3^+} + \frac{\alpha_{42}}{q_4^+} \right) |w_2^- - w_1^-| |\tilde{q}_2 - q_2^-| \\ \text{TV}_w(\bar{t}-) &= |\tilde{w}_2 - w_2^-| \\ \Rightarrow \Delta\text{TV}_w(\bar{t}) &\leq \left[\left(\frac{\alpha_{32}}{\alpha_{31}} + \frac{\alpha_{42}}{\alpha_{41}} \right) \frac{\tilde{q}_2}{q_1^-} - 1 \right] |\tilde{w}_2 - w_2^-| + \left(\frac{\alpha_{32}}{q_3^+} + \frac{\alpha_{42}}{q_4^+} \right) |w_2^- - w_1^-| |\tilde{q}_2 - q_2^-|. \end{aligned}$$

Therefore (P2), (P3) and (P4) hold.

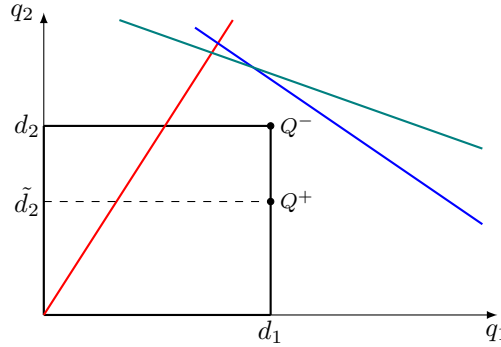


Figure 3.3. Case A2: Wave on road 2 with $\tilde{q}_2 < q_2^-$.

Case A3: Wave on road 3

We now consider a wave on road 3. The case of a wave on road 4 is analogous. Note that in this case we are not interested in what happens sending a wave in ρ and w , since the changes in w on the outgoing roads do not affect the Riemann Solver. Hence, we only study waves which involve the density ρ and keep w_3^+ fixed.

3.2. Estimates for the case of two incoming and two outgoing roads at junctions

- i) We assume $\tilde{q}_3 > q_3^+$, which implies that the straight line which maximises the outgoing flux z_3 move to the top. Therefore, in this case the solution of the algorithm is again the equilibrium U^- , thus nothing happens.
- ii) We assume $\tilde{q}_3 < q_3^+$. We send a certain $\tilde{\rho}_3$ on road 3 keeping w_3^+ fixed. In this case the straight line which maximises the outgoing flux z_3 moves to the bottom, thus we have two possibilities: the new maximisation straight line z_3 intersects the priority rule r (see Figure 3.4(a)) or the solution is such that $\hat{q}_2 = q_2^-$ and $q_2^- p_1/p_2 \leq \hat{q}_1 \leq q_1^-$ (see Figure 3.4(b)).

In the first case we have

$$q_1^- \geq \hat{q}_1, \quad q_2^- \geq \hat{q}_2, \quad \hat{q}_3 = \tilde{q}_3 = \alpha_{31}\hat{q}_1 + \alpha_{32}\hat{q}_2 \leq q_3^+, \quad \hat{q}_4 = \alpha_{41}\hat{q}_1 + \alpha_{42}\hat{q}_2 \leq q_4^+.$$

We refer to the Appendix of [26] for the estimates of $\Delta\Gamma$, $\Delta\bar{h}$ and ΔTV_Q of (P2) and (P3). Note that

$$\begin{aligned} \hat{q}_1 &= \frac{p_1\tilde{q}_3}{\alpha_{31}p_1 + \alpha_{32}p_2}, & \hat{q}_2 &= \frac{p_2\tilde{q}_3}{\alpha_{31}p_1 + \alpha_{32}p_2}, & \hat{q}_4 &= \frac{\alpha_{41}p_1 + \alpha_{42}p_2}{\alpha_{31}p_1 + \alpha_{32}p_2}\tilde{q}_3 \\ q_1^- &= \frac{p_1q_3^*}{\alpha_{31}p_1 + \alpha_{32}p_2}, & q_2^- &= \frac{p_2q_3^*}{\alpha_{31}p_1 + \alpha_{32}p_2}, \end{aligned}$$

with $q_3^* \leq q_3^+$ such that z_3 goes through the point Q^* . By (3.15) and (3.16) we have

$$\begin{aligned} |\hat{w}_3 - w_3^+| &\leq \frac{\alpha_{31}\alpha_{32}|w_1^- - w_2^-|}{\tilde{q}_3q_3^+} |\hat{q}_2(\hat{q}_1 - q_1^-) - \hat{q}_1(\hat{q}_2 - q_2^-)| \\ &\leq \frac{\alpha_{31}\alpha_{32}|w_1^- - w_2^-|}{(\alpha_{31}p_1 + \alpha_{32}p_2)q_3^+} |\tilde{q}_3 - q_3^+| \\ |\hat{w}_4 - w_4^+| &\leq \frac{\alpha_{41}\alpha_{42}|w_1^- - w_2^-|}{(\alpha_{41}p_1 + \alpha_{42}p_2)q_4^+} |\tilde{q}_3 - q_3^+| \\ \Rightarrow \Delta\text{TV}_w(\bar{t}) &\leq \left(\frac{\alpha_{31}\alpha_{32}}{(\alpha_{31}p_1 + \alpha_{32}p_2)q_3^+} + \frac{\alpha_{41}\alpha_{42}}{(\alpha_{41}p_1 + \alpha_{42}p_2)q_4^+} \right) |w_1^- - w_2^-| |\tilde{q}_3 - q_3^+|. \end{aligned}$$

In the second case we have

$$q_1^- \geq \hat{q}_1, \quad q_2^- = \hat{q}_2, \quad \hat{q}_3 = \alpha_{31}\hat{q}_1 + \alpha_{32}q_2^- \leq q_3^+, \quad \hat{q}_4 = \alpha_{41}\hat{q}_1 + \alpha_{42}q_2^- \leq q_4^+.$$

Note that $\hat{q}_3 \geq \alpha_{32}q_2^-$, $\hat{q}_4 \geq \alpha_{42}q_2^-$ and that

$$\hat{q}_1 = \frac{\hat{q}_3 - \alpha_{32}q_2^-}{\alpha_{31}}, \quad q_1^- = \frac{q_3^+ - \alpha_{32}q_2^-}{\alpha_{31}}.$$

We compute

$$\begin{aligned} * \quad \Gamma(\bar{t}+) &= \hat{q}_1 + \hat{q}_2 = \hat{q}_1 + q_2^-, & \Gamma(\bar{t}-) &= q_1^- + q_2^- \\ \Rightarrow \Delta\Gamma(\bar{t}) &= \hat{q}_1 - q_1^- = \frac{\hat{q}_3 - q_3^+}{\alpha_{31}} < 0. \\ * \quad \bar{h}(\bar{t}+) &= \bar{h}(\bar{t}-) = \frac{q_2^-}{p_2} \\ \Rightarrow \Delta\bar{h}(\bar{t}) &= 0. \\ * \quad \text{TV}_Q(\bar{t}+) &= |\hat{q}_1 - q_1^-| + |\hat{q}_3 - \tilde{q}_3| + \alpha_{41}|\hat{q}_1 - q_1^-| = \frac{1 + \alpha_{41}}{\alpha_{31}} |\hat{q}_3 - q_3^+| + |\hat{q}_3 - \tilde{q}_3| \\ \text{TV}_Q(\bar{t}-) &= |\tilde{q}_3 - q_3^+| \\ \Rightarrow \Delta\text{TV}_Q(\bar{t}) &\leq \frac{1 + \alpha_{31} + \alpha_{41}}{\alpha_{31}} |\hat{q}_3 - q_3^+| = 2|\Delta\Gamma(\bar{t})|. \end{aligned}$$

* By (3.11) and (3.12) we have

$$\begin{aligned} |\hat{w}_3 - w_3^+| &\leq \frac{\alpha_{31}\alpha_{32}q_2^-|w_1^- - w_2^-|}{\hat{q}_3q_3^+}|\hat{q}_1 - q_1^-| \leq \frac{\alpha_{31}|w_1^- - w_2^-|}{q_3^+}|\Delta\Gamma(\bar{t})| \\ |\hat{w}_4 - w_4^+| &\leq \frac{\alpha_{41}|w_1^- - w_2^-|}{q_4^+}|\Delta\Gamma(\bar{t})| \\ \Rightarrow \Delta\text{TV}_w(\bar{t}) &\leq \left(\frac{\alpha_{31}}{q_3^+} + \frac{\alpha_{41}}{q_4^+}\right)|w_1^- - w_2^-||\Delta\Gamma(\bar{t})|. \end{aligned}$$

Therefore (P2) and (P3) hold.

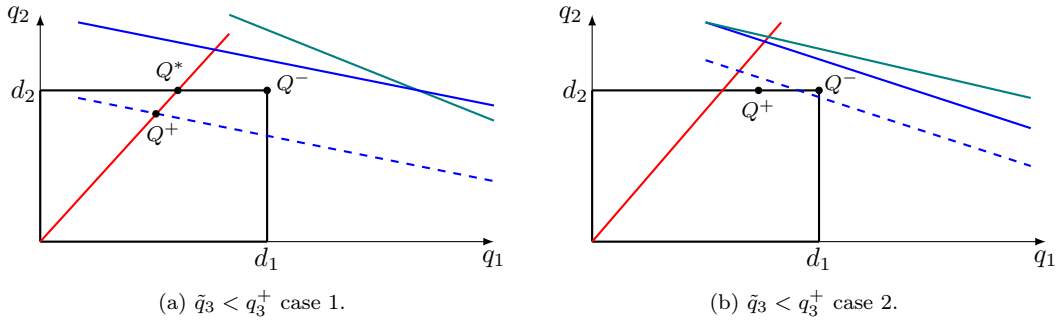


Figure 3.4. Case A3: Wave on road 3 with $\tilde{q}_3 < q_3^+$.

3.2.2 Case B

This case is verified when the equilibrium is along one of the straight lines $q_1 = d_1$ or $q_2 = d_2$. Without loss of generality, we assume that the priority rule r first intersects the straight line $q_1 = d_1$, thus the equilibrium is along the right side of the rectangle Ω_{inc} . We study the effects produced by a single wave sent on each road.

Case B1: Wave on road 1

Let us start with a wave on road 1.

- i) We assume $\tilde{q}_1 > q_1^-$. First of all we analyse the effects of a wave related only to the density ρ , i.e. we send a certain $\tilde{\rho}_1$ on road 1 keeping w_1^- fixed. We have two possibilities: \tilde{d}_1 is big enough to find an intersection between a straight line which maximises the outgoing flux z_3 or z_4 and the priority rule r (see Figure 3.5(a)), or the solution is along $q_1 = \tilde{d}_1$ (see Figure 3.5(b)).

In the first case we have

$$q_1^- \leq \hat{q}_1 \leq \tilde{q}_1, \quad q_2^- \geq \hat{q}_2, \quad \hat{q}_3 = \alpha_{31}\hat{q}_1 + \alpha_{32}\hat{q}_2, \quad \hat{q}_4 = \alpha_{41}\hat{q}_1 + \alpha_{42}\hat{q}_2 = q_4^+.$$

We refer to the Appendix of [26] for the estimates of $\Delta\Gamma$, $\Delta\bar{h}$ and ΔTV_Q of (P2). We only observe that

$$\Delta\bar{h}(\bar{t}) = \frac{\hat{q}_1 - q_1^-}{p_1} \leq \frac{|\tilde{q}_1 - q_1^-|}{p_1}.$$

3.2. Estimates for the case of two incoming and two outgoing roads at junctions

Moreover, since $\hat{q}_2 \geq p_2 q_1^- / p_1$, then $\hat{q}_3 \geq \alpha_{32} p_2 q_1^- / p_1$ and $\hat{q}_4 \geq \alpha_{42} p_2 q_1^- / p_1$. By (3.17) and (3.18) we have

$$\begin{aligned} |\hat{w}_3 - w_3^+| &\leq \frac{\alpha_{31} p_1 |w_1^- - w_2^-| (\tilde{q}_1 + q_2^-)}{p_2 q_1^- q_3^+} (|\Delta\Gamma(\bar{t})| + |\Delta\bar{h}(\bar{t})|) \\ |\hat{w}_4 - w_4^+| &\leq \frac{\alpha_{41} p_1 |w_1^- - w_2^-| (\tilde{q}_1 + q_2^-)}{p_2 q_1^- q_4^+} (|\Delta\Gamma(\bar{t})| + |\Delta\bar{h}(\bar{t})|) \\ \Rightarrow \Delta\text{TV}_w(\bar{t}) &\leq \left(\frac{\alpha_{31}}{q_3^+} + \frac{\alpha_{41}}{q_4^+} \right) \frac{p_1 |w_1^- - w_2^-| (\tilde{q}_1 + q_2^-)}{p_2 q_1^-} (|\Delta\Gamma(\bar{t})| + |\Delta\bar{h}(\bar{t})|). \end{aligned}$$

Next, we analyse the effects of a wave in ρ and w , i.e. we send a couple $(\tilde{\rho}_1, \tilde{w}_1)$ on road 1 such that we still have $\tilde{q}_1 > q_1^-$. The estimates on Γ , \bar{h} and TV_Q do not change, while for TV_w by (3.21) and (3.22) we have

$$\begin{aligned} |\hat{w}_3 - w_3^+| &\leq \frac{\alpha_{31} p_1 \tilde{q}_1 |\tilde{w}_1 - w_1^-|}{\alpha_{32} p_2 q_1^-} + \frac{\alpha_{31} p_1 |w_1^- - w_2^-| (\tilde{q}_1 + q_2^-)}{p_2 q_1^- q_3^+} (|\Delta\Gamma(\bar{t})| + |\Delta\bar{h}(\bar{t})|) \\ |\hat{w}_4 - w_4^+| &\leq \frac{\alpha_{41} p_1 \tilde{q}_1 |\tilde{w}_1 - w_1^-|}{\alpha_{42} p_2 q_1^-} + \frac{\alpha_{41} p_1 |w_1^- - w_2^-| (\tilde{q}_1 + q_2^-)}{p_2 q_1^- q_4^+} (|\Delta\Gamma(\bar{t})| + |\Delta\bar{h}(\bar{t})|) \\ \Rightarrow \Delta\text{TV}_w(\bar{t}) &\leq \left(\frac{\alpha_{31}}{q_3^+} + \frac{\alpha_{41}}{q_4^+} \right) \frac{p_1 \tilde{q}_1}{p_1 q_1^-} |\tilde{w}_1 - w_1^-| \\ &\quad + \left(\frac{\alpha_{31}}{q_3^+} + \frac{\alpha_{41}}{q_4^+} \right) \frac{p_1 |w_1^- - w_2^-| (\tilde{q}_1 + q_2^-)}{p_2 q_1^-} (|\Delta\Gamma(\bar{t})| + |\Delta\bar{h}(\bar{t})|). \end{aligned}$$

In the second case we have

$$q_1^- \leq \hat{q}_1 = \tilde{q}_1, \quad \hat{q}_3 = \alpha_{31} \hat{q}_1 + \alpha_{32} \hat{q}_2, \quad \hat{q}_4 = \alpha_{41} \hat{q}_1 + \alpha_{42} \hat{q}_2 = q_4^+,$$

with \hat{q}_2 that can be both greater or lower than q_2^- . Note that, since $\hat{q}_2 \geq p_2 \tilde{q}_1 / p_1$, then $\hat{q}_3 \geq \alpha_{32} p_2 \tilde{q}_1 / p_1$ and $\hat{q}_4 \geq \alpha_{42} p_2 \tilde{q}_1 / p_1$. We compute

$$\begin{aligned} * \quad \Gamma(\bar{t}+) &= \hat{q}_1 + \hat{q}_2 = \tilde{q}_1 + \hat{q}_2, \quad \Gamma(\bar{t}-) = q_1^- + q_2^- \\ &\Rightarrow \Delta\Gamma(\bar{t}) = (\tilde{q}_1 - q_1^-) + (\hat{q}_2 - q_2^-). \\ * \quad \bar{h}(\bar{t}+) &= \frac{\tilde{q}_1}{p_1}, \quad \bar{h}(\bar{t}-) = \frac{q_1^-}{p_1} \\ &\Rightarrow \Delta\bar{h}(\bar{t}) = \frac{\tilde{q}_1 - q_1^-}{p_1} \leq \frac{|\tilde{q}_1 - q_1^-|}{p_1}. \\ * \quad \text{TV}_Q(\bar{t}+) &= |\hat{q}_2 - q_2^-| + |\alpha_{31} \tilde{q}_1 + \alpha_{32} \hat{q}_2 - \alpha_{31} q_1^- - \alpha_{32} q_2^-| \\ &\quad + |\alpha_{41} \tilde{q}_1 + \alpha_{42} \hat{q}_2 - \alpha_{41} q_1^- - \alpha_{42} q_2^-| \leq |\tilde{q}_1 - q_1^-| + 2|\hat{q}_2 - q_2^-| \\ \text{TV}_Q(\bar{t}-) &= |\tilde{q}_1 - q_1^-| \\ \Rightarrow \Delta\text{TV}_Q(\bar{t}) &\leq 2|\hat{q}_2 - q_2^-| \leq 2(|\Delta\Gamma(\bar{t})| + |\Delta\bar{h}(\bar{t})|). \end{aligned}$$

* By (3.17) and (3.18) we have

$$\begin{aligned} |\hat{w}_3 - w_3^+| &\leq \frac{\alpha_{31} p_1 |w_1^- - w_2^-| (\tilde{q}_1 + d_2)}{p_2 \tilde{q}_1 q_3^+} (|\Delta\Gamma(\bar{t})| + |\Delta\bar{h}(\bar{t})|) \\ |\hat{w}_4 - w_4^+| &\leq \frac{\alpha_{41} p_1 |w_1^- - w_2^-| (\tilde{q}_1 + d_2)}{p_2 \tilde{q}_1 q_4^+} (|\Delta\Gamma(\bar{t})| + |\Delta\bar{h}(\bar{t})|) \\ \Rightarrow \Delta\text{TV}_w(\bar{t}) &\leq \left(\frac{\alpha_{31}}{q_3^+} + \frac{\alpha_{41}}{q_4^+} \right) \frac{p_1 |w_1^- - w_2^-| (\tilde{q}_1 + d_2)}{p_2 \tilde{q}_1} (|\Delta\Gamma(\bar{t})| + |\Delta\bar{h}(\bar{t})|). \end{aligned}$$

Next, we analyse the effects of a wave in ρ and w , i.e. we send a couple $(\tilde{\rho}_1, \tilde{w}_1)$ on road 1 such that we still have $\tilde{q}_1 > q_1^-$. The estimates on Γ , \bar{h} and TV_Q do not change, while for TV_w by (3.21) and (3.22) we have

$$\begin{aligned} |\hat{w}_3 - w_3^+| &\leq \frac{\alpha_{31}p_1|\tilde{w}_1 - w_1^-|}{\alpha_{32}p_2} + \frac{\alpha_{31}p_1|w_1^- - w_2^-|(\tilde{q}_1 + d_2)}{p_2\tilde{q}_1q_3^+} (|\Delta\Gamma(\bar{t})| + |\Delta\bar{h}(\bar{t})|) \\ |\hat{w}_4 - w_3^+| &\leq \frac{\alpha_{41}p_1|\tilde{w}_1 - w_1^-|}{\alpha_{42}p_2} + \frac{\alpha_{41}p_1|w_1^- - w_2^-|(\tilde{q}_1 + d_2)}{p_2\tilde{q}_1q_4^+} (|\Delta\Gamma(\bar{t})| + |\Delta\bar{h}(\bar{t})|) \\ \Rightarrow \Delta\text{TV}_w(\bar{t}) &\leq \left(\frac{\alpha_{31}}{\alpha_{32}q_3^+} + \frac{\alpha_{41}}{\alpha_{42}q_4^+} \right) \frac{p_1}{p_1} |\tilde{w}_1 - w_1^-| \\ &\quad + \left(\frac{\alpha_{31}}{q_3^+} + \frac{\alpha_{41}}{q_4^+} \right) \frac{p_1|w_1^- - w_2^-|(\tilde{q}_1 + d_2)}{p_2\tilde{q}_1} (|\Delta\Gamma(\bar{t})| + |\Delta\bar{h}(\bar{t})|). \end{aligned}$$

Therefore (P2) and (P4) hold.

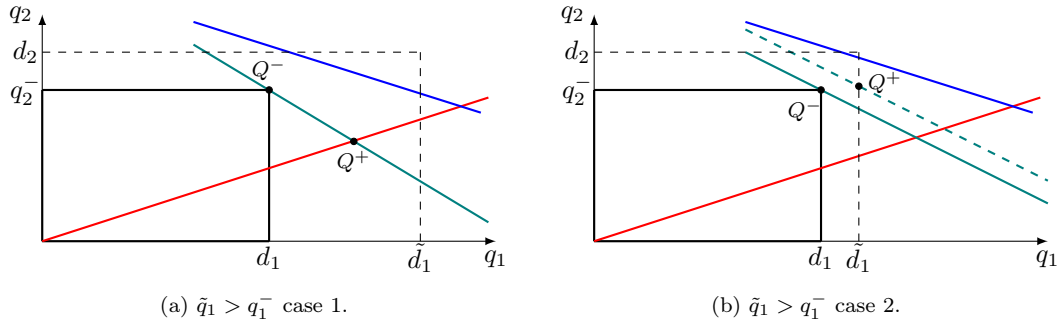


Figure 3.5. Case B1: Wave on road 1 with $\tilde{q}_1 > q_1^-$.

ii) We assume $\tilde{q}_1 < q_1^-$. First of all we analyse the effects of a wave related only to the density ρ , i.e. we send a certain $\tilde{\rho}_1$ on road 1 keeping w_1^- fixed. In Figure 3.6 we show a possible solution given by the algorithm. Specifically we have

$$q_1^- > \hat{q}_1 = \tilde{q}_1, \quad \hat{q}_3 = \alpha_{31}\tilde{q}_1 + \alpha_{32}\hat{q}_2, \quad \hat{q}_4 = \alpha_{41}\tilde{q}_1 + \alpha_{42}q_2^-.$$

Note that $\hat{q}_3 \geq \alpha_{31}\tilde{q}_1$ and $\hat{q}_4 \geq \alpha_{41}\tilde{q}_1$. Moreover, we observe that if $\hat{q}_2 < q_2^-$ then $\hat{q}_2 - q_2^- < 0$, otherwise we define the angle $\beta = \arctan(|d_2 - q_2^-|/|\tilde{q}_1 - q_1^-|)$ between the segments $|Q^-Q^*|$ and $|\hat{Q}Q^-|$ and we obtain $\hat{q}_2 - q_2^- = |\hat{q}_2 - q_2^-| \leq \tan \beta |\tilde{q}_1 - q_1^-|$. We compute

$$\begin{aligned} * \quad \Gamma(\bar{t}+) &= \hat{q}_1 + \hat{q}_2 = \tilde{q}_1 + \hat{q}_2, & \Gamma(\bar{t}-) &= q_1^- + q_2^- \\ \Rightarrow \Delta\Gamma(\bar{t}) &= (\tilde{q}_1 - q_1^-) + (\hat{q}_2 - q_2^-) \leq C|\tilde{q}_1 - q_1^-|. \\ * \quad \bar{h}(\bar{t}+) &= \frac{\tilde{q}_1}{p_1}, & \bar{h}(\bar{t}-) &= \frac{q_1^-}{p_1} \\ \Rightarrow \Delta\bar{h}(\bar{t}) &= \frac{\tilde{q}_1 - q_1^-}{p_1} < 0. \\ * \quad \text{TV}_Q(\bar{t}+) &\leq 2|\hat{q}_2 - q_2^-| + |\tilde{q}_1 - q_1^-| \leq 2(|\Delta\Gamma(\bar{t})| + |\tilde{q}_1 - q_1^-|) \\ \text{TV}_Q(\bar{t}-) &= |\tilde{q}_1 - q_1^-| \\ \Rightarrow \Delta\text{TV}_Q(\bar{t}) &\leq 2(|\Delta\Gamma(\bar{t})| + |\Delta\bar{h}(\bar{t})|). \end{aligned}$$

We refer to the Appendix of [26] for the estimates of $\Delta\Gamma$, $\Delta\bar{h}$ and ΔTV_Q of (P2) and (P3). Note that $\hat{q}_3 \geq \alpha_{31}q_1^-$ and $\hat{q}_4 \geq \alpha_{41}q_1^-$. By (3.11) and (3.12) we have

$$|\hat{w}_3 - w_3^+| \leq \frac{\alpha_{32}|w_1^- - w_2^-|}{q_3^+} |\tilde{q}_2 - q_2^-|, \quad |\hat{w}_4 - w_4^+| \leq \frac{\alpha_{32}|w_1^- - w_2^-|}{q_4^+} |\tilde{q}_2 - q_2^-|$$

$$\Rightarrow \Delta\text{TV}_w(\bar{t}) = \left(\frac{\alpha_{32}}{q_3^+} + \frac{\alpha_{42}}{q_4^+} \right) |w_1^- - w_2^-| |\tilde{q}_2 - q_2^-|.$$

Next, we analyse the effects of a wave in ρ and w , i.e. we send a couple $(\tilde{\rho}_2, \tilde{w}_2)$ on road 2 such that we still have $\tilde{q}_2 < q_2^-$. The estimates on Γ , \bar{h} and TV_Q do not change, while for TV_w by (3.13) and (3.14) we have

$$|\hat{w}_3 - w_3^+| \leq \frac{\alpha_{32}\tilde{q}_2}{\alpha_{31}q_1^-} |\tilde{w}_2 - w_2^-| + \frac{\alpha_{32}|w_2^- - w_1^-|}{q_3^+} |\tilde{q}_2 - q_2^-|$$

$$|\hat{w}_4 - w_4^+| \leq \frac{\alpha_{32}\tilde{q}_2}{\alpha_{31}q_1^-} |\tilde{w}_2 - w_2^-| + \frac{\alpha_{32}|w_2^- - w_1^-|}{q_4^+} |\tilde{q}_2 - q_2^-|$$

$$\text{TV}_w(\bar{t}+) \leq \left(\frac{\alpha_{32}}{\alpha_{31}} + \frac{\alpha_{42}}{\alpha_{41}} \right) \frac{\tilde{q}_2}{q_1^-} |\tilde{w}_2 - w_2^-| + \left(\frac{\alpha_{32}}{q_3^+} + \frac{\alpha_{42}}{q_4^+} \right) |w_2^- - w_1^-| |\tilde{q}_2 - q_2^-|$$

$$\text{TV}_w(\bar{t}-) = |\tilde{w}_2 - w_2^-|$$

$$\Rightarrow \Delta\text{TV}_w(\bar{t}) \leq \left[\left(\frac{\alpha_{32}}{\alpha_{31}} + \frac{\alpha_{42}}{\alpha_{41}} \right) \frac{\tilde{q}_2}{q_1^-} - 1 \right] |\tilde{w}_2 - w_2^-| + \left(\frac{\alpha_{32}}{q_3^+} + \frac{\alpha_{42}}{q_4^+} \right) |w_2^- - w_1^-| |\tilde{q}_2 - q_2^-|.$$

Therefore (P2), (P3) and (P4) hold.

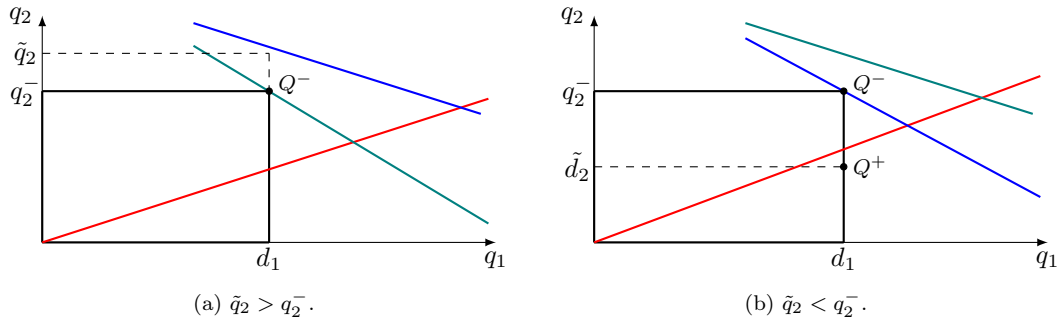


Figure 3.7. Case B2: Wave on road 2.

Case B3: Wave on road 3

We now consider a wave on road 3. The case of a wave on road 4 is analogous. Note that in this case we are not interested in what happens sending a wave in ρ and w , since the changes in w on the outgoing roads do not affect the Riemann solver. Hence, we only study waves which involve the density ρ and keep w_3^+ fixed.

- i) We assume $\tilde{q}_3 > q_3^+$. We send a certain $\tilde{\rho}_3$ on road 3 keeping w_3^+ fixed. In Figure 3.8(a) we show a possible solution given by the algorithm. Specifically we have

$$q_1^- = \hat{q}_1, \quad q_2^- \leq \hat{q}_2, \quad \hat{q}_3 = \alpha_{31}q_1^- + \alpha_{32}\hat{q}_2 \geq q_3^+, \quad \hat{q}_4 = \alpha_{41}q_1^- + \alpha_{42}\hat{q}_2 \geq q_4^+.$$

3.2. Estimates for the case of two incoming and two outgoing roads at junctions

Note that

$$\begin{aligned}\hat{q}_2 &= \frac{\hat{q}_3 - \alpha_{31}q_1^-}{\alpha_{32}}, & q_2^- &= \frac{q_3^+ - \alpha_{31}q_1^-}{\alpha_{32}} \\ \hat{q}_4^+ &= \alpha_{41}q_1^- + \frac{\alpha_{42}}{\alpha_{32}}(q_3^+ - \alpha_{31}q_1^-), & \hat{q}_4 &= \alpha_{41}q_1^- + \frac{\alpha_{42}}{\alpha_{32}}(\hat{q}_3 - \alpha_{31}q_1^-).\end{aligned}$$

We compute

$$\begin{aligned}*\quad & \Gamma(\bar{t}+) = \hat{q}_1 + \hat{q}_2 = q_1^- + \hat{q}_2, & \Gamma(\bar{t}-) &= q_1^- + q_2^- \\ & \Rightarrow \Delta\Gamma(\bar{t}) = \hat{q}_2 - q_2^- = \frac{\hat{q}_3 - q_3^+}{\alpha_{32}}. \\ *\quad & \bar{h}(\bar{t}+) = \bar{h}(\bar{t}-) = \frac{q_1^-}{p_1} \\ & \Rightarrow \Delta\bar{h}(\bar{t}) = 0. \\ *\quad & \text{TV}_Q(\bar{t}+) = |\hat{q}_2 - q_2^-| + |\hat{q}_3 - \tilde{q}_3| + \alpha_{42}|\hat{q}_2 - q_2^-| = \frac{1 + \alpha_{42}}{\alpha_{32}}|\hat{q}_3 - q_3^+| + |\hat{q}_3 - \tilde{q}_3| \\ & \text{TV}_Q(\bar{t}-) = |\tilde{q}_3 - q_3^+| \\ & \Rightarrow \Delta\text{TV}_Q(\bar{t}) = \frac{1 + \alpha_{42}}{\alpha_{32}}|\hat{q}_3 - q_3^+| + |\hat{q}_3 - \tilde{q}_3| - |\tilde{q}_3 - q_3^+| \leq \frac{2}{\alpha_{32}}|\hat{q}_3 - q_3^+|. \\ *\quad & \text{By (3.11) and (3.12)} \\ & |\hat{w}_3 - w_3^+| = \frac{\alpha_{31}q_1^-|w_1^- - w_2^-||q_3^+ - \hat{q}_3|}{\hat{q}_3q_3^+} \leq \frac{\alpha_{31}\alpha_{32}q_1^-|w_1^- - w_2^-|}{(q_3^+)^2}|\Delta\Gamma(\bar{t})| \\ & |\hat{w}_4 - w_4^+| = \frac{\alpha_{41}q_1^-|w_1^- - w_2^-||q_4^+ - \hat{q}_4|}{\hat{q}_4q_4^+} \leq \frac{\alpha_{41}\alpha_{42}q_1^-|w_1^- - w_2^-|}{(q_4^+)^2}|\Delta\Gamma(\bar{t})| \\ & \Rightarrow \Delta\text{TV}_w(\bar{t}) \leq \left(\frac{\alpha_{31}\alpha_{32}}{(q_3^+)^2} + \frac{\alpha_{41}\alpha_{42}}{(q_4^+)^2} \right) q_1^-|w_1^- - w_2^-||\Delta\Gamma(\bar{t})|.\end{aligned}$$

Therefore (P2) holds.

ii) We assume $\tilde{q}_3 < q_3^+$. We send a certain \tilde{p}_3 on road 3 keeping w_3^+ fixed. In Figure 3.8(b) we show a possible solution given by the algorithm. Specifically we have

$$q_1^- \geq \hat{q}_1, \quad q_2^- \geq \hat{q}_2, \quad \hat{q}_3 = \tilde{q}_3 = \alpha_{31}\hat{q}_1 + \alpha_{32}\hat{q}_2 \leq q_3^+, \quad \hat{q}_4 = \alpha_{41}\hat{q}_1 + \alpha_{42}\hat{q}_2 \leq q_4^+.$$

Note that

$$\begin{aligned}\hat{q}_1 &= \frac{p_1\tilde{q}_3}{\alpha_{31}p_1 + \alpha_{32}p_2}, & q_1^- &= \frac{p_1q_3^*}{\alpha_{31}p_1 + \alpha_{32}p_2} \\ \hat{q}_2 &= \frac{p_2\tilde{q}_3}{\alpha_{31}p_1 + \alpha_{32}p_2}, & q_2^- &= \frac{q_3^+ - \alpha_{31}q_1^-}{\alpha_{32}} \\ \hat{q}_4 &= \frac{\alpha_{41}p_1 + \alpha_{42}p_2}{\alpha_{31}p_1 + \alpha_{32}p_2}\tilde{q}_3.\end{aligned}$$

We refer to the Appendix of [26] for the estimates of $\Delta\Gamma$, $\Delta\bar{h}$ and ΔTV_Q of (P2) and (P3). We only observe that

$$\begin{aligned}\Delta\Gamma(\bar{t}) &= \frac{\tilde{q}_3 - q_3^*}{\alpha_{31}p_1 + \alpha_{32}p_2} + \frac{q_3^* - q_3^+}{\alpha_{32}} \\ \Delta\bar{h}(\bar{t}) &= \frac{\hat{q}_1 - q_1^-}{p_1} = \frac{\tilde{q}_3 - q_3^*}{\alpha_{31}p_1 + \alpha_{32}p_2}.\end{aligned}$$

By (3.17) and (3.18) we have

$$\begin{aligned} |\hat{w}_3 - w_3^+| &\leq \frac{\alpha_{31}\alpha_{32}p_1|w_1^- - w_2^-|}{(\alpha_{31}p_1 + \alpha_{32}p_2)q_3^+} (|\Delta\Gamma(\bar{t})| + |\Delta\bar{h}(\bar{t})|) \\ |\hat{w}_4 - w_4^+| &\leq \frac{\alpha_{41}\alpha_{42}p_1|w_1^- - w_2^-|}{(\alpha_{41}p_1 + \alpha_{42}p_2)q_4^+} (|\Delta\Gamma(\bar{t})| + |\Delta\bar{h}(\bar{t})|) \\ \Rightarrow \Delta\text{TV}_w(\bar{t}) &\leq \left(\frac{\alpha_{31}\alpha_{32}}{q_3^+(p_1\alpha_{31} + p_2\alpha_{32})} + \frac{\alpha_{41}\alpha_{42}}{q_4^+(p_1\alpha_{41} + p_2\alpha_{42})} \right) p_1|w_1^- - w_2^-| (|\Delta\Gamma(\bar{t})| + |\Delta\bar{h}(\bar{t})|). \end{aligned}$$

Therefore (P2) and (P3) hold.

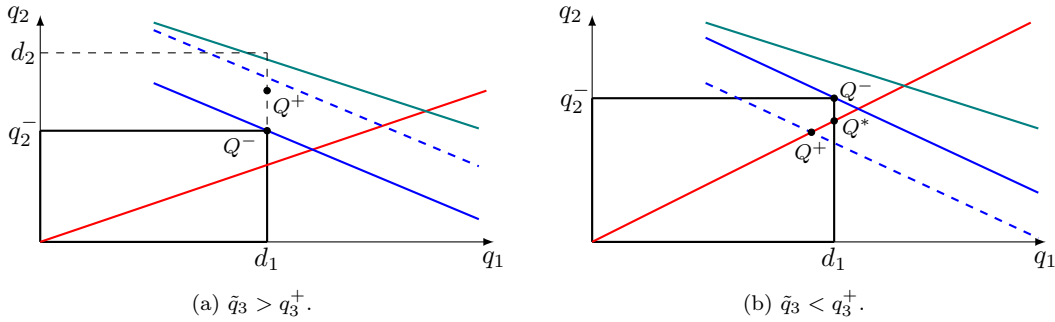


Figure 3.8. Case B3: Wave on road 3.

3.2.3 Case C

This case is verified when the equilibrium is defined by one of the straight lines which maximise the outgoing flux z_3 or z_4 . Without loss of generality, we assume that the priority rule r first intersects the straight line z_3 . We study the effects produced by a single wave sent on each road.

Case C1: Wave on road 1

Let us start with a wave on road 1.

- i) We assume $\tilde{q}_1 > q_1^-$, see Figure 3.9(a). The solution coincides with the equilibrium, thus nothing happens.
- ii) We assume $\tilde{q}_1 < q_1^-$. First of all we analyse the effects of a wave related only to the density ρ , i.e. we send a certain $\tilde{\rho}_1$ on road 1 keeping w_1^- fixed. In Figure 3.9(b) we show a possible solution given by the algorithm. Specifically we have

$$\hat{q}_1^- > \hat{q}_1 = \tilde{q}_1, \quad \hat{q}_2^- \leq \hat{q}_2, \quad \hat{q}_3 = \alpha_{31}\tilde{q}_1 + \alpha_{32}\hat{q}_2, \quad \hat{q}_4 = \alpha_{41}\tilde{q}_1 + \alpha_{42}\hat{q}_2^-.$$

Note that $\hat{q}_3 \geq \alpha_{31}\tilde{q}_1$ and $\hat{q}_4 \geq \alpha_{41}\tilde{q}_1$. Moreover, we observe that if $\hat{q}_2 < q_2^-$ then $\hat{q}_2 - q_2^- < 0$, otherwise we define the angle $\beta = \arctan(|d_2 - q_2^-|/|\tilde{q}_1 - q_1^-|)$ between the segments $|Q^-Q^*|$ and $|\hat{Q}Q^-|$ and we obtain $\hat{q}_2 - q_2^- = |\hat{q}_2 - q_2^-| \leq \tan\beta|\tilde{q}_1 - q_1^-|$. We compute

$$\begin{aligned} * \quad \Gamma(\bar{t}+) &= \hat{q}_1 + \hat{q}_2 = \tilde{q}_1 + \hat{q}_2, & \Gamma(\bar{t}-) &= q_1^- + q_2^- \\ \Rightarrow \Delta\Gamma(\bar{t}) &= (\tilde{q}_1 - q_1^-) + (\hat{q}_2 - q_2^-) < C|\tilde{q}_1 - q_1^-|. \end{aligned}$$

3.2. Estimates for the case of two incoming and two outgoing roads at junctions

$$\begin{aligned}
 * \quad & \bar{h}(\bar{t}+) = \frac{\tilde{q}_1}{p_1}, \quad \bar{h}(\bar{t}-) = \frac{q_1^-}{p_1} \\
 & \Rightarrow \Delta \bar{h}(\bar{t}) = \frac{\tilde{q}_1 - q_1^-}{p_1} < 0. \\
 * \quad & \text{TV}_Q(\bar{t}+) \leq 2|\hat{q}_2 - q_2^-| + |\tilde{q}_1 - q_1^-| \leq 2(|\Delta \Gamma(\bar{t})| + |\tilde{q}_1 - q_1^-|) \\
 & \text{TV}_Q(\bar{t}-) = |\tilde{q}_1 - q_1^-| \\
 & \Rightarrow \Delta \text{TV}_Q(\bar{t}) \leq 2(|\Delta \Gamma(\bar{t})| + |\Delta \bar{h}(\bar{t})|).
 \end{aligned}$$

$$\begin{aligned}
 * \quad & \text{By (3.17) and (3.18) we have} \\
 & |\hat{w}_3 - w_3^+| \leq \frac{\alpha_{32}|w_1^- - w_2^-|}{\tilde{q}_1 q_3^+} (\tilde{q}_1 + d_2) (|\Delta \Gamma(\bar{t})| + |\Delta \bar{h}(\bar{t})|) \\
 & |\hat{w}_4 - w_4^+| \leq \frac{\alpha_{42}|w_1^- - w_2^-|}{\tilde{q}_1 q_4^+} (\tilde{q}_1 + d_2) (|\Delta \Gamma(\bar{t})| + |\Delta \bar{h}(\bar{t})|) \\
 & \Rightarrow \Delta \text{TV}_w(\bar{t}) \leq \left(\frac{\alpha_{32}}{q_3^+} + \frac{\alpha_{42}}{q_4^+} \right) \frac{|w_1^- - w_2^-|}{\tilde{q}_1} (\tilde{q}_1 + d_2) (|\Delta \Gamma(\bar{t})| + |\Delta \bar{h}(\bar{t})|).
 \end{aligned}$$

Next, we analyse the effects of a wave in ρ and w , i.e. we send a couple $(\tilde{\rho}_1, \tilde{w}_1)$ on road 1 such that we still have $\tilde{q}_1 < q_1^-$. The estimates on Γ , \bar{h} and TV_Q do not change, while for TV_w by (3.21) and (3.22) we have

$$\begin{aligned}
 |\hat{w}_3 - w_3^+| & \leq |\tilde{w}_1 - w_1^-| + \frac{\alpha_{32}|w_1^- - w_2^-|}{\tilde{q}_1 q_3^+} (\tilde{q}_1 + d_2) (|\Delta \Gamma(\bar{t})| + |\Delta \bar{h}(\bar{t})|) \\
 |\hat{w}_4 - w_4^+| & \leq |\tilde{w}_1 - w_1^-| + \frac{\alpha_{42}|w_1^- - w_2^-|}{\tilde{q}_1 q_4^+} (\tilde{q}_1 + d_2) (|\Delta \Gamma(\bar{t})| + |\Delta \bar{h}(\bar{t})|) \\
 \text{TV}_w(\bar{t}+) & \leq 2|\tilde{w}_1 - w_1^-| + \left(\frac{\alpha_{32}}{q_3^+} + \frac{\alpha_{42}}{q_4^+} \right) \frac{|w_1^- - w_2^-|}{\tilde{q}_1} (\tilde{q}_1 + d_2) (|\Delta \Gamma(\bar{t})| + |\Delta \bar{h}(\bar{t})|) \\
 \text{TV}_w(\bar{t}-) & = |\tilde{w}_1 - w_1^-| \\
 \Rightarrow \Delta \text{TV}_w(\bar{t}) & \leq |\tilde{w}_1 - w_1^-| + \left(\frac{\alpha_{32}}{q_3^+} + \frac{\alpha_{42}}{q_4^+} \right) \frac{|w_1^- - w_2^-|}{\tilde{q}_1} (\tilde{q}_1 + d_2) (|\Delta \Gamma(\bar{t})| + |\Delta \bar{h}(\bar{t})|).
 \end{aligned}$$

Therefore (P2), (P3) and (P4) hold.

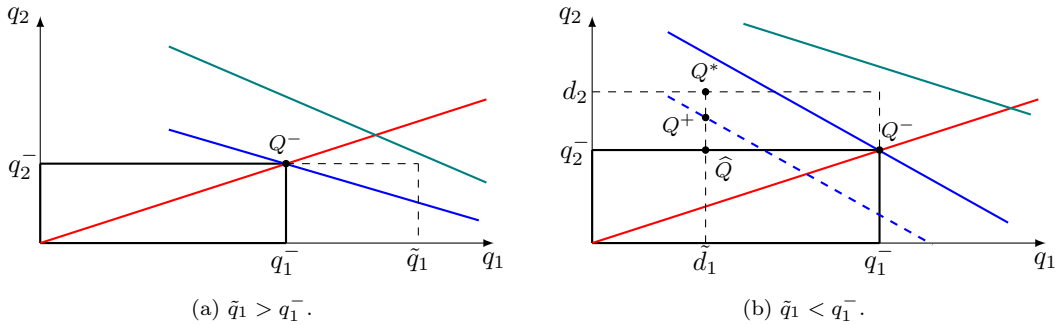


Figure 3.9. Case C1: Wave on road 1.

Case C2: Wave on road 2

Let us consider a wave on road 2.

- i) We assume $\tilde{q}_2 > q_2^-$, see Figure 3.10(a). The solution coincides with the equilibrium, thus nothing happens.
- ii) We assume $\tilde{q}_2 < q_2^-$. First of all we analyse the effects of a wave related only to the density ρ , i.e. we send a certain $\tilde{\rho}_2$ on road 2 keeping w_2^- fixed. In Figure 3.10(b) we show a possible solution given by the algorithm. Specifically we have

$$q_1^- \geq \hat{q}_1, \quad q_2^- \geq \hat{q}_2 = \tilde{q}_2, \quad \hat{q}_3 = \alpha_{31}\hat{q}_1 + \alpha_{32}\tilde{q}_2 \leq q_3^+, \quad \hat{q}_4 = \alpha_{41}\hat{q}_1 + \alpha_{42}\tilde{q}_2 \leq q_4^+.$$

Note that $\hat{q}_3 \geq \alpha_{32}\tilde{q}_2$ and $\hat{q}_4 \geq \alpha_{42}\tilde{q}_2$. We compute

$$\begin{aligned} * \quad \Gamma(\bar{t}+) &= \hat{q}_1 + \hat{q}_2 = \hat{q}_1 + \tilde{q}_2, & \Gamma(\bar{t}-) &= q_1^- + q_2^- \\ \Rightarrow \Delta\Gamma(\bar{t}) &= (\hat{q}_1 - q_1^-) + (\tilde{q}_2 - q_2^-) < 0. \end{aligned}$$

$$\begin{aligned} * \quad \bar{h}(\bar{t}+) &= \frac{\tilde{q}_2}{p_2}, & \bar{h}(\bar{t}-) &= \frac{q_2^-}{p_2} \\ \Rightarrow \Delta\bar{h}(\bar{t}) &= \frac{\tilde{q}_2 - q_2^-}{p_2} < 0. \end{aligned}$$

$$\begin{aligned} * \quad \text{TV}_Q(\bar{t}+) &\leq 2|\hat{q}_1 - q_1^-| + |\tilde{q}_2 - q_2^-| = 2|\Delta\Gamma(\bar{t}) - (\tilde{q}_2 - q_2^-)| + |\tilde{q}_2 - q_2^-| \\ &\leq 2|\Delta\Gamma(\bar{t})| + 3|\tilde{q}_2 - q_2^-| \\ \text{TV}_Q(\bar{t}-) &= |\tilde{q}_2 - q_2^-| \\ \Rightarrow \Delta\text{TV}_Q(\bar{t}) &\leq 2(|\Delta\Gamma(\bar{t})| + |\Delta\bar{h}(\bar{t})|). \end{aligned}$$

* By (3.17) and (3.18) we have

$$\begin{aligned} |\hat{w}_3 - w_3^+| &\leq \frac{\alpha_{31}(q_1^- + \tilde{q}_2)|w_1^- - w_2^-|}{\tilde{q}_2 q_3^+} (|\Delta\Gamma(\bar{t})| + |\Delta\bar{h}(\bar{t})|) \\ |\hat{w}_4 - w_4^+| &\leq \frac{\alpha_{41}(q_1^- + \tilde{q}_2)|w_1^- - w_2^-|}{\tilde{q}_2 q_4^+} (|\Delta\Gamma(\bar{t})| + |\Delta\bar{h}(\bar{t})|) \\ \Rightarrow \Delta\text{TV}_w(\bar{t}) &\leq \left(\frac{\alpha_{31}}{q_3^+} + \frac{\alpha_{41}}{q_4^+} \right) \frac{(q_1^- + \tilde{q}_2)|w_1^- - w_2^-|}{\tilde{q}_2} (|\Delta\Gamma(\bar{t})| + |\Delta\bar{h}(\bar{t})|). \end{aligned}$$

Next, we analyse the effects of a wave in ρ and w , i.e. we send a couple $(\tilde{\rho}_2, \tilde{w}_2)$ on road 2 such that we still have $\tilde{q}_2 < q_2^-$. The estimates on Γ , \bar{h} and TV_Q do not change, while for TV_w by (3.21) and (3.22) we have

$$\begin{aligned} |\hat{w}_3 - w_3^+| &\leq |\tilde{w}_2 - w_2^-| + \frac{\alpha_{31}(q_1^- + \tilde{q}_2)|w_1^- - w_2^-|}{\tilde{q}_2 q_3^+} (|\Delta\Gamma(\bar{t})| + |\Delta\bar{h}(\bar{t})|) \\ |\hat{w}_4 - w_4^+| &\leq |\tilde{w}_2 - w_2^-| + \frac{\alpha_{41}(q_1^- + \tilde{q}_2)|w_1^- - w_2^-|}{\tilde{q}_2 q_4^+} (|\Delta\Gamma(\bar{t})| + |\Delta\bar{h}(\bar{t})|) \\ \text{TV}_w(\bar{t}+) &\leq 2|\tilde{w}_2 - w_2^-| + \left(\frac{\alpha_{31}}{q_3^+} + \frac{\alpha_{41}}{q_4^+} \right) \frac{(q_1^- + \tilde{q}_2)|w_1^- - w_2^-|}{\tilde{q}_2} (|\Delta\Gamma(\bar{t})| + |\Delta\bar{h}(\bar{t})|) \\ \text{TV}_w(\bar{t}-) &= |\tilde{w}_2 - w_2^-| \\ \Rightarrow \Delta\text{TV}_w(\bar{t}) &\leq |\tilde{w}_2 - w_2^-| + \left(\frac{\alpha_{31}}{q_3^+} + \frac{\alpha_{41}}{q_4^+} \right) \frac{(q_1^- + \tilde{q}_2)|w_1^- - w_2^-|}{\tilde{q}_2} (|\Delta\Gamma(\bar{t})| + |\Delta\bar{h}(\bar{t})|). \end{aligned}$$

Therefore (P2), (P3) and (P4) hold.

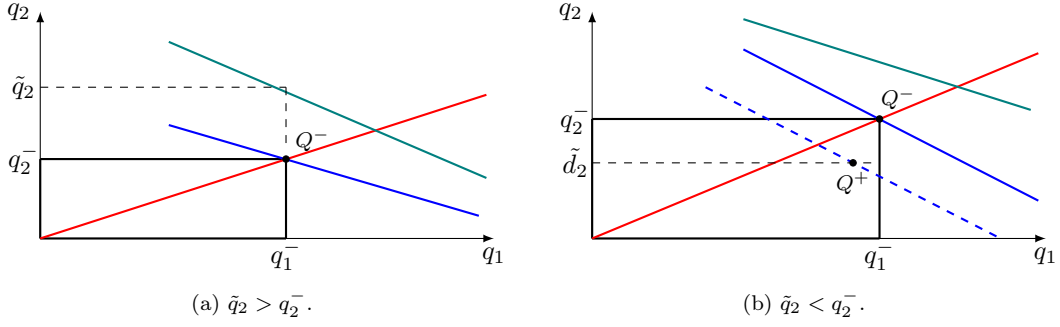


Figure 3.10. Case C2: Wave on road 2.

Case C3: Wave on road 3

We now consider a wave on road 3. The case of a wave on road 4 is analogous

- i) We assume $\tilde{q}_3 > q_3^+$. We send a certain $\tilde{\rho}_3$ on road 3 keeping w_3^+ fixed. In Figure 3.11(a) we show a possible solution given by the algorithm. Specifically we have

$$q_1^- \leq \hat{q}_1, \quad q_2^- \leq \hat{q}_2, \quad \hat{q}_3 = \alpha_{31}\hat{q}_1 + \alpha_{32}\hat{q}_2 \geq q_3^+, \quad \hat{q}_4 = \alpha_{41}\hat{q}_1 + \alpha_{42}\hat{q}_2 \geq q_4^+.$$

Note that if $\tilde{q}_3 \leq p_2 d_1 / p_1$ then this case is similar to the case C3 with $\tilde{q}_3 < q_3^+$. We have $\tilde{q}_3 > p_2 \hat{q}_1 / p_1 = q_3^*$ with $\hat{q}_1 = d_1$. Moreover

$$\begin{aligned} q_1^- &= \frac{p_1 q_3^+}{\alpha_{31} p_1 + \alpha_{32} p_2}, & \hat{q}_1 &= \frac{p_1 q_3^*}{\alpha_{31} p_1 + \alpha_{32} p_2} \\ q_2^- &= \frac{p_2 q_3^+}{\alpha_{31} p_1 + \alpha_{32} p_2}, & \hat{q}_2 &= \frac{\hat{q}_3 - \alpha_{31} \hat{q}_1}{\alpha_{32}} = \frac{\hat{q}_3}{\alpha_{32}} - \frac{\alpha_{31} p_1 q_3^*}{\alpha_{32} (\alpha_{31} p_1 + \alpha_{32} p_2)}. \end{aligned}$$

We compute

$$\begin{aligned} * \quad \Gamma(\bar{t}+) &= \hat{q}_1 + \hat{q}_2, & \Gamma(\bar{t}-) &= q_1^- + q_2^- \\ \Rightarrow \Delta\Gamma(\bar{t}) &= (\hat{q}_1 - q_1^-) + (\hat{q}_2 - q_2^-). \end{aligned}$$

$$\begin{aligned} * \quad \bar{h}(\bar{t}+) &= \frac{\hat{q}_1}{p_1}, & \bar{h}(\bar{t}-) &= \frac{q_1^-}{p_1} \\ \Rightarrow \Delta\bar{h}(\bar{t}) &= \frac{\hat{q}_1 - q_1^-}{p_1} = \frac{p_1 (q_3^* - q_3^+)}{\alpha_{31} p_1 + \alpha_{32} p_2} \leq \frac{p_1}{\alpha_{31} p_1 + \alpha_{32} p_2} |\tilde{q}_3 - q_3^+|. \end{aligned}$$

$$\begin{aligned} * \quad \text{TV}_Q(\bar{t}+) &\leq (1 + \alpha_{31} + \alpha_{41}) |\hat{q}_1 - q_1^-| + (1 + \alpha_{32} + \alpha_{42}) |\hat{q}_2 - q_2^-| \\ &= 2 |\hat{q}_1 - q_1^-| + 2 |\Delta\Gamma(\bar{t}) - (\hat{q}_1 - q_1^-)| \leq 4 (|\Delta\Gamma(\bar{t})| + |\Delta\bar{h}(\bar{t})|) \\ \text{TV}_Q(\bar{t}-) &= |\tilde{q}_3 - q_3^+| \\ \Rightarrow \Delta\text{TV}_Q(\bar{t}) &\leq 4 (|\Delta\Gamma(\bar{t})| + |\Delta\bar{h}(\bar{t})|). \end{aligned}$$

* By (3.17) and (3.18) we have

$$\begin{aligned} |\hat{w}_3 - w_3^+| &\leq \frac{\alpha_{31} \alpha_{32} (d_1 + d_2) |w_1^- - w_2^-|}{(q_3^+)^2} (|\Delta\Gamma| + |\Delta\bar{h}(\bar{t})|) \\ |\hat{w}_4 - w_4^+| &\leq \frac{\alpha_{41} \alpha_{42} (d_1 + d_2) |w_1^- - w_2^-|}{(q_4^+)^2} (|\Delta\Gamma| + |\Delta\bar{h}(\bar{t})|) \\ \Rightarrow \Delta\text{TV}_w(\bar{t}) &\leq \left(\frac{\alpha_{31} \alpha_{32}}{(q_3^+)^2} + \frac{\alpha_{41} \alpha_{42}}{(q_4^+)^2} \right) (d_1 + d_2) |w_1^- - w_2^-| (|\Delta\Gamma| + |\Delta\bar{h}(\bar{t})|). \end{aligned}$$

Therefore (P2) and (P4) hold.

ii) We assume $\tilde{q}_3 < q_3^+$. We send a certain $\tilde{\rho}_3$ on road 3 keeping \hat{w}_3 fixed. In Figure 3.11(b) we show a possible solution given by the algorithm. Specifically we have

$$q_1^- \geq \hat{q}_1, \quad q_2^- \geq \hat{q}_2, \quad \hat{q}_3 = \alpha_{31}\hat{q}_1 + \alpha_{32}\hat{q}_2 = \tilde{q}_3 \leq q_3^+, \quad \hat{q}_4 = \alpha_{41}\hat{q}_1 + \alpha_{42}\hat{q}_2 \leq q_4^+.$$

We refer to the Appendix of [26] for the estimates of $\Delta\Gamma$, $\Delta\bar{h}$ and ΔTV_Q of (P2) and (P3). Moreover, since both for Q^- and Q^+ the solution is found with first step of the algorithm we have

$$\hat{w}_3 = w_3^+ = \frac{\alpha_{31}p_1w_1^- + \alpha_{32}p_2w_2^-}{\alpha_{31}p_1 + \alpha_{32}p_2}$$

$$\hat{w}_4 = w_4^+ = \frac{\alpha_{41}p_1w_1^- + \alpha_{42}p_2w_2^-}{\alpha_{31}p_1 + \alpha_{32}p_2},$$

hence $\Delta\text{TV}_w(\bar{t}) = 0$. Therefore (P2) and (P3) hold.

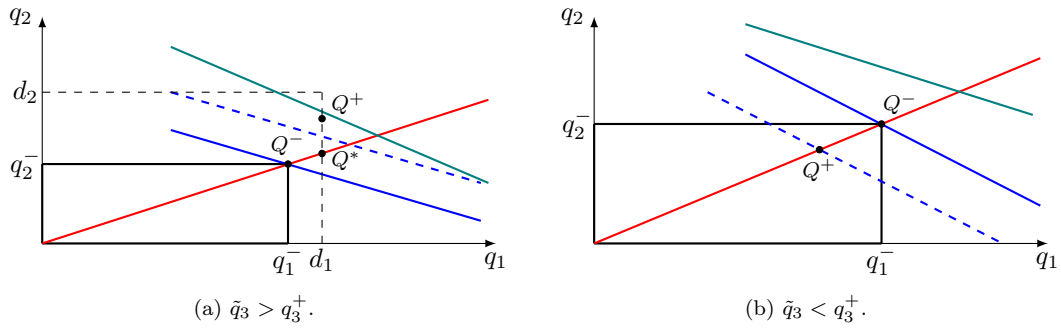


Figure 3.11. Case C3: Wave on road 3.

Chapter 4

Application of GSOM to traffic dynamics on road networks

This chapter deals with the numerical discretisation of GSOM on road networks. First of all, in Section 4.1 we introduce the numerical method on a single road, describing the second order Cell Transmission Model (2CTM), a Godunov type scheme [35] suitable for any model belonging to GSOM. In particular, we focus on the CGARZ model, which will be used to perform all the numerical simulations. As a first test, we compare the CGARZ model with the LWR one, in order to actually show the effects of the variable w on the traffic dynamic. Indeed, we show that, when $w = \text{cost}$ for the CGARZ model, the latter coincides with the LWR model, as observed in Remark 2.1.1. On the other hand, by perturbing the w values we simulate a traffic scenario with different driver behaviours which generate waves also in the density, as shown in Figure 4.3. In Section 4.2 we focus on our algorithm APRSOM for the CGARZ model, and we apply it to the diverge and merge junctions. Finally, we construct a roundabout by combining two merge with two diverge junctions, and we analyse its congestion and decongestion.

4.1 Numerical method for GSOM

This section is devoted to the numerical approximation of GSOM on a single road. First of all, we introduce the notation for numerical schemes for conservation laws, referring to [61, 77, 78] for a more complete and detailed discussion.

Let us consider a system of conservation laws (1.3) on a space interval $[0, L]$ during a time horizon $[0, T]$. We introduce the numerical grid, which we assume to be uniform. Let Δx and Δt be the space and time steps, respectively. The grid is obtained dividing $[0, T]$ into $N_t + 1$ steps of length Δt and $[0, L]$ into N_x cells $[x_{j-1/2}, x_{j+1/2})$, where $x_{j\pm 1/2} = x_j \pm \Delta x/2$ with x_j centre of the cell. The elements of the grid are couples $(x_j, t^n) = (\Delta x/2 + (j-1)\Delta x, n\Delta t)$ for $j = 1, \dots, N_x$ and $n = 0, \dots, N_t$. Since the theory of conservation laws is based on weak solutions, the numerical solution to (1.3), U_j^n , does not represent a point value but is defined as the cell average

$$U_j^n = \frac{1}{\Delta x} \int_{x_{j-1/2}}^{x_{j+1/2}} U(x, t^n) dx$$

for any time t^n .

We now focus on the numerical scheme for GSOM on a single road $[0, L]$ during a time interval $[0, T]$. The Second Order Cell Transmission Model (2CTM), introduced in [30], is a Godunov type scheme [35] and can be used for any model fitting in the framework of GSOM. In particular, we describe how to adapt

the numerical scheme to the CGARZ model, which is used for the numerical tests. The 2CTM scheme is described by the system

$$\begin{aligned}\rho_j^{n+1} &= \rho_j^n - \frac{\Delta t}{\Delta x} (F_{j+1/2}^{\rho,n} - F_{j-1/2}^{\rho,n}) \\ y_j^{n+1} &= y_j^n - \frac{\Delta t}{\Delta x} (F_{j+1/2}^{y,n} - F_{j-1/2}^{y,n}),\end{aligned}$$

where $F_{j\pm 1/2}^{\rho,n}$ and $F_{j\pm 1/2}^{y,n}$ are the incoming and outgoing numerical fluxes, represented in Figure 4.1.

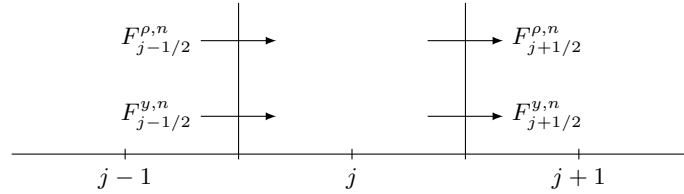


Figure 4.1. Incoming and outgoing fluxes related to cell x_j at time t^n .

In order to define $F_{j-1/2}^{\rho,n}$ and $F_{j-1/2}^{y,n}$, let us consider the two constant left and right states $(\rho^-, w^-) = (\rho_{j-1}^n, w_{j-1}^n)$ and $(\rho^+, w^+) = (\rho_j^n, w_j^n)$ respectively, and compute the solution of the Riemann problem between the two consecutive cells centred in x_{j-1} and x_j ,

$$\begin{cases} \rho_t + (\rho v)_x = 0 \\ y_t + (y v)_x = 0 \\ (\rho_0, y_0) = \begin{cases} (\rho^-, \rho^- w^-) & \text{if } x < x_{j-1/2} \\ (\rho^+, \rho^+ w^+) & \text{if } x \geq x_{j-1/2}. \end{cases} \end{cases}$$

The solution of the Riemann problem is defined by an intermediate state (ρ^*, w^*) separated from the left and right state by a 1-shock or rarefaction wave and a 2-contact discontinuity respectively. The Riemann invariants $w = \text{const.}$ and $V(\rho, w) = \text{const.}$, imply that $w^* = w^-$ and $V(\rho^*, w^*) = \min\{v^+, V(0, w^-)\}$ with $v^+ = V(\rho^+, w^+)$. Note that the minimum between the two velocities is required since vehicles from the left try to adapt their velocity to v^+ , but if $v^+ > V(0, w^-)$ they cannot exceed their maximum speed $V(0, w^-)$. The numerical flux is defined using the supply and demand functions (2.12) and (2.13) as

$$F_{j-1/2}^{\rho,n} = \min\{d(\rho_{j-1}^n, w_{j-1}^n), s(\rho_{j-1/2}^n, w_{j-1/2}^n)\} \quad (4.1)$$

where $(\rho_{j-1/2}^n, w_{j-1/2}^n)$ is the value of the intermediate state described above. In a similar way we define $F_{j+1/2}^{\rho,n}$. Moreover, since $y = \rho w$ the numerical fluxes $F_{j\pm 1/2}^{y,n}$ are such that

$$F_{j-1/2}^{y,n} = w_{j-1/2}^n F_{j-1/2}^{\rho,n} \quad \text{and} \quad F_{j+1/2}^{y,n} = w_j^n F_{j+1/2}^{\rho,n}.$$

We now consider the CGARZ model, see Section 2.1.1. By construction of the flux function for the CGARZ model, the condition $v^+ > V(0, w^-)$ never holds, since $V(0, w) = V^{\max}$ for any w . Hence the intermediate state (ρ^*, w^*) is such that $w^* = w^-$ and $V(\rho^*, w^*) = v^+$. In (4.1) we then get $w_{j-1/2}^n = w_{j-1}^n$ and $\rho_{j-1/2}^n$ such that $V(\rho_{j-1/2}^n, w_{j-1}^n) = V(\rho_j^n, w_j^n)$.

The stability of the scheme is guaranteed by the CFL condition [22]

$$\Delta t \leq \frac{\Delta x}{\Lambda} \quad (4.2)$$

with $\Lambda = \max_{j=1,2} |\lambda_j|$ and λ_j eigenvalues of the Jacobian matrix associated to (2.2). In our case Λ coincides with the maximum velocity V^{\max} .

4.1.1 Comparing CGARZ with LWR

Before introducing the numerical method for GSOM on networks, we compare the CGARZ model with the LWR model. We refer to Section 2.1.1 for the choice of flux and velocity functions. Let us consider a single road $[0, L]$, $L = 2$ km, during the time interval $[0, T]$, $T = 2$ min, fixing the parameters of the CGARZ model as $\rho_f = 19$ veh/km, $\rho^{\max} = 133$ veh/km, $V^{\max} = 120$ km/h, $\Delta x = 0.02$ km, $\Delta t = 0.3$ s, $w_L = f(\rho_f) = 1954$ and $w_R = g(\rho^{\max}/2) = 3990$ with f in (2.7) and g in (2.8), respectively. As a first test we fix the initial density for the two models as

$$\rho_0(x) = \begin{cases} 60 & x \leq L/2 \\ 100 & x > L/2, \end{cases}$$

while the initial w for the CGARZ model is $w_0(x) = w_R$, and it remains constant during the whole simulation. The density at the left boundary is $\rho(0, t) = 60$ veh/km for any time and the right boundary is such that vehicles are free to leave the road. The LWR model is numerically solved with the Godunov scheme [35]. In Figure 4.2 we compare the two numerical solutions, which coincides, as expected by Remark 2.1.1, since $w(x, t) = w_R$ at any time.

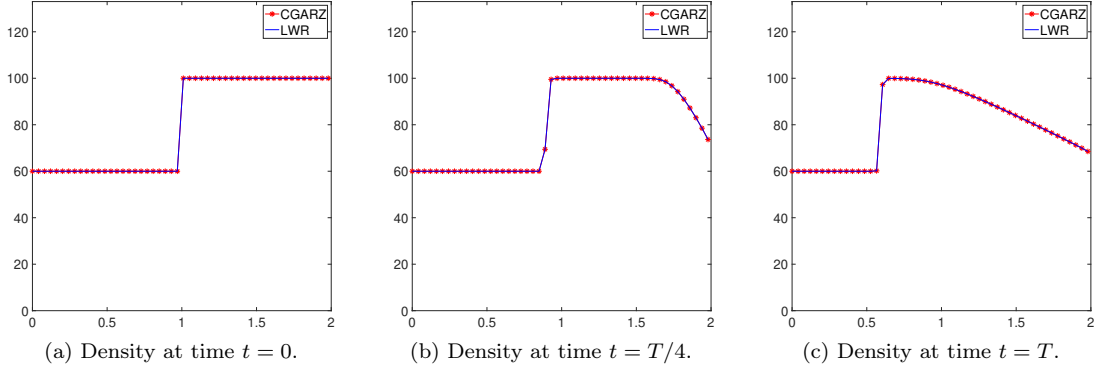


Figure 4.2. Comparison of density of vehicles obtained with the CGARZ model and with the LWR model at different times.

We now show the effects of the variable w of the CGARZ model. The initial density of the two models is fixed as

$$\rho_0(x) = \begin{cases} 60 & x \leq L/2 \\ 100 & x > L/2, \end{cases}$$

while the initial w for the CGARZ model is

$$w_0(x) = \begin{cases} w_R & \text{if } x \notin (L/4, 3L/4) \\ w_R - (w_R - w_L) \sin((4x - L_1)\pi/2L_1) & \text{if } x \in [L/4, 3L/4]. \end{cases} \quad (4.3)$$

In Figure 4.3 we compare the density of the two models on the top, and we show the variation of the w for the CGARZ model on the bottom. As observed in the plots, the variation of w generates a wave on the first half of the road which modifies the density on the whole road. The solution differs from the LWR one, where no perturbation is observed.

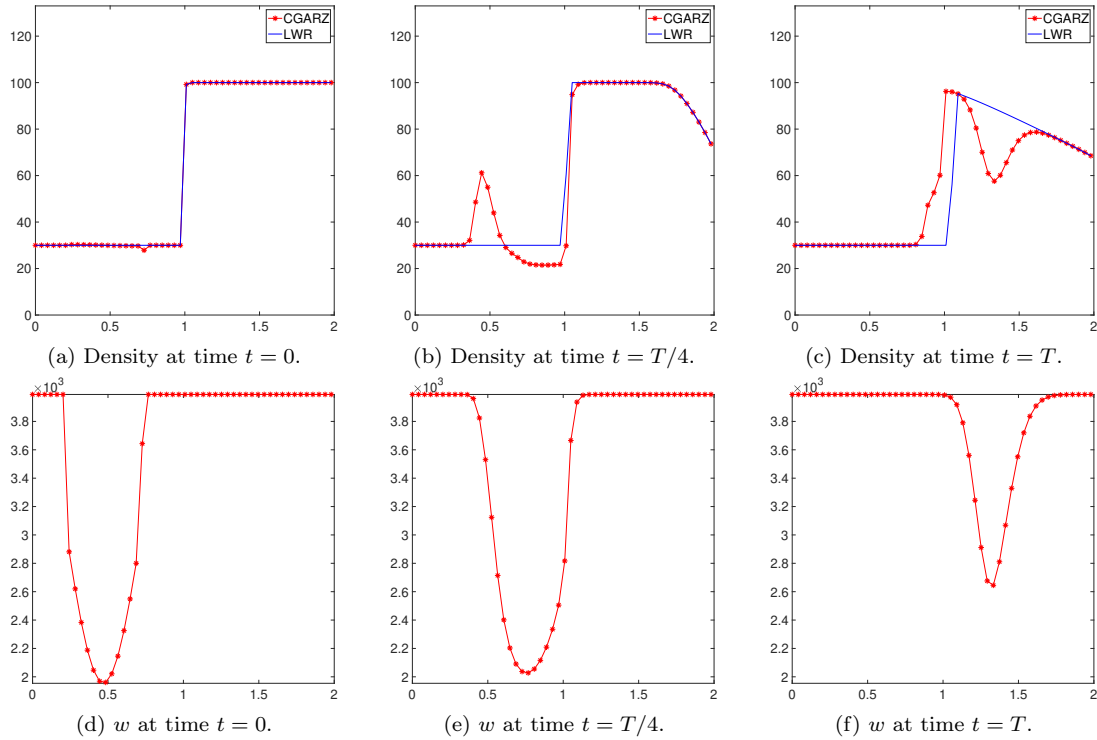


Figure 4.3. Comparison of density of vehicles (top) obtained with the CGARZ model and with the LWR model and variation of w (bottom) at different times.

4.2 The CGARZ model on road networks with APRSOM

We now focus on the road networks. We consider the traffic model (2.2) on a network with roads $I_r = [a_r, b_r]$ during the time interval $[0, T]$. For simplicity, we assume that each road I_r has length L , in order to divide the roads into N_x cells of length Δx , and the time interval into $N_t + 1$ steps of length Δt . We employ the 2CTM scheme to solve the CGARZ model along each road, with suitable boundary conditions on the cells which are at the extremes of the network. We denote by $\rho_{r,j}^n$ and $w_{r,j}^n$ the density and the w value, respectively, of road r in x_j at time t^n . Depending on the type of junction, we use APRSOM to compute the density and the w of vehicles on the junction boundary cells, treated through ghost cells, which are denoted by ρ_r^J and w_r^J respectively, for each road r .

Let us consider for example the $1 \rightarrow 1$ junction. At each iteration in time, the algorithm APRSOM computes the flux \bar{q} in (2.18) that crosses the junction, from which we recover the densities $\rho_1^J = \hat{\rho}_{1, N_x + 1}^n$ and $\rho_2^J = \hat{\rho}_{2, 0}^n$ of the ghost cells, see Figure 4.4. In particular, we observe that the 2CTM scheme corresponds to solving $1 \rightarrow 1$ junctions between the cells of the grid, since the numerical flux $F_{j-1/2}^{n, \rho}$ in (4.1) coincides with the flux \bar{q} crossing the junction.

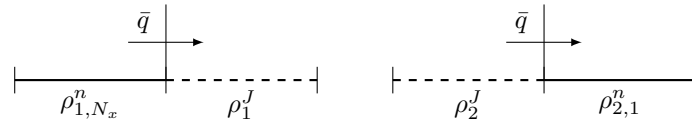


Figure 4.4. Flux crossing the $1 \rightarrow 1$ junction with ghost cells.

We now consider some numerical tests aimed at simulating traffic dynamics on different types of networks. In all the tests which follow we fix these parameters: $\rho_f = 19$ veh/km, $\rho^{\max} = 133$ veh/km, $V^{\max} = 80$ km/h, $L = 200$ m, $T = 1$ min, $\Delta x = 4$ m, $\Delta t = 0.09$ s, $w_L = f(\rho_f) = 1302$ and $w_R = g(\rho^{\max}/2) = 2660$ with f in (2.7) and g in (2.8), respectively. Moreover, we treat the boundaries of the network as follows:

- (B1) Dirichlet condition at the boundary of the roads where vehicles enter the network, i.e. $\rho_{r,1}^n = \bar{\rho}$ for a suitable $\bar{\rho}$.
- (B2) Vehicles freely leave the road at the boundary of the roads from which they exit the network. From a numerical point of view we add an empty ghost cell beside the last one of the road and we then apply the 2CTM scheme to compute ρ_{r,N_x}^n . This approach corresponds to sending the maximum possible flux from the end of the network.

4.2.1 The case of $1 \rightarrow 2$ junction

Let us consider a junction with one incoming road and two outgoing roads, depicted in Figure 4.5. The density of roads 1, 2 and 3 is computed with the 2CTM scheme inside the roads. We solve the Riemann problem at the junction as described in Section 2.3.3 to obtain $\rho_{1,N_x+1}^n = \rho_1^J$, $\rho_{2,0}^n = \rho_2^J$ and $\rho_{3,0}^n = \rho_3^J$, for $n = 0, \dots, N_t$.

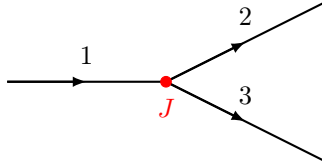


Figure 4.5. Example of $1 \rightarrow 2$ junction.

We simulate two different scenarios, with the initial data shown in Table 4.1. The parameter α which defines how vehicles from road 1 distribute in roads 2 and 3 is $\alpha = 0.7$. Moreover, the left boundary density of road 1 is $\rho_{1,1}^n = 70$ veh/km for any time and the right boundary of road 2 and 3 is such that vehicles are free to leave the road. In Figures 4.6 and 4.7 we show the results of the two tests. The top plots show the density of vehicles at different times, while the bottom plots show their speed. The first difference between the two tests is the initial speed of vehicles: in Figure 4.6(d) road 1 and 2 have same density but different w and thus different speed, while in Figure 4.7(d) the two roads have also the same speed. Moreover, the lower value of w in road 2 generates a small queue on road 1 in the first test, which is not created in the second one. At the end of the simulation, the density of road 3 is enough low to reduce the density of road 1 too. Note that the second test corresponds to what we would obtain with the LWR model on a network.

Test 1			Test 2		
Road r	$\rho_{r,\cdot}^0$ (veh/km)	$w_{r,\cdot}^0$	Road r	$\rho_{r,\cdot}^0$ (veh/km)	$w_{r,\cdot}^0$
1	70	w_R	1	70	w_R
2	70	w_L	2	70	w_R
3	5	$(w_R + w_L)/2$	3	5	w_R

Table 4.1. Initial data for the $1 \rightarrow 2$ junction: data of Test 1 (left) and of Test 2 (right).

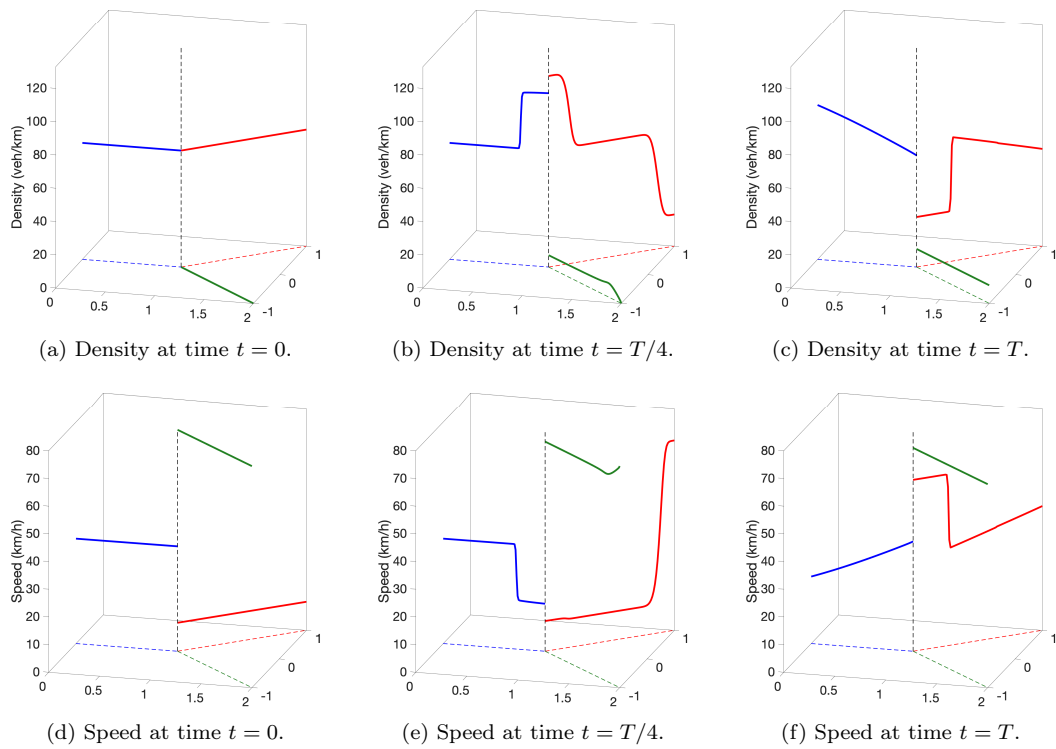


Figure 4.6. Test 1 junction $1 \rightarrow 2$: 3D plot of density (top) and speed (bottom) of vehicles at different times.

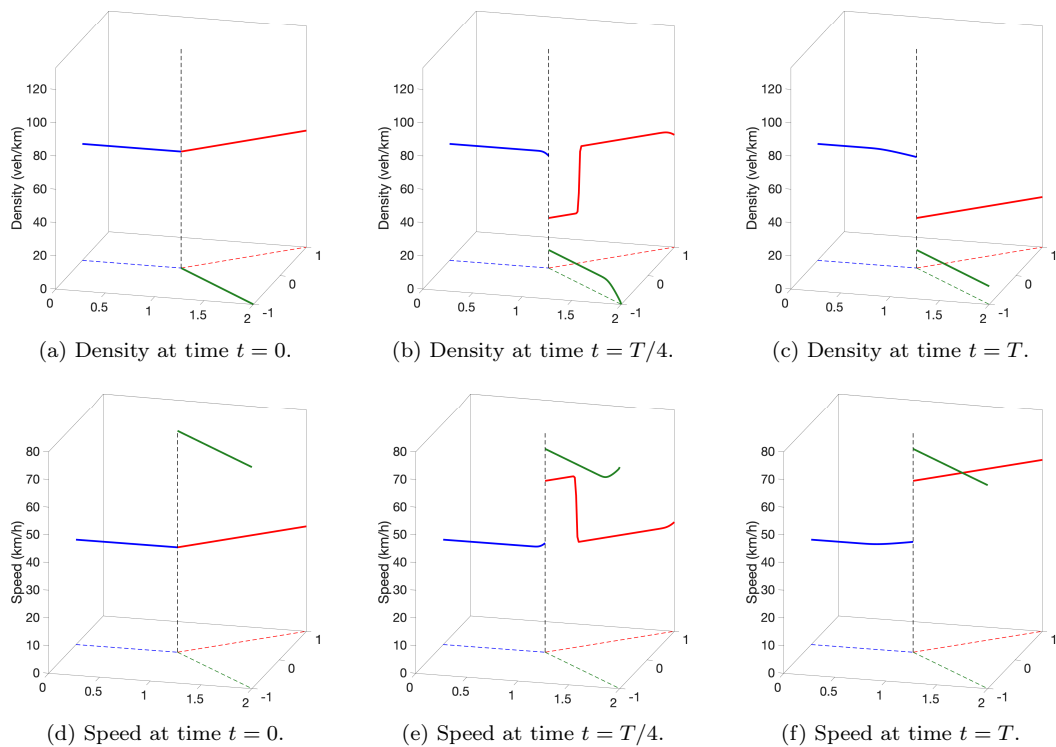


Figure 4.7. Test 2 junction $1 \rightarrow 2$: 3D plot of density (top) and speed (bottom) of vehicles at different times.

4.2.2 The case of $2 \rightarrow 1$ junction

Let us consider a junction with two incoming roads and one outgoing road, depicted in Figure 4.8. The density of roads 1, 2 and 3 is computed with the 2CTM scheme on the cells outside the junction. We solve the Riemann problem at the junction as described in Section 2.3.4 to obtain $\rho_{1,N_x+1}^n = \rho_1^J$, $\rho_{2,N_x+1}^n = \rho_2^J$ and $\rho_{3,0}^n = \rho_3^J$, for $n = 0, \dots, N_t$.

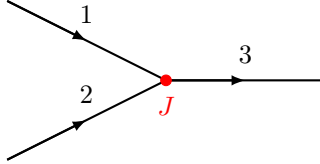


Figure 4.8. Example of $2 \rightarrow 1$ junction.

We simulate two different scenarios with the initial data taken in Table 4.2. The couple (p_1, p_2) which defines the priority rule is fixed as $(0.4, 0.6)$. In road 1 vehicles continues to enter with density equal to 110 veh/km, no more vehicles enter into road 2 and the right boundary of road 3 is such that vehicles are free to leave the road. Finally, we observe that in both the tests we allow vehicles to not respect the priority rule. The test in Figure 4.9 shows that the lower value of w on road 2 is such that vehicles slowly reach the junction, while road 1 fills up quickly. Once road 2 is empty, all vehicles of road 1 move to road 3. The test in Figure 4.10, instead, starts with all the roads with same w . In this case vehicles of both roads 1 and 2 reach quickly the junction and thus road 2 empties more quickly with respect to test 1.

Test 1			Test 2		
Road r	$\rho_{r,\cdot}^0$ (veh/km)	$w_{r,\cdot}^0$	Road r	$\rho_{r,\cdot}^0$ (veh/km)	$w_{r,\cdot}^0$
1	110	w_R	1	110	w_R
2	40	w_L	2	40	w_R
3	10	$(w_R + w_L)/2$	3	10	w_R

Table 4.2. Initial data for the $2 \rightarrow 1$ junction: data of Test 1 (left) and of Test 2 (right).

4.2.3 The case of a roundabout

Let us consider the roundabout depicted in Figure 4.11. We have four junctions: J_1 and J_3 of type $2 \rightarrow 1$, involving roads 1 and 8 in 2, roads 4 and 5 in 6, J_2 and J_4 of type $1 \rightarrow 2$, involving road 2 in 3 and 4, road 6 in 7 and 8. We treat junctions J_1 and J_3 as explained in Section 4.2.2 and junctions J_2 and J_4 as in Section 4.2.1. Vehicles enter into roads 1 and 5 with constant rate and roads 3 and 7 are such that vehicles are free to leave the network. The parameter α , which defines the distribution of vehicles for the $1 \rightarrow 2$ junction is $\alpha = 0.4$. In order to promote the motion on the roundabout, we define the parameters $(p_1, p_2) = (1/3, 2/3)$ for the junction J_1 and $(p_1, p_2) = (2/3, 1/3)$ for the junction J_3 . With this choice of parameters the dynamic favours the flux of vehicles from road 8 more than road 1, and from road 4 more than road 5. We test two scenarios: the congestion and the decongestion of the roundabout.

The first test is the congestion of the roundabout starting from the initial data of the left panel of Table 4.3. With these initial data, vehicles enter into the roundabout with a higher flux from junction J_1 with respect to junction J_3 , where the value of w is lower. Indeed, the speed of vehicles is higher in road 1 than road 5. As a consequence, road 2 fills up more quickly than road 6. The dynamic of road 3, 4, 7 and 8 is quite similar. At the end of the simulation the dynamic reaches a sort of equilibrium.

To better analyse the dynamic of the roundabout, we focus on the four junctions. In Figure 4.13, we show how the boundary values (ρ^J, w^J) vary in time. In Figure 4.13(a) we see that, during the first half

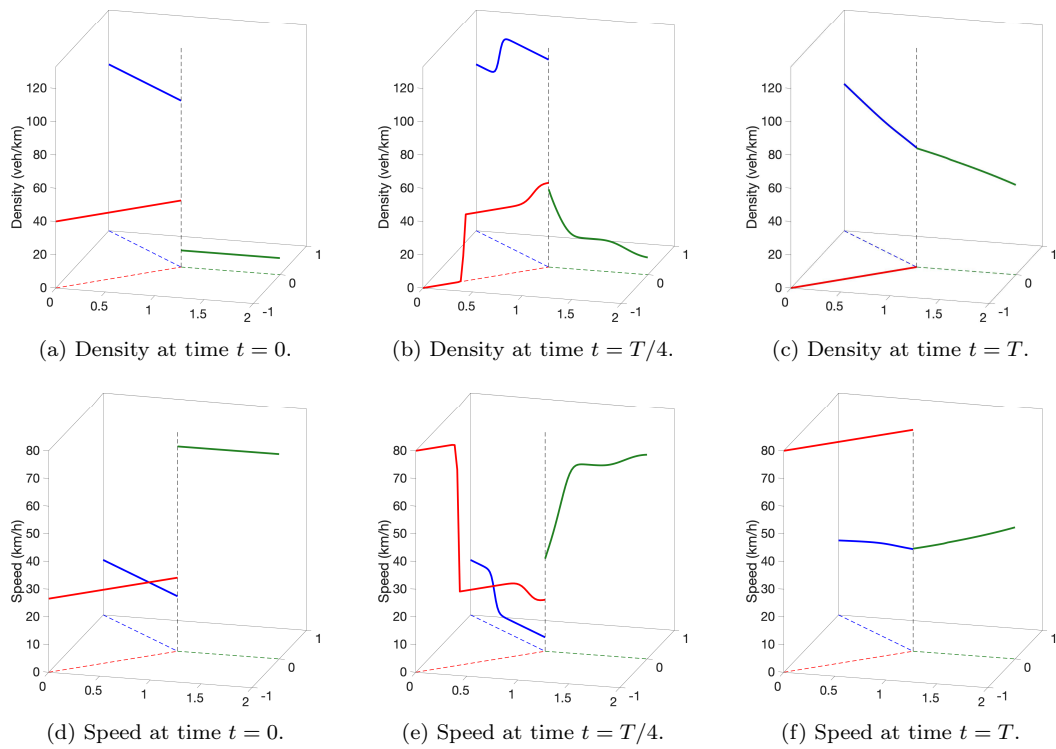


Figure 4.9. Test 1 junction 2 \rightarrow 1: 3D plot of density (top) and speed (bottom) of vehicles at different times.

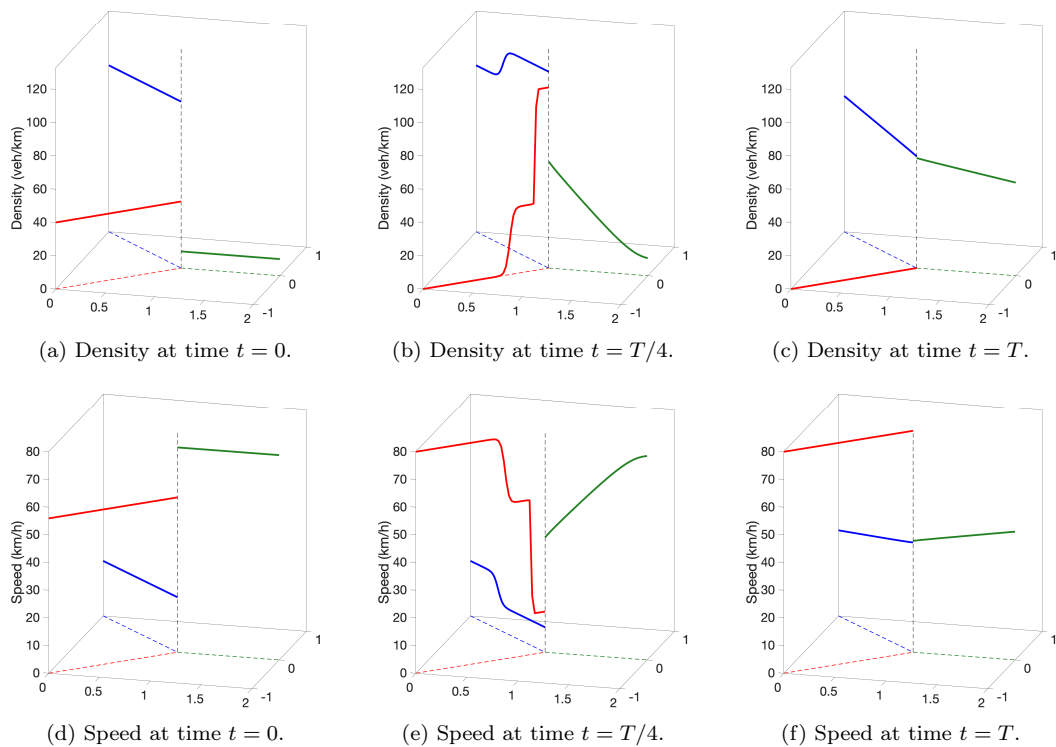


Figure 4.10. Test 2 junction 2 \rightarrow 1: 3D plot of density (top) and speed (bottom) of vehicles at different times.

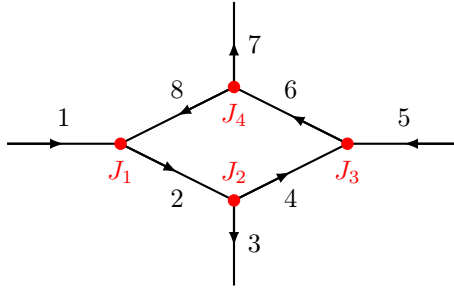


Figure 4.11. Example of roundabout.

Test 1: congestion of roundabout			Test 2: decongestion of roundabout		
Road r	$\rho_{r,\cdot}^0$ (veh/km)	$w_{r,\cdot}^0$	Road r	$\rho_{r,\cdot}^0$ (veh/km)	$w_{r,\cdot}^0$
1	60	w_R	1	0	w_R
2	0	$(w_R + w_L)/2$	2	100	$(w_R + w_L)/2$
3	0	w_R	3	0	w_R
4	0	$(w_R + w_L)/2$	4	50	$(w_R + w_L)/2$
5	50	$(w_R + w_L)/2$	5	0	$(w_R + w_L)/2$
6	0	w_L	6	100	w_L
7	0	w_R	7	50	w_R
8	0	$(w_R + w_L)/2$	8	0	$(w_R + w_L)/2$

Table 4.3. Initial data for the roundabout: data of Test 1 (left) and of Test 2 (right).

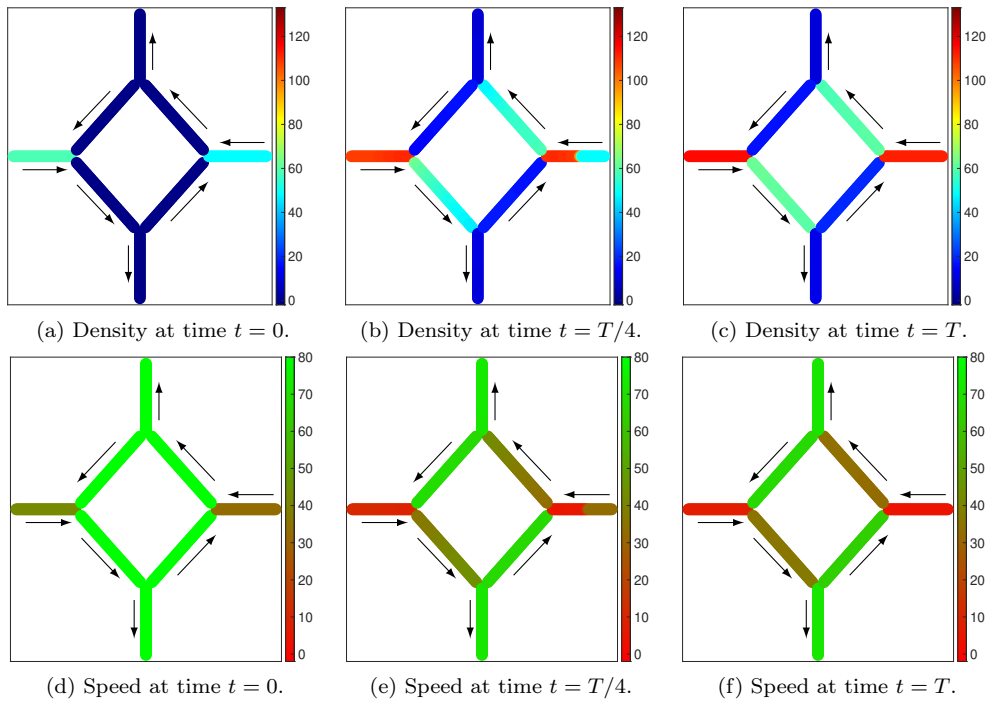


Figure 4.12. Test 1 roundabout: plot of density (top) and speed (bottom) of vehicles at different times with colours scaling with respect to the corresponding colour-bar.

minute of simulation, all vehicles from road 1 enter into road 2 (blue-circle and black-diamond lines), since there are still no vehicles into road 8. Once vehicles of road 8 reach the right boundary, they have the priority with respect to road 1, for our choice of (p_1, p_2) , therefore we see the formation of a queue at the

end of road 1. The dynamic of the density at junction J_3 represented in Figure 4.13(c) is quite similar, but it is slowed down by the lower value of w along the roads, see Figures 4.13(g) and 4.13(e). Such analysis is applied also to junctions J_2 and J_3 , since vehicles reach the right boundary of road 2 faster than road 6, as we can see from the red-circle lines of Figures 4.13(b) and 4.13(d), due to the different values of w . Note that the parameter α is such that there are more vehicles which remain into the roundabout with respect to those which exit from it. Moreover, we observe that for the $1 \rightarrow 2$ junctions (J_2 and J_4) we have same boundary w for all the roads by construction of the solution, except when the roads are empty. Finally, we note that the shape of the black-diamond line of Figure 4.13(g), which corresponds to road 6, is equal to the shape of the three lines of Figure 4.13(h), but with a delay. Indeed, road 6 has incoming property $w = w_6^{J_3}$, and it moves towards the road until it reaches the outgoing boundary and influences the junction J_4 .

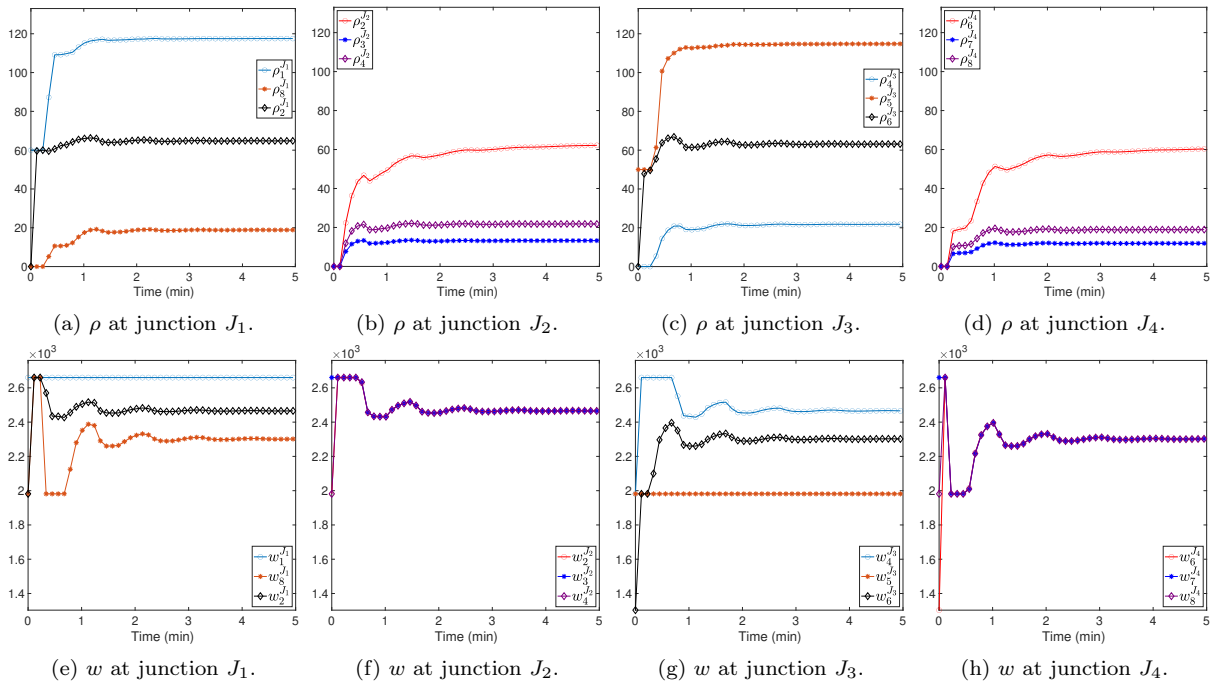


Figure 4.13. Test 1 roundabout: variation in time of the boundary density (top) and w (bottom) at junctions.

In Figure 4.14 we show the decongestion of the roundabout with the initial data given in the right panel of Table 4.3. In Figure 4.14(d), the different values of w define a different initial speed in road 2 and 6, even if they have same density. The emptying process is slowed down in road 6 by its lower w , which is inherited by the other roads of the roundabout during the motion. After 5 minutes of simulation the roads are almost empty. In Figure 4.15 we focus again on the junctions. In Figures 4.15(a) and 4.15(c) the densities $\rho_1^{J_1}$ and $\rho_5^{J_3}$ are null since no vehicles enter into the roads. The dynamic of $\rho_8^{J_1}$ and $\rho_2^{J_1}$ is quite similar, since they both decrease to 0 in time. Analogously for $\rho_4^{J_3}$ and $\rho_6^{J_3}$. The dynamic of junction J_2 is different with respect to junction J_4 . Indeed, $\rho_2^{J_2}$ is initially constant and then it starts to decrease to 0, while $\rho_6^{J_4}$ decreases immediately to a constant value, then it increases for a while, since the road is quite full, and finally it starts to decrease to 0, as the other four roads of the two junctions. Since road 1 and 5 are always empty, in junctions J_1 and J_3 the outgoing roads inherit the property of vehicles w of the other incoming roads, and this explains why $w_2^{J_1} = w_8^{J_1}$ and $w_3^{J_3} = w_4^{J_3}$ during all the simulation. Finally we observe that the dynamic of w at junctions is cyclical, since vehicles counterclockwise move

inside the roundabout until they all exit from it, except for roads 1 and 5, where anything changes.

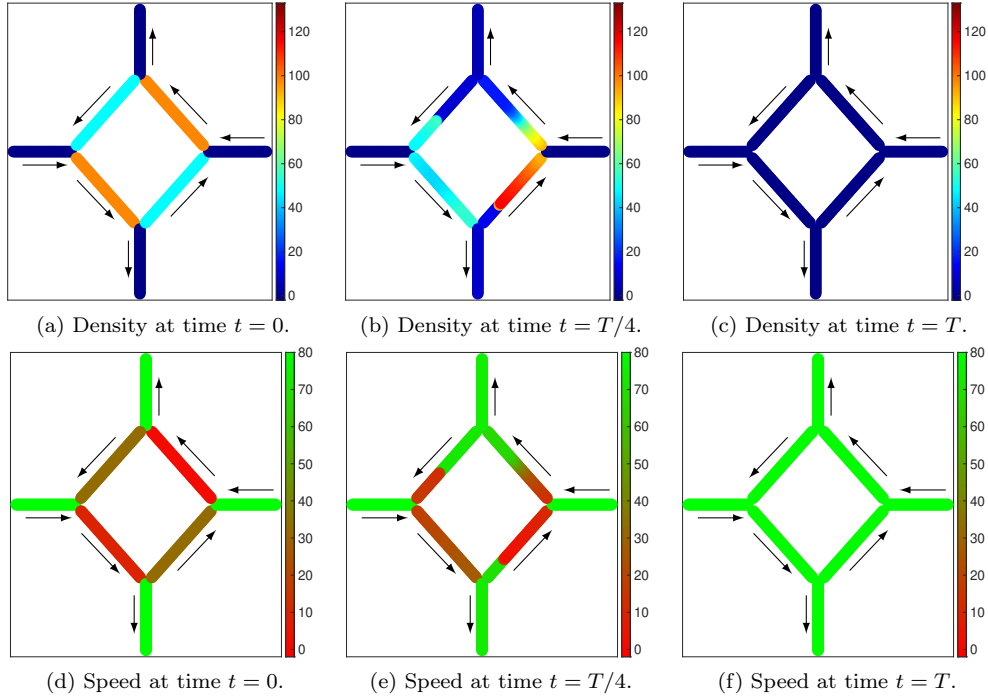


Figure 4.14. Test 2 roundabout: plot of density (top) and speed (bottom) of vehicles at different times with colours scaling with respect to the corresponding color-bar.

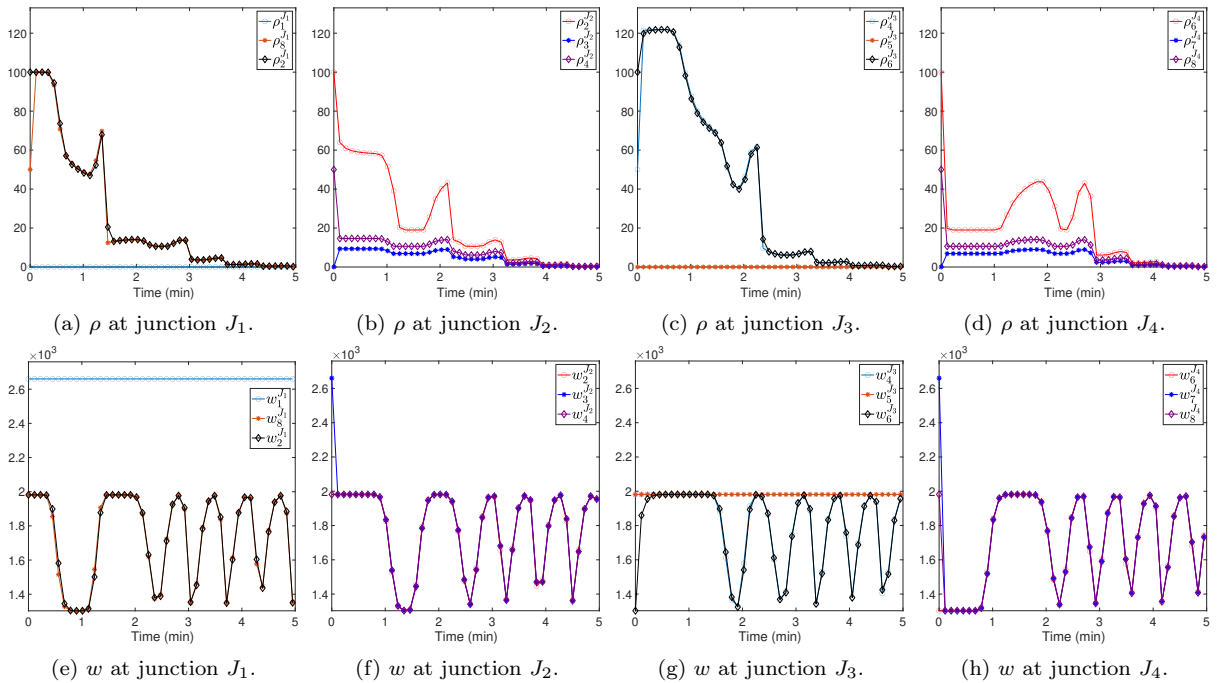


Figure 4.15. Test 2 roundabout: variation in time of the boundary density (top) and w (bottom) at junctions.

Chapter 5

Application of traffic dynamics to pollution

This chapter deals with the environmental impact of vehicular traffic. We propose a procedure consisting in three consecutive steps. First, we estimate the traffic quantities, i.e. density, speed and acceleration of vehicles, through the CGARZ model. Then, we estimate the emission rates of a specific pollutant with a model powered by the traffic quantities. Finally, we analyse the chemical reactions associated to the estimated emissions. In Section 5.1 we deal with traffic variables, describing two formulations for the acceleration. In Section 5.2 we introduce the emission model and we validate it using the NGSIM dataset [88]. Once defined the emission model, we investigate how to reduce the emission rates through actions on the priority rule of APRSOM. To this end, in Section 5.3 we set up an emission minimisation problem which computes the optimal priority rule in terms of emissions produced. Finally, in Section 5.4 we analyse the chemical reactions which lead to ozone production and we perform several numerical tests.

5.1 Approximation of traffic quantities

Let us start with the estimate of traffic quantities. First of all we observe that the great part of emission models makes use of the speed v and acceleration a of vehicles [12]. Hence, the traffic variables we are interested in are the density, the speed and the acceleration of vehicles.

The resolution of system (2.2) gives us the density ρ , the property $w = y/\rho$ and the velocity $v = V(\rho, w)$ of vehicles, therefore we only have to estimate the acceleration. In time-continuous second-order models, the acceleration equation is a second partial differential equation of the general form

$$\frac{Dv(x,t)}{Dt} = (v_t(x,t) + v(x,t)v_x(x,t)) = a(\rho(x,t), v(x,t)),$$

where $\frac{D}{Dt}$ is the total derivative and v is the speed function. This equation implies that the rate of change of the local speed $\frac{Dv(x,t)}{Dt} = (v_t + vv_x)$ in Lagrangian coordinates is equal to an acceleration function $a(x,t) = a(\rho(x,t), v(x,t))$.

For the GSOM we derive the function acceleration by computing the total derivative of $V(\rho, w)$, i.e.

$$a(x,t) = \frac{Dv(x,t)}{Dt} = v_t(x,t) + v(x,t)v_x(x,t),$$

where $v(x,t) = V(\rho(x,t), w(x,t))$, $v_t = V_\rho \rho_t + V_w w_t$, $v_x = V_\rho \rho_x + V_w w_x$. Then,

$$a(x,t) = (\rho_t + v\rho_x) V_\rho + (w_t + vw_x) V_w,$$

and by applying the homogeneous equation in (2.1) for w we get

$$a(x, t) = V_\rho (\rho_t + v\rho_x) = -V_\rho \rho v_x. \quad (5.1)$$

5.1.1 An alternative discrete formula for vehicles acceleration

Here we describe a discrete formulation for the acceleration recovered by average quantities, as an alternative to (5.1). We follow the approach proposed in [64, 93] for the particular case of a single road with n_ℓ lanes. To define the average acceleration of a numerical cell, we distinguish between the *temporal acceleration* and the *spatial-temporal acceleration*. The former refers to the change of the average speed for the vehicles which remain in the same cell i between time t^n and t^{n+1} ,

$$a_j^{tmp}(n) = \frac{v_j^{n+1} - v_j^n}{\Delta t}. \quad (5.2)$$

Let q_j^n be the flux of vehicles which cross the cell j between time t^n and t^{n+1} . The total number of vehicles which remain inside the cell and therefore which are subjected to the temporal acceleration is $c_j^{tmp}(n) = n_\ell \Delta x \rho_j^n - \Delta t q_j^n$. The spatial-temporal acceleration refers to the change of the average speed for the vehicles which move from a cell to the following one. It is defined as

$$a_j^{spt}(n) = \frac{v_{j+1}^{n+1} - v_j^n}{\Delta t}, \quad (5.3)$$

and the total number of vehicles subjected to this acceleration is $c_j^{spt}(n) = \Delta t q_j^n$. By combining the definitions of temporal (5.2) and spatial-temporal (5.3) acceleration, we can introduce the average acceleration of vehicles in cell j at time t^n as

$$a_j^n = \frac{a_j^{tmp}(n)c_j^{tmp}(n) + a_j^{spt}(n)c_j^{spt}(n)}{c_j^{tmp}(n) + c_j^{spt}(n)},$$

which, after some computations, can be rewritten as

$$a_j^n = \frac{v_j^{n+1} - v_j^n}{\Delta t} + v_j^n \frac{v_{j+1}^{n+1} - v_j^{n+1}}{\Delta x}. \quad (5.4)$$

Hereafter we refer to this formulation as discrete acceleration.

5.2 Estimating emissions from traffic quantities

In this section we deal with the emission model, describing the one proposed in [70] appropriate for several air pollutants. Emitted by different sources, primary and secondary air pollutants mainly include: sulphur oxides, nitrogen oxides (NO_x), volatile organic compounds, particulates, free radicals, toxic metals, etc. [83, 91]. In areas with heavy street traffic and high amounts of UV radiation, ozone, NO_x and hydrocarbons are of particular interest. Here we focus on emission models for NO_x.

We use the microscopic emission model proposed in [70]. This model gives the instantaneous emission rate of four pollutant types: carbon dioxide, nitrogen oxides, volatile organic compounds and particulate matter. The emission rate E_i of vehicle i at time t is computed using vehicle's instantaneous speed $v_i(t)$ and acceleration $a_i(t)$

$$E_i(t) = \max\{E_0, f_1 + f_2 v_i(t) + f_3 v_i(t)^2 + f_4 a_i(t) + f_5 a_i(t)^2 + f_6 v_i(t) a_i(t)\}, \quad (5.5)$$

where E_0 is a lower-bound of emission and f_1 to f_6 are emission constants. The parameters are experimentally calibrated using non-linear multiple regression techniques as explained in [70]. Both the

emission lower-bound and coefficients differ according to the type of pollutant and of vehicle (i.e. petrol car, diesel car, truck, etc.). The coefficients associate to the NO_x emission rate depend on whether the vehicle is in acceleration (defined as $a_i(t) \geq -0.5 \text{ m/s}^2$) or deceleration (with $a_i(t) < -0.5 \text{ m/s}^2$) mode. In Table 5.1 we report the NO_x emission coefficients for a petrol car, for which $E_0 = 0$. Note that, in our analysis we assume to have a unique typology of vehicles, i.e. petrol cars. We refer to [70, Table 2] for the coefficients related to the other pollutants and vehicles type.

Vehicle mode	f_1 [g/s]	f_2 [g/m]	f_3 [g s/m ²]	f_4 [g s/m]	f_5 [g s ³ /m ²]	f_6 [g s ² /m ²]
If $a_i(t) \geq -0.5 \text{ m/s}^2$	6.19e-04	8e-05	-4.03e-06	-4.13e-04	3.80e-04	1.77e-04
If $a_i(t) < -0.5 \text{ m/s}^2$	2.17e-04	0	0	0	0	0

Table 5.1. NO_x parameters in emission rate formula (5.5) for a petrol car.

Assuming to have N vehicles in a stretch of road going all at the same speed \bar{v} , with the same acceleration \bar{a} , the emission rate is given by the N contributes of the vehicles, such that

$$E(t) = \sum_{i=1}^N E_i(t) = N \max\{E_0, f_1 + f_2\bar{v}(t) + f_3\bar{v}(t)^2 + f_4\bar{a}(t) + f_5\bar{a}(t)^2 + f_6\bar{v}(t)\bar{a}(t)\}. \quad (5.6)$$

In particular this equation can be used in conjunction with quantities provided by a numerical solution to a macroscopic model such as the CGARZ one.

5.2.1 Validation of the emission model

This section is devoted to the validation of the emission model described above. We compare the NO_x emission rates given by (5.5) computed using the NGSIM dataset [88] with that given by (5.6) computed along numerical solutions to the CGARZ model, with the flux and velocity functions introduced in Section 2.1.1. In other words, the macroscopic CGARZ model is fed by real data only at initial time, then the emission rate is computed along the numerical solution to CGARZ and compared with that resulting from the NGSIM complete dataset, considered as a *ground truth*.

The NGSIM database contains detailed vehicle trajectory data on the interstate I-80 in California, recorded on April 13, 2005. The area under analysis is approximately 500 meters in length and consists of six freeway lanes. Several video cameras recorded vehicles moving through the monitored area, while a specific software has transcribed the vehicle trajectory data from video. The data include the precise location, velocity and acceleration of each vehicle within the study area every 0.1 seconds. The period analysed here refers to three time slots: 4:00 pm – 4:15 pm, 5:00 pm – 5:15 pm and 5:15 pm – 5:30 pm.

First of all we estimate the flow-density and velocity-density relationships from the dataset. We divide the study area into space-time cells $C_i^n = [x_i, x_{i+1}] \times [t^n, t^{n+1}]$ of length $120 \text{ m} \times 4 \text{ s}$. The density in C_i^n is equal to the number of vehicles (denoted by *veh*) which cross the cell during the time interval $[t^n, t^{n+1}]$. The velocity in C_i^n is the mean of all the velocities measured in the cell, and the flux is the product between density and velocity. The relationships between flow and density and between velocity and density have been shown in Figure 2.1. In the two graphs we clearly see two “clouds” in which data are concentrated (except a small number of outliers accounting for less than 3% of points). From the analysis of these data we have estimated a possible set of parameters for the CGARZ model: $V^{\max} = 65 \text{ km/h}$, $\rho_f = 110 \text{ veh/km}$, $\rho^{\max} = 800 \text{ veh/km}$, $\rho_c = \rho^{\max}/2$, $w_L = 5687$ and $w_R = 13000$. Specifically, the parameters V^{\max} and ρ_f are chosen such that the area enclosed between the curves f in (2.7) and g in (2.8) covers more than the 97% of data points of the real data clouds; ρ^{\max} is a property of the road, defined by

$$\rho^{\max} = \frac{\text{Number of lanes}}{\text{Length of vehicles}} = \frac{6}{7.5 \times 10^{-3} \text{ km}},$$

and we set the two extreme w_L and w_R as $w_L = g(\rho_f)$ and $w_R = g(\rho_c)$. The families of curves generated by the data set given above are shown in Figure 5.1.

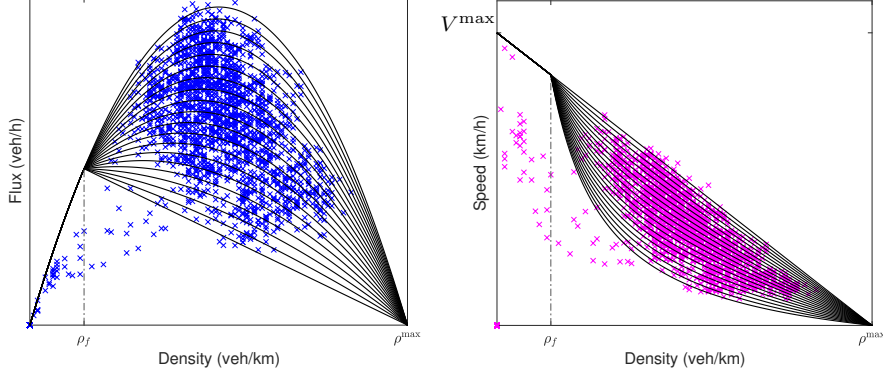


Figure 5.1. Family of flux functions (2.10) (left) and family of velocity functions (2.1.1) (right) for the calibrated parameters.

We now focus on NO_x emissions. The microscopic speed and acceleration included in the NGSIM dataset can be fed directly in (5.5) providing microscopic NO_x emissions produced by each vehicle. Then, we sum the emissions of vehicles along the entire road

$$E^{\text{true}}(t^n) = \sum_{i=1}^{N_{\text{car}}(t^n)} E_i(t^n), \quad (5.7)$$

where $N_{\text{car}}(t^n)$ is the number of vehicles crossing the road at time t^n and $E_i(t^n)$ is the emission rate of vehicle i at time t^n .

The CGARZ model, calibrated with the NSGIM dataset, is used here to estimate the average density and speed of vehicles along the road. Let us consider a numerical grid (x_j, t^n) with $j = 1, \dots, N_x$ and $n = 0, \dots, N_t$ which discretises our domain. The initial density ρ_0 and velocity v_0 are obtained with the kernel density estimation described in Section 1.4. Therefore, given a vehicle location $x_i(t)$ and velocity $v_i(t)$, we define ρ_0 by (1.19) and v_0 by (1.20), using the Gaussian kernel

$$K(x - x_i) = \phi\left(\frac{x - x_i}{h}\right) + \phi\left(\frac{x - (2a - x_i)}{h}\right) + \phi\left(\frac{x - (2b - x_i)}{h}\right) \quad \text{where} \quad \phi(x) = \frac{e^{-x^2/h}}{\sqrt{2\pi h}},$$

h is a distance parameter, a and b are the extremes of the road. In particular, we fix $h = 25$ m. The initial w_0 is defined such that $V(\rho_0(x_j), w_0(x_j)) = v_0(x_j)$, for $j = 1, \dots, N_x$ and then $y_0(x_j) = \rho_0(x_j)w_0(x_j)$. We apply the 2CTM scheme to approximate ρ_j^n , y_j^n and $w_j^n = y_j^n/\rho_j^n$ and we then compute the average emission rate E_j^n of the cell x_j at time t^n , for all j and n , by means of (5.6). Similar to microscopic case (5.7), we sum the emission rates all over the cells

$$E^{\text{mod}}(t^n) = \sum_{j=1}^{N_x} E_j^n, \quad (5.8)$$

where $t^n = n\delta t$ and $\delta t = 0.1$ s is the time frame of the NGSIM dataset.

Two formulas to compute the acceleration were proposed in (5.1) and (5.4). The first is analytical and adapted for macroscopic models, while the second is discrete and can be used to any type of data. In Figure 5.2 we compare the numerical results using the two formulations. The red-solid line of the left plot represents the NO_x emission rate computed using the discrete acceleration on average density

and speed values obtained via kernel density estimation from NGSIM trajectory data. The blue-circles line, instead, represents the ground-truth emission rate (5.7). The results are quite similar, suggesting the accuracy of the discrete acceleration (5.4). Finally, on the right plot of Figure 5.2 we compare the emission rate of NO_x computed with equation (5.6), using the two different definitions of the acceleration function (5.1) and (5.4). The results are almost identical and have same computational cost, and this further certifies the efficiency of the CGARZ model and suggests the use of the analytical formula (5.1) to estimate emissions.

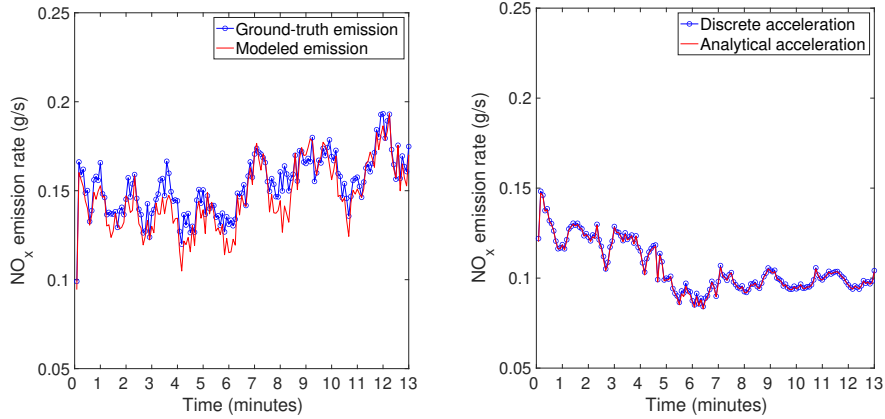


Figure 5.2. Comparison between ground-truth emission rate and modeled emission rate computed using discrete acceleration (5.4) on density and speed via kernel density estimation (left). Comparison of emission rate computed with the discrete (5.4) and analytical (5.1) acceleration (right). Both the results refer to 500 meters of road and 13 minutes of simulation (data from 4:01 pm - 4:14 pm of NGSIM dataset).

We compare now the emission rate along the entire road obtained with (5.7) and (5.8) respectively, for each period of the NGSIM dataset. The results are computed with 13-minute simulations, in which we exclude the first and the last minute of recorded trajectories for corruption of data. In Figure 5.3 we observe that the emission rate obtained with the CGARZ model (5.8) (black-dotted) is lower than the ground-truth emission (5.7) (blue-solid). Improved results are obtained by multiplying the modelled emissions by a proper correction factor (red-circles). Specifically, for each data period j , we have computed a correction factor r_j via linear regression between the ground-truth emission and the modelled one. Moreover, we define the following error

$$\text{Error}(r_j) = \frac{\|E^{\text{true}} - r_j E^{\text{mod}}\|_{L^1}}{\|E^{\text{true}}\|_{L^1}}, \quad j = 1, 2, 3, \quad (5.9)$$

where E^{true} and E^{mod} are vectors whose k -th components are given by (5.7) and (5.8) respectively. Table 5.2 shows the errors (5.9) obtained using the three different correction factors for all the time periods of the NSGIM dataset, where $r_1 = 1.42$, $r_2 = 1.35$ and $r_3 = 1.15$. We observe that the correction factors r_1 , r_2 and r_3 give similar results.

Period	Error(r_1)	Error(r_2)	Error(r_3)
4:01 pm - 4:14 pm	0.1604	0.1666	0.2204
5:01 pm - 5:14 pm	0.0819	0.0842	0.1625
5:16 pm - 5:29 pm	0.2304	0.1773	0.0586

Table 5.2. Errors given by (5.9) for the three slots of the NGSIM dataset and different correction factor $r_1 = 1.42$, $r_2 = 1.35$ and $r_3 = 1.15$.

5.2. Estimating emissions from traffic quantities

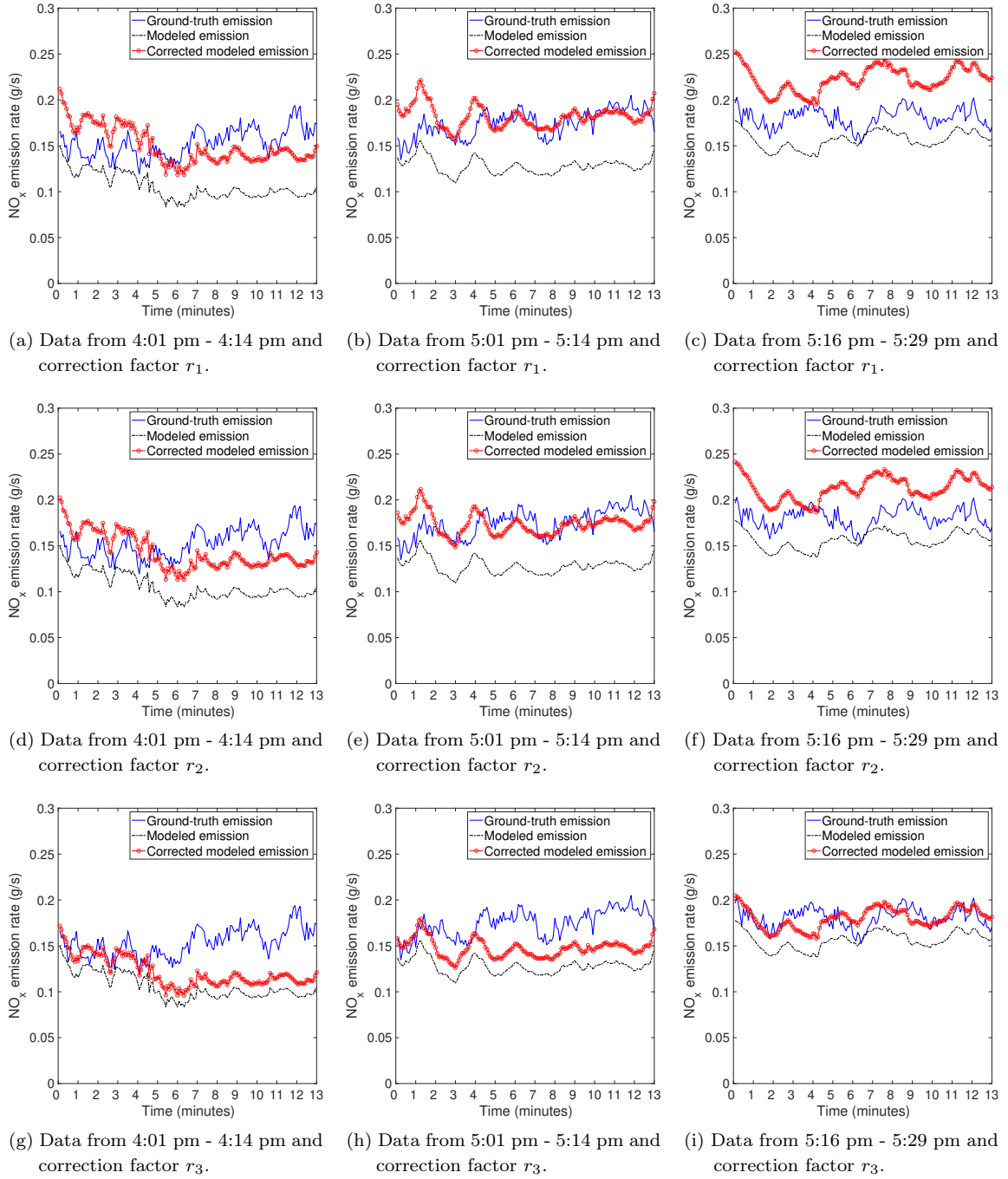


Figure 5.3. Comparison of modeled (black-dotted), modeled with correction factors r_j (red-circles) and ground-truth (blue-solid) emission rates along 500 meters of road during 13 minutes of simulation for the three time periods of the NSGIM dataset. The top row is computed for $r_1 = 1.42$, the central row for $r_2 = 1.35$ and the bottom row for $r_3 = 1.15$.

5.3 Optimising the priority rule to minimise emission rates

In the previous sections we have proposed an emission model fed by traffic quantities approximated through the CGARZ model. Now we investigate how to reduce emissions through actions on our solver APRSOM. In particular, we recall that the latter is based on a priority rule, therefore we introduce an optimisation problem aimed at finding the optimal priority rule which minimises the emissions produced by vehicular traffic. Let us consider the merge junction, see Section 2.3.4. The priority is defined by a vector (p_1, p_2) such that $p_1 + p_2 = 1$. We set up $p = p_2$ and $p_1 = 1 - p$.

Our aim is to define a functional which finds the p value that minimises the emission rates. To this end we introduce

$$\mathcal{F}_E(p) = \sum_{r=1}^{N_r} \int_0^T \int_0^L E_r^p(x, t) dx dt, \quad (5.10)$$

where N_r is the number of roads and $E_r^p(x, t)$ is the emission rate in x at time t derived from the traffic dynamic related to the priority $(1 - p, p)$ and to road r , for each of the roads involved in the junction.

Let us consider the numerical grid introduced in Section 4.1. As described in Sections 4.2, for each road r and cell centred at x_j at time t^n we estimate the traffic quantities $\rho_{r,j}^n, w_{r,j}^n, v_{r,j}^n = V(\rho_{r,j}^n, w_{r,j}^n)$. We then compute $a_{r,j}^n$ as in (5.1) and the emission rates $E_{r,j}^n = E_r(x_j, t^n)$ as in (5.8). We then discretise \mathcal{F}_E as

$$\mathcal{F}_E(p) = \Delta x \Delta t \sum_{r=1}^{N_r} \sum_{n=1}^{N_t} \sum_{j=1}^{N_x} E_r^p(x_j, t^n).$$

As a first test we consider a 20 minutes simulation on a merge junction whose roads are 300 meters in length. We fix the initial densities of the incoming roads as $\rho_1(x, 0) = \rho_2(x, 0) = 15$ veh/km while the outgoing road is empty. The variable w is equal to w_R for all of the three roads, where w_R identifies the curve $Q(\cdot, w_R)$ of model (2.1) sending the highest flux of vehicles. We propose two approaches for APRSOM: one which strictly respects the priority rule and one which changes it to maximise the flux. Since the emission rates are strictly connected to changes in velocity and acceleration, the best case is when the velocity remains constant. The symmetry of the problem combined with the low density of incoming roads suggests that the optimal priority rule should be $(1 - p, p) = (0.5, 0.5)$. Since the maximisation of the flux is obtained with $p = 0.5$, our solver automatically adapts the priority rule to this value and thus we obtain a plateau of optimal p values in terms of emission rates rather than a unique value when respecting the priority rule, see Figure 5.4.

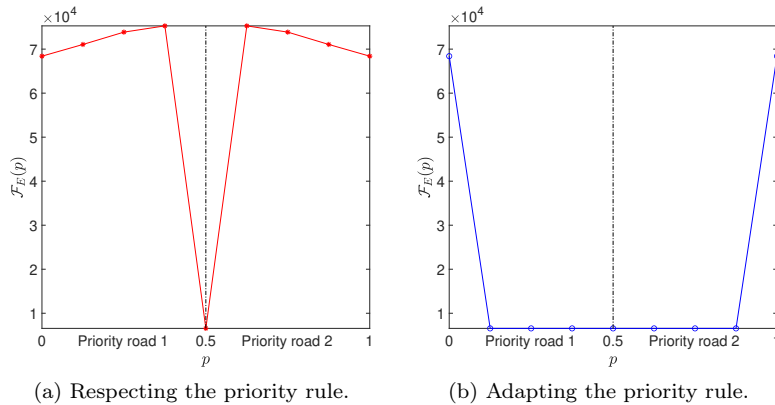


Figure 5.4. $\mathcal{F}_E(p)$ as p changes in $[0, 1]$ respecting or adapting the priority rule when $\rho_1(x, 0) = \rho_2(x, 0) = 15$ veh/km, $\rho_3(x, 0) = 0$ veh/km and $w_1(x, 0) = w_2(x, 0) = w_3(x, 0) = w_R$.

5.3. Optimising the priority rule to minimise emission rates

We now consider a non-symmetric case. We fix the initial densities of the merge junction as $\rho_1(x, 0) = 15$ veh/km, $\rho_2(x, 0) = 30$ veh/km and $\rho_3(x, 0) = 10$ veh/km. The variable w is such that $w_1(x, 0) = w_R$, $w_2(x, 0) = (w_R + w_L)/2$ and $w_3(x, 0) = w_L$, where w_L identifies the curve $Q(\cdot, w_L)$ of model (2.1) sending the least flux of vehicles. We look for the minimisation of the functional $\mathcal{F}_E(p)$ using the MATLAB tool `GlobalSearch`, both respecting and adapting the priority rule. In Figure 5.5 we show the variation of $\mathcal{F}_E(p)$ for p varying in a set of points in $[0, 1]$ chosen by the MATLAB tool. It is immediately clear that the results are not realistic, since the optimal priority rule in both cases is defined by $p = 0$, which acts as a fixed red traffic light on road 2. Again, when we allow the algorithm to not respect the priority we obtain a plateau of p values having same functional $\mathcal{F}_E(p)$ with higher emissions than those produced respecting the priority. Finally, we observe that in both cases the emissions are lower when the priority is on road 1, i.e. where the property is $w = w_R$.

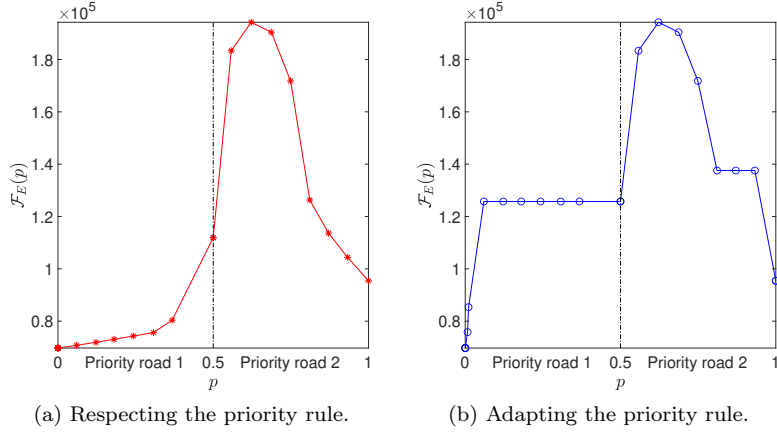


Figure 5.5. $\mathcal{F}_E(p)$ as p changes in $[0, 1]$ respecting or adapting the priority rule when $\rho_1(x, 0) = 15$ veh/km, $\rho_2(x, 0) = 30$ veh/km, $\rho_3(x, 0) = 10$ veh/km, $w_1(x, 0) = w_R$, $w_2(x, 0) = (w_R + w_L)/2$ and $w_3(x, 0) = w_L$.

The solution proposed in the previous example cannot be accepted, since the optimal p value implies that one of the two incoming roads must be completely stopped. Therefore we modify the functional introduced above in order to take into account also the travel time. To this end we introduce

$$\mathcal{F}(p) = \sum_{r=1}^{N_r} \left(\frac{1}{c_1} \int_0^T \int_0^L E_r^p(x, t) dx dt + \frac{1}{c_2} \int_0^T \int_0^L \frac{1}{\mathcal{V}_r^p(x, t)} dx dt \right) = \mathcal{F}_E + \mathcal{F}_T,$$

where $\mathcal{V}_r^p = \max\{V_r^p(x, t), \varepsilon\}$, $\varepsilon > 0$. Such function is used to remove the singularity of V in 0. We discretise \mathcal{F}_E as (5.10) and \mathcal{F}_T as

$$\mathcal{F}_T = \Delta x \Delta t \sum_{r=1}^{N_r} \sum_{n=1}^{N_t} \sum_{j=1}^{N_x} \frac{1}{\mathcal{V}_r^p(x_j, t^n)}$$

and we define the weights c_1 and c_2 as

$$c_1 = \mathcal{F}_E^{\max} = N_x \Delta x N_t \Delta t E^{\max}$$

$$c_2 = \mathcal{F}_T^{\max} = \frac{N_x \Delta x N_t \Delta t}{\varepsilon}$$

where E^{\max} is the maximum emission rate, which depends on ρ^{\max} and V^{\max} . We then have

$$\mathcal{F}(p) = \sum_{r=1}^{N_r} \left(\frac{1}{N_x N_t E^{\max}} \sum_{n=1}^{N_t} \sum_{j=1}^{N_x} E_r^p(x_j, t^n) + \frac{\varepsilon}{N_x N_t} \sum_{n=1}^{N_t} \sum_{j=1}^{N_x} \frac{1}{\mathcal{V}_r^p(x_j, t^n)} \right),$$

and our goal is to solve the minimisation problem

$$\min_{p \in [0,1]} \mathcal{F}(p). \quad (5.11)$$

We now repeat the numeral test proposed in the previous example computing how the functionals \mathcal{F}_T and \mathcal{F} vary as a function of $p \in [0, 1]$, fixing $\varepsilon = 1$. In Figure 5.6 we show the variation of $\mathcal{F}_T(p)$ respecting and adapting the priority rule. We observe that the travel time is highly reduced in the second case, since the solver is free to maximise the flux when possible. The advantage of adding the functional related to the travel time is that we can exclude solutions that are not acceptable in reality. As we can see from Figure 5.7, the optimal p for the functional \mathcal{F} moves close to 0.5 when APRSOM respects the priority rule while it is defined by a plateau of values between approximately 0.15 and 0.5 otherwise. More precisely, the numerical resolution of the minimisation problem (5.11) using the tool `GlobalSearch` found the optimal p equal to 0.48 in the first case and to 0.37 in the second one. Note that 0.37 belongs to the plateau, which consists of global minima.

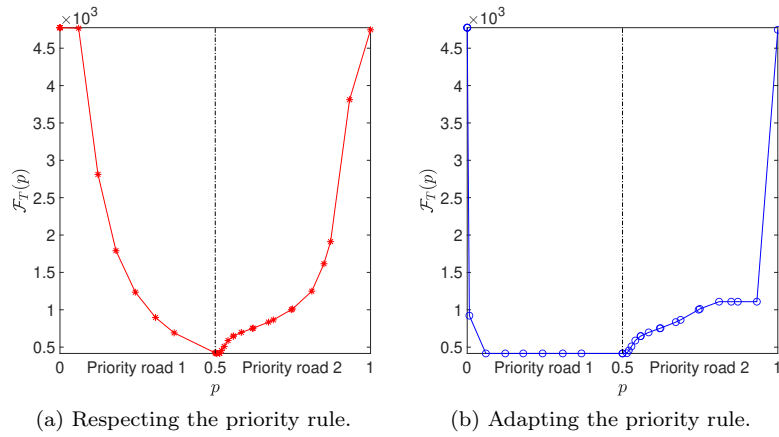


Figure 5.6. $\mathcal{F}_T(p)$ as p changes in $[0, 1]$ respecting or adapting the priority rule when $\rho_1(x, 0) = 15$ veh/km, $\rho_2(x, 0) = 30$ veh/km, $\rho_3(x, 0) = 10$ veh/km, $w_1(x, 0) = w_R$, $w_2(x, 0) = (w_R + w_L)/2$ and $w_3(x, 0) = w_L$.

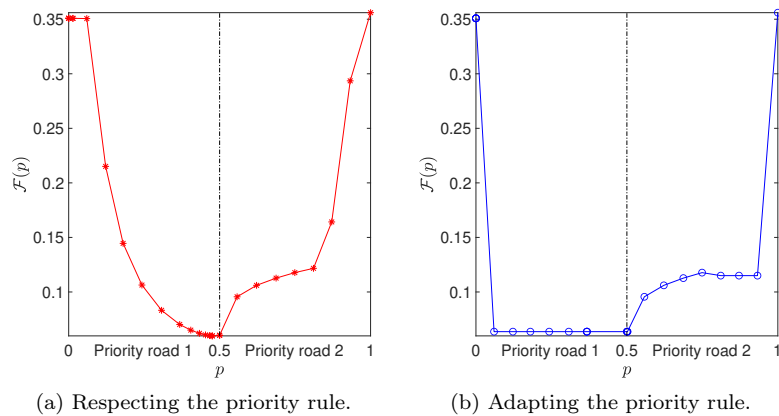


Figure 5.7. $\mathcal{F}(p)$ as p changes in $[0, 1]$ respecting or adapting the priority rule when $\rho_1(x, 0) = 15$ veh/km, $\rho_2(x, 0) = 30$ veh/km, $\rho_3(x, 0) = 10$ veh/km, $w_1(x, 0) = w_R$, $w_2(x, 0) = (w_R + w_L)/2$ and $w_3(x, 0) = w_L$.

To summarise, in the following Algorithm 1 we collect the steps which lead to the computation of the

functional \mathcal{F} for a generic network with N_J junctions. For notational convenience we assume that each junction is of $n \rightarrow m$ type, where n and m are the maximum number of incoming and outgoing roads at the intersections of the network, respectively, and we set to 0 the density into the exceeding roads when necessary. Starting from the initial data $(\rho_r(x, 0), w_r(x, 0))$ of each road of the network, and according to suitable network boundary conditions, for each $n = 1, \dots, N_t$ and $j = 0, \dots, N_x$ we compute the traffic quantities and the emission rates. The time step Δt satisfies the CFL condition (4.2). We recall that $F_{r,j-1/2}^{\rho,n}$ is defined in (4.1), the analytical acceleration in (5.1) and the emission formula in (5.6) with coefficients f_1 to f_6 in Table 5.1. At each junction J we associate a priority rule $P^J = (p_1^J, \dots, p_n^J)$ and our aim is to find the ones which minimise \mathcal{F} . Therefore, defining \mathcal{P}_n as the set of acceptable priority rules such that $\sum_{i=1}^n p_i = 1$, the problem becomes

$$\min_{P^{J_1}, \dots, P^{J_{N_J}} \in \mathcal{P}_n} \mathcal{F}(P^{J_1}, \dots, P^{J_{N_J}}).$$

Note that line 3 of Algorithm 1 computes ρ and w at the junction boundary cells of the incoming and outgoing roads of each junction J_l applying the solver APRSOM with priority rule P^{J_l} .

Algorithm 1: Pseudocode of the procedure to compute the functional \mathcal{F} for a generic network

Input: Traffic state at $t = 0$, steps of the numerical grid N_x and N_t , number of roads N_r and of junctions N_J , priority rules $P^J = (p_1^J, \dots, p_n^J)$ related to each junction J .

Output: Functional \mathcal{F} .

```

1: for  $n = 1$  to  $N_t$  do
2:   for  $l = 1$  to  $N_J$  do
3:      $[(\rho, w)_{\text{inc}(J_l), N_x+1}^n, (\rho, w)_{\text{out}(J_l), 0}^n] = \text{APRSOM}((\rho, w)_{\text{inc}(J_l), N_x}^{n-1}, (\rho, w)_{\text{out}(J_l), 1}^{n-1}, P^{J_l});$ 
4:   for  $r = 1$  to  $N_r$  do
5:     for  $j = 1$  to  $N_x$  do
6:        $\rho_{r,j}^{n+1} = \rho_{r,j}^n - \frac{\Delta t}{\Delta x} (F_{r,j+1/2}^{\rho,n} - F_{r,j-1/2}^{\rho,n});$   $\triangleright F_{r,j\pm 1/2}^{\rho,n}$  defined in (4.1).
7:        $y_{r,j}^{n+1} = y_{r,j}^n - \frac{\Delta t}{\Delta x} (w_{r,j}^n F_{r,j+1/2}^{\rho,n} - w_{r,j-1}^n F_{r,j-1/2}^{\rho,n});$ 
8:        $w_{r,j}^n = \frac{y_{r,j}^n}{\rho_{r,j}^n};$ 
9:        $v_{r,j}^n = V(\rho_{r,j}^n, w_{r,j}^n);$ 
10:       $\mathcal{V}_{r,j}^n = \max(v_{r,j}^n, \varepsilon);$   $\triangleright \varepsilon > 0$ 
11:       $a_{r,j}^n = -V_\rho(\rho_{r,j}^n, w_{r,j}^n) \rho_{r,j}^n \frac{v_{r,j+1}^n - v_{r,j-1}^n}{2\Delta x};$   $\triangleright$  It can be replaced by (5.4).
12:       $E_{r,j}^n = \rho_{r,j}^n \Delta x \max(E_0, f_1 + f_2 v_{r,j}^n + f_3 (v_{r,j}^n)^2 + f_4 a_{r,j}^n + f_5 (a_{r,j}^n)^2 + f_6 v_{r,j}^n a_{r,j}^n);$ 
13:       $\mathcal{F} = \mathcal{F} + \frac{1}{N_x N_t E^{\max}} E_{r,j}^n + \frac{\varepsilon}{N_x N_t} \frac{1}{\mathcal{V}_{r,j}^n};$ 

```

5.3.1 Estimate of NO_x emission rates on a network

In this section we show a numerical test related to the estimate of NO_x emissions on a road network. We perform tests with and without traffic lights, in order to compare the resulting NO_x emission rates. As in Section 4.2.3, let us consider the roundabout depicted in Figure 4.11. The traffic dynamic is given by the simulation of the congestion of the roundabout described in Section 4.2.3 with the initial data in the left panel of Table 4.3, for a time interval of 60 min. We fix the length of each road of the roundabout equal

to 200 m and the maximum velocity equal to 80 km/h. We assume that vehicles enter into road 1 and 5 with density equal to 60 veh/km and 50 veh/km, respectively, and that vehicles are free to leave roads 3 and 7, see (B1) and (B2) at the end of Section 4.2. The parameter α of the $1 \rightarrow 2$ junctions J_2 and J_4 is $\alpha = 0.4$. The priority rules $(p_1^{J_1}, p_2^{J_1})$ and $(p_1^{J_3}, p_2^{J_3})$ of the $2 \rightarrow 1$ junctions J_1 and J_3 are obtained from Algorithm 1 applied to the four junctions of the roundabout, which solve the minimisation problem

$$\min_{P^{J_1}, P^{J_3} \in \mathcal{P}_2} \mathcal{F}(P^{J_1}, P^{J_3}),$$

where \mathcal{P}_2 is the set of acceptable priorities such that $p_1^J + p_2^J = 1$. Note that, for this test, APRSOM does not strictly respects the priority rule. The MATLAB tool `GlobalSearch` applied to Algorithm 1 gives us the optimal parameters $(p_1^{J_1}, p_2^{J_1}) = (0.04, 0.96)$ and $(p_1^{J_3}, p_2^{J_3}) = (0.9, 0.1)$, which are used for the roundabout.

In order to analyse the effects of traffic lights on the network, we compare the emission rates produced by the dynamic of the roundabout with those produced in presence of traffic lights. Indeed, we assume to have a traffic light on junction J_1 and one on junction J_3 , with both the red and the green phase 1 min long. The two traffic lights are opposite, i.e. when the first one is red, the other one is green and vice versa. In this way, every 60 s only vehicles from road 1 or road 8 can enter into road 2 and only vehicles from road 5 or road 4 can enter into road 6. More precisely, every 60 s we change the priority rules from $(1, 0)$ to $(0, 1)$ and vice versa. In Figure 5.8 we compare the NO_x emission rates on the eight roads of the network with and without traffic lights. The differences between the two scenarios are mainly related to roads involved in junctions J_1 and J_3 . The NO_x emission rates of Figures 5.8(a) and 5.8(d) both refer to the initial congestion of the roundabout. The configuration of NO_x emissions shown in Figures 5.8(e) and 5.8(b) is quite different. Indeed, in the case without traffic lights, the NO_x emissions are going to an equilibrium, while the presence of traffic lights causes an higher production of emissions in roads 1 and 4, due to the green traffic lights which allows vehicles to leave the roads and accelerate. Finally, in Figures 5.8(c) and 5.8(f) we show the NO_x emission rates at $t = T$ and we observe that the case without traffic has reached an equilibrium while the NO_x production is higher in presence of traffic lights.

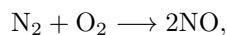
In Figure 5.9 we compare the total emission rates along the roundabout during the 60 minutes of simulation. For each road r we define

$$E_r^{\text{tot}} = \sum_{j,n} E_{r,j}^n, \quad (5.12)$$

and then we sum the emissions of the eight roads, to obtain the total emission. We observe that the total amount of NO_x emissions reaches a constant value without traffic lights and a periodical behaviour in presence of traffic lights. In this case, we obtain a percentage increase of about 37% on the total emissions in presence of traffic lights.

5.4 Chemical reactions

We conclude the chapter with the study of chemical reactions associated to pollutant emissions. Our aim is to exploit the estimates on NO_x emission rates derived from vehicular traffic, described in the previous sections, to analyse the reactions which lead to the ozone (O_3) formation. NO_x gases are usually produced from the reaction among nitrogen and oxygen (O_2) during combustion of fuels, such as hydrocarbons, in air, especially at high temperatures, such as occurs in car engines [69]. They include nitrogen oxide (NO) and nitrogen dioxide (NO_2), the latter is classified as a secondary pollutant. NO is produced according to the following reaction with O_2 and nitrogen (N_2) [65],



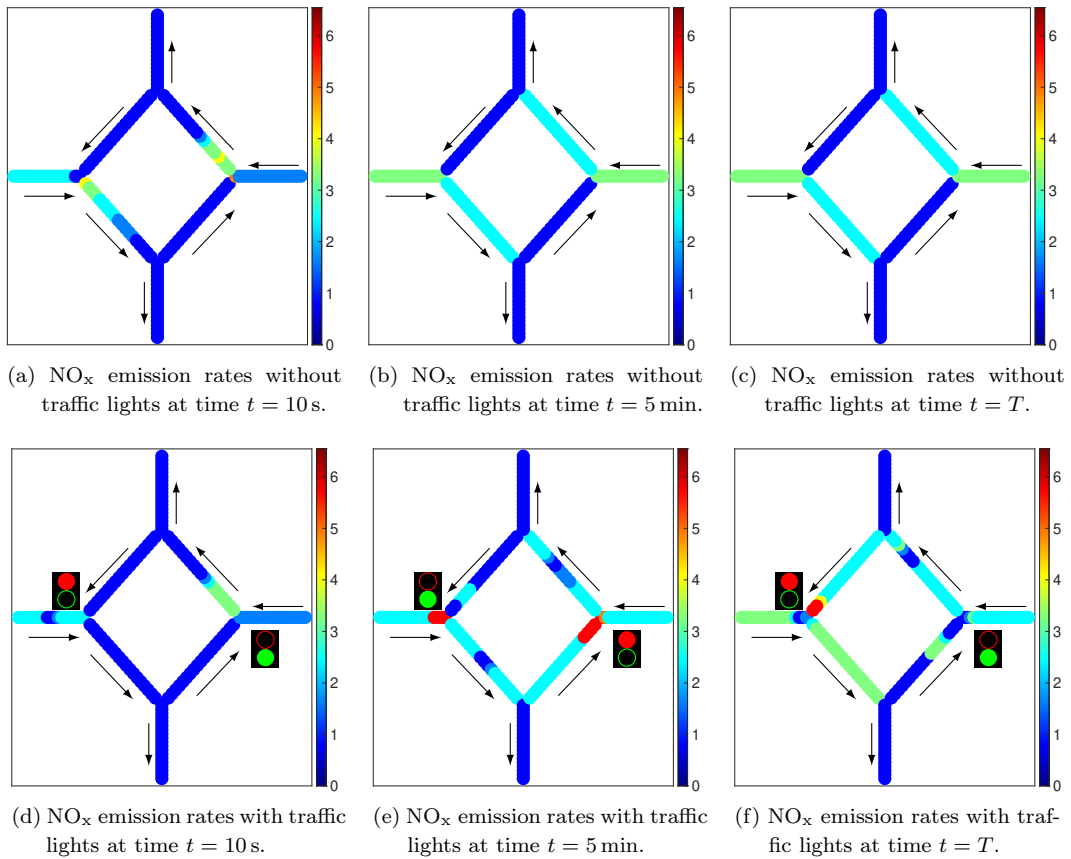


Figure 5.8. NO_x emission rates (g/h) on a roundabout without traffic lights (top) and with traffic lights in J_1 and J_3 (bottom).

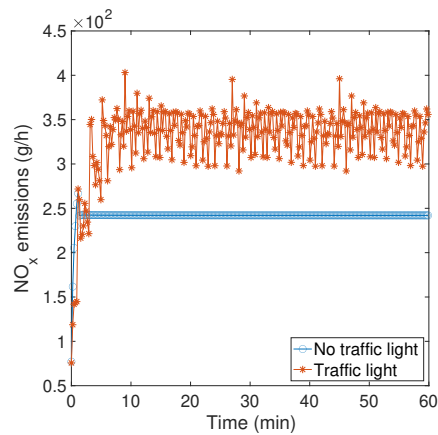
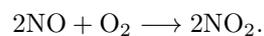


Figure 5.9. Total NO_x emission rates (g/h) along the whole roundabout.

where the rate of the chemical reaction can be increased by raising the temperature. In the combustion mechanism, NO can react with O₂ thus forming NO₂,



NO₂ is a very reactive compound that can be photo-dissociated into atomic oxygen (O), this mechanism is considered one of key steps in the formation of tropospheric ozone [4]. Nitrogen oxides and volatile organic compounds are considered ozone precursors, where traffic is the main source (more than 50% of anthropogenic source). The photolysis of NO₂ is speeded up in warmer conditions and with more UV-light. In the troposphere with strong solar irradiation, NO₂ is a relevant precursor substance for the ozone in photochemical smog and it is due to the following reactions:



where h is Planck's constant, ν its frequency and k_1, k_2 are the reaction rate constants. M is a chemical species, such as O₂ or N₂, that adsorbs the excess of energy generated in reaction (5.14) [65]. Moreover, in presence of NO, O₃ reacts with it and this reaction destroys the ozone and reproduces the NO₂, with kinetic constant k_3 :



This means that the previous reactions do not result net ozone production, because the reactions only recycle O₃ and NO_x. Net ozone production occurs, when other precursors, such as carbon monoxide, methane, non-methane hydrocarbons or certain other organic compounds (volatile organic compounds) are present in the atmosphere and fuel the general pathways to tropospheric O₃ formation. Although it would be interesting to consider the whole ground-level ozone production, here we focus only on the photochemical smog reactions (5.13), (5.14) and (5.15).

For vehicle's emissions, the maximum NO₂ concentration is recorded at medium engine load and low engine speed. At high speed, the NO₂ emissions are reduced to a minimum (in most cases less than 4%) [81]. According to a recent study using British data [18], the fraction of NO₂ in vehicle NO_x emissions (all fuels) increased from around 5-7% in 1996 to 15-16% in 2009. For this reason we will consider in our simulation a NO₂ concentration equal to 15% of NO_x.

We now merge the traffic and emission models with the chemical reactions. Specifically, we estimate the NO_x emission rates produced by the traffic dynamic and then we set up the system of ordinary differential equations associated to the chemical reactions (5.13), (5.14) and (5.15). We assume that the reactions take place in a volume of dimension Δx^3 , during the daily hours and that the chemical specie M in (5.14) is O₂. We add the traffic emissions contribution as a source term for the concentration of NO and NO₂. Hence, we denote the chemical species concentration by $[\cdot] = \left[\frac{\text{weight unit}}{\text{volume unit}} \right]$ and we define the variation of the concentration of NO_x in Δx^3 , at each time t as

$$S_{\text{NO}_x} = \frac{E_{\text{NO}_x}(t)}{\Delta x^3}, \quad (5.16)$$

where the emission rate $E_{\text{NO}_x}(t)$ is given by (5.6).

The final system of equations, given by coupling the three reactions (5.13)-(5.15) and the source term (5.16), becomes

$$\begin{aligned} \frac{d[\text{O}]}{dt} &= -k_2[\text{O}][\text{O}_2]^2 + k_1[\text{NO}_2] \\ \frac{d[\text{O}_2]}{dt} &= -k_2[\text{O}][\text{O}_2]^2 + k_3[\text{O}_3][\text{NO}] \\ \frac{d[\text{O}_3]}{dt} &= k_2[\text{O}][\text{O}_2]^2 - k_3[\text{O}_3][\text{NO}] \\ \frac{d[\text{NO}]}{dt} &= k_1[\text{NO}_2] - k_3[\text{O}_3][\text{NO}] + (1-p)S_{\text{NO}_x} \\ \frac{d[\text{NO}_2]}{dt} &= -k_1[\text{NO}_2] + k_3[\text{O}_3][\text{NO}] + pS_{\text{NO}_x}, \end{aligned} \quad (5.17)$$

where $p = 0.15$ corresponding to 15% of NO_2 derived from the emission rate of NO_x , and the parameters k_1 , k_2 and k_3 , shown in Table 5.3, are estimated according to [49].

k_1	k_2	k_3
0.02 s^{-1}	$6.09 \times 10^{-34} \text{ cm}^6 \text{ molec.}^{-2} \text{ s}^{-1}$	$1.81 \times 10^{-14} \text{ cm}^3 \text{ molec.}^{-1} \text{ s}^{-1}$

Table 5.3. Parameters k_1 , k_2 , and k_3 of system (5.17).

5.4.1 Numerical discretisation of the complete procedure

Here we resume the procedure we propose to estimate the ozone production due to vehicular traffic:

1. Estimate the traffic quantities, i.e. the density and the speed of vehicles with the CGARZ model and the analytical acceleration with (5.1).
2. Estimate the emission rate with (5.6) and the corresponding source term in the chemical reactions per unit of volume given by (5.16).
3. Solve system (5.17) to estimate the chemical species concentration per unit of volume.

We observe that for a more complete description of the effects of traffic on pollution we should also consider the diffusion of pollutant in air, as done for example in [3]. The inclusion of such a description is currently under investigation. We now focus on the numerical discretisation of this procedure on a single road, using the numerical grid introduced in Section 4.1. For each cell centred at x_j and time t^n our aim is to estimate the traffic quantities ρ_j^n , v_j^n , a_j^n , the emission rates E_j^n , the source term s_j^n and the concentration of the five chemical species $\{(\psi_i)_j^n\}_{i=1,\dots,5}$, where $\psi_1(x, t) = [\text{O}]$, $\psi_2(x, t) = [\text{O}_2]$, $\psi_3(x, t) = [\text{O}_3]$, $\psi_4(x, t) = [\text{NO}]$ and $\psi_5(x, t) = [\text{NO}_2]$.

The traffic quantities ρ_j^n and v_j^n are numerically approximated using the 2CTM scheme described in Section 4.1. The acceleration is defined by (5.1) and the emission rates by (5.6). The chemical dynamic is obtained with the resolution of system (5.17), which gives us the concentration of the chemical species. We rewrite the system as

$$\begin{cases} \partial_t \psi_1(x, t) = k_1 \psi_5(x, t) - k_2 \psi_1(x, t) \psi_2^2(x, t) \\ \partial_t \psi_2(x, t) = k_3 \psi_3(x, t) \psi_4(x, t) - k_2 \psi_1(x, t) \psi_2^2(x, t) \\ \partial_t \psi_3(x, t) = k_2 \psi_1(x, t) \psi_2^2(x, t) - k_3 \psi_3(x, t) \psi_4(x, t) \\ \partial_t \psi_4(x, t) = k_1 \psi_5(x, t) - k_3 \psi_3(x, t) \psi_4 + (1 - p)s(x, t) \\ \partial_t \psi_5(x, t) = k_3 \psi_3(x, t) \psi_4(x, t) - k_1 \psi_5(x, t) + ps(x, t), \end{cases} \quad (5.18)$$

with $s(x, t)$ source term defined in (5.16) and $p = 0.15$. System (5.18) in vectorial form is

$$\partial_t \Psi(x, t) = G(\Psi(x, t)) + S(x, t) \quad (5.19)$$

with $\Psi = (\psi_1, \psi_2, \psi_3, \psi_4, \psi_5)$, $S(x, t) = (0, 0, 0, (1 - p)s(x, t), ps(x, t))$ and G represents the chemical reactions. First of all we analyse the stiffness of (5.19), see e.g. [56, Chapter 6], without source term, i.e. $s(x, t) = 0$. Therefore, we consider the linearisation of G in a neighbourhood of the initial data $\Psi^0 = \Psi(x, 0)$. The eigenvalues of the Jacobian of G range in a large interval of values, due to the order of magnitude of chemical species and reaction coefficients k_1 , k_2 and k_3 (see Table 5.3). In particular, we have λ_1 with order of magnitude 10^7 , λ_2 of 10^1 and $\lambda_3 = \lambda_4 = \lambda_5 = 0$. A similar result is obtained adding the source term $s(x, t) \neq 0$. Hence, the problem is stiff and we need to approximate system (5.19) with an adaptive step size method. To this end we solve (5.19) using the Matlab tool `ode23s`, which uses a modified Rosenbrock formula of order 2 and works with an adaptive step size.

5.4.2 Estimate of NO_x emission rates and ozone production on a single road

In this section we describe some numerical tests related to NO_x emissions and ozone production on a single road. Let us consider the CGARZ traffic model on a time horizon $[0, T]$ and on a road with one lane parametrised by $[0, L]$. We fix the maximum speed $V^{\max} = 70$ km/h, maximum density $\rho^{\max} = 133$ veh/km and left boundary condition $\rho(0, t) = 52$ veh/km $\forall t$, while we allow vehicles to leave the road on the right boundary, as explained in (B2) at the end of Section 4.2. The other parameters used in all simulations are $T = 30$ min, $L = 3$ km, $\Delta x = 30$ m, $\Delta t = 1.5$ s, the initial density $\rho_0(x) = 52$ veh/km and the initial property $w_0(x) = w_R$ for $x \leq 2L/3$ and $w_0(x) = w_L$ otherwise, where $w_L = f(\rho_f) = 1140$ and $w_R = g(\rho^{\max}/2) = 2327$, with f in (2.7) and g in (2.8).

Traffic dynamic 1: road without traffic lights

The dynamic is described by an initial shock wave around the middle of the road and a rarefaction wave stemming from the right end of the road. The shock wave propagates backward for approximately the first half of the simulation, when the interaction with the rarefaction wave, and the consequent cancellation, changes the shock speed to positive. In Figure 5.10 we compare the 3D plots of density, speed, acceleration and NO_x emission rates. The four graphs have the same shape, since they depend on the density of vehicles. The acceleration reaches the minimum value along the blue curve shown in the graph, while the maximum value is reached at the beginning of the simulation at the end of the road, when the vehicles leave the road with maximum flux. Finally, the NO_x emission rate has a peak in correspondence of the highest values of acceleration and it is equal to 0 along the curve with the darkest blue.

On the left plot of Figure 5.11 we show data points of speed, acceleration and emission obtained along the numerical test. More precisely, the horizontal and vertical axes denote speed and acceleration, respectively, while the colour gives the NO_x emission value. We observe that the NO_x emission is higher for positive value of the acceleration and at low speed with values of acceleration near to -0.5 m/s², and it decreases with negative acceleration. On the right plot of Figure 5.11 we show the variation in time of the total emission, defined as the sum on the cells of the emission rates, at any time. For this test, the total emission increases until the dynamics is described by the shock wave, and then it starts to decrease.

Traffic dynamic 2: road with traffic lights

Here we test the effect of different traffic light cycles varying the time frame of the red phase. The latter corresponds to a Neumann boundary condition imposing vanishing outflow, while the green phase correspond to Neumann boundary condition allowing all cars to leave the road. We start by showing the solution obtained with a traffic light cycle of 5 minutes with a 2 minutes red phase. In Figure 5.12 we show density, speed, acceleration and NO_x emission rate in space and time. The wave with high density created by the red traffic lights takes about 9 minutes to reach the left boundary of the road. Once it reaches the left boundary of the road we see a periodic behaviour in all the graphs, determined by the traffic lights. The graphs related to density and speed have opposite behaviour: when the density increases the speed decreases and vice versa. Similar to test Traffic dynamic 1, the acceleration reaches the maximum values when the traffic light turns green and the vehicles leave the road. Again, the peaks of NO_x emission rates correspond to the highest acceleration values.

In Figure 5.13 we show on the left the emission rate as a function of speed and acceleration, and on the right the total emission along the road in time. Similar to Figure 5.11, the left graph shows higher emission levels at positive acceleration and at low speed and values of acceleration near to -0.5 m/s². In

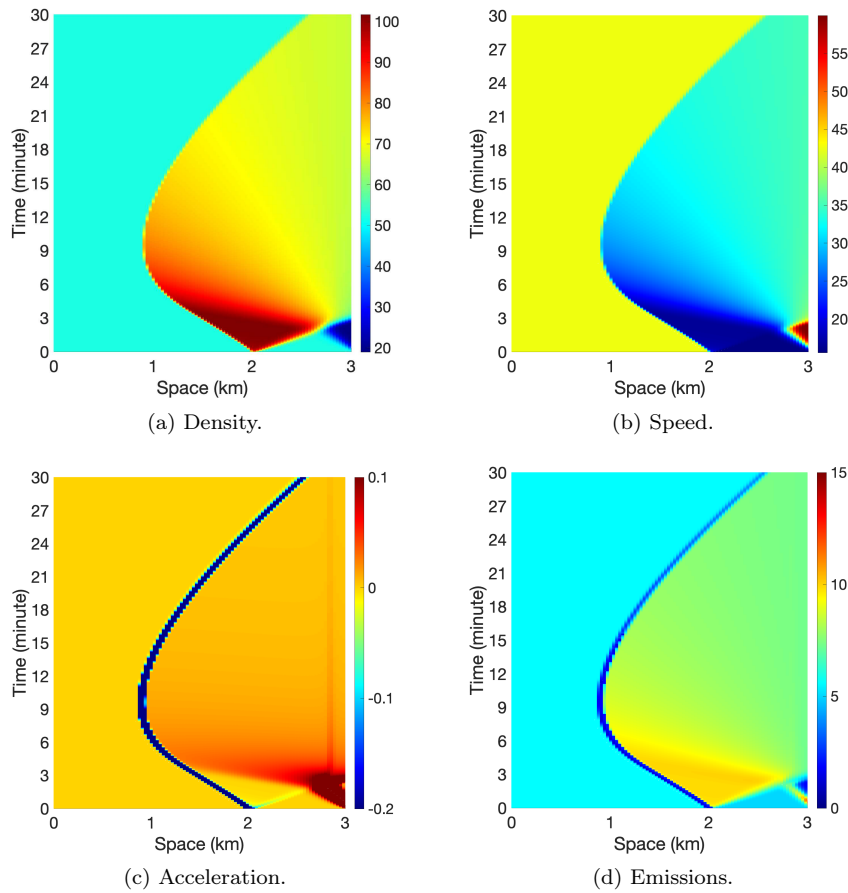


Figure 5.10. **Traffic dynamic 1**: Variation of density (a), speed (b), analytical acceleration (c) and NO_x emissions (d) in space and time.

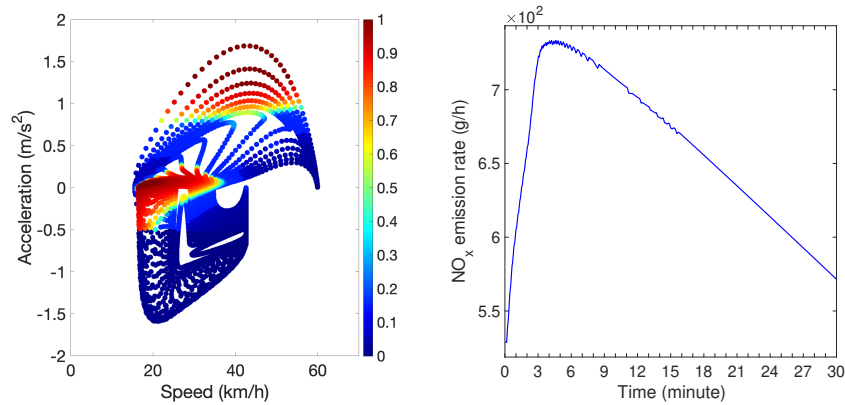


Figure 5.11. **Traffic dynamic 1**: NO_x emission rate as a function of speed and acceleration (left); variation in time of the total emission rate along the entire road (right).

the graph we can see two phases, horizontally divided at height -0.5 . We observe that -0.5 m/s^2 is the acceleration value which distinguishes the two possible choices of the parameters in (5.5), see Table 5.1. The right graph of Figure 5.13 shows the total emission in time, where the red and green lines represent the relative traffic light. We observe that, during the first 10 minutes, the emission rate increases faster

when the traffic light is green and slower when it is red. Then, it reaches a maximum value after which it assumes a periodic behaviour which depends on the traffic light.

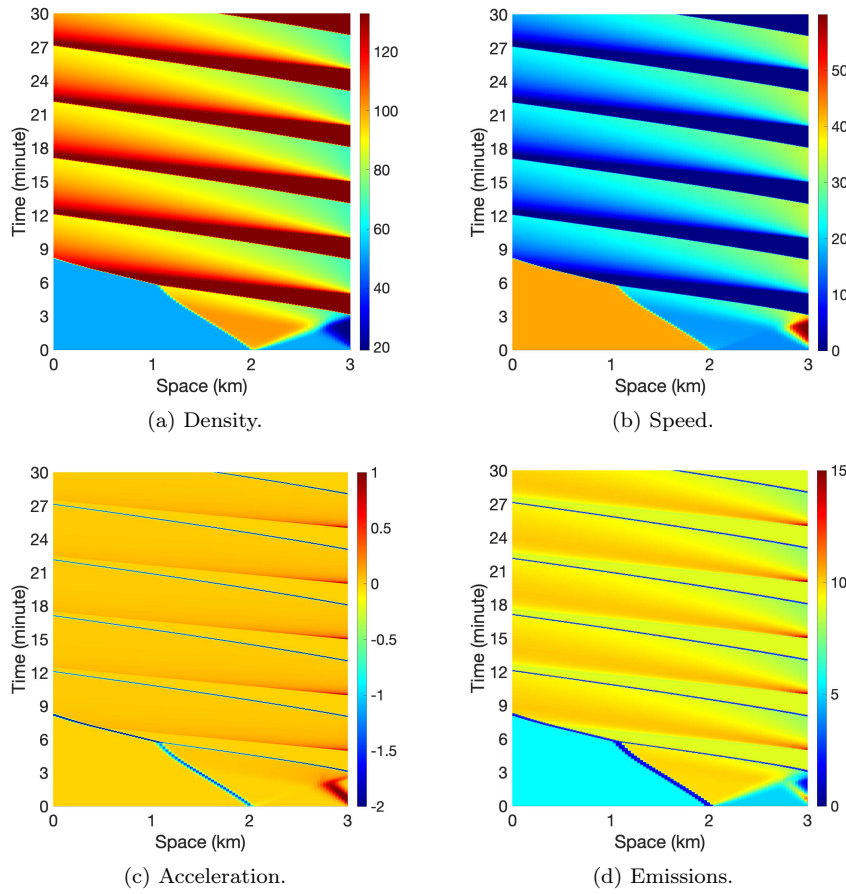


Figure 5.12. **Traffic dynamic 2:** Variation of density (a), speed (b), analytical acceleration (c) and NO_x emissions (d) in space and time.

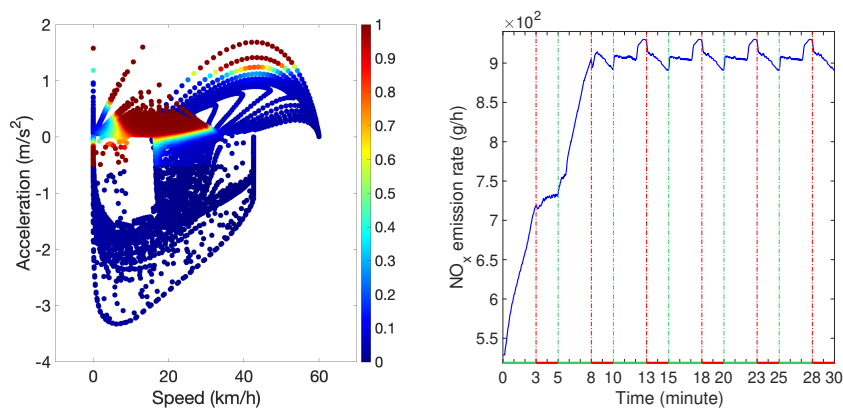


Figure 5.13. **Traffic dynamic 2:** NO_x emission rate as a function of speed and acceleration (left); variation in time of the total emission rate along the entire road (right).

Let now $r = t_g/t_r$ be the ratio between the time t_g of the green phase and the time t_r of the red

phase respectively, and let t_c be the time of the whole traffic light phase, i.e. $t_c = t_g + t_r$. We consider two different test cases: first we fix the ratio r and we vary the time t_c ; then, conversely we fix t_c and we vary r .

Traffic dynamic 2.1: Emissions when the ratio r is constant In Figure 5.14 we show the NO_x emissions obtained with $r = 3/2$ and three different values of traffic light duration in minutes: on the left we set $t_c = 7.5$ and $t_r = 3$, in the centre $t_c = 5$ and $t_r = 2$ and on the right $t_c = 2.5$ and $t_r = 1$. We observe that the maximum value of the NO_x emission rate increases when the frequency of vehicles restarts augments, namely when the time t_r of the red phase is lower.

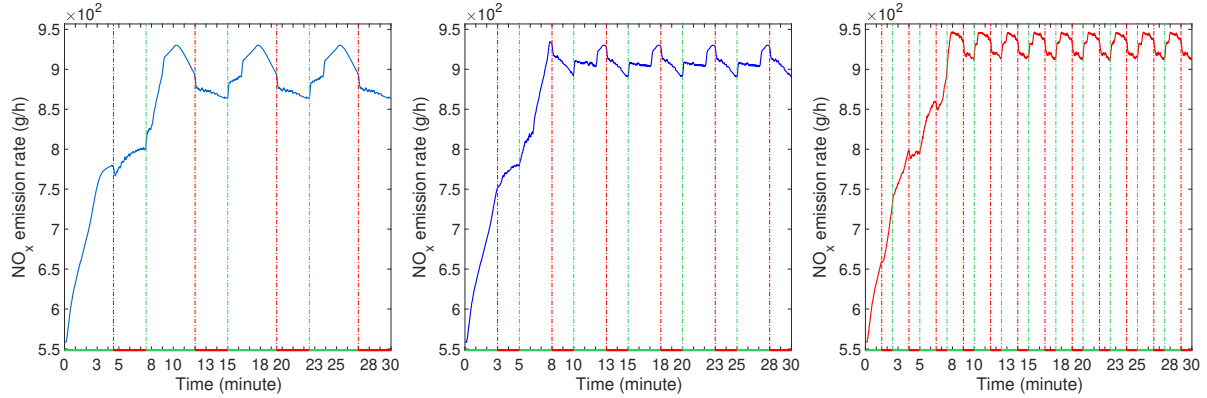


Figure 5.14. **Traffic dynamic 2.1:** Variation in time of the total NO_x emission rate along the entire road with $r = 3/2$ and varying the traffic light duration t_c in minutes: $t_c = 7.5$ with $t_r = 3$ (left); $t_c = 5$ with $t_r = 2$ (centre); $t_c = 2.5$ with $t_r = 1$ (right).

Traffic dynamic 2.2: Emissions when the traffic light duration t_c is constant In Figure 5.15 we show how the NO_x emissions vary with different ratio r . Specifically, we plot NO_x total emissions (defined as the sum on the cells of the emission rates, at any time) for one hour of simulation with $r = \{4, 3/2, 2/3\}$ which is equivalent to assume $(t_g, t_r) = (4, 1)$, $(t_g, t_r) = (3, 2)$, $(t_g, t_r) = (2, 3)$ in minutes, respectively. We observe that until $t_r \leq t_g$ (solid line and line with circle) the maximum of the emission rate increases when t_r grows, since there are more vehicle restarts; while it decreases with $t_r > t_g$ (line with stars) when there are less vehicles restarts and more phases of stopped traffic.

To sum up, the two last examples developed in **Traffic dynamic 2.1** and **Traffic dynamic 2.2**, suggest that the emissions grow with the increase of vehicles restarts. In particular, we observe from Figure 5.14 that the length of the traffic light cycle t_c has a high influence on emissions, while Figure 5.15 shows that the ratio r between red-light and green-light has a less effect on the asymptotic emission values.

Production of ozone

In this section we are interested in estimating the concentration of ozone along the entire road by means of the system (5.17). The reaction rate parameters k_1 , k_2 and k_3 are listed in Table 5.3. For each cell x_j , $j = 1, \dots, N_x$, we set the initial concentrations $\{\psi_i(x_j, 0)\}_{i=1, \dots, 5}$ as $\psi_1(x_j, 0) = \psi_3(x_j, 0) = 0$, $\psi_2(x_j, 0) = 5.02 \times 10^{18}$ molec./cm³ and, according to Section 5.4 and relation (5.16), for NO and NO_2 we have

$$\psi_4(x_j, 0) = (1 - p) \frac{E_{\text{NO}_x}(0)}{\Delta x^3}, \quad \psi_5(x_j, 0) = p \frac{E_{\text{NO}_x}(0)}{\Delta x^3} \quad \text{with } p = 0.15.$$

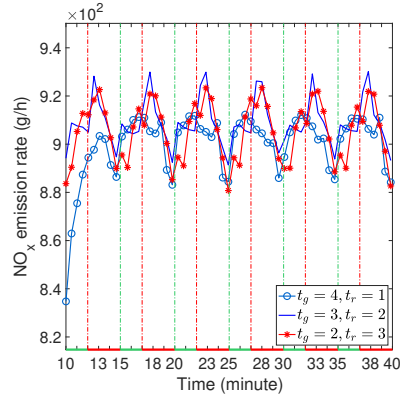


Figure 5.15. **Traffic dynamic 2.2:** Variation in time of the total emission rate along the entire road with $t_c = 5$ min and varying the ratio r .

For each time step n and for each x_j , we compute the source term due to traffic by using the emission rate given in **Traffic dynamic 1** and **Traffic dynamic 2**.

In Figure 5.16, we show the O_3 evolution along the entire road, during half an hour of simulation. We observe a behaviour amenable to the traffic variables dynamics given in Figures 5.10 – 5.12. To obtain now the total concentration of all the chemical species along the entire road, for every time t^n we sum the results on all the cells. In Figure 5.17 we show the variation in time of the concentration of O_3 and O_2 . We observe that the ozone concentration has a huge growth (**Traffic dynamic 1** - blue-solid line), which is further amplified by the presence of the traffic light (**Traffic dynamic 2** - red-circles line). On the other hand, the oxygen concentration is almost constant in both the cases, with moderated dependence on traffic light.

To further investigate the impact of the traffic light on all the chemical species concentration, we solve our system starting from the NO_x emission rates computed in **Traffic dynamic 2.1** in which we fix the ratio r constant. Thus, we compute the total amount of O_3 , NO , NO_2 and O , obtained during the whole simulation along the entire road. Then, we measure the variation of each concentration with respect to the one obtained in the test case without traffic light **Traffic dynamic 1**. The results in Table 5.4 show that all the concentrations increase coherently with the behaviour of the NO_x source term, see Figure 5.14. So, we can conclude that the duration of traffic cycles affects all the chemical species production more than the ratio between green and red phase.

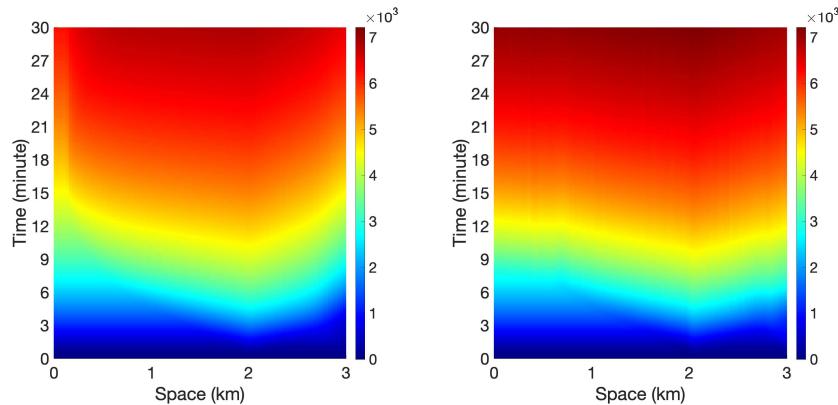


Figure 5.16. O_3 evolution along the entire road, for half an hour of simulation, in the case of dynamics without (left) and with (right) traffic light.

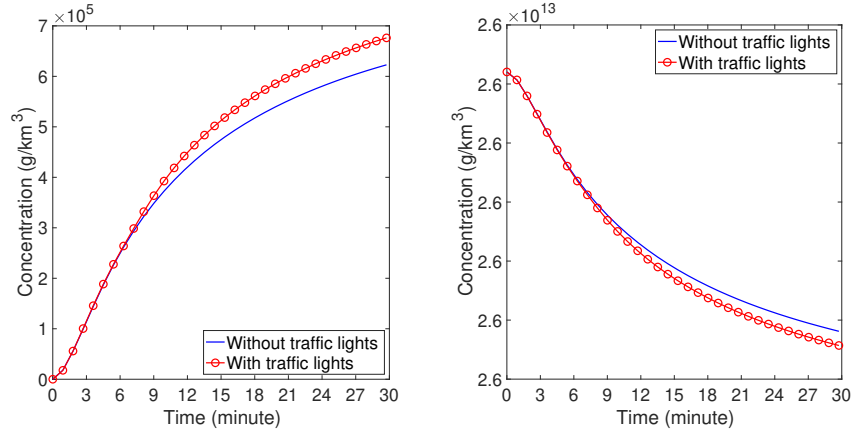


Figure 5.17. Variation in time of the total concentration of O_3 (left) and O_2 (right), in the case of dynamics with (red-circles) and without (blue-solid) traffic light.

$t_c = t_r + t_g$	(3 + 4.5) min	(2 + 3) min	(1 + 1.5) min
O_3	2.95e+07	3.54e+07	3.91e+07
NO	1.09e+09	1.28e+09	1.43e+09
NO_2	1.55e+08	1.81e+08	2.02e+08
O	7.00e+01	8.21e+01	9.13e+01

Table 5.4. Variation of the total amount of O_3 , NO, NO_2 and O concentration (g/km^3) computed with three different traffic light duration ([Traffic dynamic 2.1](#)) with respect the total amount of concentrations without traffic light ([Traffic dynamic 1](#)).

Chapter 6

A two-dimensional multi-class traffic model

In this chapter, we study of a two-dimensional multi-class traffic model on a single road, treated in the paper [11]. The model presented here aims at exploiting all the information collected in a dataset of real trajectory data [50]. Indeed, the great part of traffic datasets contain data on multi-lane highways and distinguish the type of vehicle. Most traffic models refer to dynamics of single-lane traffic and therefore do not consider the movements related to lane changes. We propose an extension of the work by Herty, Fizek and Visconti for a single-class traffic model in two space dimensions [40] to a multi-class model. The latter is defined by the coupling of LWR-type models for two classes of vehicles in the x and y direction. The interaction between the two classes of vehicles is modelled by means of the flux functions which depend on the sum of vehicle densities as in [41]. With suitable assumptions on the flux functions, we study the two-dimensional Riemann problems and validate the model comparing the theoretical results with the solutions given by a numerical approximation of Lax-Friedrichs type [57]. Then, we calibrate the flux and velocity functions with the German dataset [50] and compare the results of our model with real trajectories data. We also test the ability of the model of capturing vehicles overtaking.

The chapter is organised as follows. In Section 6.1 we introduce the traffic model and study the Riemann problems. In Section 6.2, we describe the numerical scheme and validate the model via numerical tests. In Section 6.3, we calibrate the model with a German dataset and compare the results with the real trajectories of vehicles. In Section 6.4, we propose a modified version of the model calibrated with real data, and finally we investigate the ability of the model to simulate vehicles overtaking.

6.1 A LWR-type two-dimensional multi-class model

Let us consider two classes of vehicles, whose densities are denoted by $\rho = \rho(x, y, t)$ and $\mu = \mu(x, y, t)$, respectively. Our aim is to describe the dynamics of the two classes by means of a two-dimensional multi-class model. To this end, following [40], we introduce a LWR-type model in two dimensions for two classes of vehicles, i.e.,

$$\begin{cases} \rho_t + (q_\rho^x(\rho, \mu))_x + (q_\rho^y(\rho, \mu))_y = 0 \\ \mu_t + (q_\mu^x(\rho, \mu))_x + (q_\mu^y(\rho, \mu))_y = 0, \end{cases} \quad (6.1)$$

where $q_{\rho,\mu}^x$ are the fluxes of ρ and μ along the x -direction, and $q_{\rho,\mu}^y$ are the fluxes of ρ and μ along the y -direction. Similarly to [41], we define the flux functions as

$$\begin{aligned} q_{\rho}^x(\rho, \mu) &= \rho c^x \left(1 - \left(\frac{\rho + \mu}{r^{\max}}\right)\right) & q_{\rho}^y(\rho, \mu) &= \rho c^y \left(1 - \left(\frac{\rho + \mu}{r^{\max}}\right)\right) \\ q_{\mu}^x(\rho, \mu) &= \mu c^x \left(1 - \left(\frac{\rho + \mu}{r^{\max}}\right)\right) & q_{\mu}^y(\rho, \mu) &= \mu c^y \left(1 - \left(\frac{\rho + \mu}{r^{\max}}\right)\right), \end{aligned} \quad (6.2)$$

where c^x and c^y are parameters to be calibrated and r^{\max} is the maximum density of vehicles. The velocity functions in x and y directions coincide for ρ and μ , and are defined by

$$u^x = c^x \left(1 - \left(\frac{\rho + \mu}{r^{\max}}\right)\right), \quad u^y = c^y \left(1 - \left(\frac{\rho + \mu}{r^{\max}}\right)\right).$$

Hence, c^x and c^y represent the maximum velocity in x and y direction. Note that we assume that the two classes of vehicles have the same velocity c^x and c^y , and they have the same maximum density r^{\max} .

First of all, we present the properties of model (6.1). To simplify the notation, we normalise ρ and μ in order to fix $r^{\max} = 1$. We introduce the following vectors

$$U = \begin{pmatrix} \rho \\ \mu \end{pmatrix}, \quad f(U) = \begin{pmatrix} \rho c^x (1 - (\rho + \mu)) \\ \mu c^x (1 - (\rho + \mu)) \end{pmatrix}, \quad g(U) = \begin{pmatrix} \rho c^y (1 - (\rho + \mu)) \\ \mu c^y (1 - (\rho + \mu)) \end{pmatrix}$$

and matrices $A(U) = Df(U)$, $B(U) = Dg(U)$.

Therefore, we can rewrite system (6.1) as

$$U_t + AU_x + BU_y = 0. \quad (6.3)$$

System (6.3) is hyperbolic if any linear combination of A and B is diagonalisable. Thus, for $(\kappa_1, \kappa_2) \in \mathbb{R}^2$, we define $C = \kappa_1 A + \kappa_2 B$. The eigenvalues of C are

$$\lambda_1 = (\kappa_1 c^x + \kappa_2 c^y)(1 - (\rho + \mu)), \quad \lambda_2 = (\kappa_1 c^x + \kappa_2 c^y)(1 - 2(\rho + \mu))$$

which are real for any couple (κ_1, κ_2) , and coincide if and only if $(\rho, \mu) = (0, 0)$ or $\kappa_1 = -c^y \kappa_2 / c^x$. The associated eigenvectors are

$$\gamma_1 = \begin{pmatrix} -1 \\ 1 \end{pmatrix}, \quad \gamma_2 = \begin{pmatrix} \rho/\mu \\ 1 \end{pmatrix}.$$

The first eigenvalue is linearly degenerate, i.e., $\nabla \lambda_1 \cdot \gamma_1 = 0$, while the second one is genuinely nonlinear, i.e., $\nabla \lambda_2 \cdot \gamma_2 \neq 0$. The Riemann invariants are

$$z_1 = \rho + \mu, \quad z_2 = \log(\rho/\mu).$$

6.1.1 The Riemann problem associated to the model

Next, we describe the two-dimensional Riemann problem [23, 95] associated with (6.1). To simplify the computations, we introduce the variable $r = \rho + \mu$, so that problem (6.1) can be rewritten as

$$\begin{cases} r_t + (rc^x(1-r))_x + (rc^y(1-r))_y = 0 \\ r(0, x, y) = r_0(x, y). \end{cases} \quad (6.4)$$

The Riemann problem in two dimensions is given by (6.4) with constant initial data in the four quadrants

$$r_0(x, y) = \begin{cases} v_1 & x > 0, \quad y > 0 \\ v_2 & x < 0, \quad y > 0 \\ v_3 & x < 0, \quad y < 0 \\ v_4 & x > 0, \quad y < 0. \end{cases} \quad (6.5)$$

For convenience, we define $\hat{f}(r) = rc^x(1-r)$ and $\hat{g}(r) = rc^y(1-r)$.

Remark 6.1.1. *The treatment of the two-dimensional Riemann problem proposed in [23] assumes convex flux functions f and g . In order to recover this hypothesis in our case, it is sufficient to choose the parameters c^x and c^y negative. However, the concave case can be recovered from the following analysis through proper sign changes.*

We look for self-similar solutions $r(x, y, t) = v(x/t, y/t)$ and therefore introduce $\xi = \frac{x}{t}$ and $\eta = \frac{y}{t}$. We can rewrite the first equation of (6.4) as

$$(c^x(1-2v) - \xi)v_\xi + (c^y(1-2v) - \eta)v_\eta = 0 \quad (6.6)$$

which leads us to

$$(c^x(1-2v) - \xi)d\eta + (c^y(1-2v) - \eta)d\xi = 0,$$

where $c^x(1-2v) = \hat{f}'(v)$ and $c^y(1-2v) = \hat{g}'(v)$.

The set of singular points parametrised by v is the straight line

$$\mathcal{S} = \{(\xi, \eta) \mid \xi = c^x(1-2v), \eta = c^y(1-2v)\}.$$

By defining

$$\begin{aligned} \gamma(v_-, v_+) &= \frac{\hat{f}(v_+) - \hat{f}(v_-)}{v_+ - v_-} = c^x(1 - v_+ - v_-) \\ \nu(v_-, v_+) &= \frac{\hat{g}(v_+) - \hat{g}(v_-)}{v_+ - v_-} = c^y(1 - v_+ - v_-), \end{aligned} \quad (6.7)$$

the Rankine-Hugoniot jump condition is

$$\frac{d\eta}{d\xi} = -\frac{\nu(v_-, v_+) - \eta}{\gamma(v_-, v_+) - \xi} = -\frac{c^y(1 - v_+ - v_-) - \eta}{c^x(1 - v_+ - v_-) - \xi}. \quad (6.8)$$

Assuming that the normal vector $(d\eta, d\xi)$ is directed towards the positive side of the shock curves, the Oleinik's entropy condition is

$$\begin{aligned} &(\gamma(v_-, v_0) - \gamma(v_-, v_+))d\eta + (\nu(v_-, v_0) - \nu(v_-, v_+))d\xi \\ &= c^x(1 - v_+ - v_0)d\eta + c^y(1 - v_+ - v_0)d\xi \geq 0 \end{aligned} \quad (6.9)$$

for v_0 between v_- and v_+ .

The initial data in (6.5) for problem (6.4) in the variables (ξ, η) is given by

$$\lim_{\substack{\xi/\eta = \text{const}, \\ \xi^2 + \eta^2 \rightarrow \infty}} v(\xi, \eta) = \begin{cases} v_1 & \xi > 0, \quad \eta > 0 \\ v_2 & \xi < 0, \quad \eta > 0 \\ v_3 & \xi < 0, \quad \eta < 0 \\ v_4 & \xi > 0, \quad \eta < 0. \end{cases} \quad (6.10)$$

The solution of problem (6.6) with initial data (6.10) is composed of elementary waves. There are five possible cases: (1) no shocks, (2) no rarefaction waves, (3) exactly one shock, (4) exactly one rarefaction wave, (5) two rarefaction waves and two shocks. We skip the full details of the possible cases and refer to [95] for a detailed discussion. Let us highlight the five cases now:

(1) No shocks: This case is verified when $v_3 < v_2 < v_4 < v_1$. Each couple (v_2, v_1) , (v_3, v_4) (v_1, v_4) and (v_2, v_3) is connected by rarefaction waves and the straight line \mathcal{S} defines the points of connection between them. The solution is represented in Figure 6.1(a).

(2) No rarefaction waves: This case is verified when $v_3 > v_4 > v_2 > v_1$. The couples (v_2, v_1) and (v_2, v_3) are connected by two shocks which collide in $A = (\gamma(v_1, v_2), \nu(v_2, v_3))$ while the couples (v_3, v_4)

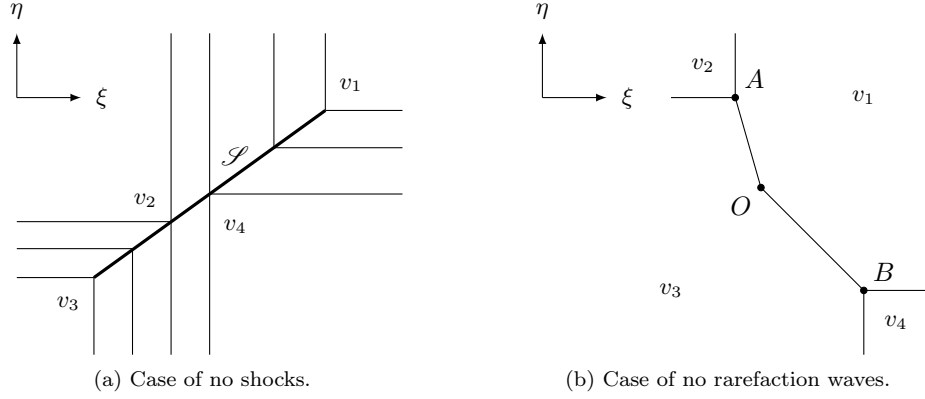


Figure 6.1. Representation of no shocks (a) and no rarefaction waves (b).

and (v_4, v_1) are connected by two shocks colliding in $B = (\gamma(v_3, v_4), \nu(v_1, v_4))$. Then, we have two shocks which connect v_1 and v_3 . They start from the point $O = (\gamma(v_1, v_3), \nu(v_1, v_3))$ and terminate either in A or in B . The solution is represented in Figure 6.1(b).

(3) Exactly one shock: This case is verified when

$$v_4 > v_1 \geq v_2 \geq v_3 \quad \text{or} \quad v_2 < v_3 \leq v_4 \leq v_1.$$

The first sub-case is represented in Figure 6.2(a). Using the Rankine-Hugoniot condition (6.8) it can be shown that the shock curve is concave, monotonically increasing in (v_1, v_4) , bounded by the base curve \mathcal{S} , tangentially intersects \mathcal{S} and satisfies the entropy condition (6.9). A similar analysis holds for the second sub-case which is represented in Figure 6.2(b).

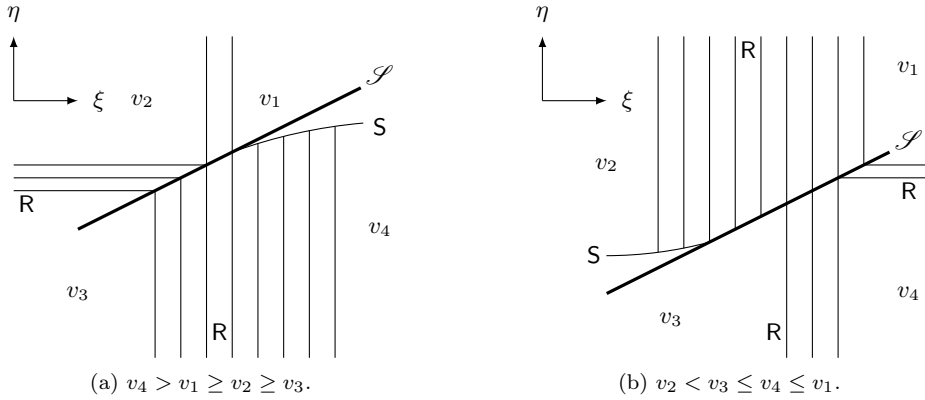


Figure 6.2. Representation of exactly one shock, where R denotes rarefaction waves and S shocks.

(4) Exactly one rarefaction wave: This case is verified when

$$v_1 \leq v_2 \leq v_3 < v_4 \quad \text{or} \quad v_2 < v_1 \leq v_4 \leq v_3.$$

The first possible initial data gives results similar to the previous case of exactly one shock wave. For the second initial data there exist several sub-cases but we omit the details. In Figure 6.3 we show two examples for the two initial configurations.

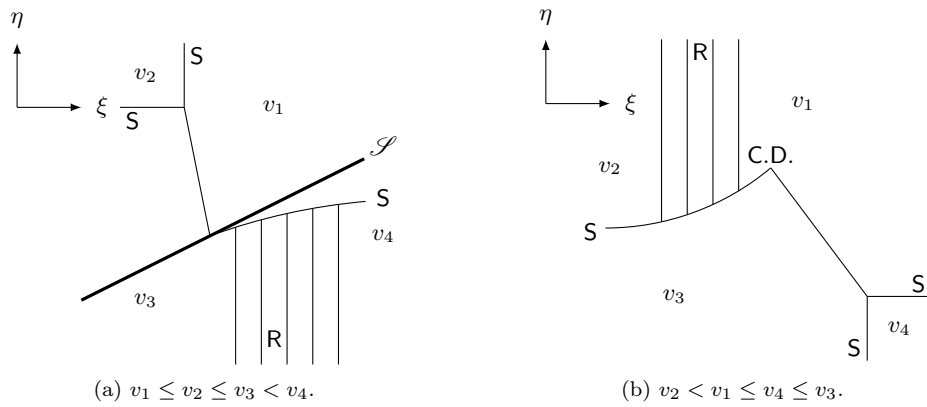


Figure 6.3. Representation of exactly one rarefaction wave, where R denotes rarefaction waves, S shocks and C.D. contact discontinuities.

(5) **Two shocks and two rarefaction waves:** This case is verified when

$$v_4 > v_1 \geq v_3 > v_2 \quad \text{or} \quad v_4 > v_3 > v_1 > v_2.$$

The main difference between the two options of initial data is that in the first case the shock curves are not neighbours as they are in the second case. There are again several sub-cases, we only show an example of the two possible initial data in Figure 6.4.

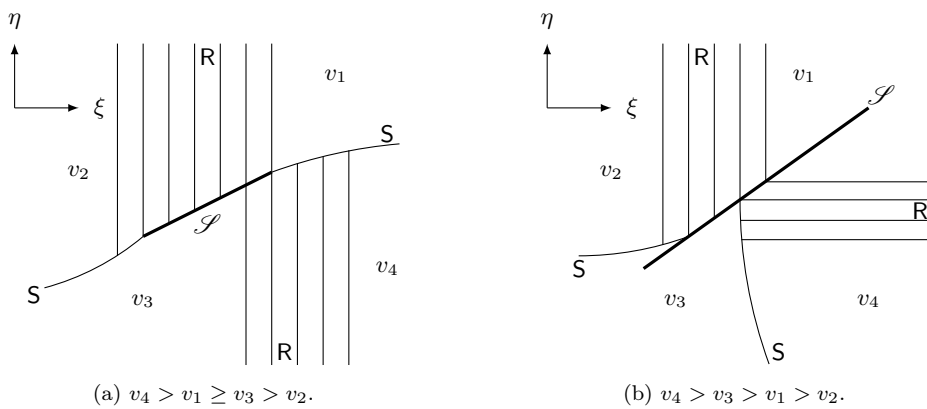


Figure 6.4. Representation of two shocks and two rarefaction waves, where R denotes rarefaction waves and S shocks.

6.2 Numerical discretisation

The numerical analysis of system (6.3) can be done using the dimensional splitting approach [62, Chapter 19] which means that the two-dimensional problem is split into two one-dimensional problems. Thus, equation (6.3) is split into

$$U_t + AU_x = 0, \quad U_t + BU_y = 0.$$

We uniformly divide the two-dimensional space $[0, L^x] \times [0, L^y]$ into a grid $\Omega = [0, N_x] \times [0, N_y]$ with x -step Δx and y -step Δy . We refer to the cell of the grid as Ω_{ij} . Defining $\lambda_{1,2}$ and $\gamma_{1,2}$ the eigenvalues of A and B respectively, the time step Δt is determined by

$$\frac{\Delta t}{\Delta x} \leq \frac{1}{2} \left(\max_{i,j=1,2} \{|\lambda_i|, |\gamma_j|\} \right)^{-1}. \quad (6.11)$$

Then, the time interval $[0, T]$ is divided into time steps of length Δt . Starting from a given initial datum U_{ij}^0 , the numerical scheme is defined by the Strang splitting as

$$\begin{aligned} U_{ij}^* &= U_{ij}^n - \frac{\Delta t}{2\Delta x} (F_{i+1/2,j}^n - F_{i-1/2,j}^n) \\ U_{ij}^{**} &= U_{ij}^* - \frac{\Delta t}{\Delta y} (G_{i,j+1/2}^* - G_{i,j-1/2}^*) \\ U_{ij}^{n+1} &= U_{ij}^n - \frac{\Delta t}{2\Delta x} (F_{i+1/2,j}^{**} - F_{i-1/2,j}^{**}). \end{aligned}$$

The idea of this scheme is to solve a one dimensional problem in the x -direction, i.e. at fixed j , over only a half time step of length $\Delta t/2$. Then, we use the result as data for a full time step on a one dimensional problem in the y -direction, i.e. at fixed i , and finally we take another half time step in the x -direction. We use the Local Lax-Friedrichs flux (also known as Rusanov flux) [14, Chapter 3, Part II] for F and G

$$F_{i+1/2,j} = \frac{1}{2} (f(U_{i+1,j}) + f(U_{i,j}) - \alpha_{i+1/2,j} (U_{i+1,j} - U_{i,j})),$$

where $\alpha_{i+1/2,j}$ is the maximum modulus of the eigenvalues of the Jacobian matrix in the interval $(U_{i,j}, U_{i+1,j})$.

6.2.1 Validation

We now test the discretisation method for the two-dimensional multi-class model (6.3) while comparing the numerical results to the theoretical solutions of the Riemann problems introduced in Section 6.1.1.

Our test setting is given by $\Omega = [-5, 5] \times [-5, 5]$ with $\Delta x = \Delta y = 0.02$. We fix the parameters of (6.2) to $c^x = c^y = -1$. As already observed in Remark 6.1.1, we fix negative parameters to recover convex flux functions. The time interval $[0, T] = [0, 1]$ is divided into time steps of length Δt satisfying condition (6.11). The initial data for the two classes ρ and μ is taken as in (6.10)

$$\rho_0(x, y) = \begin{cases} \rho_1 & (x, y) \in (0, 5) \times (0, 5) \\ \rho_2 & (x, y) \in (-5, 0) \times (0, 5) \\ \rho_3 & (x, y) \in (-5, 0) \times (-5, 0) \\ \rho_4 & (x, y) \in (0, 5) \times (-5, 0). \end{cases}$$

and $\mu_0(x, y) = \rho_0(x, y)/2$. For simplicity of notation we take the values $\rho_i \in \{1, 2, 3, 4\}$ and then normalise ρ and μ dividing by $r^{\max} = \rho^{\max} + \mu^{\max} = 6$.

Since we aim at recovering the results of the analysis done in Section 6.1.1, where the plots are defined for the plane (ξ, η) with $\xi = x/t$ and $\eta = y/t$, we note that for $t = 1$ the variables ξ and η coincide with x and y . Therefore, we plot the contours of the numerical solution U_{ij}^n at time $t^n = 1$ in order to identify the plane (x, y) with the plane (ξ, η) for a better comparison. As we have explained in Section 6.1.1, there are only five possible configurations of the solution, which are determined by the initial values ρ_i , $i = 1, \dots, 4$.

(1) No shocks: We fix $\rho_1 = 4$, $\rho_2 = 2$, $\rho_3 = 1$ and $\rho_4 = 3$. As shown in Figure 6.5(a), we have

only rarefaction waves connected by the straight line $\mathcal{S} = \{(x, y) \mid y = x\}$. The results in Figure 6.5(a) coincide with the theoretical solution shown in Figure 6.1(a).

(2) No rarefaction waves: We fix $\rho_1 = 1$, $\rho_2 = 2$, $\rho_3 = 4$ and $\rho_4 = 3$. In Figure 6.5(b), the points of connection between the shocks are $A = (\gamma(\rho_1 + \mu_1, \rho_2 + \mu_2), \nu(\rho_2 + \mu_2, \rho_3 + \mu_3)) = (-0.25, 0.5)$, $B = (\gamma(\rho_3 + \mu_3, \rho_4 + \mu_4), \nu(\rho_4 + \mu_4, \rho_1 + \mu_1)) = (0.75, 0)$ and $O = (\gamma(\rho_1 + \mu_1, \rho_3 + \mu_3), \nu(\rho_1 + \mu_1, \rho_3 + \mu_3)) = (0.25, 0.25)$ with γ and ν defined in (6.7). The results in Figure 6.5(b) coincide with the theoretical solution shown in Figure 6.1(b).

(3) Exactly one shock: We fix $\rho_1 = 3$, $\rho_2 = 2$, $\rho_3 = 1$ and $\rho_4 = 4$. As shown in Figure 6.5(c), we consider the first sub-case described in Section 6.1.1, and the shock wave is below the straight line $\mathcal{S} = \{(x, y) \mid y = x\}$. The results in Figure 6.5(c) coincide with the theoretical solution shown in Figure 6.2(a).

(4) Exactly one rarefaction wave: We fix $\rho_1 = 1$, $\rho_2 = 2$, $\rho_3 = 3$ and $\rho_4 = 4$. The results in Figure 6.5(d) coincide with the theoretical solution shown in Figure 6.2(a), and similarly to the previous case we have that the only rarefaction wave is below the straight line $\mathcal{S} = \{(x, y) \mid y = x\}$.

(5) Two shocks and two rarefaction waves: We fix $\rho_1 = 3$, $\rho_2 = 1$, $\rho_3 = 2$ and $\rho_4 = 4$. As shown in Figure 6.5(e), the shock waves are not neighbours, but they are separated by the rarefaction waves and the straight line $\mathcal{S} = \{(x, y) \mid y = x\}$. The results in Figure 6.5(e) coincide with the theoretical solution shown in Figure 6.4(a).

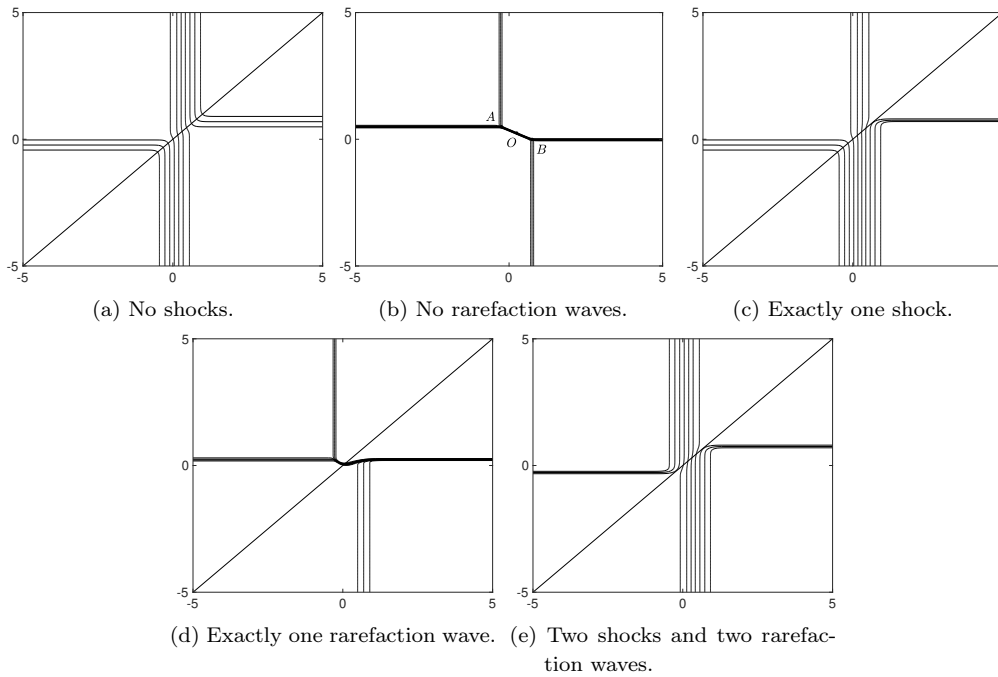


Figure 6.5. Numerical solutions of Riemann problems depending on the initial datum.

6.3 Data-driven multi-class model in 2D

In this section, we calibrate the two-dimensional multi-class model with a dataset of real trajectories data. We employ the public German dataset [50] which contains vehicle trajectories data recorded on the

German motorway A3, nearby Frankfurt am Main. The analysed area is a three lanes highway of about 900 meters in length and 12 meters in width, depicted in Figure 6.6. A system of five video cameras recorded the vehicles passing through the study area, collecting trajectory data for 20 minutes with a sampling period of about 0.2 seconds. We refer to [50] for a detailed description of the dataset and of the data collection method. We observe that the dataset distinguishes several types of vehicles, and we focus on the dynamics of cars and trucks.

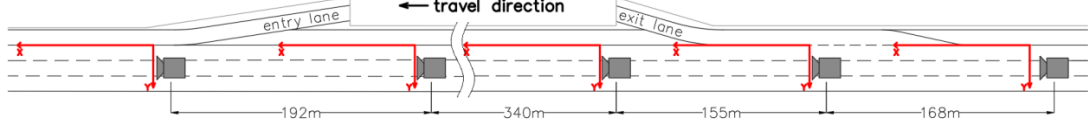


Figure 6.6. German motorway A3 structure, cf. [50].

6.3.1 Fundamental diagrams

In order to calibrate the two-dimensional model with the German dataset, we need first to derive macroscopic quantities from the microscopic information provided. Following [40], we describe how we derive the density of cars and trucks, ρ and μ , the speed in the two directions, u^x and u^y , and the flux in the two directions, $q_{\rho,\mu}^x$ and $q_{\rho,\mu}^y$. Note that, as we have already observed in Section 6.1, the velocity functions coincide for ρ and μ since c^x and c^y do not distinguish the class of vehicles. Although this hypothesis is restrictive, it allows us to apply the theoretical results of the previous sections to a real traffic description. However, the following numerical simulation gives a good approximation of the traffic dynamic.

We consider the data from the second camera from the right of Figure 6.6, thus we work with 20 minutes of real data. We introduce the time interval (t_0, t_M) , with $t_0 = 0$ and $t_M = 20$ min, and uniformly divide it with a time step dt . Note that dt is used to derive the macroscopic quantities from the microscopic ones, and is independent of the time step Δt of the numerical scheme. We call $N_{\rho,\mu}(t_k)$ the total number of cars and trucks at time t_k and L^x the length of the road along the main direction of travel. Then, we define

$$\tilde{\rho}(t_k) = \frac{N_{\rho}(t_k)}{L^x}, \quad \tilde{\mu}(t_k) = \frac{N_{\mu}(t_k)}{L^x}. \quad (6.12)$$

The German dataset only provides the position of vehicles with respect to the two directions, thus we need to derive the speed of vehicles from their positions. We assume that each vehicle travels at constant speed which corresponds to the slope of a linear approximation in the least square sense of the vehicle positions. We denote by $v_i^{x,y}$ the resulting microscopic speed of car i and by $w_i^{x,y}$ the analogous speed of truck i . Since we assume that the two classes have the same speed function, we define the average speed as a function of the two classes

$$\begin{aligned} \tilde{u}^x(t_k) &= \frac{1}{N_{\rho}(t_k)} \sum_{i=1}^{N_{\rho}(t_k)} v_i^x + \frac{1}{N_{\mu}(t_k)} \sum_{i=1}^{N_{\mu}(t_k)} w_i^x \\ \tilde{u}^y(t_k) &= \frac{1}{N_{\rho}(t_k)} \sum_{i=1}^{N_{\rho}(t_k)} v_i^y + \frac{1}{N_{\mu}(t_k)} \sum_{i=1}^{N_{\mu}(t_k)} w_i^y. \end{aligned} \quad (6.13)$$

Finally, we combine equations (6.12) and (6.13) to define the flux functions as

$$\begin{aligned} \tilde{q}_{\rho}^x(t_k) &= \tilde{\rho}(t_k) \tilde{u}^x(t_k), & \tilde{q}_{\rho}^y(t_k) &= \tilde{\rho}(t_k) \tilde{u}^y(t_k) \\ \tilde{q}_{\mu}^x(t_k) &= \tilde{\mu}(t_k) \tilde{u}^x(t_k), & \tilde{q}_{\mu}^y(t_k) &= \tilde{\mu}(t_k) \tilde{u}^y(t_k). \end{aligned} \quad (6.14)$$

Once we have the density, speed and flux data as functions of time, we aggregate them with respect to a certain time period $\tilde{T} = \kappa dt$. In particular, we fix $dt = 1$ s and $\kappa = 60$. In Figure 6.7, we show the speed-density and flux-density diagrams for the two classes of vehicles in the x and y directions.

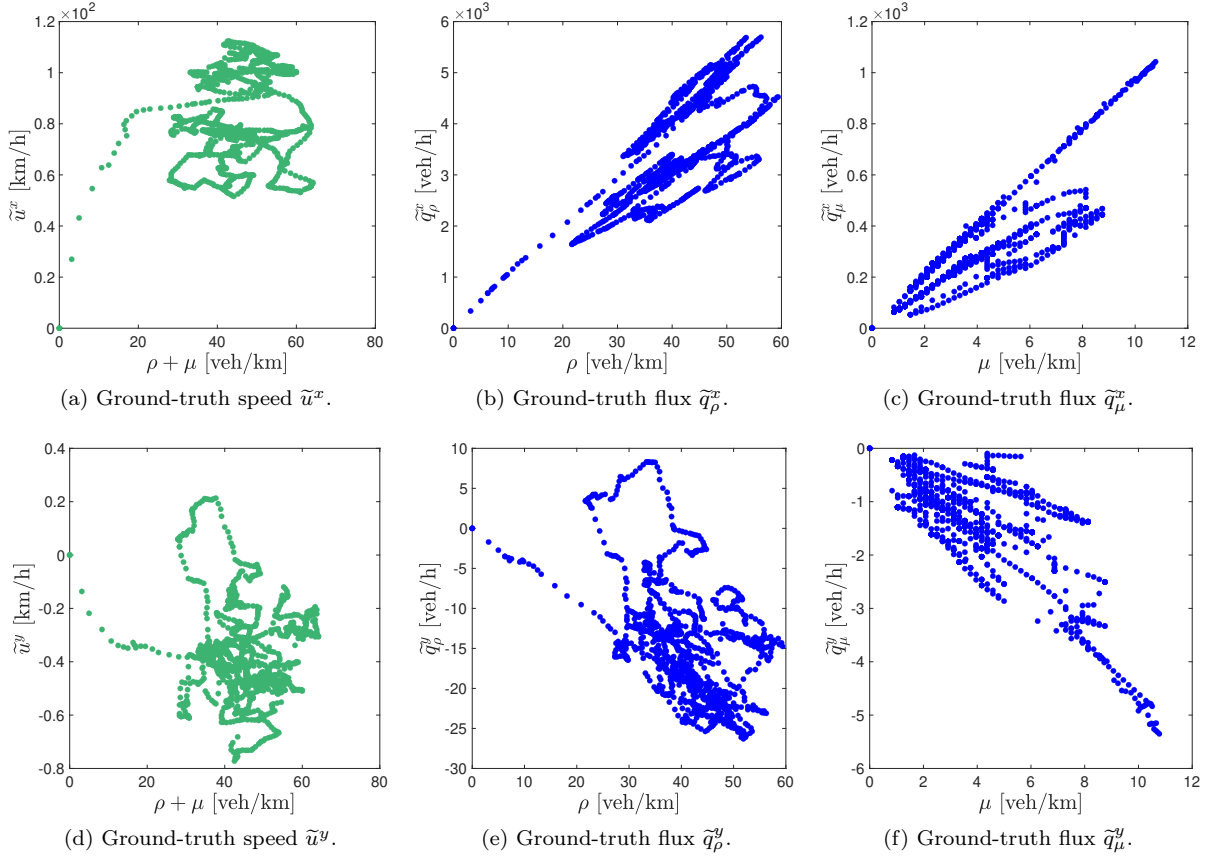


Figure 6.7. Speed-density and flux-density diagrams for the two classes related to the x -direction in the first row, and to the y -direction on the second row.

The graphs show that the main direction of the flow is along the x -axis, according to the structure of the analysed road, while the movements along the y -axis represent the lane changes. Note that both the flux and the velocity along the y -direction show negative values, due to the lane change that can occur in both directions. The maximum density value reached in Figure 6.7 is 60 veh/km for cars and 12 veh/km for trucks, and both values are much smaller than the maximum density of the road given by $r^{\max} = 400$ veh/km. More specifically, as we observe from Figure 6.7, there are more cars than trucks along the road, thus we calibrate the maximum density fixing the length of vehicles as if there are only cars on the road. Hence, we assume that the length of vehicles plus the safety distance is 7.5 m, thus r^{\max} is defined as

$$r^{\max} = \frac{\# \text{ lanes}}{\text{length of vehicles} + \text{safety distance}} = \frac{3}{7.5 \text{ m}} = 400 \frac{\text{veh}}{\text{km}}. \quad (6.15)$$

However, it should be noted that the dataset only contains data in free-flow regimes without capturing congested traffic phase.

Now we need to compute the parameters c^x and c^y . These parameters are chosen in order to minimise the L^2 -norm between the flux functions defined in (6.2) and the fluxes derived from data in (6.14), i.e.,

we consider

$$\min_{c^x} \left(\|\tilde{q}_\rho^x - q_\rho^x(\rho, \mu)\|_2^2 + \|\tilde{q}_\mu^x - q_\mu^x(\rho, \mu)\|_2^2 \right), \quad \min_{c^y} \left(\|\tilde{q}_\rho^y - q_\rho^y(\rho, \mu)\|_2^2 + \|\tilde{q}_\mu^y - q_\mu^y(\rho, \mu)\|_2^2 \right).$$

The computation is performed using the MATLAB tool `fminbnd`, which is a specific solver for minimisation problems. We obtain $c^x = 97.04$ and $c^y = -0.41$. Note that c^y is negative, since the lane changes mainly occur towards the rightmost lane. The flux diagrams chosen in this chapter do not allow to consider movements towards both the directions in the y -component. Anyway, this choice well fits the analysed dataset, where there are few movements towards the leftmost lanes. The resulting speed and flux functions are shown in Figure 6.8. Since the flux functions depend on both ρ and μ , we have a family of flux and velocity functions. In particular, in Figure 6.8(b) we show the family of flux functions q_ρ^x as μ changes. This means that at fixed value of μ we can move only along one of the flux curves. For instance, if $\mu = 0$, i.e. there are no trucks, then the fundamental diagram q_ρ^x corresponds to the maximum flux curve in Figure 6.8(b), if $\mu = r^{\max}$ then no car can enter into the road, and thus $q_\rho^x \equiv 0$. A similar discussion holds for the other plots of Figure 6.8.

We observe that the advantage of the multi-class model is that we can cover quite well the clouds of real data by means of the family of flux and velocity functions. However, we note that, since the German dataset contains data which refer only to the not congested phase of traffic, we do not have enough data to better calibrate congested traffic situations. In particular, the choice of c^x and c^y equal for both of the classes seems to overestimate the flux for the class μ , in both the directions.

6.3.2 Reconstruction of density from data

In this section we describe how to treat the microscopic data to define the initial density for the numerical scheme and the reference solution for the comparison of the results. The German dataset gives information about the position of vehicles every 0.2 seconds, thus we work with point-wise data. In order to define a density function $\rho(x, y, t)$ on a domain \mathcal{D} , we use the kernel density estimation introduced in Section 1.4. Specifically, denoting by $N(t)$ the number of cars at time t and $(x_i(t), y_i(t))$ their positions, we introduce the two-dimensional Gaussian kernel

$$K(x, y) = \frac{1}{2\pi h_x h_y} \exp\left(-\frac{x^2}{2h_x^2} - \frac{y^2}{2h_y^2}\right),$$

and we then define the density ρ modifying (1.19) as

$$\rho(x, y, t) = \sum_{i=1}^{N(t)} K(x - x_i(t), y - y_i(t)). \quad (6.16)$$

We follow a similar procedure to estimate the density of trucks μ . The parameters h_x and h_y depend on the dimensions of the road. On a road of dimensions $L^x \times L^y$ we fix $h_x = L^x/20$ and $h_y = L^y/20$, with L^x being the length of the road along the x -axis and L^y the length along the y -axis.

For each video camera of the dataset we work with records data for about 80 m in length and 12 m in width. The average speed of vehicles is such that they exit from the recording area after a few seconds. In order to test longer simulations and compare them with real data, we assume that the trajectory of each vehicle can be approximated by a linear movement. Indeed, let us consider a vehicle i which crosses the road between a time interval $[t_0, t_1]$. We compute the coefficients $a_i^{x,y}$ and $b_i^{x,y}$ such that we can approximate the x and y position as $x(t) = a_i^x + b_i^x t$ and $y(t) = a_i^y + b_i^y t$ by minimising the L^2 -norm of the difference with the real positions. In this way, we are able to compute the ‘‘real’’ position of vehicles even when they exit the supervised area. The computed positions also allow for a comparison to the numerical results.

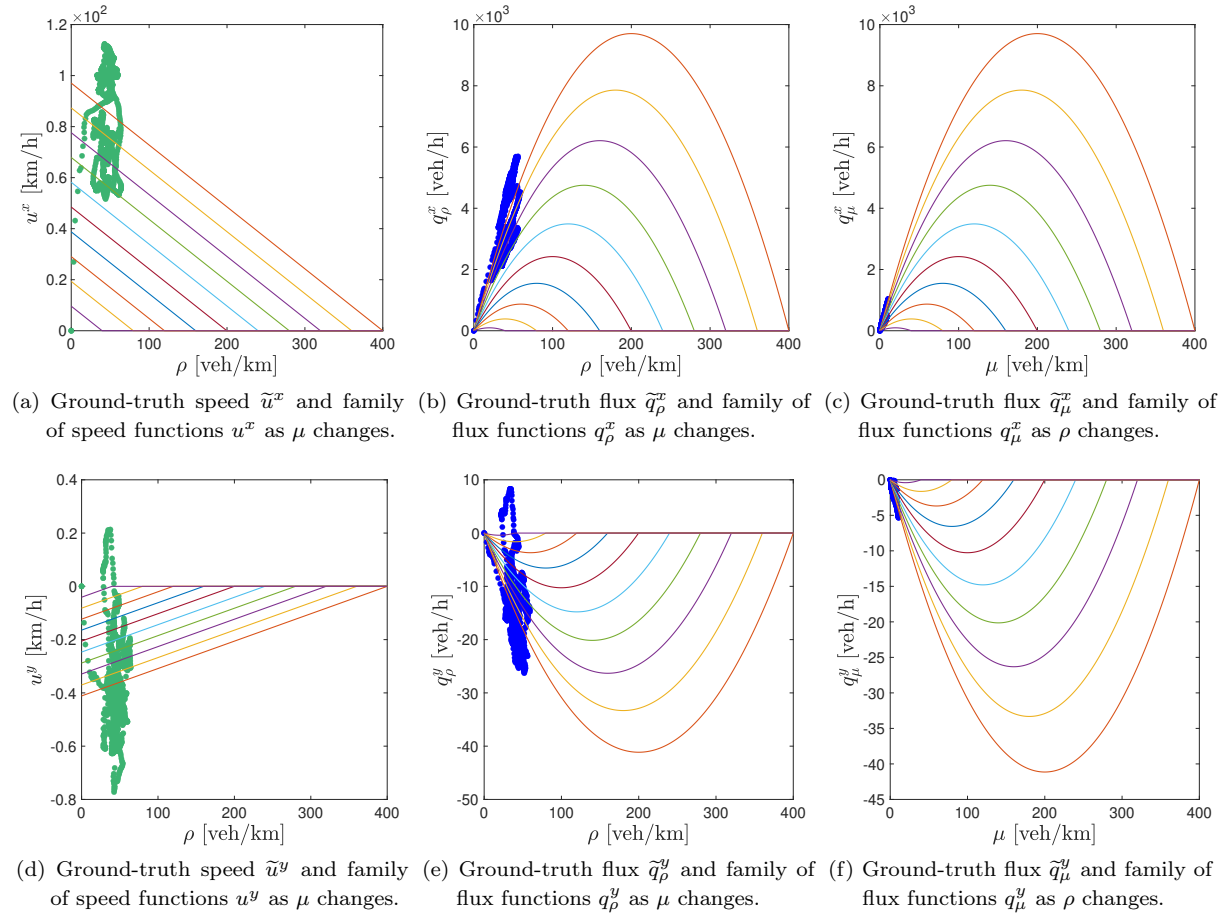


Figure 6.8. Speed-density and flux-density diagrams for the two classes defined from real data (green and blue circles) and family of speed and velocity functions related to the x -direction in the first row, and to the y -direction in the second row.

6.3.3 Numerical test

Now, we compare the numerical simulations of model (6.1) with the real data computed from equation (6.16). The simulation refers to the data recorded by the second video camera of the German dataset. It is well-known that macroscopic descriptions are computationally convenient with respect to microscopic ones for simulating scenarios with a high number of vehicles. The aim of this test is to show that our model well approximates the real traffic dynamics even in presence of few vehicles. Thus, this test is specially chosen to compare simulated trajectories with the real ones by tracking the position of each vehicle.

Let us consider the domain $[0, L^x] \times [0, L^y]$ uniformly divided into a numerical grid $\Omega = [0, N_x] \times [0, N_y]$ with x -steps of length Δx and y -steps of length Δy during a time interval $[0, T]$ divided into time steps of length Δt satisfying (6.11). The numerical solutions are computed by means of the numerical scheme introduced in Section 6.2, and they are denoted by

$$\bar{\rho}_{ij}^n = \bar{\rho}(x_i, y_j, t^n), \quad \bar{\mu}_{ij}^n = \bar{\mu}(x_i, y_j, t^n)$$

for cars and trucks respectively, with $x_i = \Delta x/2 + (i-1)\Delta x$, $y_j = \Delta y/2 + (j-1)\Delta y$ and $t^n = n\Delta t$, with $i = 1, \dots, N_x$, $j = 1, \dots, N_y$ and $n = 0, \dots, N_t$. We impose homogeneous Dirichlet conditions on

the west and north boundary of the road, i.e. $\rho_{1j}^n = \rho_{iN_y}^n = 0$ for $i = 1, \dots, N_x$ and $j = 1, \dots, N_y$, and we allow vehicles to leave the road on the south and east boundary, as explained in (B2) at the end of Section 4.2. In particular, vehicles can leave the road from the south boundary in correspondence of the exit lane, see Figure 6.6.

The ground-truth data are estimated by (6.16) as explained in Section 6.3.2, and they are denoted by

$$\rho_{ij}^{\text{true},n} = \rho^{\text{true}}(x_i, y_j, t^n), \quad \mu_{ij}^{\text{true},n} = \mu^{\text{true}}(x_i, y_j, t^n)$$

for cars and trucks, respectively. The parameters used in the following test are $L^x = 450$ m, $L^y = 14$ m, $\Delta x = \Delta y = 0.5$ m, $T = 5$ s, $h_x = 22.5$ and $h_y = 0.7$. The initial configuration of densities is recovered by the ground-truth data (6.16) starting from the time $\hat{t} = 14$ s of the dataset. Therefore, at the beginning, the numerical solution coincides with the ground-truth solution. At time \hat{t} there are three cars and one truck along the three-lanes highway, so we analyse their dynamics. In Figure 6.9, we compare the contours of the ground-truth density data with the contours of the reconstructed density by the numerical simulation at the final time T . The dotted lines divide the road into three lanes. After 5 s of simulation the real and the numerical configurations of density are quite similar for both populations of vehicles. We observe that the truck is leaving the road in correspondence of the exit lane.

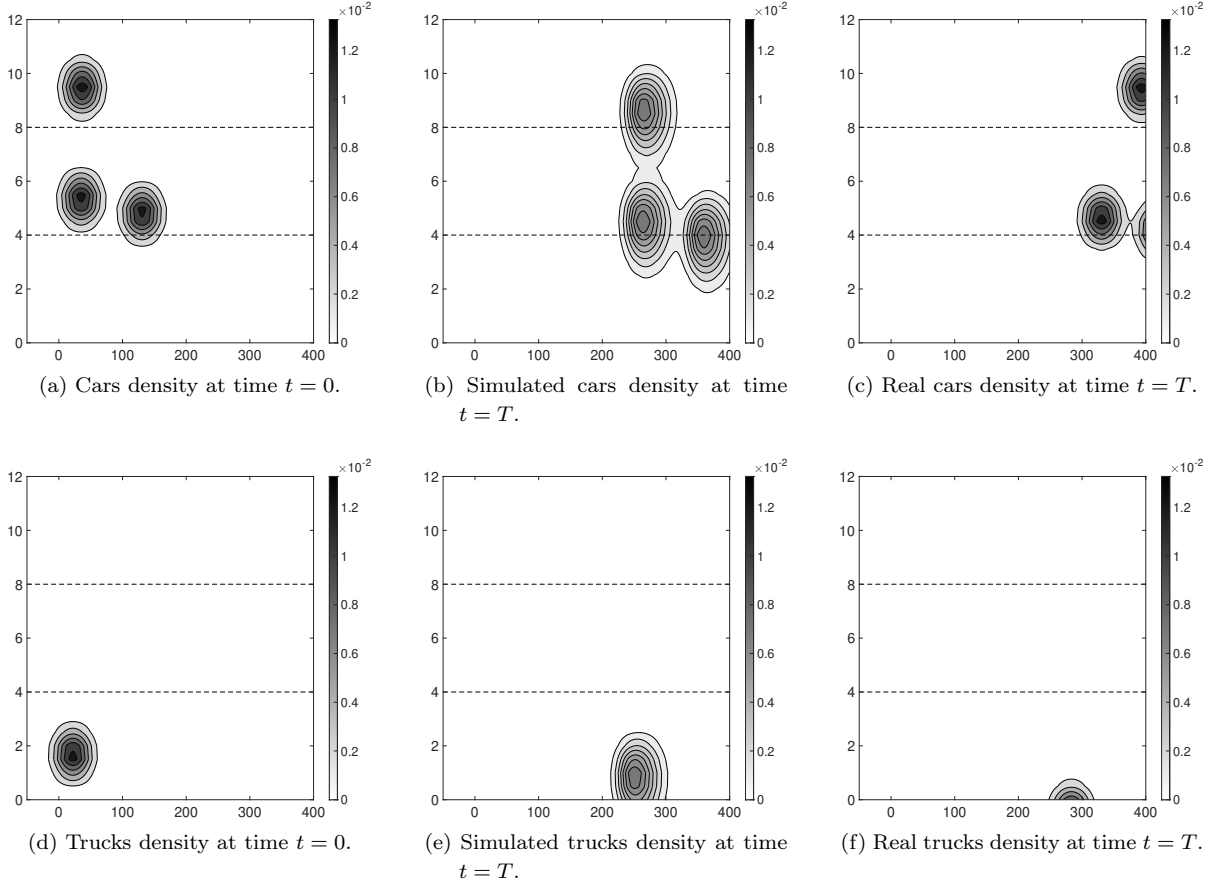


Figure 6.9. Contours of the density of cars (top) and trucks (bottom): initial condition at time $t = 0$ (left), simulated results at time $t = 5$ s (middle) and reconstructed real data at time $t = 5$ s (right).

In order to better compare the numerical results with the ground-truth data, we introduce the following

errors to estimate how much the model deviates from the real data

$$E_\rho(t^n) = \|\rho^{\text{true}}(\cdot, \cdot, t^n) - \bar{\rho}(\cdot, \cdot, t^n)\|_{L^1}, \quad (6.17)$$

$$E_\mu(t^n) = \|\mu^{\text{true}}(\cdot, \cdot, t^n) - \bar{\mu}(\cdot, \cdot, t^n)\|_{L^1}. \quad (6.18)$$

The errors at time T of the previous simulation are $E_\rho(T) = 0.06$ and $E_\mu(T) = 0.02$ computed with (6.17) and (6.18), respectively. In Figure 6.10 we plot the numerical errors between the numerical density and real data during 10 seconds of simulation computed every 0.5 seconds. We observe that the error related to the truck is lower than the error related to cars and that both errors increase in time. However, they remain of order 10^{-2} .

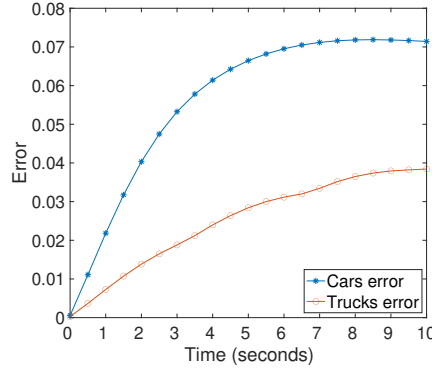


Figure 6.10. Error between real and numerical density of cars and trucks during 10 seconds of simulation, computed every 0.5 seconds.

6.4 Further data analyses

In the previous section we have seen that the two dimensional multi-class LWR (6.1) with the flux functions defined in (6.2) and calibrated with real data is able to simulate the dynamics of vehicles. However, our main assumption on the flux functions is that the coefficients r^{\max} , c^x and c^y are equal for both the classes of vehicles. This is a strong assumption, since it implies that cars and trucks have the same length and velocity. Therefore, we modify now the definition of the flux functions to differentiate more clearly the dynamics of the two classes.

6.4.1 Test with real data

We consider again the German dataset [50]. Our aim is to consider different maximum density of cars and trucks, due to the different length of vehicles, and different parameters c_ρ^x , c_μ^x , c_ρ^y and c_μ^y in order to take into account velocity functions which depend on the class of vehicles. The maximum density of cars $r^{\max} = r_\rho^{\max} = 400$ veh/km coincides with equation (6.15), and we assume that the length of trucks is twice that of cars, hence we have $r_\mu^{\max} = 200$ veh/km. We slightly modify the flux functions of (6.1) as

$$\begin{aligned} q_\rho^x(\rho, \mu) &= \rho c_\rho^x \left(1 - \left(\frac{\rho + 2\mu}{r^{\max}} \right) \right), & q_\rho^y(\rho, \mu) &= \rho c_\rho^y \left(1 - \left(\frac{\rho + 2\mu}{r^{\max}} \right) \right) \\ q_\mu^x(\rho, \mu) &= \mu c_\mu^x \left(1 - \left(\frac{\rho + 2\mu}{r^{\max}} \right) \right), & q_\mu^y(\rho, \mu) &= \mu c_\mu^y \left(1 - \left(\frac{\rho + 2\mu}{r^{\max}} \right) \right). \end{aligned} \quad (6.19)$$

Note that in (6.19) the different maximum densities between cars and trucks is expressed by the term $(\rho + 2\mu)/r^{\max}$.

With the introduction of different coefficients c_ρ^x , c_μ^x , c_ρ^y and c_μ^y we are able to better distinguish the behaviour of the two classes of vehicles, by means of different maximum velocities for the two classes in both the directions.

Next, we repeat a procedure analogous to the one proposed in Section 6.3.1 to estimate the velocity functions and the fundamental diagrams. In particular, we define different velocity functions for ρ and μ as

$$\begin{aligned}\tilde{u}_\rho^x(t_k) &= \frac{1}{N_\rho(t_k)} \sum_{i=1}^{N_\rho(t_k)} v_i^x, & \tilde{u}_\rho^y(t_k) &= \frac{1}{N_\rho(t_k)} \sum_{i=1}^{N_\rho(t_k)} v_i^y \\ \tilde{u}_\mu^x(t_k) &= \frac{1}{N_\mu(t_k)} \sum_{i=1}^{N_\mu(t_k)} w_i^x, & \tilde{u}_\mu^y(t_k) &= \frac{1}{N_\mu(t_k)} \sum_{i=1}^{N_\mu(t_k)} w_i^y,\end{aligned}$$

from which we recover the flux functions as

$$\begin{aligned}\tilde{q}_\rho^x(t_k) &= \tilde{\rho}(t_k) \tilde{u}_\rho^x(t_k), & \tilde{q}_\rho^y(t_k) &= \tilde{\rho}(t_k) \tilde{u}_\rho^y(t_k) \\ \tilde{q}_\mu^x(t_k) &= \tilde{\mu}(t_k) \tilde{u}_\mu^x(t_k), & \tilde{q}_\mu^y(t_k) &= \tilde{\mu}(t_k) \tilde{u}_\mu^y(t_k).\end{aligned}\tag{6.20}$$

We estimate the parameters c_ρ^x , c_μ^x , c_ρ^y and c_μ^y in order to minimise the L^2 -norm between the flux functions defined in (6.19) and the fluxes derived from data in (6.20) and compute

$$\begin{aligned}\min_{c_\rho^x} \left(\|\tilde{q}_\rho^x - q_\rho^x(\rho, \mu)\|_2^2 \right) & \quad \min_{c_\rho^y} \left(\|\tilde{q}_\rho^y - q_\rho^y(\rho, \mu)\|_2^2 \right) \\ \min_{c_\mu^x} \left(\|\tilde{q}_\mu^x - q_\mu^x(\rho, \mu)\|_2^2 \right) & \quad \min_{c_\mu^y} \left(\|\tilde{q}_\mu^y - q_\mu^y(\rho, \mu)\|_2^2 \right),\end{aligned}$$

using again the `fminbnd` MATLAB tool. We obtain $c_\rho^x = 99.61$, $c_\rho^y = -0.40$, $c_\mu^x = 74.86$ and $c_\mu^y = -0.49$. Hence, the cars have a faster velocity than the trucks along the main direction of travel, while the velocity of lane-changing is quite similar between the two classes.

In Figure 6.11, we show the family of speed and flux functions obtained with the above described procedure. Note that the speed and flux functions related to trucks, shown in Figures 6.11(b), 6.11(d), 6.11(g) and 6.11(h), are defined for $\mu \in [0, r_\mu^{\max}]$, with r_μ^{\max} being the half of r^{\max} . Again, we are able to cover the clouds of real data, but in this case the plots of q_μ^x and q_μ^y (Figures 6.11(g) and 6.11(h)) reach lower flux values with respect to Figures 6.8(c) and 6.8(f), according to the lower density and velocity of trucks recorded by the dataset. Hence, the overestimation of flux values for the class of trucks is highly reduced with the introduction of c_μ^x and c_μ^y compared to the results obtained in Section 6.3.1.

We repeat the same numerical test proposed in Section 6.3.3 with the new flux functions (6.19), estimating again the resulting errors with (6.17) and (6.18). The density plots we obtain are similar to the plots shown in Figure 6.9, thus we omit the picture. However, as shown in Figure 6.12, we obtain a better estimate of the errors compared to the test done in Section 6.3.3.

6.4.2 Vehicles overtaking

A further investigation of our model is the testing of the ability of capturing vehicles overtaking. We consider the following flux functions

$$\begin{aligned}q_\rho^x(\rho, \mu) &= \rho c_\rho^x \left(1 - \left(\frac{\rho + \mu}{r^{\max}} \right) \right), & q_\rho^y(\rho, \mu) &= \rho c_\rho^y \left(1 - \left(\frac{\rho + \mu}{r^{\max}} \right) \right) \\ q_\mu^x(\rho, \mu) &= \mu c_\mu^x \left(1 - \left(\frac{\rho + \mu}{r^{\max}} \right) \right), & q_\mu^y(\rho, \mu) &= \mu c_\mu^y \left(1 - \left(\frac{\rho + \mu}{r^{\max}} \right) \right),\end{aligned}$$

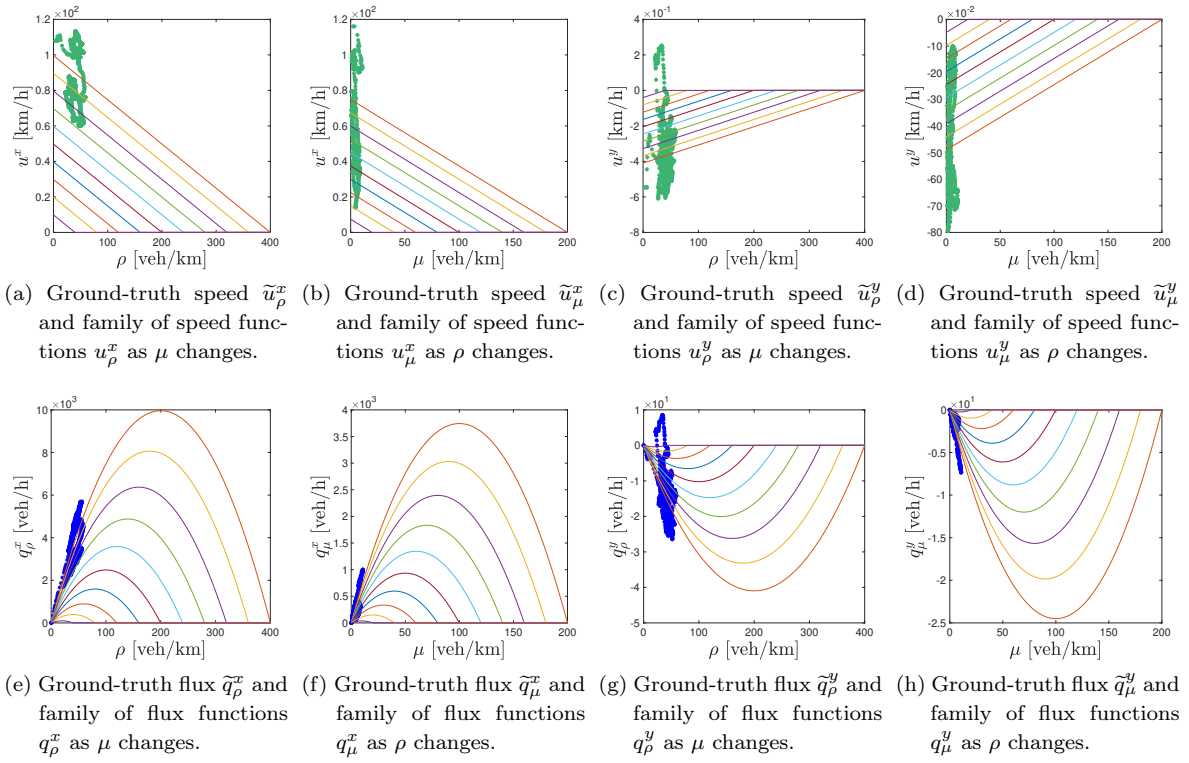


Figure 6.11. Speed-density and flow-density diagrams for the two classes defined from real data (green and blue circles) and family of speed and flux functions defined by (6.19).

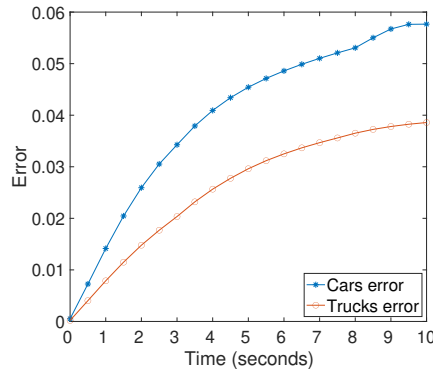


Figure 6.12. Error between real density and numerical density of cars and trucks during 10 seconds of simulation, computed every 0.5 seconds.

where we have different parameters c_ρ^x , c_μ^x , c_ρ^y and c_μ^y but the same maximum density r^{\max} . The idea is to simulate traffic dynamics with different maximum velocities for the two classes and verify if the faster vehicles are able to overtake the slower ones. Indeed, the presence of the component transverse to the main direction of motion naturally lends itself to the modeling of vehicles overtaking.

We consider a numerical grid $\Omega = [0, N_x] \times [0, N_y]$ with x -steps Δx and y -steps Δy during a time interval $[0, T]$ divided into time steps Δt satisfying (6.11). In particular we work on a road with two lanes, with two cars and one truck. We fix the following parameters: $L^x = 100$ m, $L^y = 6$ m, $\Delta x = \Delta y = 0.2$ m and $T = 4$ s. Moreover, we assume that $c_\rho^x = 80$ and $c_\rho^y = -0.4$, while $c_\mu^x = c_\mu^y = 0$, thus the truck does

not move. We impose homogeneous Dirichlet condition on the west, south and north boundary and we allow vehicles to leave the road from the east boundary, see (B2) at the end of Section 4.2.

As we can see in Figure 6.13, we consider a road with two lanes with two cars and a truck. At the beginning of the simulation there is a car in the top lane and a truck in front of the other car in the bottom lane. Since the truck does not move and the cars are free to move along the y -axis, in Figure 6.13(b) we see that both cars move towards the north-east direction. In particular, the car in the top lane is leaving the road and the other one starts to overtake the truck, which acts as an obstacle along the main travel direction. Finally, Figure 6.13(c) shows that the car has been able to overtake the truck since it is exiting the road while the truck is still inside the domain.

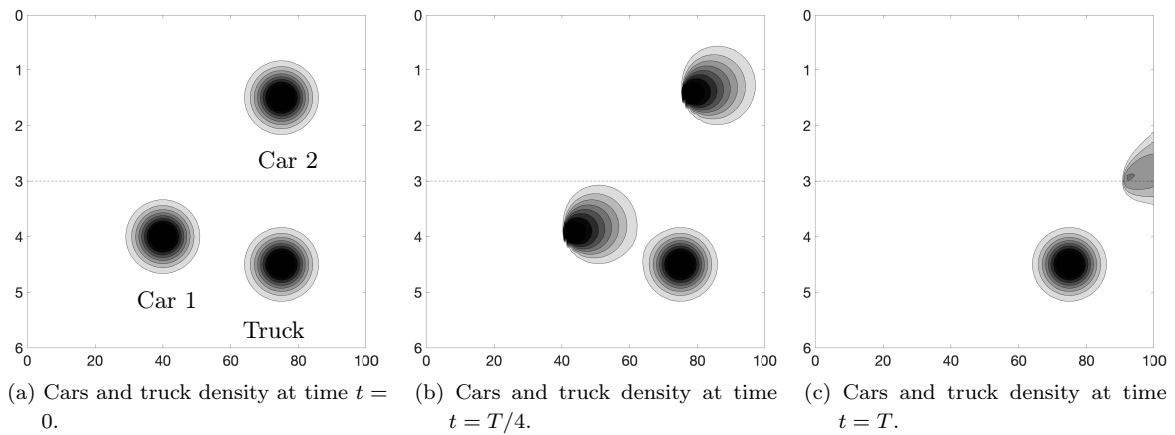


Figure 6.13. Contours of the density of cars and truck at time $t = 0$ (left), $t = T/4$ (middle) and $t = T$ (right). The truck does not move, Car 1 leaves the road during the simulation and Car 2 overtakes the truck and is exiting the road at time T .

Chapter 7

Understanding mass transfer directions via data-driven models

The contents of this chapter can be found in paper [1]. The research described here is aimed at solving an inverse problem which regards a mass moving in a bounded domain with finite velocity. We assume that the mass moves following an unknown velocity field and that the evolution of the mass density can be described by an unknown PDE. The input data of the problem are given by some snapshots of the mass distribution at certain times, while the sought information is the velocity field that drives the mass along its displacement. The basic idea can be summarised as follows: given two snapshots of the mass distribution at two instants of time, we want to understand where each portion of the mass (which is assumed to be conserved from one instant of time to the other) is transported from/to, i.e. how the first spatial distribution is rearranged in the second one. The goal is pursued by computing a numerical approximation of the Wasserstein distance between the two consecutive density profiles, specifying a suitable cost function which measures the “energy” consumed by the system for moving forward. The computation of the Wasserstein distance gives, as a by-product, the minimum-cost mass flow from the first to the second configuration, i.e. how the mass distributes in space and time.

Despite the good preliminary results obtained by the Wasserstein-based approach [7, 96], the algorithm is found to be excessively expensive both in terms of CPU time and memory requirements. This fact strongly restricts the applicability of the method. To fix this, we propose to couple the method with the Dynamic Mode Decomposition (DMD): a data-driven technique that takes in input the snapshots of the mass distribution and returns a system of ODEs describing the evolution of the mass in any point of the domain. Solving the ODEs, we are able to recover the mass distribution at any time, thus increasing at will the number of available snapshots or, analogously, decreasing at will the time frame between them. Controlling the time frame between two consecutive snapshots is the key to simplify the computation of the Wasserstein distance and makes the computation of the flows feasible even on large domains.

Finally, a real-world application of the proposed methodology is illustrated. We are interested in inferring activity-based human mobility flows from mobile phone data. We assume that mobile devices are not singularly tracked, but their logs are aggregated in order to obtain the total number of users in a given area. In this way we get the density profiles of people in a given area at various instants of time. The dataset we have at our disposal is provided by the Italian telecommunication company TIM. The time frame between two consecutive snapshots is 15 minutes. The goal is to “assign a direction” to the presence data, obtaining a “where-from-where-to” type of information, which reveals travel flows and patterns of people providing a sort of origin-destination matrix.

The chapter is organised as follows. In Section 7.1 we present the DMD method and the Wasserstein

distance. In Section 7.2 we show how to couple the two methods to obtain an efficient algorithm. In Section 7.3 we apply the proposed approach to real-life data.

7.1 Mathematical background

In this section we recall the building blocks of the methodology proposed in this chapter, namely the DMD method used to build a data-driven model, and the Wasserstein distance to determine the transport map driving the moving mass. Note that we use a different notation with respect to the previous chapters, denoting vectors in bold and matrices in bold upper case.

7.1.1 DMD method

DMD is a data-driven method capable of providing accurate assessments of the spatio-temporal coherent structures in a given complex system, or short-time future estimates of such a system. Here we follow the approach proposed in [87]. Let us assume to have a set of data $\mathcal{X} = \{\mathbf{y}(t_0), \dots, \mathbf{y}(t_{n_f})\}$ for some time instances $\{t_j\}_{j=0}^{n_f}$ with $\mathbf{y}(t_j) \in \mathbb{R}^N$, $j = 0, \dots, n_f$ and $\Delta t = t_{j+1} - t_j$ for $j = 0, \dots, n_f - 1$. The goal of the method is to build a mathematical model upon the dataset $\mathcal{X} \in \mathbb{R}^{N \times (n_f+1)}$. The DMD procedure thus constructs the approximate linear evolution $\widehat{\mathbf{y}}(t)$ for the dataset \mathcal{X} exploiting its low-rank structure:

$$\frac{d\widehat{\mathbf{y}}}{dt} = \widehat{\mathbf{A}}\widehat{\mathbf{y}} \quad (7.1)$$

where $\widehat{\mathbf{A}} \in \mathbb{R}^{N \times N}$ is unknown, $\widehat{\mathbf{y}}(0) = \widehat{\mathbf{y}}_0$, and the solution has the form

$$\widehat{\mathbf{y}}(t) = \sum_{i=1}^r \beta_i \boldsymbol{\psi}_i \exp(\omega_i t), \quad (7.2)$$

where $r < N$, $\boldsymbol{\psi}_i$ and ω_i are the eigenvectors and eigenvalues of the unknown matrix $\widehat{\mathbf{A}}$. The coefficients β_i of the vector $\boldsymbol{\beta}$ can be determined from the initial data. For example, at $t = t_0$ we have $\mathbf{y}(t_0) = \mathbf{y}_0$ so that (7.2) gives $\boldsymbol{\beta} = \boldsymbol{\Psi}^\dagger \mathbf{y}_0$, where $\boldsymbol{\Psi}$ is a matrix comprised of the DMD modes $\boldsymbol{\psi}_i$ and \dagger denotes the Moore-Penrose pseudo-inverse. To compute the matrix $\widehat{\mathbf{A}}$, we first split the dataset into two snapshot matrices

$$\mathbf{Y} = \left[\mathbf{y}(t_0) \mid \mathbf{y}(t_1) \mid \dots \mid \mathbf{y}(t_{n_f-1}) \right], \quad \mathbf{Y}' = \left[\mathbf{y}(t_1) \mid \mathbf{y}(t_2) \mid \dots \mid \mathbf{y}(t_{n_f}) \right] \quad (7.3)$$

and suppose the following linear relation hold true:

$$\mathbf{Y}' = \mathbf{A}\mathbf{Y}, \quad (7.4)$$

where $\mathbf{A} := \exp(\widehat{\mathbf{A}}\Delta t)$.

Specifically, we assume that $\mathbf{y}(t_j)$ is an initial condition to obtain $\mathbf{y}(t_{j+1})$, i.e. its corresponding output after some prescribed evolution time $\Delta t > 0$. Thus, the DMD method computes the best linear operator \mathbf{A} relating to the matrices above:

$$\mathbf{A} = \mathbf{Y}'\mathbf{Y}^\dagger. \quad (7.5)$$

We refer to \mathbf{Y} and \mathbf{Y}' as input and output snapshot matrices respectively.

The DMD algorithm aims at optimally constructing the matrix \mathbf{A} so that the error between the true and approximate solution is small in a least-square sense, i.e. $\|\mathbf{y}(t) - \widehat{\mathbf{y}}(t)\| \ll 1$. Of course, the optimality of the approximation holds only over the sampling window where \mathbf{A} is constructed, but the

approximate solution can be used to make future state predictions, and to decompose the dynamics into various time-scales.

The matrix \mathbf{A} is often highly ill-conditioned and when the state dimension n is large, the aforementioned matrix may be even intractable to analyse directly. Instead, DMD circumvents the eigen-decomposition of \mathbf{A} by considering a low rank representation in terms of a matrix $\hat{\mathbf{A}}$ projected with the Proper Orthogonal Decomposition (POD). Although the description of the POD method goes beyond the scopes of this paper, we recall that the POD projection solves the following optimisation problem

$$\min_{\varphi_1, \dots, \varphi_r \in \mathbb{R}^n} \sum_{j=0}^{n_f-1} \left\| \mathbf{y}(t_j) - \sum_{i=1}^r \langle \mathbf{y}(t_j), \varphi_i \rangle \varphi_i \right\|^2 \quad \text{such that } \langle \varphi_i, \varphi_j \rangle = \delta_{ij}, \quad (7.6)$$

where $\{\varphi_i\}_{i=1}^r$ are the POD projectors. The solution of the optimization problem (7.6) is obtained by means of a Singular Value Decomposition (SVD) of the dataset \mathbf{Y} , where the first $r \ll N$ columns of the left singular eigenvectors are the required POD basis. We refer to [90] for a complete description of the POD method.

The exact DMD algorithm proceeds as follows [87]: first, we collect data \mathbf{Y}, \mathbf{Y}' as in (7.3) and compute the reduced, or economy, singular value decomposition of \mathbf{Y}

$$\mathbf{Y} = \mathbf{U}\mathbf{\Sigma}\mathbf{V}^T.$$

Then, we compute the least-squares fit \mathbf{A} that satisfies $\mathbf{Y}' = \mathbf{A}\mathbf{Y}$ and project onto the POD modes \mathbf{U} . Specifically, the Moore-Penrose pseudo-inverse of \mathbf{Y} allows us to compute $\mathbf{A} = \mathbf{Y}'\mathbf{Y}^\dagger$, where the Moore-Penrose algorithm provides the least-square fitting procedure. In terms of its low-rank projection, this yields

$$\hat{\mathbf{A}} = \mathbf{U}^T \mathbf{A} \mathbf{U} = \mathbf{U}^T \mathbf{Y}' \mathbf{V} \mathbf{\Sigma}^{-1},$$

and then, we compute the eigen-decomposition of $\hat{\mathbf{A}} \in \mathbb{R}^{r \times r}$

$$\hat{\mathbf{A}} \mathbf{W} = \mathbf{W} \mathbf{\Lambda},$$

where $\mathbf{\Lambda}$ are the DMD eigenvalues. Finally, the DMD modes $\mathbf{\Psi}^{\text{DMD}}$ are given by

$$\mathbf{\Psi}^{\text{DMD}} = \mathbf{Y}' \mathbf{V} \mathbf{\Sigma}^{-1} \mathbf{W}. \quad (7.7)$$

The algorithm is summarised in Algorithm 2.

Algorithm 2: Exact DMD

- Input:** Snapshots $\{\mathbf{y}(t_0), \dots, \mathbf{y}(t_{n_f})\}$, Time step Δt .
- 1: Set $\mathbf{Y} = [\mathbf{y}(t_0), \dots, \mathbf{y}(t_{n_f-1})]$ and $\mathbf{Y}' = [\mathbf{y}(t_1), \dots, \mathbf{y}(t_{n_f})]$.
 - 2: Compute the reduced SVD of rank r of \mathbf{Y} , $\mathbf{Y} = \mathbf{U}\mathbf{\Sigma}\mathbf{V}^T$.
 - 3: Define $\hat{\mathbf{A}} := \mathbf{U}^T \mathbf{Y}' \mathbf{V} \mathbf{\Sigma}^{-1}$.
 - 4: Compute eigenvalues and eigenvectors of $\hat{\mathbf{A}} \mathbf{W} = \mathbf{W} \mathbf{\Lambda}$.
 - 5: Set $\mathbf{\Psi}^{\text{DMD}} = \mathbf{\Lambda}^{-1} \mathbf{Y}' \mathbf{V} \mathbf{\Sigma}^{-1} \mathbf{W}$.
 - 6: Set $\omega_i = \frac{\log(\lambda_i)}{\Delta t}$ for (7.2).
-

7.1.2 Wasserstein distance and optimal mass transfer problem

The notion of Wasserstein distance is strictly related to the Monge–Kantorovich optimal mass transfer problem [89], which can be easily explained as follows: given a sandpile with mass distribution ρ^i and a pit with equal volume and mass distribution ρ^f , find a way to minimise the cost of transporting sand into

the pit. The cost for moving mass depends on both the distance from the point of origin to the point of arrival and the amount of mass is moved along that path. We are interested in minimising this cost by finding the optimal path to transport the mass from the initial to the final configuration.

Given two density functions $\rho^i, \rho^f : \Omega \rightarrow \mathbb{R}$ for some bounded $\Omega \subset \mathbb{R}^n$ such that $\int_{\mathbb{R}^n} \rho^i = \int_{\mathbb{R}^n} \rho^f$, we define the L^p -Wasserstein distance between ρ^i and ρ^f as

$$W_p(\rho^i, \rho^f) = \left(\min_{T \in \mathcal{T}} \int_{\Omega} c(\boldsymbol{\xi}, T(\boldsymbol{\xi}))^p \rho^i(\boldsymbol{\xi}) d\boldsymbol{\xi} \right)^{\frac{1}{p}} \quad (7.8)$$

where

$$\mathcal{T} := \left\{ T : \Omega \rightarrow \Omega : \int_B \rho^f(\boldsymbol{\xi}) d\boldsymbol{\xi} = \int_{\{\boldsymbol{\xi} : T(\boldsymbol{\xi}) \in B\}} \rho^i(\boldsymbol{\xi}) d\boldsymbol{\xi}, \quad \forall B \subset \Omega \right\}$$

and $c : \Omega \times \Omega \rightarrow \mathbb{R}$ is a given cost function, which defines the cost of transferring a unit mass between any two points in Ω . Note that \mathcal{T} is the set of all possible maps which transfer the mass from one configuration to the other.

It is important to note here that we are not really interested in the actual value of the Wasserstein distance W_p , instead we look for the *optimal map* T^* which realises the arg min in (7.8), and represents the paths along which the mass is transferred.

7.1.3 Numerical approximation of the Wasserstein distance

A direct numerical approximation of definition (7.8) is unfeasible, but a discrete approach is still possible. Indeed, we can resort to classical problems (see Hitchcock's paper [45]) and methods (see e.g., [82, Sec. 6.4.1] and [84, Chap. 19]) to recast the original mass transfer problem in the framework of linear programming (LP). We also refer to [17] for a recent application of this methodology to traffic flow problems.

The idea consists in approximating the set Ω with a structured grid with N square cells C_1, \dots, C_N , as it is commonly done for the numerical approximation of PDEs. We denote by Δx the length of each side of the cells. Then, we define a graph \mathcal{G} whose nodes coincide with the centers of the N cells. Graph's edges are defined in such a way that each node is directly connected with each other, including itself.

Introducing a numerical error (controlled by the parameter Δx), we are allowed to assume that $\forall j = 1, \dots, N$ all the mass distributed in the cell C_j is concentrated in its centre, i.e. in a node of the graph. We come up with an initial mass $m_j^i := \int_{C_j} \rho^i dx$ and a final mass $m_j^f := \int_{C_j} \rho^f dx$, for $j = 1, \dots, N$, distributed on the graph nodes. Now, we simply aim at optimally rearranging the first mass into the second one moving it among the graph's nodes.

We denote by c_{jk} the cost to transfer a unit mass from node j to node k , and by x_{jk} the (unknown) mass moving from node j to node k . The problem is then formulated as

$$\text{minimise } \mathcal{H} := \sum_{j,k=1}^N c_{jk} x_{jk}$$

subject to

$$\sum_k x_{jk} = m_j^i \quad \forall j, \quad \sum_j x_{jk} = m_k^f \quad \forall k \quad \text{and} \quad x_{jk} \geq 0.$$

Defining

$$\begin{aligned} \mathbf{x} &= (x_{11}, x_{12}, \dots, x_{1N}, x_{21}, \dots, x_{2N}, \dots, x_{N1}, \dots, x_{NN})^T, \\ \mathbf{c} &= (c_{11}, c_{12}, \dots, c_{1N}, c_{21}, \dots, c_{2N}, \dots, c_{N1}, \dots, c_{NN})^T, \end{aligned}$$

$$\mathbf{b} = (m_1^i, \dots, m_N^i, m_1^f, \dots, m_N^f)^T,$$

and the $2N \times N^2$ matrix

$$\mathbf{M} = \begin{bmatrix} \mathbb{1}_N & 0 & 0 & \dots & 0 \\ 0 & \mathbb{1}_N & 0 & \dots & 0 \\ 0 & 0 & \mathbb{1}_N & \dots & 0 \\ \vdots & \vdots & \vdots & \ddots & \vdots \\ 0 & 0 & 0 & \dots & \mathbb{1}_N \\ \mathbf{I}_N & \mathbf{I}_N & \mathbf{I}_N & \mathbf{I}_N & \mathbf{I}_N \end{bmatrix},$$

where \mathbf{I}_N is the $N \times N$ identity matrix and $\mathbb{1}_N = \underbrace{(1 \ 1 \ \dots \ 1)}_{N \text{ times}}$, our problem is written as a standard LP problem:

$$\begin{aligned} \min \quad & \mathbf{c}^T \mathbf{x}, \\ \text{subject to} \quad & \mathbf{M}\mathbf{x} = \mathbf{b}, \\ & \mathbf{x} \geq 0. \end{aligned} \tag{7.9}$$

The result of the algorithm is a vector $\mathbf{x}^* := \arg \min \mathbf{c}^T \mathbf{x}$ whose elements x_{jk}^* represent how much mass moves from node j to node k employing the minimum-cost mass rearrangement.

Remark 7.1.1. *The dimension of the LP problem (7.9) is given by the dimensions of the matrix/vectors involved:*

$$\dim \mathbf{x} = \dim \mathbf{c} = N^2, \quad \dim \mathbf{b} = 2N, \quad \dim \mathbf{M} = 2N^3.$$

Remark 7.1.2. *Hereafter we will refer to problem (7.9) as global, in order to stress the fact that it is possible to move the mass from and to any node of the graph.*

7.2 Coupling DMD and optimal mass transfer problem

In this section we describe how we can drastically reduce the size of the LP problem (7.9) by using the DMD method. The resulting algorithm will allow us to study the mass transfer problem on large domains.

7.2.1 Main idea

The large size of the LP problem (7.9), stressed in Remark 7.1.1, mainly comes from the fact that the mass is allowed to be transferred from any graph node to any other graph node. However physical constraints prevent this to happening: assuming that the maximal velocity of the mass is V_{\max} and denoting by Δt the time frame from one snapshot to the following one, the maximal distance travelled is $V_{\max} \Delta t$.

In order to reduce the size of the LP problem (7.9), we restrict the set of all possible movements trajectories. The ideal time frame δt of the snapshots would be the one which guarantees that the CFL-like condition

$$V^{\max} \delta t \leq \Delta x \tag{7.10}$$

holds true. Indeed, under condition (7.10) the mass is allowed to move only towards the adjacent cells or not move at all.

Consider now a generic set of mass distributions $\mathcal{X} = \{\mathbf{m}(t_0), \dots, \mathbf{m}(t_{n_f})\}$, where $t_j = j\Delta t$, $j = 0, \dots, n_f$, and Δt is the time frame of the snapshots of the set \mathcal{X} . *A priori*, the time step Δt does not necessarily satisfy condition (7.10). In particular, a large distance in time between the snapshots means that there are not enough information for reducing the set of possible movements. However, with the DMD we are able to reconstruct the state of the system at any time instance, even if it is not provided in the original dataset. The coupling of DMD and of optimal mass transfer problem is done in this order:

- i) We first fix $\delta t < \Delta t$ such that it satisfies condition (7.10) and then we reconstruct the solution for each $\tilde{t}_j = j\delta t$ via DMD, using Algorithm 2. The new set of snapshots we work with is $\tilde{\mathcal{X}} = \{\mathbf{m}(\tilde{t}_0), \dots, \mathbf{m}(\tilde{t}_{\tilde{n}_f})\}$, where $\mathbf{m}(\tilde{t}_j)$ is computed from (7.2), $j = 0, \dots, \tilde{n}_f$. We observe that $\tilde{n}_f > n_f$.
- ii) We recover the flows from the new set $\tilde{\mathcal{X}}$ by means of an approximation of Wasserstein distance similar to the one done in Section 7.1.3, but with reduced size, as described in detail below. Note that, since $\tilde{n}_f > n_f$, we have to solve more LP problems with respect to the global approach, but, despite this, we will get advantages by using this new approach.

Let us denote by d the maximum number of neighbors per cell. The new unknown \tilde{x}_{jk} , corresponding to the mass to be moved from node j to node k , is defined only if j and k are adjacent or j is equal to k . Analogously we define the cost function \tilde{c}_{jk} . We denote by $\tilde{\mathbf{x}}$ the vector of the unknowns and by $\tilde{\mathbf{c}}$ the vector associated to the cost function. We introduce the vector \mathbf{s} whose components are indexes of nodes. The first components are the indexes of the nodes adjacent to the node 1, then those adjacent to the node 2 and so until the node N . Vectors $\tilde{\mathbf{x}}$ and $\tilde{\mathbf{c}}$ are ordered similarly to \mathbf{s} . Since the mass can move only towards a maximum of d nodes, the dimensions of $\tilde{\mathbf{x}}$ and $\tilde{\mathbf{c}}$ are lower or equal than dN . We introduce the matrix

$$\tilde{\mathbf{M}} = \begin{bmatrix} \mathbb{1}_{r_1} & 0 & 0 & \dots & 0 \\ 0 & \mathbb{1}_{r_2} & 0 & \dots & 0 \\ 0 & 0 & \mathbb{1}_{r_3} & \dots & 0 \\ \vdots & \vdots & \vdots & \ddots & \vdots \\ 0 & 0 & 0 & \dots & \mathbb{1}_{r_N} \\ & & \tilde{\mathbf{D}} & & \end{bmatrix},$$

where $\mathbb{1}_{r_i} = \underbrace{(1 \ 1 \ \dots \ 1)}_{r_i \text{ times}}$, with r_i the number of adjacent nodes for each node i , $r_i \leq d$, and $\tilde{\mathbf{D}}_{ij} = 1$ if the j -th element of \mathbf{s} is equal to i , otherwise $\tilde{\mathbf{D}}_{ij} = 0$. Defining the vector $\tilde{\mathbf{b}} = (m_1^i, \dots, m_N^i, m_1^f, \dots, m_N^f)^T$ the LP problem becomes

$$\begin{aligned} \min \quad & \tilde{\mathbf{c}}^T \tilde{\mathbf{x}}, \\ \text{subject to} \quad & \tilde{\mathbf{M}} \tilde{\mathbf{x}} = \tilde{\mathbf{b}} \\ & \tilde{\mathbf{x}} \geq 0. \end{aligned} \tag{7.11}$$

Remark 7.2.1. *The dimension of the LP problem (7.11) is given by the dimensions of the matrix/vectors involved:*

$$\dim \tilde{\mathbf{x}} = \dim \tilde{\mathbf{c}} \leq dN, \quad \dim \tilde{\mathbf{b}} = 2N, \quad \dim \tilde{\mathbf{M}} \leq 2dN^2.$$

Remark 7.2.2. *Hereafter we will refer to problem (7.11) as local, in order to stress the fact that it is possible to move the mass from and to adjacent nodes of the graph only.*

7.2.2 A toy example for the complete algorithm: the advection equation

In this test we propose an example for the complete algorithm described in Section 7.2.1. Let us consider the advection equation:

$$\begin{cases} \partial_t u(\mathbf{x}, t) + \mathbf{v} \cdot \nabla u(\mathbf{x}, t) = 0 & \mathbf{x} \in \Omega, t \in [0, T] \\ u(\mathbf{x}, t) = 0 & \mathbf{x} \in \partial\Omega \\ u(\mathbf{x}, 0) = u_0(\mathbf{x}) & \mathbf{x} \in \Omega, \end{cases} \tag{7.12}$$

with $\mathbf{x} = (x_1, x_2)$, $\Omega = [-2, 2] \times [-2, 2]$, $u_0(\mathbf{x}) = \max(0.5 - x_1^2 - x_2^2, 0)$ and constant velocity $\mathbf{v} = (0.5, 0.5)$. It is well known that the analytical solution of (7.12) is $u(\mathbf{x}, t) = u_0(\mathbf{x} - \mathbf{v}t)$ provided that we set T small

enough to have inactive boundary conditions, as it is the case here. Hereafter we denote by *reference solution* the analytical solution u of (7.12). In Figure 7.1 we show the plot of the reference solution at times $t = 0$ and $t = 2$.

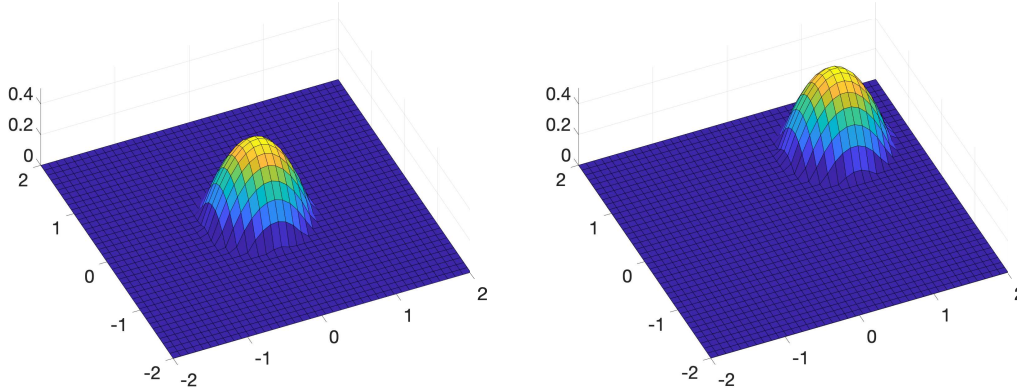


Figure 7.1. Reference solution of equation (7.12) at time $t = 0$ (left) and time $t = 2$ (right).

Starting from some snapshots of the solution, we aim at reconstructing the velocity field driving the dynamics, i.e. the vector $\mathbf{v} = (0.5, 0.5)$. In doing this, we will also compare the global and the local problem in terms of CPU time, see (7.9) and (7.11) respectively.

We choose a time step δt , and we collect snapshots with a larger temporal step size $\Delta t = \kappa \delta t$ with $\kappa > 1$ and we reconstruct the solution via the DMD method. We note that here the snapshots are computed from the analytical solution of (7.12). In particular, we work on a grid 40×40 and we choose $T = 2$, $\Delta x = 0.1$, $\delta t = 0.05$ and $\Delta t = 2 \delta t$. We observe that, since $V^{\max} = \|\mathbf{v}\| = \sqrt{2}/2$, this choice of δt fulfills the condition (7.10). The number of snapshots is 40 and the rank r in Algorithm 2 for the DMD reconstruction is 20. Moreover we identify the nodes of the graph \mathcal{G} of the numerical approximation of Wasserstein distance with the cells of the grid.

Choice of the cost function. Since the cost function is used to figure out the “price to pay” for moving the mass from a node of the graph to another one, the most intuitive definition of c is the Euclidean distance in \mathbb{R}^2 . This choice was proved to be unsuitable for the global problem, see [7]. Indeed, since the global algorithm allows any movements between the nodes of the graph, using the Euclidean distance for the function c we loose the uniqueness of the optimal transfer map T^* . To see this let us assume that we have to move three unit masses one to the right. In the picture on the left of Figure 7.2 we move the three unit masses of one to the right while in the picture on the right we move only the first mass of three to the right. The Wasserstein distance between the two configuration is clearly the same and equal to three.

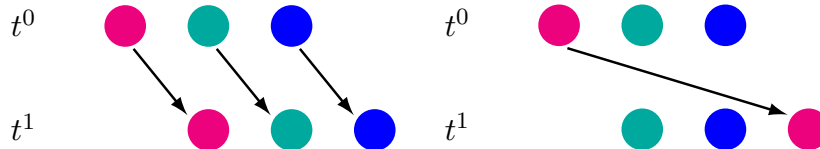


Figure 7.2. Three small movements versus one large movement.

The solution proposed in [7] to fix this issue was to force the minimisation algorithm to select primarily

7.2. Coupling DMD and optimal mass transfer problem

the small movements penalising the large ones. To get this, the cost function was defined as

$$c(\boldsymbol{\xi}_1, \boldsymbol{\xi}_2) = \|\boldsymbol{\xi}_1 - \boldsymbol{\xi}_2\|_{\mathbb{R}^2}^{1+\varepsilon}, \quad (7.13)$$

where $\boldsymbol{\xi}_1$ and $\boldsymbol{\xi}_2$ are the coordinates of the nodes of the graph and $\varepsilon > 0$ is a small parameter which accounts for the penalisation.

In Figure 7.3 we show the level sets of the solution to (7.12) together with some arrows indicating the reconstructed velocity field \mathbf{v} . More precisely, on the left column of figure we show the results obtained with the local algorithm (7.11), on the centre with the global algorithm with Euclidean distance and on the right with the global algorithm with the cost function defined in (7.13) (with $\varepsilon = 0.1$). Similarly, the panels on the top show the results obtained with the reference solution whereas the panels on the bottom those obtained with the DMD solution.

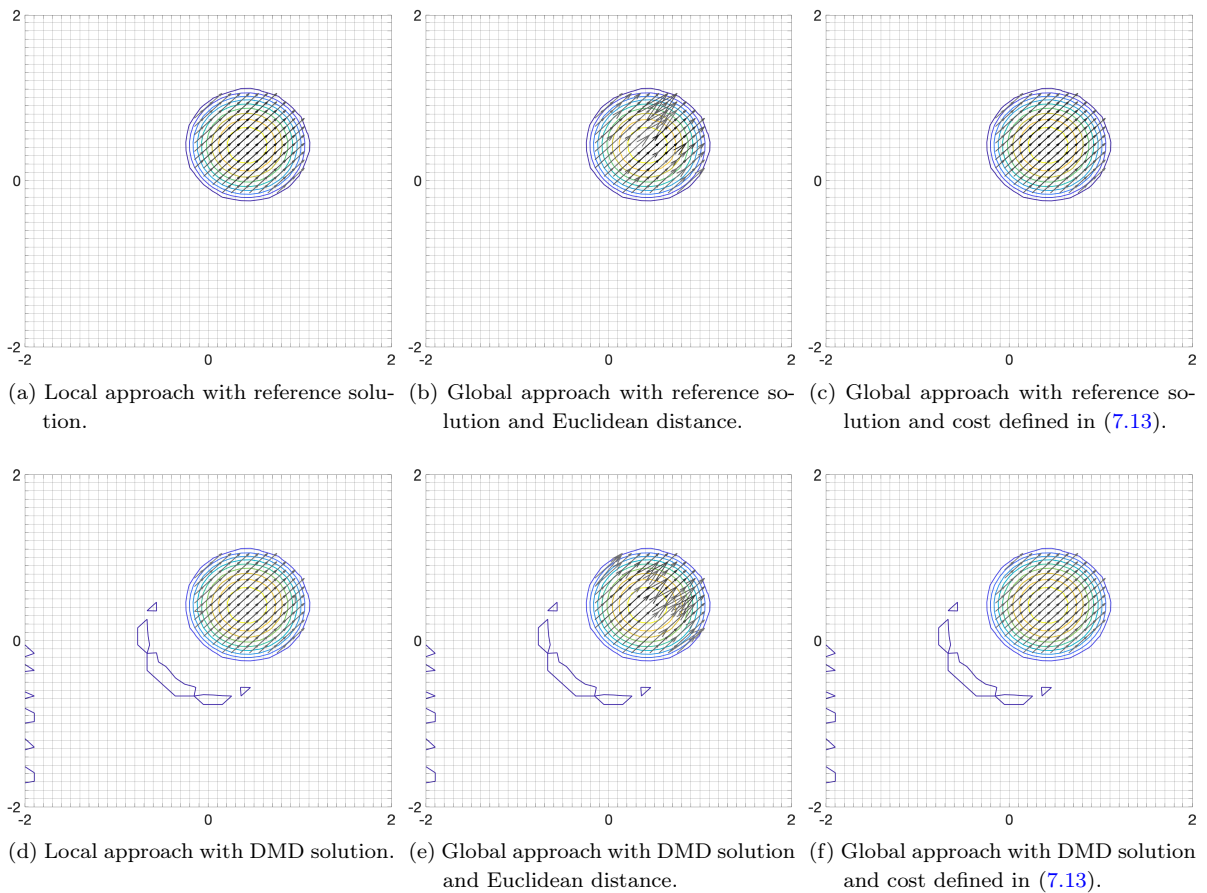


Figure 7.3. Reconstructed flows between $t_1 = 0.725$ and $t_2 = t_1 + \delta t$ superimposed to the level sets of the solution to (7.12) at t_2 . Left column: local algorithm. Central column: global algorithm with c equal to the Euclidean distance. Right column: global algorithm with c defined in (7.13). Top row: the reference solution to (7.12) is used for computation. Bottom row: the DMD reconstruction of the solution to (7.12) is used for computation.

The local algorithm and the global one with the correction in (7.13) are able to reconstruct the velocity field $\mathbf{v} = (0.5, 0.5)$ with accurate approximation. The global algorithm with Euclidean distance, instead, is less precise, since the optimal flow does not correspond to the velocity field. Moreover, the algorithm

based on the DMD reconstruction of the solution introduces small oscillations in the solution to (7.12). This is expected in such hyperbolic problems since the decay of the singular values of the dataset is very slow and the initial condition is non-smooth. However, such oscillations do not have an effect in the reconstruction of the flow.

To further validate our approach we compute the numerical error of the proposed algorithm. Since the results obtained with the global algorithm (7.9) with the Euclidean distance as cost function are the least accurate, we focus only on the other two approaches. For each time step $t_n = n\delta t$ we define $\mathbf{x}_E^*(t_n)$ and $\tilde{\mathbf{x}}_E^*(t_n)$ as the solutions to the LP problems (7.9) and (7.11) respectively at time t_n , when the known terms $\mathbf{b}(t_n)$ and $\tilde{\mathbf{b}}(t_n)$ are chosen as the reference solution to (7.12) at time t_n . Analogously, \mathbf{x}_D^* and $\tilde{\mathbf{x}}_D^*$ are the solution when the known terms are obtained with the DMD method. The vectors $\mathbf{x}_E^*(t_n)$, $\tilde{\mathbf{x}}_E^*(t_n)$, $\mathbf{x}_D^*(t_n)$ and $\tilde{\mathbf{x}}_D^*(t_n)$, for $n = 1, \dots, \lfloor \frac{T}{\delta t} \rfloor + 1$, are finally collected as the columns of the matrices \mathbf{X}_E^* , $\tilde{\mathbf{X}}_E^*$, \mathbf{X}_D^* and $\tilde{\mathbf{X}}_D^*$ respectively. We define the errors

$$E^G := \frac{\|\mathbf{X}_E^* - \mathbf{X}_D^*\|_F}{\|\mathbf{X}_E^*\|_F}, \quad E^L := \frac{\|\tilde{\mathbf{X}}_E^* - \tilde{\mathbf{X}}_D^*\|_F}{\|\tilde{\mathbf{X}}_E^*\|_F}, \quad (7.14)$$

where $\|\cdot\|_F$ is the Frobenius norm. In Table 7.1 we compare the errors defined in (7.14) obtained from the simulations on a grid with $N \times N$ nodes, for $N = 20, 30$ and 40 . As we can see from the table, increasing the number of nodes we reduce the space step $\Delta x = 4/N$ and the time step $\Delta t = \Delta x/2$ and we obtain the decrease of the error between the reference solution and the DMD reconstruction. Moreover, the error obtained with the local algorithm is significantly smaller than the one obtained with the global approach.

N	Δx	Δt	E^G	E^L
20	0.20	0.100	0.185	0.030
30	0.13	0.067	0.159	0.028
40	0.10	0.050	0.122	0.020

Table 7.1. Comparison of the errors defined in (7.14).

Finally, in Table 7.2 we compare the computational time between the global approach (7.9), with the cost function as in (7.13), and the local approach (7.11) with respect to the nodes of the graph. We observe that the local algorithm is always faster than the global one. The difference between the two approaches becomes more relevant when we refine the grid by increasing the number of nodes, and thus the number of time steps. Specifically, for a grid 40×40 , the local algorithm required a few seconds whereas the global one more than three hours.

N	Global Exact	Global DMD	Local Exact	Local DMD
20	18.10 s	18.89 s	0.28 s	0.36 s
30	11 min	11 min	0.93 s	1.41 s
40	3 h 6 min	3 h 7 min	2.40 s	4.85 s

Table 7.2. Computational time.

7.3 Application to real mobile phone data

In this section we focus on a specific application of the proposed approach. The real dataset gives information about the spatial distribution of people in a large populated area. The goal is to understand

the travel flows of people, focusing in particular on recurring patterns and daily flows of commuters.

7.3.1 Dataset

The Italian telecommunication company TIM provides estimates of mobile phones presence in a given area in raster form: the area under analysis is split into a number of elementary territory units (ETUs) of the same size (about $130 \times 140 \text{ m}^2$ in urban areas). The estimation algorithm does not singularly recognise users and does not track them using GPS. It simply counts the number of phone attached to network nodes and, knowing the location and radio coverage of the nodes, estimates the number of TIM users within each ETU at any time. TIM has now a market share of 30% with about 29.4 million mobile lines in Italy (AGCOM, Osservatorio sulle comunicazioni 2/2017).

The data we considered refer to the area of the province of Milan (Italy), which is divided in 198,779 ETUs, distributed in a rectangular grid 389×511 . Data span six months (February, March and April 2016 and 2017). The entire period is divided into time intervals of 15 minutes, therefore we have 96 data per day per ETU in total. In Figure 7.4 we graphically represent presence data at a fixed time. We observe that the peak of presence is located in correspondence of Milan city area. Figure 7.5 shows

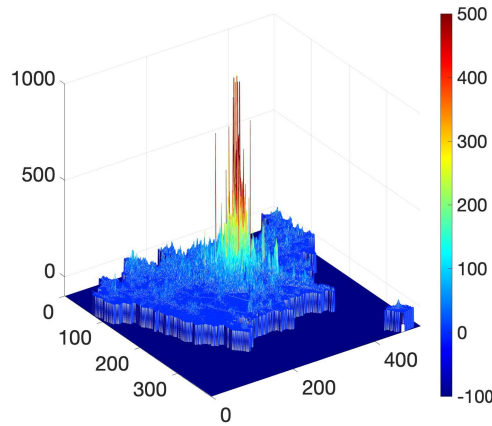


Figure 7.4. 3D-plot of the number of TIM users in each ETU of Milan's province on April 18, 2017.

the presences in the province of Milan in a typical working day in the left panel. The curve in the image decreases during the night, it increases in the day-time and decreases again in the evening. These variations are due to two main reasons: first, the arrival to and departure from Milan's province of visitors and commuters. Second, the fact that when a mobile phone is switched off or is not communicating for more than six hours, its localization is lost. The presence value that most represents the population of the province is observed around 9 pm., when an equilibrium between traveling and phone usage is reached. This value changes between working days and weekends, but it is always in the order of 1.3×10^6 . On the right panel of Figure 7.5 we show the trend of presence data during April 2017. We can observe a cyclical behaviour: in the working days the number of presences in the province is significantly higher than during the weekends. It is interesting to note the presence of two low-density periods on April 15-18 and on April 22-26, 2017, determined respectively by the Easter and the long weekend for the Italy's Liberation Day holiday.

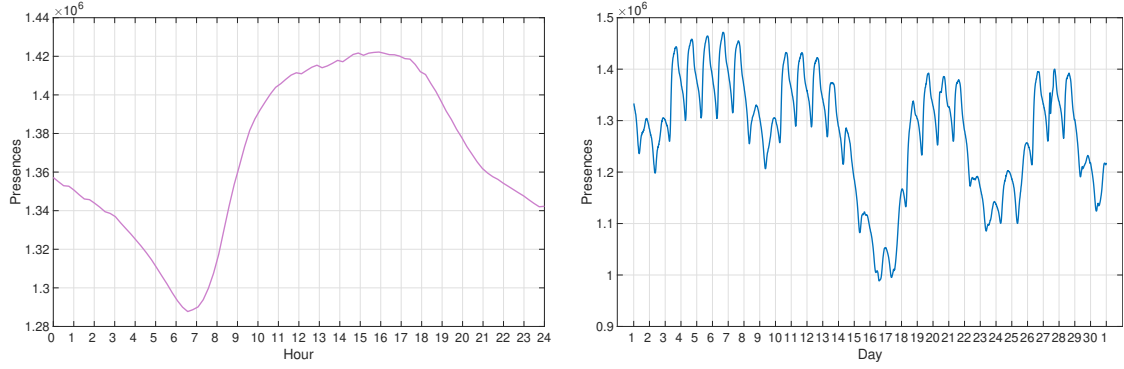


Figure 7.5. Trend of presences in the province of Milan during a typical working day (left). Trend of presences in the province of Milan during April 2017 (right).

7.3.2 DMD approach on TIM data

As explained in Section 7.1.1, we can reconstruct the presence data in each cell at any time. We denote by $\mathbf{m}(t^i) \in \mathbb{R}^N$ the vector containing the number of people present in the N cells at a certain quarter of an hour and by $\mathbf{m}(t^i + 15 \text{ min}) \in \mathbb{R}^N$ the same quantities at the consecutive time step. Applying the DMD method we are able to calculate $\mathbf{m}(t) \in \mathbb{R}^N$ for any $t \in [t^i, t^i + 15 \text{ min}]$, see (7.2). We also note that DMD can be applied to higher dimensional dataset through randomised methods as explained in [2].

To validate the DMD approach on the TIM dataset we study the daily error using only half of the data at our disposal in the DMD reconstruction. More precisely, we denote by \mathbf{P}^{data} the matrix whose columns correspond to the real data of presences stored every 15 minutes. Then, we reconstruct the data of presences every minute with the DMD algorithm, using snapshots every 30 minutes. In other words, we exploit only one column out of two of \mathbf{P}^{data} to build the matrix $\tilde{\mathbf{P}}^{\text{DMD}}$, which collects the reconstructed data every minute. Since a day contains 96 quarters of an hour and 1440 minutes, \mathbf{P}^{data} is a matrix $96 \times N$, while $\tilde{\mathbf{P}}^{\text{DMD}}$ is a matrix $1440 \times N$. Finally, to compare the real data with the DMD reconstruction, we extract from $\tilde{\mathbf{P}}^{\text{DMD}}$ the rows corresponding to the original interval of 15 minutes into the matrix $\tilde{\mathbf{P}}^{\text{DMD}}$, of dimensions $96 \times N$, and then we define the error as:

$$E = \frac{\|\mathbf{P}^{\text{data}} - \tilde{\mathbf{P}}^{\text{DMD}}\|_F}{\|\mathbf{P}^{\text{data}}\|_F}. \quad (7.15)$$

In Figure 7.6 we show the daily error (7.15) for an entire month of data in the whole area of the province of Milan. The daily error is of order 10^{-2} , which certifies the accuracy of the DMD method.

7.3.3 Understanding human mobility flows

Following the approach described in Section 7.2, we define the graph \mathcal{G} by exploiting the subdivision of the area of the province of Milan (Italy) into ETUs; we identify the N nodes of the graph with the corresponding centre of the ETUs, ordered from the left to the right and from the top to the bottom. The result is a rectangular graph \mathcal{G} divided into N_R rows and N_C columns ($N = N_R \times N_C$). The mass $m_j(t_n)$ is defined as the average number of presences in the node j at time $t_n = n \cdot 15 \text{ min}$.

Let us assume that V_{max} in (7.10) is equal to 50 km/h. Since the dimensions of the ETUs is around 150 m, to apply the DMD we fix the new time step δt equal to 10 seconds. With this choice we assume that people can move only towards the eight adjacent nodes of the rectangular graph, or not move at all. We observe that the mass in the nodes on the four corners of the graph can move only towards four

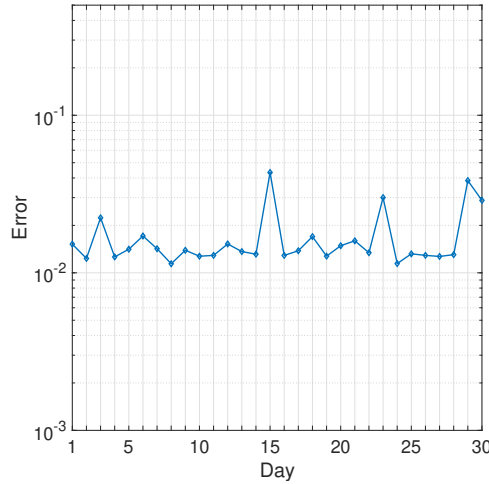


Figure 7.6. Daily error defined in (7.15) where DMD has been computed with $r = 95$ in step 2 of Algorithm 2.

directions (adjacent nodes or no movement), while the mass along the boundaries can move only towards six directions. In this way, the total number of possible movements between the cells is given by

$$\tilde{N} = \underbrace{4 \cdot 4}_{\text{corners}} + \underbrace{6 \cdot 2(N_R + N_C - 4)}_{\text{boundaries}} + \underbrace{9(N - 4 - 2(N_R + N_C - 4))}_{\text{internal nodes}} < 9N. \quad (7.16)$$

The vectors $\tilde{\mathbf{x}}$ and $\tilde{\mathbf{c}}$ associated to the unknown moving mass and to the cost function have length \tilde{N} , while the matrix $\tilde{\mathbf{M}}$ of the LP problem (7.11) has dimension $2N \times \tilde{N}$. In Table 7.3, we compare the dimensions of the vectors and the matrices of the two different LP problems: it is clear that the computational time to solve problem (7.11) is significantly reduced respect to problem (7.9).

Algorithm	Vectors Dimension	Matrix Dimension
Global	N^2	$2N^3$
Local	$\tilde{N} (< 9N)$	$2N \times \tilde{N} (< 18N^2)$

Table 7.3. Comparison between dimensions of matrices and vectors for the two methods.

Choice of the cost function c . Since the ETUs are rectangles of length $\ell_x = 130$ m and $\ell_y = 140$ m, we define the cost function c_{jk} for the local algorithm as follows:

$$c_{jk} = \begin{cases} 0 & \text{if } j = k \text{ or } j \text{ and } k \text{ are not adjacent} \\ \ell_x & \text{if } j \text{ and } k \text{ are horizontally adjacent} \\ \ell_y & \text{if } j \text{ and } k \text{ are vertically adjacent} \\ \sqrt{\ell_x^2 + \ell_y^2} & \text{if } j \text{ and } k \text{ are diagonally adjacent.} \end{cases}$$

For the global approach, we use the cost function defined in (7.13) with $\varepsilon = 0.1$.

To sum up, in order to solve the mass transfer problem for a whole day using snapshots taken every 15 minutes (real data) we have to solve 96 global LP-problems (7.9), whereas with the DMD algorithm we have to solve 8640 local LP-problems (7.11). As we will see in the following section, despite the larger number of LP problems, the local approach is more convenient than the global one.

Remark 7.3.1. *The Wasserstein distance is defined between two distributions of equal mass (see (7.8)). In our case the conservation of mass between two consecutive snapshots is not guaranteed. Let us consider a couple of snapshots with different total mass $\sum_j m_j^0 \neq \sum_j m_j^1$. To correctly apply the algorithms for the identification of flows, we compute the mass in excess between the two snapshots and then we uniformly distribute it in all the nodes of the graph with lower mass. A more sophisticated approach could be the one suggested in [73], where a definition of Wasserstein distance between two distributions with different mass is proposed.*

7.3.4 Numerical results

In this section we show the results obtained with the local algorithm (7.11) to study the flows of commuters and the influence of great events on human mobility. In both cases the rank r in step 2 of Algorithm 2, used for the construction of the DMD solution, is 95. The flows are represented by arrows; we draw only those which correspond to the most significant movements, and we associate a darker colour to the arrows corresponding to a larger movement of people. For graphical purposes, in the following plots we aggregate 6 time steps δt to show 1-minute mass transport.

Flows of commuters

In the following simulations we consider the area of the Province of Milan during a generic working day. Milan is one of the biggest Italian city and it attracts many workers from outside. The city of Milan is located in the right part of the Province, therefore we mainly see movements from/to the left part of the analysed area. In the top panel of Figure 7.7 we show the morning flows of a working day: we clearly see that the arrows are directed towards the city of Milan. In particular, we zoom on the arrows which overlap the roads heading to Milan. In the bottom panel of Figure 7.7 we show the opposite phenomenon: in the evening people go away from work to come back home inside the Province of Milan.

CPU times. Considering data for a 6 hours frame on an area of 144×240 ETUs the local algorithm requires 144 hours of CPU time and works with 360 snapshots. The global approach (7.9) is not able to analyse such an area, since the matrix \mathbf{M} in (7.9) has a computationally unmanageable dimension.

Flows influenced by a great event

In this test we show how the algorithm is able to capture the way a big event influences human flows. The event we have considered is the exhibition of the *Salone del Mobile*, held every April at Fiera Milano exhibition centre in Rho, near Milan. We analyse a square area of 31×31 ETUs centred around Fiera Milano. In the left panel of Figure 7.8 we show the morning fluxes directed to the exhibition area whereas in the right panel we show the evening flows directed from the exhibition area to the outside.

CPU times. For a simulation of 18 hours, from 06:00 to 23:45, on an area of 31×31 ETUs, the local algorithm requires 6 minutes of CPU time while the global approach requires 30 minutes. Furthermore, the local algorithm works with 1065 snapshots of data, whereas the global one with 266 snapshots.

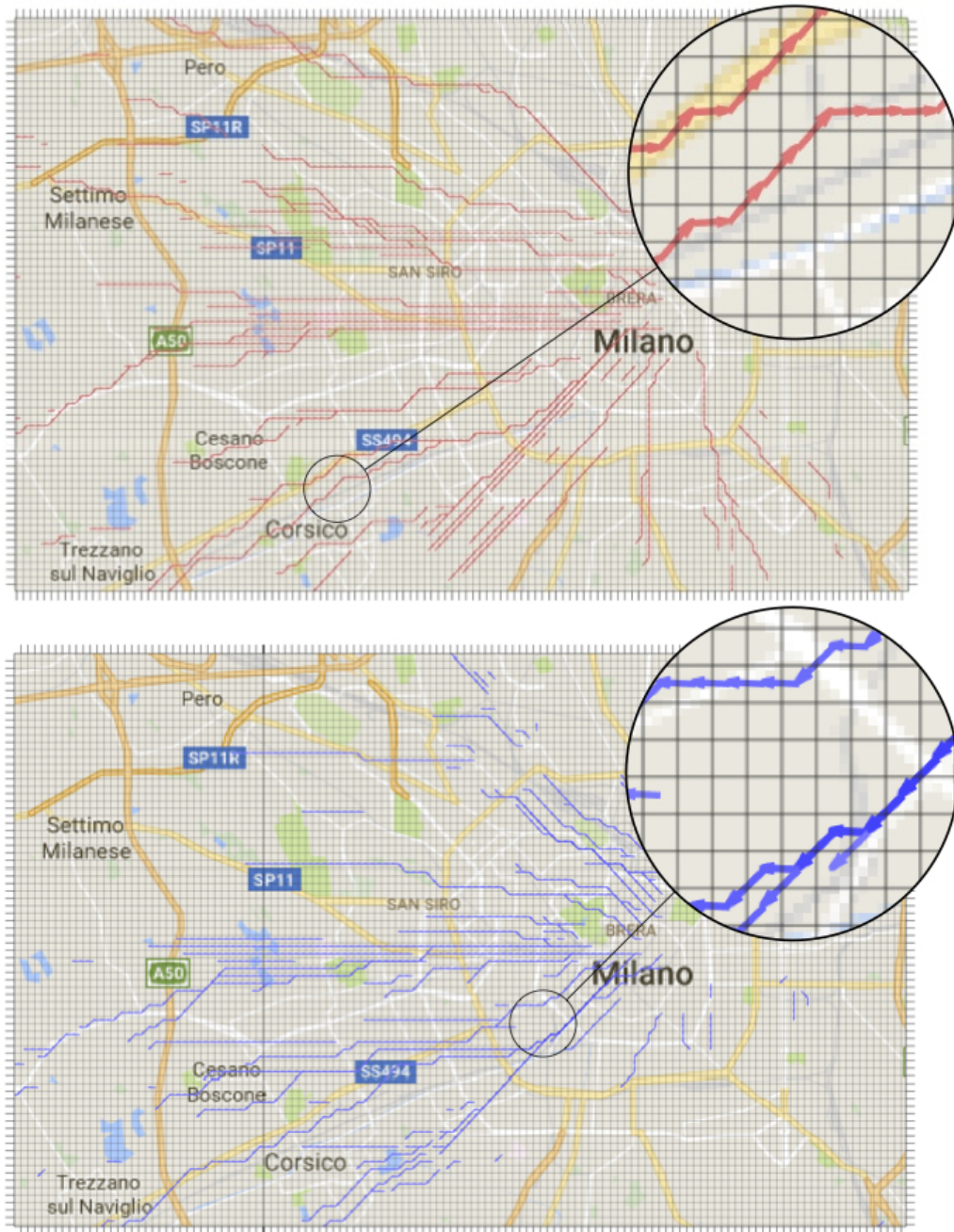


Figure 7.7. Flows of commuters during the morning (09:00-09:01) of a generic working day (top). Flows of commuters during the evening (18:00-18:01) of a generic working day (bottom).

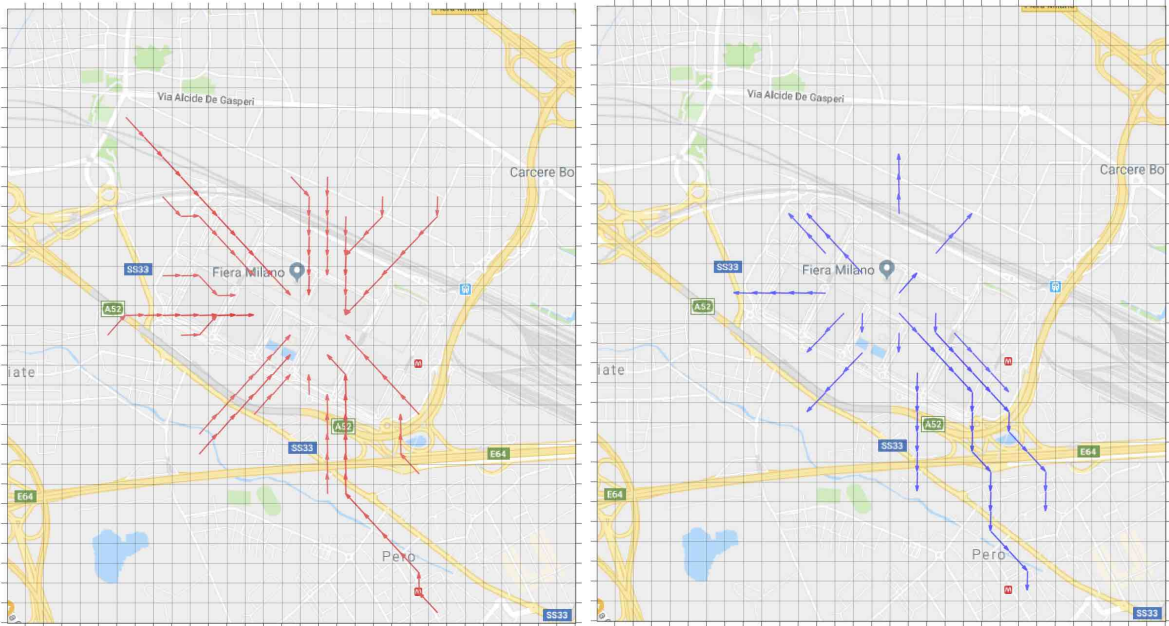


Figure 7.8. Main flows directed to the exhibition area in the morning (09:45 - 09:46) (left). Main flows from the exhibition area in the evening (18:00 - 18:01) (right).

Conclusions

In this thesis we have extended the GSOM family of macroscopic second order traffic models to road networks. We proposed a Riemann Solver based on a priority rule, providing an iterative algorithm which builds the solution to junctions with n incoming and m outgoing roads. According to the traffic dynamics to simulate, the Riemann Solver adapts the priority rule, modifying it in order to maximise the flux of vehicles at junctions. Then we provided bounds on the total variation of the flux Q and of w for waves interacting with the junction, which are preliminary to the existence result of weak solutions to Cauchy problems, giving explicit computations for the case of two incoming and two outgoing roads at the intersection. Next, we analysed different traffic dynamics, focusing on diverge and merge junctions and on roundabouts. Moreover, we investigated the environmental impact of vehicular traffic, proposing a tool to estimate the pollutant emissions resulting from traffic dynamics and we set up a minimisation problem that finds the priority rule of the Riemann Solver which minimises the emission rates. The analysis of pollutants has been mainly devoted to nitrogen oxides (NO_x) and the chemical reactions leading to ozone production, focusing on the effects of traffic lights presence on the roads. The numerical results showed the growth of NO_x emissions and ozone production with the increase of vehicles restarts, suggesting to prefer long time traffic lights rather than short ones. Furthermore, we have introduced a macroscopic two-dimensional multi-class traffic model on a single road, aimed at exploiting all the information of traffic datasets, which generally contain data on multi-lane roads with different types of vehicles. We proposed a multi-class model consisting of a coupled system of conservation laws in two space dimensions. We studied the two-dimensional Riemann problems, recovering the theoretical results by means of numerical tests with a Lax-Friedrichs type discretisation. We also calibrated the multi-class model with real data, comparing the fitted model to the real trajectories, and tested its ability to simulate the overtaking of vehicles. Finally, we presented a new methodology to recover mass movements from snapshots of its distribution. We proposed an algorithm based on the combination of the dynamic mode decomposition, which creates a mathematical model describing the mass transfer, and the Wasserstein distance, which reconstructs the underlying velocity field responsible for the displacement. The methodology has been used for a real-life application aimed at reconstructing the travel flows of people in large populated areas using, as input data, density profiles of people in given areas, derived from the mobile phone network, at different time instants.

To conclude, we present some open problems related to the topics treated in this thesis. As a first issue, we are working on the proof of the existence result of weak solutions to Cauchy problems for GSOM on networks via Wave-Front-Tracking. The technical details are still under investigation and will be treated in a forthcoming work. Another future perspective regards the estimate of the effects of vehicular traffic on pollution, which can be developed in several ways. We are interested in extending the optimal control problem aimed at minimising the production of pollutants through the action on the traffic flow. Moreover, it is necessary to include the analysis of the diffusion of pollutants in the atmosphere through a suitable reaction-diffusion model. Furthermore, the analysis of other chemical

Conclusions

species, such as the particulate matter, which requires a specific chemical model, should be examined. Finally, we are investigating how to extend the two-dimensional multi-class model to second order models. The inclusion of different classes of vehicles is interesting to better estimate the pollution due to vehicular traffic, distinguishing not only for the type of vehicle but also, for instance, for the type of fuel, resulting in more accurate analyses.

Bibliography

- [1] A. ALLA, C. BALZOTTI, M. BRIANI, AND E. CRISTIANI, *Understanding Mass Transfer Directions via Data-Driven Models with Application to Mobile Phone Data*, SIAM J. Appl. Dyn. Syst., 19 (2020), pp. 1372–1391.
- [2] A. ALLA AND J. N. KUTZ, *Randomized model order reduction*, Adv. Comput. Math., 45 (2019), pp. 1251–1271.
- [3] L. ALVAREZ-VÁZQUEZ, N. GARCÍA-CHAN, A. MARTÍNEZ, AND M. VÁZQUEZ-MÉNDEZ, *Numerical simulation of air pollution due to traffic flow in urban networks*, J. Comput. Appl. Math., 326 (2017), pp. 44 – 61.
- [4] R. ATKINSON AND W. P. CARTER, *Kinetics and mechanisms of the gas-phase reactions of ozone with organic compounds under atmospheric conditions*, Chem. Rev., 84 (1984), pp. 437–470.
- [5] A. AW, A. KLAR, T. MATERNE, AND M. RASCLE, *Derivation of continuum traffic flow models from microscopic follow-the-leader models*, SIAM J. Appl. Math., 63 (2002), pp. 259–278.
- [6] A. AW AND M. RASCLE, *Resurrection of “Second Order” Models of Traffic Flow*, SIAM J. Appl. Math., 60 (2000), pp. 916–944.
- [7] C. BALZOTTI, A. BRAGAGNINI, M. BRIANI, AND E. CRISTIANI, *Understanding Human Mobility Flows from Aggregated Mobile Phone Data*, IFAC-PapersOnLine, 51-9 (2018), pp. 25–30. 15th IFAC Symposium on Control in Transportation Systems CTS 2018.
- [8] C. BALZOTTI, M. BRIANI, B. DE FILIPPO, AND B. PICCOLI, *Evaluation of NO_x emissions and ozone production due to vehicular traffic via second-order models*, arXiv preprint arXiv:1912.05956, (2019).
- [9] ———, *Towards a comprehensive model for the impact of traffic patterns on air pollution*, in Proceedings of the 6th International Conference on Vehicle Technology and Intelligent Transport Systems, vol. 1, 2020, pp. 221–228.
- [10] C. BALZOTTI, M. BRIANI, AND B. PICCOLI, *Estimate of emissions on road networks via generic second order models*, arXiv preprint arXiv:2004.11202, (2020).
- [11] C. BALZOTTI AND S. GÖTTLICH, *A two-dimensional multi-class traffic flow model*, Netw. Heterog. Media, 16 (2021), pp. 69–90.
- [12] M. BARTH, F. AN, T. YOUNGLOVE, G. SCORA, C. LEVINE, M. ROSS, AND T. WENZEL, *Development of a comprehensive modal emissions model: Final report*, tech. rep., National Research Council, Transportation Research Board, National Cooperative Highway Research Program, NCHRP Project 25-11, 2000.

Bibliography

- [13] N. BELLOMO AND C. DOGBE, *On the modeling of traffic and crowds: a survey of models, speculations, and perspectives*, SIAM Rev., 53 (2011), pp. 409–463.
- [14] S. BERTOLUZZA, S. FALLETTA, G. RUSSO, AND C.-W. SHU, *Numerical solutions of partial differential equations*, Advanced Courses in Mathematics. CRM Barcelona, Birkhäuser Verlag, Basel, 2009. Lecture notes from the Advanced School on Numerical Solutions of Partial Differential Equations: New Trends and Applications held in Bellaterra, November 15–22, 2007.
- [15] S. BLANDIN, D. WORK, P. GOATIN, B. PICCOLI, AND A. BAYEN, *A General Phase Transition Model for Vehicular Traffic*, SIAM J. Appl. Math., 71 (2011), pp. 107–127.
- [16] A. BRESSAN, *Hyperbolic Systems of Conservation Laws: The One-dimensional Cauchy Problem*, vol. 20, Oxford Univ. Press, 2000.
- [17] M. BRIANI, E. CRISTIANI, AND E. IACOMINI, *Sensitivity analysis of the LWR model for traffic forecast on large networks using Wasserstein distance*, Commun. Math. Sci., 16 (2018), pp. 123–144.
- [18] D. C. CARSLAW, S. D. BEEVERS, J. E. TATE, E. J. WESTMORELAND, AND M. L. WILLIAMS, *Recent evidence concerning higher NO_x emissions from passenger cars and light duty vehicles*, Atmos. Environ., 45 (2011), pp. 7053–7063.
- [19] B. N. CHETVERUSHKIN, N. G. CHURBANOVA, Y. N. KARAMZIN, AND M. A. TRAPEZNIKOVA, *A two-dimensional macroscopic model of traffic flows based on KCFD-schemes*, in ECCOMAS CFD 2006: Proceedings of the European Conference on Computational Fluid Dynamics, Egmond aan Zee, The Netherlands, September 5–8, 2006, Citeseer, 2006.
- [20] R. M. COLOMBO, *A 2×2 hyperbolic traffic flow model*, Math. Comput. Modelling, 35 (2002), pp. 683–688. Traffic flow—modelling and simulation.
- [21] ———, *Hyperbolic Phase Transitions in Traffic Flow*, SIAM J. Appl. Math., 63 (2003), pp. 708–721.
- [22] R. COURANT, K. FRIEDRICHS, AND H. LEWY, *On the partial difference equations of mathematical physics*, IBM J. Res. Develop., 11 (1967), pp. 215–234.
- [23] C. M. DAFERMOS, *Hyperbolic conservation laws in continuum physics*, vol. 325 of Grundlehren der Mathematischen Wissenschaften [Fundamental Principles of Mathematical Sciences], Springer-Verlag, Berlin, fourth ed., 2016.
- [24] C. F. DAGANZO, *The cell transmission model: A dynamic representation of traffic consistent with the hydrodynamic theory*, Transport. Res. B-Meth., 28 (1994), pp. 269–287.
- [25] ———, *Requiem for second-order fluid approximations of traffic flow*, Transport. Res. B-Meth., 29 (1995), pp. 277–286.
- [26] M. L. DELLE MONACHE, P. GOATIN, AND B. PICCOLI, *Priority-based Riemann solver for traffic flow on networks*, Commun. Math. Sci., 16 (2018), pp. 185–211.
- [27] S. FAN, *Data-fitted generic second order macroscopic traffic flow models*, PhD thesis, Temple University, 2013.
- [28] S. FAN, M. HERTY, AND B. SEIBOLD, *Comparative model accuracy of a data-fitted generalized Aw-Rascle-Zhang model*, Netw. Heterog. Media, 9 (2014), pp. 239–268.

-
- [29] S. FAN AND B. SEIBOLD, *Data-fitted first-order traffic models and their second-order generalizations: Comparison by trajectory and sensor data*, *Transport. Res. Rec.*, 2391 (2013), pp. 32–43.
- [30] S. FAN, Y. SUN, B. PICCOLI, B. SEIBOLD, AND D. B. WORK, *A Collapsed Generalized Aw-Rascle-Zhang Model and Its Model Accuracy*, arXiv preprint arXiv:1702.03624, (2017).
- [31] M. GARAVELLO AND B. PICCOLI, *Traffic flow on a road network using the Aw-Rasclé Model*, *Commun. Part. Diff. Eq.*, 31 (2006), pp. 243–275.
- [32] M. GARAVELLO AND B. PICCOLI, *Traffic flow on networks: Conservation Laws Models*, vol. 1 of AIMS Series on Applied Mathematics, American Institute of Mathematical Sciences (AIMS), Springfield, MO, 2006.
- [33] ———, *Conservation laws on complex networks*, *Ann. Inst. H. Poincaré Anal. Non Linéaire*, 26 (2009), pp. 1925–1951.
- [34] D. C. GAZIS, R. HERMAN, AND R. W. ROTHERY, *Nonlinear follow-the-leader models of traffic flow*, *Oper. Res.*, 9 (1961), pp. 545–567.
- [35] S. K. GODUNOV, *A difference method for numerical calculation of discontinuous solutions of the equations of hydrodynamics*, *Matematicheskii Sbornik*, 89 (1959), pp. 271–306.
- [36] S. GÖTTLICH, M. HERTY, S. MOUTARI, AND J. WEISSEN, *Second-order traffic flow models on networks*, arXiv preprint arXiv:2005.12060, (2020).
- [37] B. GREENSHIELDS, *A study of traffic capacity*, *Proceedings of the Highway Research Board*, 14 (1935), pp. 448–477.
- [38] B. HAUT AND G. BASTIN, *A second order model of road junctions in fluid models of traffic networks*, *Netw. Heterog. Media*, 2 (2007), pp. 227–253.
- [39] D. HELBING, *From microscopic to macroscopic traffic models*, in *A perspective look at nonlinear media*, vol. 503 of *Lecture Notes in Phys.*, Springer, Berlin, 1998, pp. 122–139.
- [40] M. HERTY, A. FAZEKAS, AND G. VISCONTI, *A two-dimensional data-driven model for traffic flow on highways*, *Netw. Heterog. Media*, 13 (2018), pp. 217–240.
- [41] M. HERTY, C. KIRCHNER, AND S. MOUTARI, *Multi-class traffic models on road networks*, *Commun. Math. Sci.*, 4 (2006), pp. 591–608.
- [42] M. HERTY, S. MOUTARI, AND M. RASCLE, *Optimization criteria for modelling intersections of vehicular traffic flow*, *Netw. Heterog. Media*, 1 (2006), pp. 275–294.
- [43] M. HERTY, S. MOUTARI, AND G. VISCONTI, *Macroscopic modeling of multilane motorways using a two-dimensional second-order model of traffic flow*, *SIAM J. Appl. Math.*, 78 (2018), pp. 2252–2278.
- [44] M. HERTY AND M. RASCLE, *Coupling conditions for a class of second-order models for traffic flow*, *SIAM J. Math. Anal.*, 38 (2006), pp. 595–616.
- [45] F. L. HITCHCOCK, *The distribution of a product from several sources to numerous localities*, *J. Math. Phys. Mass. Inst. Tech.*, 20 (1941), pp. 224–230.
- [46] H. HOLDEN AND N. H. RISEBRO, *A mathematical model of traffic flow on a network of unidirectional roads*, *SIAM J. Math. Anal.*, 26 (1995), pp. 999–1017.

Bibliography

- [47] ———, *Front Tracking for Hyperbolic Conservation Laws*, vol. 152 of Applied Mathematical Sciences, Springer, Heidelberg, second ed., 2015.
- [48] R. ILLNER, A. KLAR, AND T. MATERNE, *Vlasov-Fokker-Planck Models for Multilane Traffic Flow*, *Commun. Math. Sci.*, 1 (2003), pp. 1–12.
- [49] M. Z. JACOBSON, *Fundamentals of Atmospheric Modeling*, Cambridge University Press, 2005.
- [50] E. KALLO, A. FAZEKAS, S. LAMBERTY, AND M. OESER, *Microscopic traffic data obtained from videos recorded on a German motorway*. <https://data.mendeley.com/datasets/tzckcsrpn6/1>, 2019.
- [51] B. S. KERNER, *Phase transitions in traffic flow*, in *Traffic and Granular Flow '99*, Springer, 2000, pp. 253–283.
- [52] ———, *The Physics of Traffic: Empirical Freeway Pattern Features, Engineering Applications, and Theory*, Springer, 2012.
- [53] A. KLAR AND R. WEGENER, *A hierarchy of models for multilane vehicular traffic I: Modeling*, *SIAM J. Appl. Math.*, 59 (1999), pp. 983–1001.
- [54] ———, *A hierarchy of models for multilane vehicular traffic II: Numerical investigations*, *SIAM J. Appl. Math.*, 59 (1999), pp. 1002–1011.
- [55] O. KOLB, G. COSTESEQUE, P. GOATIN, AND S. GÖTTLICH, *Pareto-optimal coupling conditions for the Aw-Rasclé-Zhang traffic flow model at junctions*, *SIAM J. Appl. Math.*, 78 (2018), pp. 1981–2002.
- [56] J. D. LAMBERT, *Numerical methods for ordinary differential systems*, John Wiley & Sons, Ltd., Chichester, 1991.
- [57] P. D. LAX, *Weak solutions of nonlinear hyperbolic equations and their numerical computation*, *Comm. Pure Appl. Math.*, 7 (1954), pp. 159–193.
- [58] J.-P. LEBACQUE, *Two-phase bounded-acceleration traffic flow model: analytical solutions and applications*, *Transp. Res. Rec.*, 1852 (2003), pp. 220–230.
- [59] J.-P. LEBACQUE, S. MAMMAR, AND H. HAJ SALEM, *Generic second order traffic flow modelling*, in *Transportation and Traffic Theory 2007*, 2007, pp. 755–776.
- [60] ———, *An intersection model based on the GSOM model*, *IFAC Proceedings Volumes*, 41 (2008), pp. 7148–7153.
- [61] R. J. LEVEQUE, *Numerical methods for conservation laws*, *Lectures in Mathematics ETH Zürich*, Birkhäuser Verlag, Basel, second ed., 1992.
- [62] ———, *Finite volume methods for hyperbolic problems*, *Cambridge Texts in Applied Mathematics*, Cambridge University Press, Cambridge, 2002.
- [63] M. J. LIGHTHILL AND G. B. WHITHAM, *On kinematic waves II. A theory of traffic flow on long crowded roads*, *Proceedings of the Royal Society of London. Series A. Mathematical and Physical Sciences*, 229 (1955), pp. 317–345.
- [64] T. LUSPAY, B. KULCSAR, I. VARGA, S. K. ZEGEYE, B. DE SCHUTTER, AND M. VERHAEGEN, *On acceleration of traffic flow*, in *Proceedings of the 13th International IEEE Conference on Intelligent Transportation Systems (ITSC 2010)*, IEEE, 2010, pp. 741–746.

- [65] S. MANAHAN, *Environmental chemistry*, CRC press, 2017.
- [66] P. NELSON, *A kinetic model of vehicular traffic and its associated bimodal equilibrium solutions*, in Special issue devoted to the Proceedings of the 13th International Conference on Transport Theory (Riccione, 1993), vol. 24, 1995, pp. 383–409.
- [67] G. F. NEWELL, *Nonlinear Effects in the Dynamics of Car Following*, Oper. Res., 9 (1961), pp. 209–229.
- [68] ———, *A simplified theory of kinematic waves in highway traffic, part II: Queueing at freeway bottlenecks*, Transport. Res. B-Meth., 27 (1993), pp. 289–303.
- [69] H. OMIDVARBORNA, A. KUMAR, AND D.-S. KIM, *NO_x emissions from low-temperature combustion of biodiesel made of various feedstocks and blends*, Fuel Process. Technol., 140 (2015), pp. 113 – 118.
- [70] L. I. PANIS, S. BROEKX, AND R. LIU, *Modelling instantaneous traffic emission and the influence of traffic speed limits*, Sci. Total Environ., 371 (2006), pp. 270–285.
- [71] E. PARZEN, *On estimation of a probability density function and mode*, Ann. Math. Statist., 33 (1962), pp. 1065–1076.
- [72] H. J. PAYNE, *Model of freeway traffic and control*, Math. Models Publ. Syst. Simul. Council. Proc., (1971), pp. 51–61.
- [73] B. PICCOLI AND F. ROSSI, *Generalized Wasserstein distance and its application to transport equations with source*, Arch. Ration. Mech. Anal., 211 (2014), pp. 335–358.
- [74] B. PICCOLI AND A. TOSIN, *Vehicular traffic: a review of continuum mathematical models*, in Mathematics of complexity and dynamical systems. Vols. 1–3, Springer, New York, 2012, pp. 1748–1770.
- [75] I. PRIGOGINE AND F. C. ANDREWS, *A Boltzmann-like approach for traffic flow*, Oper. Res., 8 (1960), pp. 789–797.
- [76] G. PUPPO, M. SEMPLICE, A. TOSIN, AND G. VISCONTI, *Kinetic models for traffic flow resulting in a reduced space of microscopic velocities*, Kinet. Relat. Models, 10 (2017), pp. 823–854.
- [77] A. QUARTERONI, R. SACCO, AND F. SALERI, *Numerical mathematics*, vol. 37 of Texts in Applied Mathematics, Springer-Verlag, Berlin, second ed., 2007.
- [78] A. QUARTERONI AND A. VALLI, *Numerical Approximation of Partial Differential Equations*, vol. 23 of Springer Series in Computational Mathematics, Springer-Verlag, Berlin, 1994.
- [79] P. I. RICHARDS, *Shock waves on the highway*, Oper. Res., 4 (1956), pp. 42–51.
- [80] M. ROSENBLATT, *Remarks on some nonparametric estimates of a density function*, Ann. Math. Statist., 27 (1956), pp. 832–837.
- [81] M. RÖSSLER, T. KOCH, C. JANZER, AND M. OLZMANN, *Mechanisms of the NO₂ formation in diesel engines*, MTZ Worldw., 78 (2017), pp. 70–75.
- [82] F. SANTAMBROGIO, *Optimal transport for applied mathematicians: Calculus of variations, PDEs, and modeling*, vol. 87 of Progress in Nonlinear Differential Equations and their Applications, Birkhäuser/Springer, Cham, 2015.

Bibliography

- [83] J. H. SEINFELD AND S. N. PANDIS, *Atmospheric chemistry and physics: from air pollution to climate change*, John Wiley & Sons, 2016.
- [84] S. SINHA, *Mathematical Programming: Theory and Methods*, Elsevier, 2005.
- [85] J. SMOLLER, *Shock Waves and Reaction-Diffusion Equations*, vol. 258 of Grundlehren der Mathematischen Wissenschaften [Fundamental Principles of Mathematical Sciences], Springer-Verlag, New York, second ed., 1994.
- [86] E. F. TORO, *Riemann Solvers and Numerical Methods for Fluid Dynamics: A practical introduction*, Springer-Verlag, Berlin, third ed., 2009.
- [87] J. H. TU, C. W. ROWLEY, D. M. LUCHTENBURG, S. L. BRUNTON, AND J. N. KUTZ, *On dynamic mode decomposition: theory and applications*, J. Comput. Dyn., 1 (2014), pp. 391–421.
- [88] US DEPARTMENT OF TRANSPORTATION AND FEDERAL HIGHWAY ADMINISTRATION, *Next Generation Simulation (NGSIM)*. <http://ops.fhwa.dot.gov/trafficanalysistools/ngsim.htm>.
- [89] C. VILLANI, *Optimal transport: Old and New*, vol. 338, Springer-Verlag Berlin Heidelberg, 2008.
- [90] S. VOLKWEIN, *Model Reduction using Proper Orthogonal Decomposition*, Lecture notes, University of Konstanz, 2011.
- [91] R. P. WAYNE, *Chemistry of atmospheres*, Clarendon Press, Oxford, 1991.
- [92] G. B. WHITHAM, *Linear and Nonlinear Waves*, Pure and Applied Mathematics (New York), John Wiley & Sons, Inc., New York, 1999.
- [93] S. ZEGEYE, B. DE SCHUTTER, J. HELLENDORF, E. BREUNESSE, AND A. HEGYI, *Integrated macroscopic traffic flow, emission, and fuel consumption model for control purposes*, Transp. Res. Part C–Emerg. Technol., 31 (2013), pp. 158–171.
- [94] H. M. ZHANG, *A non-equilibrium traffic model devoid of gas-like behavior*, Transp. Res. B, 36 (2002), pp. 275–290.
- [95] T. ZHANG AND Y. X. ZHENG, *Two-dimensional Riemann problem for a single conservation law*, Trans. Amer. Math. Soc., 312 (1989), pp. 589–619.
- [96] D. ZHU, Z. HUANG, L. SHI, L. WU, AND Y. LIU, *Inferring spatial interaction patterns from sequential snapshots of spatial distributions*, Int. J. Geogr. Inf. Sci., 32 (2018), pp. 783–805.